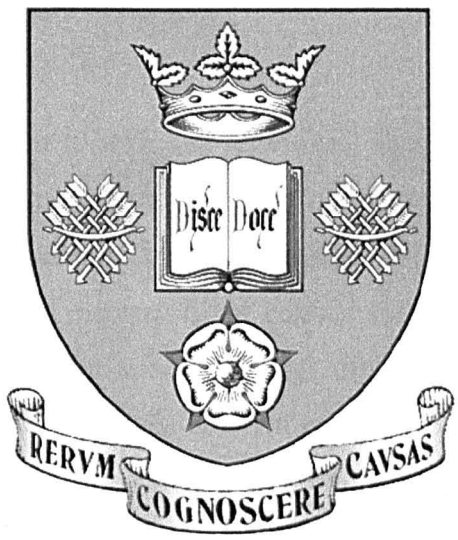

Modelling of high power density electrical machines for aerospace

By

David James Powell

A thesis submitted for the degree of PhD in the department of Electronic and Electrical Engineering at the University of Sheffield

May 2003

SUMMARY

This thesis is concerned with the electrical, thermal and mechanical modelling of electrical machines for the 'more-electric' aircraft. Two specific applications are considered viz. a permanent magnet brushless DC (BLDC) machine for an electro-hydraulic actuator for a primary flight control surface, and a switched reluctance (SR) starter/generator for the HP spool of a large civil aero-engine. As a consequence of the highly variable and often hostile ambient environment and constrained available space envelope, these electrical machines can rarely be designed in isolation, with thermal and mechanical constraints often having a significant influence on the design.

In view of these considerations, a transient lumped parameter thermal model has been developed for the BLDC machine, and validated by experimental measurements on a prototype machine at various stages of manufacture. Since the rotor cavity of the BLDC machine is flooded with hydraulic fluid leaking from the pump, fluid friction losses have been modelled, and validated by tests on a prototype machine. Optimisation of the BLDC machine airgap has also been investigated using analytical electromagnetic/fluid-dynamic modelling.

Detailed investigation of the mechanical stresses in the rotor of the HP spool machine have led to the development of a novel rotor structure for SR machines which is shown to have comparable electromagnetic performance with a conventional SR machine. A specific design of SR machine is analysed in detail in terms of dynamic current waveforms and the subsequent iron losses, and its thermal performance is modelled in a representative aero-engine environment.

ACKNOWLEDGEMENTS

I would like to express my sincere thanks to Geraint Jewell, and Dave Howe for their continuous guidance and encouragement during the course of the research. I am also grateful to Nigel Schofield for his wealth of experience in the field of electrical machines.

I would also like to thank the Engineering and Physical Sciences Research Council for the award of a research studentship, the staff in the Rolls-Royce strategic research centre, and Goodrich systems for the use of their test-rigs. Special thanks are also due to the technical staff in the Electrical Machines and Drives group who were particularly helpful in the installation of the oil cooling test-rig.

I am indebted to my colleagues in the Machines and Drives group for their friendship, good humour, and support. Finally, thanks to Pippa for all her love, support and understanding throughout the course of writing this thesis.

CONTENTS

NOMENCLATURE

Nomenclature is listed in the order in which it appears in this thesis.

EHA	Electro Hydraulic Actuator
EMA	Electromechanical Actuator
MTBF	Mean Time Between Failures
MEA	More Electric Aircraft
BLDC	Brushless DC
q_r	radiation heat transfer, W
ε_r	surface emissivity
σ_{sb}	Stefan-Boltzman constant, 56.7 e^{-9} W/m^2K^4
A	area considered for heat transfer, m^2
T_s	surface temperature, K
T_∞	temperature of ambient air, K
σ	electrical conductivity, S
δ	thickness of lamination steel, m
k_{exc}	excess loss coefficient
B	flux density, T
δ_x	maximum random offset distance in x direction, m
δ_y	maximum random offset distance in y direction, m
β	random number ($-0.95<\beta<0.95$)
ϕ	conductor diameter, m
k	thermal conductivity, W/mK
q_x	unidirectional heat flow, W
$\Delta\theta$	temperature differential
k_{sl}	slot liner thermal conductivity, W/mK
k_{wdg}	conductor bundle thermal conductivity, W/mK
k_{p1}	slot liner thermal conductivity at high pressure, W/mK
k_{p2}	slot liner thermal conductivity at low pressure, W/mK
k_{wdg1}	conductor bundle thermal conductivity for process 1 winding, W/mK

Re	Reynolds number
ρ	density, kg/m^3
ω	angular velocity, rad/s
r	radius of cylinder, m
μ	kinematic viscosity, mm^2/s
δ	radial airgap length, m
Cf	surface friction coefficient
P_{drag}	fluid friction loss, W
L	axial length of rotor, m
T	torque, Nm
r_1	rotor outer radius, m
r_2	stator inner bore radius, m
v_t	tangential velocity, m/s
v_a	axial velocity, m/s
C_v	velocity coefficient
Nu	Nusselt number
h	heat transfer coefficient, W/m^2K
Ta	Taylor number
r_m	mean airgap radius, m
m	mass flow rate, kg/s
C_p	specific heat at constant pressure, J/kg.K
D_{ro}	rotor outer diameter, m
B_g	airgap flux density, T
Q	electric loading, A/m
N_{ph}	number of phases
N_t	number of turns
N_c	number of coils
I_{ph}	phase current, A
D_{si}	stator inner diameter, m
Br	remanent flux density, T
μ_o	permeability of free space, $4\pi x10^{-7}$ N/A^2
lg	electromagnetic radial airgap length, m
lm	radial magnet length, m

σ_θ	hoop stress in a thick walled cylindrical disk, Pa
ν	Youngs modulus
R_1	cylinder outer radius, m
R_2	cylinder inner radius, m
d_{xy}	element edge length, m
κ	normalised element scaling factor
h_c	coil height, m
δ	skin depth, m
f	electrical frequency, Hz
μ	permeability, H/m
D_h	hydraulic diameter, m
U	axial air velocity, m/s
f	friction factor
f_s	shape factor
ΔP	pressure drop, Pa
L	length of duct, m
P_f	power loss due to frictional pressure drop, W

CHAPTER 1

INTRODUCTION

1.1 Background

International air transport is presently the fastest growing sector of transport worldwide. Technological advances in the aircraft industry have improved aircraft efficiency and reduced the costs of air transport by such a degree that worldwide air passenger traffic has grown at an average yearly rate of 9% since 1960 [BOE 96], with freight and mail traffic also growing by some 11 and 7%, respectively. In 1995 for instance, some 1.3 billion passengers were carried by the world's airlines [BOE 96].

Despite this strong historical growth, the industry remains relatively volatile and prone to sudden short term declines. However, Button [BUT 99] has postulated that passenger air traffic will grow at a rate of between 5 and 7% into the foreseeable future, with much of the growth in the Asia-Pacific region (up to 9% a year), while more recent predictions by the Airbus Group [AIA 02] have suggested that the growth in the passenger markets will slow to 4.7% up to 2020, again with more of the market share moving towards Asia-Pacific (the Chinese domestic market is predicted to grow by over 8%). The vast majority of large civil aircraft with >500 seats operate in Asia and the demand for such aircraft, as the Asian pacific economies grow, is likely to increase. Further, these very large aircraft will be able to carry a greater volume of passengers through the worlds' increasingly congested airports and air traffic control systems.

This projected increase in air travel will occur against a background of ever-increasing concerns regarding the environmental impact of air traffic. Although this was largely confined to problems of noise pollution in the past, concern has more recently shifted to atmospheric pollution around airports and damage caused to the atmosphere by jet engine exhaust emissions at cruising altitude. This change is a result of increased public awareness of issues such as greenhouse gas emissions and the potential damage to the

ozone layer. In terms of pollution on a global scale, British Airways [BA 99] estimated that their aviation fleet as a whole produced some 18 million metric tons of carbon dioxide, 79000 tons of nitrogen oxides, and 5000 tons of sulphur dioxide in 1999, and thus contributing significantly to world greenhouse gas emissions. nitrogen oxide emissions in the middle atmosphere where the majority of jet-engine aircraft cruise may also affect the ozone layer, and sulphur dioxide emissions at lower levels may contribute to acid rain. These examples of pollution to the atmosphere are a by-product of the combustion process, and are thus fundamental to the operation of a jet engine.

From these examples it is clear that there are many commercial and environmental pressures on aircraft operators, and in turn aircraft manufacturers, to improve the performance of future aircraft. However, aircraft safety is a critical feature that permeates the entire civil aerospace industry and often hinders the adoption of radical technologies. Air travel remains, by most objective criteria, the safest way to travel. The current rate of incidents involving all carriers in the USA has remained fairly constant since the 1970s at around 0.05 fatalities per 100,000 departures or 8×10^{-4} per million aircraft-miles [BOE 96]. During the period 1987 to 1996, there were 205 commercial jet-engine aircraft losses in the world, with over 65% of these crashes occurring during take-off or landing, where the airframe, engines, flight control actuators, and hence power generation capacity are generally at there most stressed from a mechanical, electrical, and thermal point of view. Despite the remarkable safety record of civil aircraft, the potentially catastrophic consequences of component and/or system failure dictate that it is by nature very conservative, even compared to the automotive sector where safety is also of paramount importance. However, even against this conservative background, there is growing interest in adopting new technologies for performing key functions on aircraft. Arguably, the most significant in terms of its far-reaching effects on aircraft architecture, is the wider adoption of electrical systems in preference to established hydraulic, pneumatic and mechanical systems.

1.2 The more-electric aircraft and more-electric engine

In the civil aircraft market, it is likely that ever more functions on future aircraft will be implemented using electrical systems, as the necessary improvements in electrical drive systems are realised. Although there are several ancillary systems in which electrical drives are being proposed, e.g. brake actuation, fuel pumping and environmental control systems, the most significant electrical loads are likely to be those associated with the adoption of electrically actuated flight control surfaces. The flight control surfaces of current modern large civil aircraft are generally powered by means of three independent and segregated hydraulic systems that deliver hydraulic power to actuators that are local to the flight surface under control, as shown in figure 1.1. In general, these systems are complex to install and costly to maintain, comprising substantial lengths of high-pressure hydraulic lines, and hence fluid volume and weight.

The concept of ultimately replacing all hydraulic actuation systems with entirely electromechanical actuation systems is commonly referred to as the *all-electric aircraft* (AEA). However, it is likely that the so-called *more-electric aircraft* (MEA) will be adopted as an important intermediate step. In the MEA, it is proposed to gradually convert more aircraft functions to electrical systems rather than using hydraulic or high-pressure bleed air, which is presently the case. In some cases, electrical systems may be used in conjunction with tailored hydraulic sub-systems as an interim technology.

Future large civil aircraft which embrace either the AEA or MEA concepts are likely to have many electrically powered control surface actuators (potentially up to 50 or so - each having a peak power capability of several tens of kWs), together with increased ancillary electrical loads. The resulting step change in aircraft electrical loading has far reaching implications for the electrical generation systems. Indeed, future electrical power requirements are unlikely to be met by simply scaling up existing technologies such as generators driven by take-off shafts and gearboxes, particularly as they suffer from a number of inherent drawbacks in relation to efficiency, reliability, maintainability and can compromise engine design. To address the power generation

challenges, considerable effort is being directed towards realising the so-called 'more-electric engine', in which electrical machines are integrated within the main aircraft engines.

1.3 Historical background to the 'more-electric' aircraft

The concept of the more-electric aircraft is by no means new, and indeed, the first civil aircraft equipped with fly-by-wire technology, the Airbus A320, made its maiden flight on 22nd February 1987 [PRA 00]. Aircraft with electrically powered actuators first flew in the late 1940's, on aircraft such as the Bristol Brabazon [MOI 01] and later on the Vickers Valiant V-Bomber [JON 99]. The Brabazon was the first aircraft with 100% powered flying controls, electric engine controls, and the first with an AC power system. Large weight savings were made over conventional aircraft of the day due to the individually highly optimised systems. Electrical machines used in actuation systems on the Bristol Brabazon and Vickers Valiant were typically low power density machines, with a torque per rotor volume of less than 10kNm/m^3.

Torque density or torque per unit rotor volume is often quoted as a means of comparing the specific power density of machines [MIL 93]. Typical values of torque per rotor volume for various types and size of electrical machine with different types of cooling are shown in Table 1.1. Traditionally, electric actuation was a heavy and cumbersome alternative to hydraulics (which can achieve equivalent torque per rotor volume figures of ~500kNm/m^3). As a consequence, hydraulic systems have historically dominated flight control surface actuators, landing gear, steering, brakes and various secondary actuators in modern civil and military aircraft.

However, with the advent of rare earth permanent magnet materials in the early 1980's, improvements in electrical steels, and more recently in high power semiconductor devices, higher power density electrical machines and their associated converters have emerged as a potentially competitive option for next-generation flight surface actuation.

Although they are still unable to directly match the specific torque capacity of hydraulic actuators, there are a number of system level benefits which merit serious consideration, e.g. enhanced efficiency, benefits of electrical distribution over hydraulic distribution, reduced maintenance etc.

The benefits and challenges of the more-electric aircraft have been widely researched and published, particularly in the United States, where military programs provide ideal technology platforms for such research. The all-electric airplane was first conceived as a more efficient means of transport as far back as 1980 [CRO 90], at a time when concerns over energy conservation and escalating fuel costs threatened to hinder the growth of the aerospace industry as a whole. The momentum behind the more-electric initiative was strengthened in 1991 when Northrop/Grumman were awarded a long-term US Department of Defence project to develop a power management and distribution system for the more-electric aircraft [MAL 97, 99]. The programme sought to develop power generation architectures with twice the reliability of existing systems by 1998, and five times the reliability by 2003. Specific goals included a starter/generator with 25000 hrs MTBF, highly reliable fault tolerant distribution, and a 50% power density and reliability improvement in power electronics and motor drives.

1.4 Perceived benefits of the more-electric aircraft

The relative merits of electrical and hydraulic actuation systems are influenced to a significant degree by aircraft size. Electrically powered actuation becomes more attractive to air-framers as the size of the aircraft increases, as hydraulic distribution networks have been shown to have a higher mass per unit length for a given operating power level than an equivalent electrical system. Despite the fact that the fundamental torque and force density of hydraulic machines are much higher than their electro-magnetic counterparts, the elimination of the hydraulic fluid distribution system leads to the electrical flight control systems having a higher net power density. EHAs are also safer in terms of fire and corrosion risk. Studies carried out in the U.S.A [CLO 97] have

identified that the adoption of more-electric technologies could yield potential benefits including:

- 6.5% reduction in take-off gross weight
- 3.2% reduction in life-cycle costs
- 5.4% increase in MTBF
- 4.2% reduction in maintenance man-hours per flying hour.

However, these estimates are based on specific weight savings of each active component in the various aircraft systems, and do not consider the contributory effects of an increased volume due to the fundamentally lower power density of EMAs and EHAs. Moreover, no specific consideration was given to the large increase in the number and size of electrical contactors, isolators and other switchgear that is required to attain an acceptable level of reliability and partitioning.

More-electric technology has been identified as being especially attractive to military aircraft since elimination of a centralised hydraulic power source reduces the vulnerability of the aircraft in a combat situation [MAL 97]. Indeed, electrically powered flight control surface actuators have been under test in aerospace applications in the military field since the mid 1990's. For example, both EHA and EMA actuators have been tested on the left aileron of a General Dynamics F/A-18 Hornet systems research aircraft under the Electrically Powered Actuator Design (EPAD) validation program [WIL 97]. The United States Air Force has embarked upon an MEA initiative encompassing starter/generator technologies, power distribution systems and electric actuation technologies [ELB 97] [MAL 96, 97, 99]. Table 1.2 lists some of the key projects in the development of electrically powered actuation technology in the United States, and in Europe. In summary, although the benefits in terms of weight saving, MTBF and safety are difficult to quantify without a specific study and the availability of proven hardware, the advantages of the MEA are well recognised, and in turn provides a strong driver for the development of key enabling technologies, in particular high

reliability electrical machines and associated power electronic converters. Many of the challenges of realising robust hardware are common to both actuation and power generation systems, although as will be demonstrated in this thesis, these do offer somewhat different constraints and performance requirements.

1.5 Electrically actuated flight control surfaces

Figure 1.2 shows the flight surfaces on a typical aircraft that could potentially be controlled by electrical actuation systems. Electrical actuation of flight surfaces can be realised using electro-mechanical actuators (EMA), which utilise a mechanical gearing and clutch system coupled to a lead-screw mechanism, or electro-hydraulic actuators (EHA), in which an electrically driven hydraulic pump is connected to a conventional hydraulic ram. With current technology, EHAs have higher overall force densities than equivalent EMAs and hence they may well remain as the preferred choice for highly demanding applications such as actuation of the rudder in a large aircraft. It is envisaged ultimately that the trend towards the all-electric aircraft may well result in the total adoption of EMAs, with the total exclusion of hydraulic devices from the aircraft control systems. However, currently civil air-framers favour EHA technology, since it retains many of the characteristics and advantages of conventional hydraulic actuators, and requires minimal change in system definition. Hence, EHAs are seen as an intermediate but nonetheless necessary development in proving new technologies and gaining operational experience.

The adoption of EHAs to de-centralise the three hydraulic systems of an aircraft eliminates a significant proportion of the heavy and unreliable hydraulic lines that currently distribute power around the aircraft. In the particular EHA system studied in this thesis, hydraulic power is produced locally to the flight control surface via a speed and torque controlled integrated electric motor and pump. The volume of hydraulic fluid in such a de-centralised system is greatly reduced, as the fluid is no longer routed along the length of the fuselage, but is confined to individual actuators at the flight control surfaces. This has significant benefits in terms of enhancing reliability and safety of the

actuation system with regard to corrosion caused by leakage, and more importantly mitigating safety concerns over the risk of fire in the hydraulic systems. Each EHA system comprises a BLDC motor and associated power electronic inverter, a slipperless hydraulic piston pump, hydraulic ram, accumulator, and various hydraulic control and safety valves. The system is shown schematically in Fig. 1.3, while the proposed packaging of such a unit for service is shown in Fig. 1.4.

The ability to control the speed of the pump enables a fixed angle swash plate to be employed, which offers significant simplifications and increased reliability when compared to variable angle swash-plate pumps [CRD 96]. The slipperless type piston pump which is employed in this EHA has an inherent axial leakage flow, and would in many applications be sealed from the motor by means of an appropriate dynamic seal. However, concerns over the reliability of such seals have resulted in a design that eliminates the need for any seals between the pump and machine. Hence, the fluid leakage path is routed through the machine, causing substantial losses due to fluid friction and subsequent heat dissipation in the airgap, while also providing some degree of additional cooling.

Given the safety critical role of many control surfaces, the management of potential failures plays an important role in both their design and subsequent operation. At present, the strategy for managing failure modes in primary flight control surface actuators (i.e. rudder, ailerons, flaps) is one of active/standby, in which three independent actuators are connected to each individual control surface (each having the capability to perform the necessary function in the event of a failure of one or both of the other actuators). This is known as triplex redundancy, and is commonplace in civil aircraft. Military aircraft have taken this approach a step further by adopting quadruplex redundancy systems that provide continued capability even following a high degree of damage. The EHA system considered in this thesis follows the same basic triplex redundancy design seen in most modern civil aircraft, i.e. there are three separate EHAs on each surface. In the event of a failure of the active actuator, a standby actuator is brought on-line and the failed actuator is switched to a so-called damping mode in

which the hydraulic pump is switched out of the hydraulic circuit, allowing hydraulic fluid to flow via a restrictor valve in a shorted loop from either side of the ram, as illustrated in figure 1.3. The duplication of the complete actuation system relaxes the component redundancy that would otherwise have to be included in the actuator drive-train.

Thus, in the active/standby system, each EHA need only achieve the same level of reliability as its hydraulic counterpart, since the system level fault tolerance requirements are met by employing sub-system redundancy. Consequently, the electrical machine and its associated power electronic converter can have a fairly conventional topology (e.g. a 3 phase star connected machine and a conventional 6 switch converter), as opposed to so-called 'fault-tolerant' drive topologies which have been proposed for other safety critical applications [HAY 98] [MEC 99]. These fault-tolerant machines and converters may well feature prominently as candidate machines for the next-generation aircraft as they offer the potential for built-in redundancy, e.g. by complete separation of the windings, the use of separate H-bridge converters in the converter, the use of 1 per unit reactance windings to limit fault currents. This approach to internal fault tolerance avoids the need for the duplication that is required in duplex or triplex redundancy systems. This has obvious benefits in terms of weight reduction, while reliability of the system is designed to meet or exceed that of the multi-component duplex or triplex redundant systems that they are designed to replace. The general requirements for a fault tolerant power system have been described previously by White [WHI 95] and can be equally applied to a fault tolerant drive systems with minor modifications to the terminology. The key features are:

- Partitioning and redundancy
- Isolation between units
- Fault detection and reporting
- Continued operation until the next service opportunity

A typical fault tolerant BLDC machine topology is illustrated in Figure 1.5. The machine stator is wound such that it provides the physical, thermal, electrical and magnetic isolation between phases by having one concentrated winding which fills the entire slot either side of a tooth. Hence if the machine has n teeth, then it is wound with $n/2$ coils. The mutual coupling between phases is designed to be very low (typically <5% [MIT 02]). In a permanent magnet fault tolerant machine, the synchronous reactance X_s is normally designed to be 1.0 per unit so that rated current is generated in a short-circuited phase, thus maintaining the same level of dissipation in that particular coil, albeit that the overall copper losses in the machine is increased as the currents in the remaining healthy phases are increased to maintain the rated torque. However, the requirement to achieve 1.0 per unit reactance usually involves major design penalties for fault tolerant machines, as a higher reactance design often requires 10-20% increase in the total mass of the machine due to deeper slots and thicker tooth tips in order to encourage more inter-pole leakage in the stator to boost the inductance. Fault tolerant machines have been proposed in the development of various aerospace electrical drive systems for applications such as EMA's, [GRI 98], fuel pumps [HAY 98], and aero-engine starter/generator systems [MAC 89a].

Although fault tolerant machines provide an improved degree of reliability in terms of electrical failures, they do not provide any fault tolerance with respect to failures in the mechanical system, in particular the bearings. It has been demonstrated that bearing failures are statistically by far the most common failure mechanism in the vast majority of electrical machines. By way of illustration, in military electrical machines in the range 10-100kW, mean time between failures (MTBF) is approximately 7.1×10^{-6} failures per hour, with 95% and 2% due to bearing failure and stator winding failure respectively. For industrial machines rated less than 50kW, the MTBF is 6.31×10^{-6} hours, with 51% due to bearings, and 16% due to winding failures [TAV 99]. Therefore, any fault tolerant application must be considered carefully in view of these statistics, particularly when considering actuation for primary flight control surfaces that are fundamental to the stability of the aircraft. One long-term possibility for addressing the

problems of bearing failure is to levitate the rotor using either magnetic bearings, or so-called self-bearing machines (in which the stator winding performs the dual role of torque production and rotor levitation) [OKA 96] [OOS 96]. However, there are considerable research issues to be addressed before such machines are a sufficiently mature and well-proven technology to be considered for service. Hence, in this particular application a conventional electrical machine topology is likely to result in a similar MTBF for the system as a fault-tolerant machine.

1.6 Future aircraft electrical power generation

Electrical power generation requirements will inevitably feature prominently in next-generation civil aircraft. As well as the actuation systems described previously, increased levels of electrical power will be required by galley loads, satellite navigation /communications and advanced in-flight entertainment systems. By way of illustration of this trend, a typical large civil aircraft in the 1960s required ~40kVA per engine, whereas modern civil aircraft require upwards of 200kVA per engine. It is envisaged that very large, next-generation civil aircraft such as the Airbus A380 will require in excess of 350kVA per engine [MOI 99] in order to meet the spiralling demand in electrical power. In order to achieve this increased generating capability, it is inevitable that the generators will become increasingly integrated into the aircraft engine itself. However, the architecture and operating requirements of large aircraft engines impose severe constraints on electrical machine design.

In its most elementary form, a jet engine consists of three main parts: a compressor, a combustor, and a turbine as shown schematically in fig. 1.6. The compressor stage compresses the incoming air to a high pressure (typically 150psi), which is then fed into the combustor. Fuel is introduced to the high pressure air in the combustor where it is burnt continuously, the resulting high pressure, high velocity gas being forced out through the turbine, which recoups a proportion of the energy from the 'jet' of exhaust gas to drive the compressors, thus maintaining a constant flow of high-pressure air

through the combustor. Whereas this basic mechanism is common to all gas-turbine aero engines, the final thrust is derived by different means depending on the demands of the particular application.

In a simple jet engine (such as those which dominate military aircraft), thrust is derived by the rapid expulsion of exhaust gases from the rear of the engine. However, although this provides extremely high thrust densities (particularly with features such as after-burners), it is inefficient in terms of fuel consumption. Large civil aircraft employ high-bypass, turbo-fan engines, which employ either two-shaft designs (used by General Electric and Pratt and Whitney), or three-shaft designs (used by Rolls-Royce). In a three-shaft engine, the three concentric shafts (or spools) rotate at different speeds and are generally classified in terms of their operating pressures, viz. the low-pressure (LP), intermediate-pressure (IP), and high-pressure (HP) spools as illustrated by figure 1.7. The inlet air is compressed in turn by the LP, IP and finally HP compressors before entering the combustor. The high velocity exhaust gases drive the HP, IP and finally LP turbines. The final stage LP turbine drives the LP shaft and hence the very large LP compressor fan. This large compressor fan generates most of the thrust in a turbo-fan engine, by driving large volumes of air at a relatively low velocity through the engine nacelle, which in effect by-passes the core (in contrast to a pure jet engine that moves small amounts of air at high velocity). This airflow is known as by-pass air, with a by-pass ratio defined as the ratio between the volume of by-pass air to the volume of air flowing through the core of the jet engine. Bypass ratios of 5:1 are common in modern civil turbo-fans, with the large compressor fan producing as much as 80% of the thrust [COH 96]. Although inevitably more complex, three-shaft designs tend to offer greater fuel economy than a double or single-shaft design [COH 96].

The electrical power required for various aircraft systems is currently generated using a constant-speed, wound-field, synchronous machine which is mounted outside the main core of the engine. The generator requires a constant speed input in order to generate an AC output with a constant frequency. Since the engine speed typically varies over a 2:1

range from take-off to cruise, a constant speed drive (CSD) mechanism is required to continuously vary the effective gearing between the engine take-off shaft and the electrical machine. This is accomplished by means of a variable hydraulic transmission that is mechanically linked to the HP spool via external, intermediate, and internal gearboxes. These are complex hydro-mechanical devices that by their very nature are not highly reliable. Figure 1.8 shows a simplified representation of a typical three-shaft turbo-fan engine with accessory gearbox, and constant speed drive, whilst fig. 1.9 illustrates a typical external gearbox for a large civil aircraft. However, the losses generated in these CSD mechanisms are very high, and the complex oil systems involved in lubricating and cooling the gearbox and electrical machine are a major factor in determining the maintenance schedules of aero-engines. In an attempt to overcome this problem, several alternatives have been considered for directly coupling the generator to the engine. Variable-speed, constant frequency systems (VSCF) have been employed on military and civil aircraft, in which the generator is interfaced to the supply via a cyclo-converter [ELB 97]. Another system which has received considerable attention is the use of variable frequency AC systems since these avoid the need for any power electronic converters (which are currently viewed as being considerably less reliable than the generators themselves). Table 1.3 lists the recent developments in civil and military aircraft power systems.

The 'more-electric' engine concept envisages electrical machines integrated co-axially with the engine spools, to supply electrical power directly to the aircraft system loads, thus eliminating the need for a large accessory gearbox and take-off shaft. Moreover, it is proposed that the various hydraulic pumps, fuel pumps, governors and the air-starter which are shown in fig. 1.9 would be replaced with electrical counterparts, with the task of engine starting being performed by an embedded electrical machine integrated with the HP spool [FER 95] [RIC 88] [RIC 95] [RAD 92] [RAD 98]. The major perceived benefits of the all/more-electric engine that have been identified in key trade studies are: [MOI 99].

- Improved specific fuel consumption
- Simplified power-plant/engine architectures
- Improved reliability
- Reduced operating and maintenance costs
- Reduced weight
- Reduced engine change times
- Scope for novel nacelle designs and hence aerodynamic efficiency gains
- Improved power-plant/airframe integration
- Scope for controlled power transfer between shafts

One potential configuration of a three-shaft more-electric engine is shown in fig. 1.10. In the particular case shown, electrical machines are incorporated on all three spools. In principle, each of these machines can operate in both motoring and generating modes, thus providing integral starting capability (via the HP spool machine), power generation from all three spools when appropriate, and allow a degree of controlled power transfer between the shafts.

Whereas the integration of electrical machines within an engine has several advantages, it presents an extremely challenging environment, particularly with regard to temperature. Figure 1.11 shows the maximum temperature variation within a Rolls-Royce RB-211 turbo-fan engine. The region near the HP/IP bearing housing (the region in which the HP machine will be located) reaches temperatures of ~350°C under full load engine conditions. The HP spool machine is also exposed to the highest mechanical loads since its rotational speed is ~15,000 - 20,000 rpm.

1.7 Design of electrical machines for aerospace application

As will be evident from the preceding review of the more-electric aircraft and the more-electric engine, there are several challenging constraints on the design of electrical machines for use in aircraft. By way of illustration, although a pump motor for an EHA and a starter/alternator for the HP spool have very different performance specifications,

they have several key requirements which are common to the all electrical machines in aircraft, viz:

- High power densities to minimise system weight
- High reliability to ensure safe operation with minimal redundancy and over-rating
- An ability to operate in highly variable, and often harsh, environmental conditions
- An ability to operate with highly transient duty cycles without over-rating (and hence over-sizing) the machine.

It is worth noting that efficiency is often not a paramount consideration, apart from its consequent impact on dissipation and hence power density. Another frequently encountered requirement is the need to integrate the machine closely with its prime-mover or end-effector. Moreover, in system level optimisation, little weighting is often given to the demands of the electrical machine, particularly within an aero-engine where the electrical power typically constitutes less than 1% of the total power flow (e.g. a large civil engine such as the Rolls-Royce Trent series where the powers are ~350kVA and ~50MW respectively). Thus electrical machines are often designed to operate in severely confined space envelopes with non-optimal geometries (e.g. stators with very short axial lengths relative to their diameters), as this often results in the best system level solution in terms of engine layout.

As a consequence of these factors, which manifest themselves to differing degrees in various aircraft applications, the design of high power aerospace electrical machines (i.e. >10kW) often requires very different considerations and analysis tools when compared to electrical machines for less demanding industrial applications, for example. Although based on the same design principles, the higher stress levels (thermal, electrical and magnetic) encountered in aerospace applications, requires far greater cognisance of the external systems and thermal / mechanical issues than a comparably rated machine for more benign applications.

This thesis addresses many of the research issues associated with the realisation of high performance electrical machines for next-generation aircraft systems by focussing on two specific machines, viz. a permanent magnet brushless DC (BLDC) machine for an EHA and an embedded HP spool starter-generator for a large civil engine. As shown by table 1.4, these applications have somewhat contrasting performance specifications and operating environments. The research findings presented in chapters 2 and 3 on the EHA system are primarily concerned with the thermal modelling and design optimisation of a pre-existing machine design which operates in a well defined environment and whose design synthesis was relatively unconstrained, albeit that there was a considerable premium associated with reducing system mass. In contrast, chapters 4 to 6 are concerned with the design synthesis of an HP spool generator, which requires concurrent consideration of its electromagnetic, mechanical and thermal behaviour since the design is severely compromised by the combination of a very limited space envelope, high rotational speeds (and hence high mechanical stresses) and an ambient temperature of ~350°C. This latter example serves to quantify, in a representative example, the performance trade-offs that result from closely integrating an electrical machine into the harsh environment of an aircraft engine.

1.8 References:

[AIA 02] Airbus Industrie Annual, 1997, 1999, 2000, 2002.

[BA 99] British Airways annual environmental report. BA report number 4/99, 1999.

[BAU 94] K.A.Bauer, S. Geson, D.M. Griffon, A.K. Triha, E.J. Woods. 'Fly-by-Light/Power-by-Wire Integrated requirements analysis and preliminary design: Boeing results,' NASA contractor report 4590, NAS1-19360, April 1994.

[BLA 97] D.E. Blanding. 'An assessment of developing dual use electric actuation technologies for military aircraft and commercial application.' Proceedings of the Intersociety Energy Conversion Engineering Conference, Vol. 1, Aerospace Power Systems and Technologies, 1997, 97517, pp. 716-721.

[BOE 96] Boeing Commercial Airline Group Annual A. 1996. Air Cargo Forecast.

[BUT 99] K.Button. 'The usefulness of current international air transport statistics'. Journal of Transportation and Statistics, May 1999, p.71-92.

[CLO 97] J.S. Cloyd. 'A status of the United States Air Force's More Electric Aircraft initiative.' Proceedings of the 32nd Intersociety Energy Conversion Engineering conference, Vol. 1, 1997, p. 691 – 686.

[COH 96] H. Cohen, G.F.C. Rogers, H.I.H. Saravanamuttoo. 'Gas turbine theory.' Longman publishing, 1996, ISBN: 0582236320.

[CRD 96] R.M. Crowder. 'Electrically powered actuation for civil aircraft.' IEE colloquium on actuator technology, current practice and new developments, No. 110 May 1996, London, UK.

[CRO 90] M.J.J. Cronin. 'The all-electric aircraft.' IEE review, Vol. 36, Issue 8, 1990, p. 309 – 311.

[ELB 95] M.E. Elbuluk, D. Kankam. 'Motor drive technologies for the power-by-wire (PBW) program: options, trends and tradeoffs, part 1: motors and controllers.' IEEE AES systems magazine, November 1995, pp. 37-42.

[ELB 97] M.E. Elbuluk, D. Kankam. 'Potential starter/generator technologies for future aerospace applications.' IEEE AES systems magazine, May 1997, pp. 24-31.

[FER 95] C.A. Ferraira, S.R. Jones, W.S. Heglund, W.D. Jones. 'Detailed design of a 30kW switched reluctance starter/generator system for a gas turbine engine application.' IEEE Transactions on Industry Applications. Vol 31, No. 3, May/June 1995.

[GMF 02] Airbus Global Market Forecast, September, 2002. Airbus S.A.S. 31707 Blagnac Cedex, France. Reference: CB 390.0008/02.

[GRI 98] J.J. Gribble, P.C. Kjaer, C. Cossar, L. Kelly, J.J. Bremner, T.J.E. Miller, C.J. Maxwell, R. Capewell, D.G. Moorhouse. 'Feasibility study of a large switched reluctance spoiler actuator system.' IEE Colloquium on All Electric Aircraft (Digest No. 1998/260), June 1998, p. 6/1 – 6/3

[HAY 98] J.A. Haylock, B.C. Mecrow, D.J. Atkinson, A.G. Jack.: 'Operation of a fault tolerant PM drive for an aerospace fuel pump application.' IEE Proceedings, Electric Power Applications, Vol.145, No.5, September 1998, p 441-448

[JON 99] R.I. Jones. 'The more electric aircraft: The past and the future?' Electrical machines and systems for the more electric aircraft, IEE colloquium, 1999, Ref No. 1999/180, p. 1 – 4.

[MAC 89A] S.R. MacMinn, W.D. Jones.: 'A very high speed switched-reluctance starter-generator for aircraft engine applications' IEEE Proceedings of the National Aerospace and Electronics Conference, v 4, 1989, p 1758-1764.

[MAC 89B] S.R. MacMinn, J.W. Sember. 'Control of a switched-reluctance aircraft engine starter-generator over a very wide speed range.' 899215. IEEE, CH2781 –3/89/0000 – 0631.

[MAL 96] M.A. Maldonado, N.M. Shah, K.J. Cleek, P.S. Walia, G.J. Korba. 'Power management and distribution system for a more-electric aircraft (MADMEL) – program status.' Proceedings of the Intersociety Energy Conversion Engineering Conference, Vol.1, 1996, p.148-152.

[MAL 97] M.A. Maldonado, N.M. Shah, K.J. Cleek, P.S. Walia, G.J. Korba. 'Power management and distribution system for a more-electric aircraft (MADMEL) – program status.' Proceedings of the Intersociety Energy Conversion Engineering Conference, Aerospace Power Systems and Technologies, 1997, No. 97257, p 274-279.

[MAL 99] M.A. Maldonado, N.M. Shah, K.J. Cleek, G.J. Korba. 'Power management and distribution system for a more-electric aircraft (MADMEL) – program status.' IEEE Aerospace and Electronic Systems Magazine, Vol. 14, No.12, Dec 1999, p 3-8.

[MEC 99] B.C. Mecrow, D.J. Atkinson, A.G. Jack, S. Green, J.A. Haylock, J.Coles.: 'The need for fault tolerance in an aeroengine electric fuel control system.' IEE Colloquium on the more-electric aircraft, 1999.

[MIL 93] T.J.E. Miller. 'Switched reluctance motors and their control.' Monographs in Electrical and Electronic Engineering No. 31. Magna Physics publishing 1993. ISBN 1-881855-02-3

[MIT 02] A.J. Mitcham, J.J.A. Cullen. 'Permanent magnet generator options for the more electric aircraft.' Power Electronics Machines and Drives conference, 2002, p. 241 – 245.

[MOI 01] I. Moir, A. Seabridge. 'Aircraft Systems: Mechanical, Electrical, and Avionics Subsystems Integration'. American Institute of Aeronautics and Astronautics, Inc., Reston, Virginia. Education Series, 2001. ISBN: 1-56347-506-5.

[MOI 99] I. Moir. 'More electric aircraft system considerations.' IEE colloquium on electrical machines and systems for the more electric aircraft, Ref 1999/180, p 10/1 – 10/9

[NIG 91] R.E. Niggeann, S. Peecher, G. Rozman. '270VDC/Hybrid 115VAC electric power generating system technology demonstrator'. IEEE NAECON record, 1991, pp.448-454.

[OKA 96] Y. Okada, S. Miyamoto and T. Ohishi, "Levitation and Torque Control of Internal Permanent Magnet Type Bearingless Motor", IEEE Trans. Control Syst. Tech., vol.4, no.5, pp.565-571, Sept.1996.

[OOS 96] M.Ooshima et al., "Design and Analysis of Permanent Magnet-Type Bearingless Motors", IEEE Trans. Industrial Electronics, vol.43, no.2, pp.292-299, April 1996.

[PRA 00] R.W. Pratt. 'Flight control systems: Practical issues in design implementation.' IEE Control Engineering series 57. ISBN 0-85296-766-7

[RAD 92] A.V. Radun, J. Rulison, P. Sanza. 'Switched reluctance starter/generator' SAE Technical Paper Series, 1992, No. 921974, p 1-12.

[RAD 98] A.V. Radun, C.A. Ferreira, E. Richter. 'Two channel switched reluctance starter/generator results.' IEEE Transactions on Industry Applications. Vol. 34, No. 5, Sept/Oct 1998.

[RIC 88] E. Richter. 'High temperature, lightweight, switched reluctance motors and generators for future aircraft engine applications.' Proceedings of the 1988 American Control Conference. Atlanta, USA, Jun 15-17, 1988, Vol. 88, p.1846-1851.

[RIC 95] E. Richter, C. Ferreira. 'Performance evaluation of a 250kW switched reluctance starter generator.' Conference Record of the 1995 IEEE Industry Applications 30th IAS Annual Meeting. Part 1 (of 3).

[TAV 99] P.J. Tavner, J.P.Hasson. 'Predicting the design life of high integrity rotating electrical machines'. Proceedings EMD Conference, Canterbury, September 1st – 3rd, 1999.

[WEI 93] J.A. Weimer. 'Electrical power technology for the more electric aircraft.' Proceedings of the IEEE/AIAA 12th Digital Avionics Systems Conference. 1993, p.445-450.

[WHI 95] R.V.White.: 'Fault tolerance in distributed power systems', EPE '95, pp 851-857.

[WIL 97] K. Williams, D. Brown, 'Electrically Powered Actuator Design (EPAD).' NASA/ USAF/ Navy. Release: 97-274, Nov. 1997.

Table 1.1 Typical torque per rotor volume of various types of electrical machine. Source: [MIL 93]

Machine type	Torque per rotor volume (kNm/m^3)
Small totally enclosed motors	2.5 – 7
Small industrial motors	7 – 30
High performance servo motors	15 – 50
Aerospace machines	30 – 75
Large liquid cooled machines	100 - 250

Table 1.2. EMA/EHA projects within the U.S and Europe.

Program	Time-span	Type	Flight tested
FLASH	1989 -	Smart actuation	Boeing B757
Lockheed / Parker		EHA	Lockheed C-130
EPAD	1993-1999	'Smart', EHA, EMA	General Dynamics F-18
EPICA	1993-1996	EHA	Airbus A321
ELISA	1996-2001	EHA + EMA	-

Table 1.3. Recent civil and military aircraft power system developments.

Source: [MOI 01]

Generation type	Civil application		Military application	
IDG / CF [115v AC/400Hz]	B777	2 × 120 kVA		
	A340	4 × 90 kVA		
	B737	4 × 90 kVA		
	MD-12	4 × 120 kVA		
	B747	4 × 120 kVA		
	B717	2 × 40 kVA		
	B767-400	2 × 120 kVA		
	Do728	2 × 40 kVA		
VSCF (Cycloconverter) [115v AC/400Hz)			F-18E/F	2 × 60 kVA
VSCF (DC link) [115v AC/400Hz]	B777 (backup)	2 × 20 kVA		
	MD-90	2 × 75 kVA		
VF [115v AC/380-760Hz]	Global Ex	4 × 40 kVA	Boeing JSF	2 × 50 kVA
	Horizon	2 × 25 kVA		
	A380	4 × 150 kVA		
270 VDC			F-22 Raptor	2 × 70 kVA
			Lockheed-Martin JSF	2 × 50 kVA

Table 1.4. Top-level specification of the electrical machines under investigation in this thesis.

Specification	BLDC machine for the EHA application.	SR starter generator for the HP spool of an aero-engine.
Mass requirement	Minimum	Minimum
Max outer diameter (mm)	None specified	400
Minimum inner diameter (mm)	None specified	200
Max total length (mm)	None specified	100
Max torque (Nm)	55	200
Maximum speed (rpm)	9000	15000
Rated power (kW)	4.0	100
Max ambient temperature (°C)	70	350

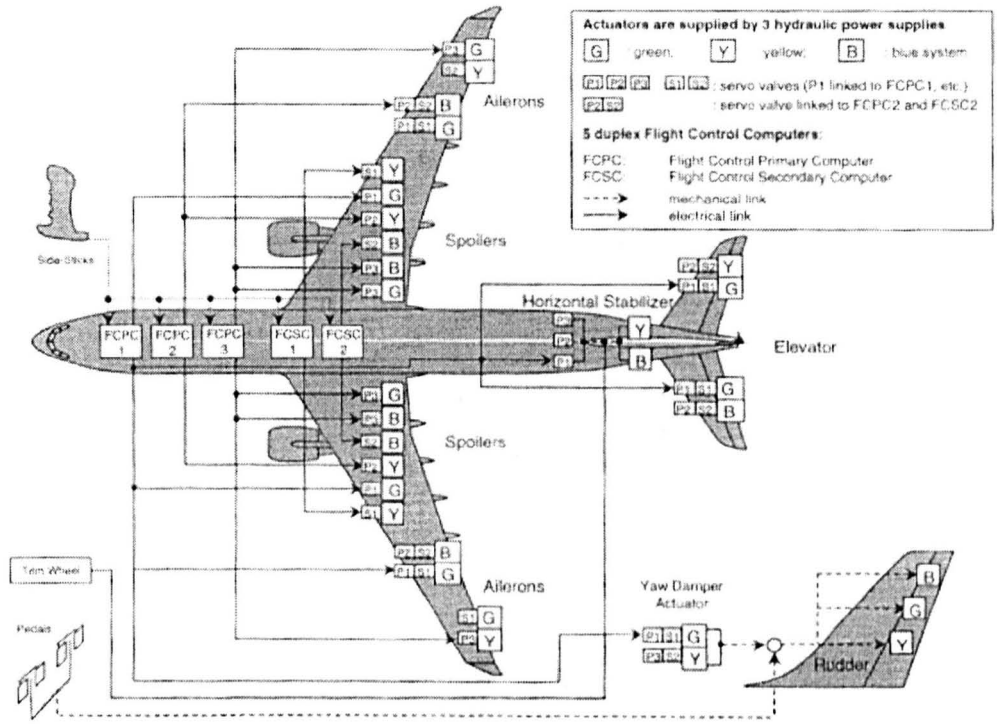

Figure 1.1. Three segregated hydraulic systems on a large civil aircraft

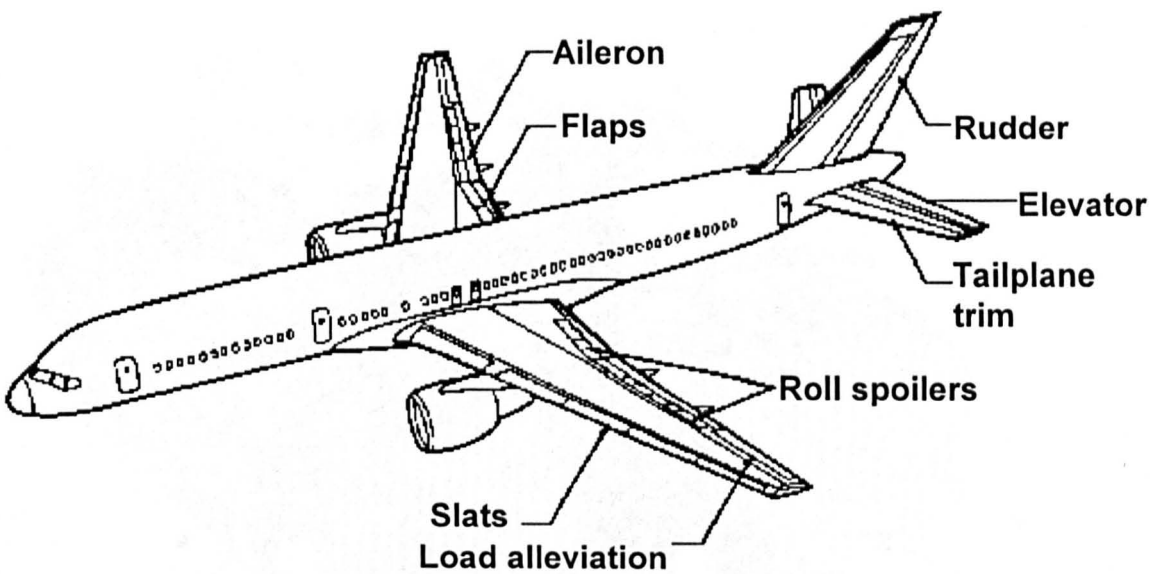

Figure 1.2. Flight surfaces suitable for electric actuation technology (EHA/EMA).

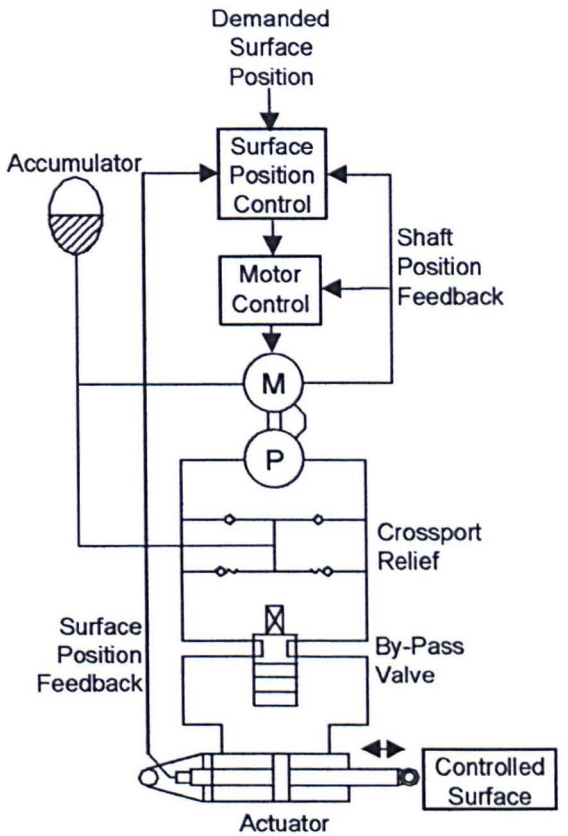

Figure 1.3. Electro-hydrostatic Actuator (EHA) system diagram.

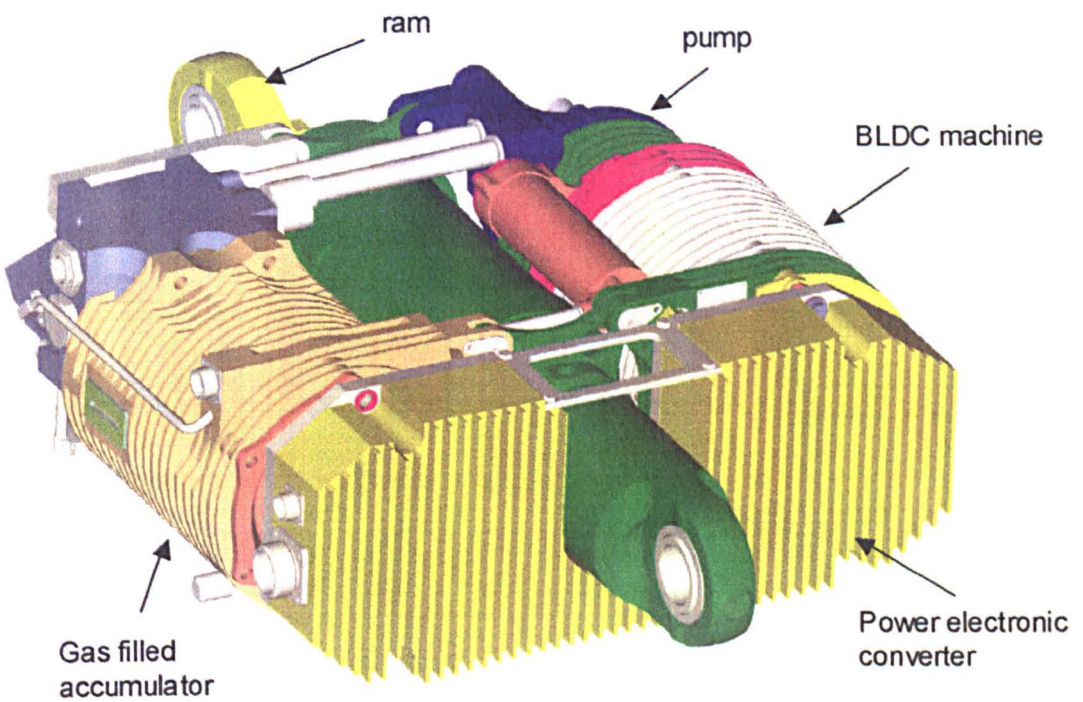

Figure 1.4. Proposed packaging of the EHA system.

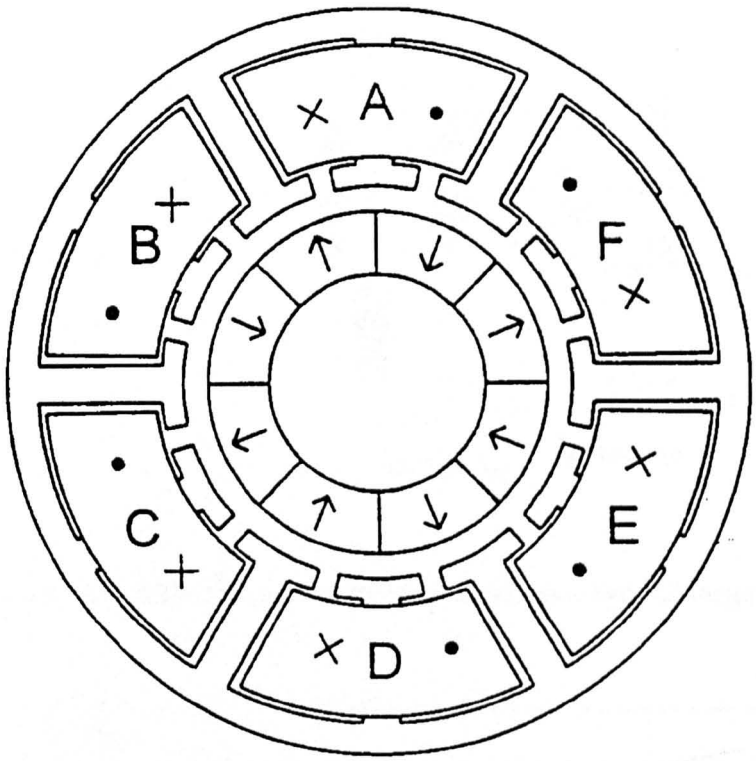

Figure 1.5. Fault tolerant permanaent magnet motor design showing the single coil per slot design, and large tooth tips to increase the reactance to 1.0 per unit.

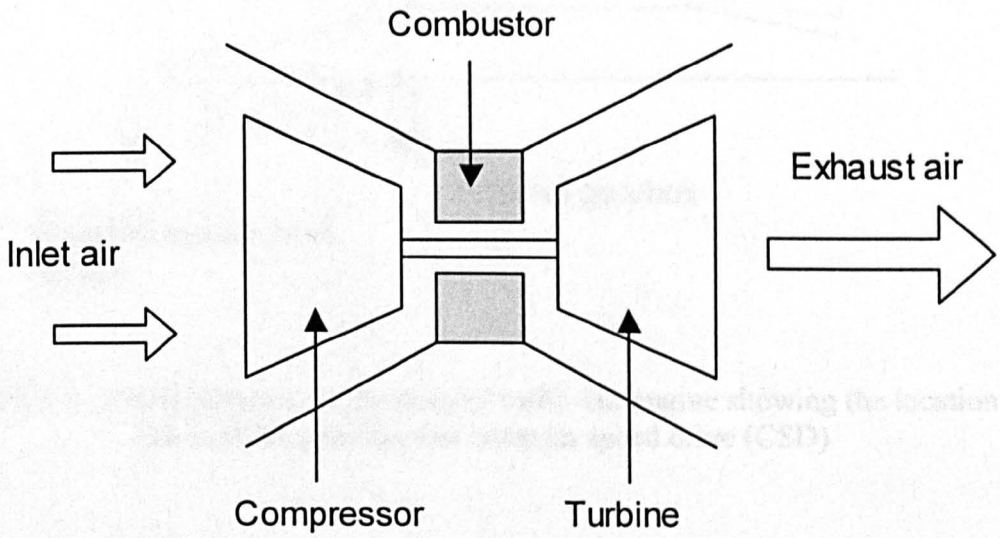

Figure 1.6. Simplified illustration of a gas turbine engine.

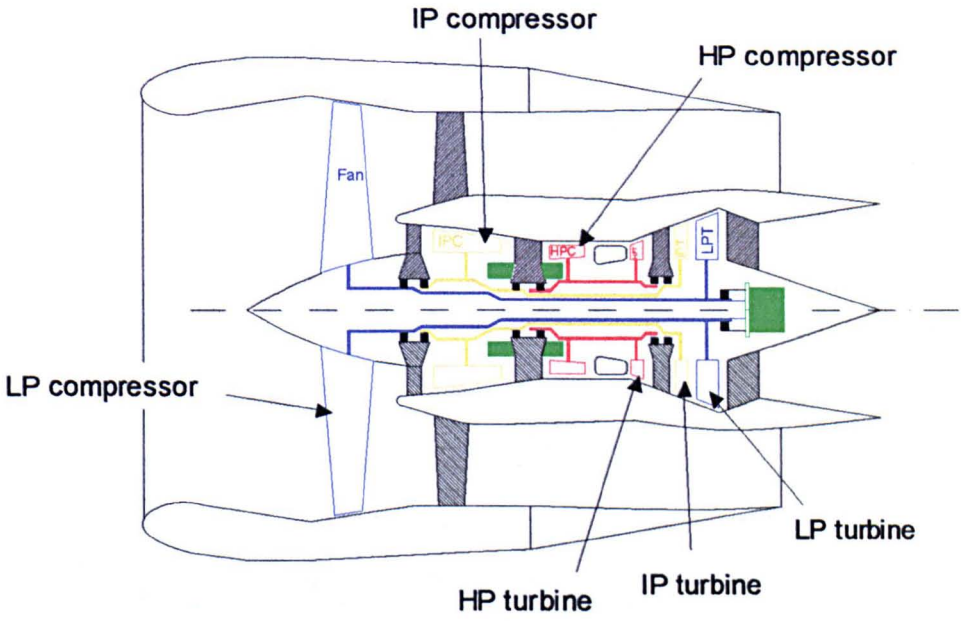

Figure 1.7. Location of the three rotating spools within a typical large civil aero-engine.

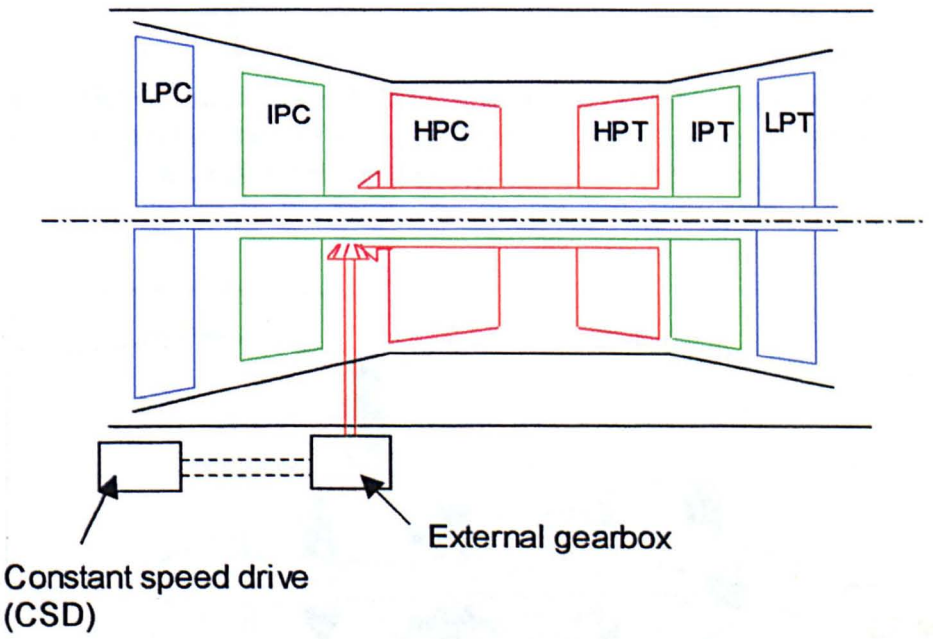

Figure 1.8. Cross-section of a three-spool turbo-fan engine showing the location of the external gearbox and constant speed drive (CSD).

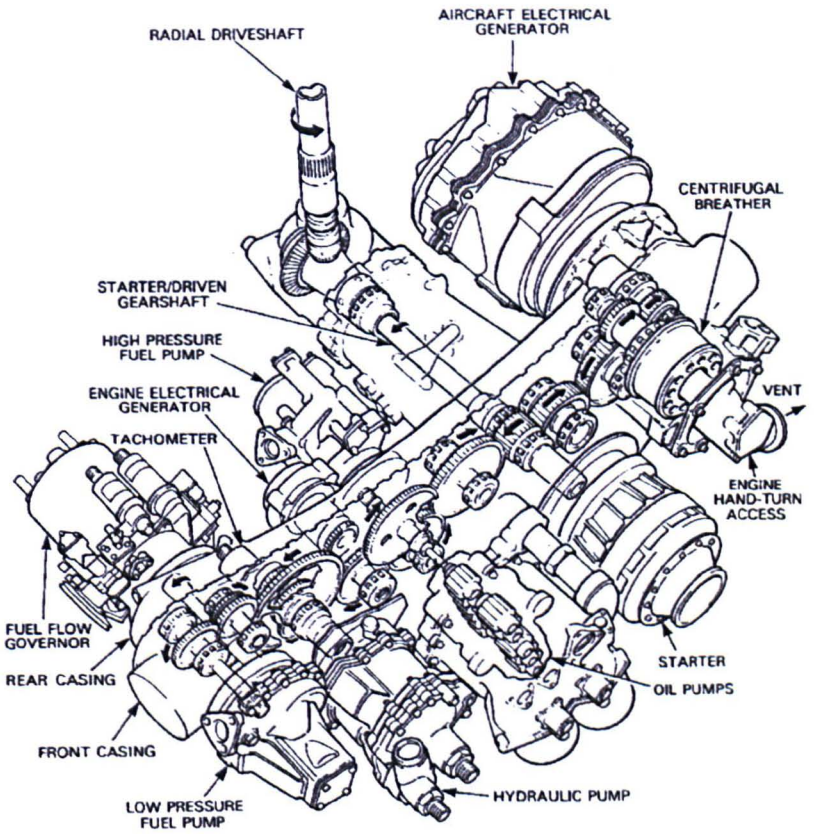

Figure 1.9. Typical external gearbox for a large civil aircraft showing the electrical generator (top) and air starter (bottom right) as is commonplace on the majority of large civil aero-engines. [Source: Rolls-Royce]

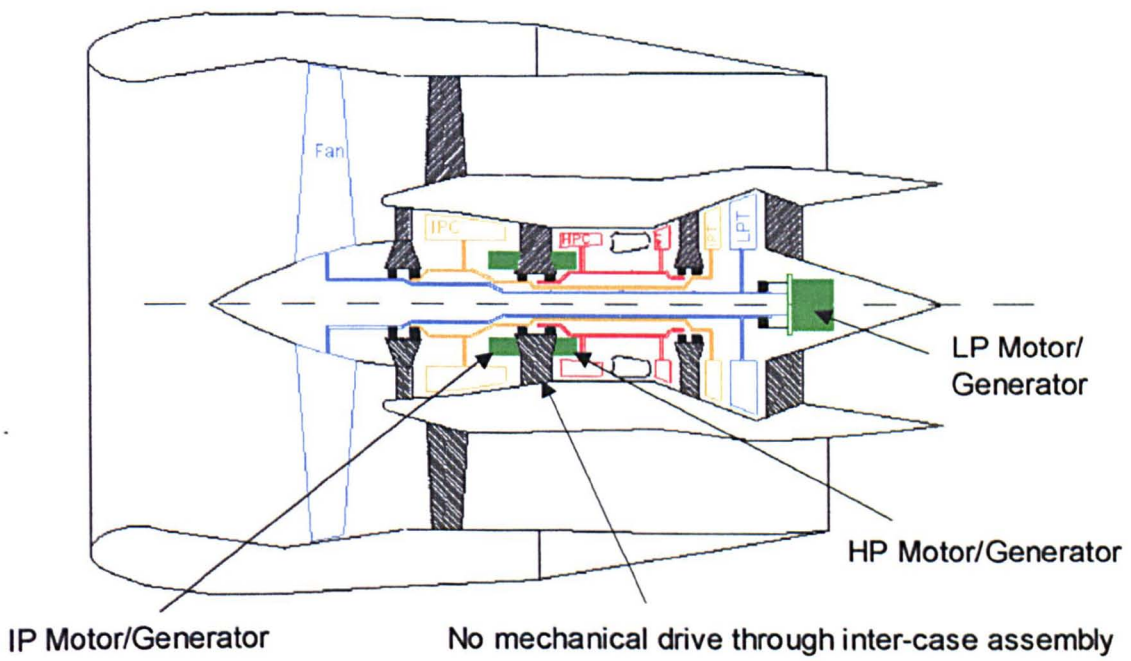

Figure 1.10. One potential configuration of a three-shaft more-electric engine.

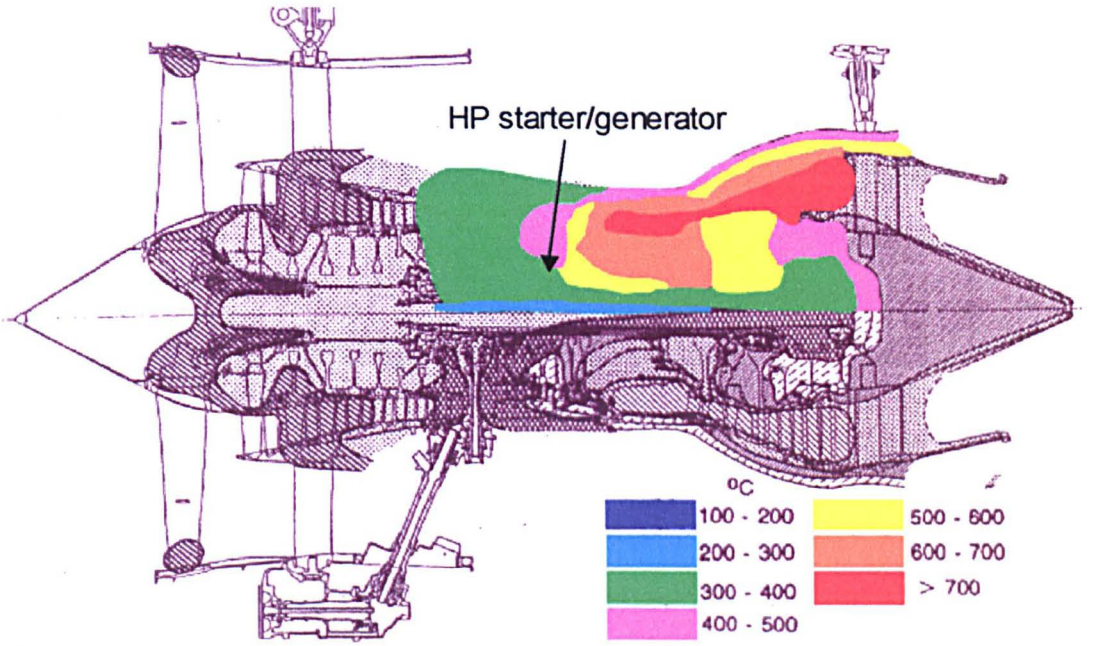

Figure 1.11. Maximum temperature variation within a Rolls-Royce RB-211 turbo-fan engine.

CHAPTER 2

THERMAL MODELLING OF A BRUSHLESS PERMANENT MAGNET MACHINE IN AN EHA SYSTEM

2.1 Introduction to thermal modelling of machines

Electrical machines for use in aerospace are usually subject to the highly variable ambient conditions. By way of example, ground temperatures may reach as high as 70°C in extreme climates while during high altitude flight; temperatures may descend as low as –60°C. The problem of designing a machine to operate in such a variable environment is compounded in many aerospace applications since the emphasis is often placed on minimising mass, as a consequence of which, electrical machines are often required to operate with high levels of specific loss. Accurate thermal modelling is therefore critical in order to ensure that a given machine design is able to operate within given maximum temperature constraints while at the same time is not over-sized.

The extent to which thermal modelling features in the design synthesis of electrical machines depends on the demands of the particular application. In some cases, successful machine designs may be established with reference to suitable electromagnetic models, with steady-state and dynamic performance being predicted for an assumed operating temperature. Initial design studies are typically formed around a maximum permissible current density in the conductors based on a-priori assumptions regarding the likely winding temperature rise for a given cooling method. For instance, a naturally cooled machine may operate at a current density of $5A/mm^2$, whereas a forced water-cooled machine may be able to operate at $25A/mm^2$ or so on a continuous rating owing to the increased heat transfer from the windings. This rudimentary and somewhat empirical approach can compromise the machine design, as inaccuracies in temperature estimation of windings and magnets can result in an excessive temperature rise (which could in some cases lead to thermal runaway) or an over-sized machine.

Thermal runaway is a consequence of the positive temperature coefficient of resistivity of the windings and the negative temperature coefficient of the magnet remanence. In some cases this can result in an exponential rise in temperature until some part of the system fails.

Whereas thermal modelling is important in the design of machines that operate under essentially steady-state conditions, it is even more critical in machines that operate on a prescribed duty cycle or 'flight cycle', which may contain many transients. In such cases, by exploiting the thermal capacity of the machine, it can intermittently operate at current densities many times higher than those under steady-state conditions. This chapter illustrates the importance of thermal modelling for machines with transient load profiles by considering the specific case of a BLDC machine that is at the heart of the EHA actuator described in chapter 1.

2.2 Mechanical construction of the BLDC machine

The BLDC machine that is investigated in this chapter is directly coupled to a slipperless piston pump with no requirement for a dynamic seal between them as discussed in Chapter 1, section 5. The pump itself is subject to relatively high drag losses at high speed, and its effects on the temperature distribution in the BLDC machine must therefore be included in a system thermal model of the EHA. Figure 2.1 shows a cross-section through the machine and pump, (with the pump on the right hand side). The leading dimensions of the BLDC machine are shown in figure 2.2, and table 2.1. A design feature of this motor and pump unit, which exerts a significant influence on its thermal performance, is that the rotor is flooded in hydraulic fluid as the pump design allows hydraulic fluid to leak from the pump to the far end of the machine. The presence of hydraulic fluid in the airgap gives rise to significant drag loss on the rotor and a marked increase in the heat transfer within the airgap. Another interesting feature of the machine that has a significant bearing on its thermal performance is the presence of a PTFE sleeve on the stator bore to prevent the ingress of hydraulic fluid into the

stator and frame. As will be demonstrated in detail in chapter 3, the relatively poor thermal conductivity of the sleeve and the cooling provided in the airgap by the hydraulic fluid has the effect of largely de-coupling the heat transfer within the stator from that in the rotor and the airgap. This in turn enables these regions to be considered separately in terms of heat transfer and sources of loss. The electrical machine has been designed for natural convection cooling so as to eliminate ancillary cooling parts, hence maintaining a high level of reliability.

Annular cooling fins have been incorporated over the entire length of the frame to augment heat transfer. The fin geometry was optimised for maximum heat transfer with natural convection at a frame surface temperature of 135°C (which arises from the assumed frame temperature at the maximum ambient of 70°C. This optimisation was based on the assumption that the radial fins can be regarded as parallel isothermal plates of rectangular section, with equivalent heat dissipation being evaluated from standard fin efficiency calculations [BAR 84] and methods for representing convection heat transfer [INC 90]. As the fins describe an annular geometry around the periphery of the frame, it is assumed that the lowest and highest regions of the fins do not contribute to the convective air-flow since their location prevents air flow through the buoyancy effect of the heated air. It was therefore assumed that all heat transfer by convection only occurs over half of the case outer circumference. However, the fin geometry obtained using standard design guidelines [INC 90] would have resulted in a very tall and narrow fin (80mm by 1.5mm respectively) and ultimately, due to engineering requirements, a fin with a non-optimum profile has been chosen (17mm by 3.5mm). However, despite this significant departure from the optimal geometry, calculated fin efficiencies for the specified operating temperature are 0.90 and 0.74 for optimal and final designs respectively. For the particular fin design employed in the prototype machine, this efficiency results in the frame being capable of dissipating 361W of loss by convection for a frame temperature of 135°C and an ambient of 70°C.

Although convective heat loss tends to dominate in naturally ventilated and force cooled machines at moderate temperatures (i.e. frame temperature up to ~150°C or so), due account can also be taken of radiation from the frame. There are well-established analytical expressions [HOL 90] for calculating the loss from cylindrical and circular surfaces, which could be applied to the frame (including the circular end-caps). However, in a finned frame, there are difficulties associated with defining an equivalent surface area, because of the considerable emission and subsequent absorption that occurs between the sides of the fins that face each other. Assuming a worst-case in which the side faces of the fins do not make a significant contribution to the radiation, then the frame can be represented as a smooth cylinder and a pair of cylindrical end-plates. The heat transfer rate for this simplified representation is hence given by [HOL 90]:

$$q_r = \varepsilon_r \sigma_{sb} A \left(T_S^4 - T_\infty^4 \right) \tag{2.1}$$

However, even allowing for the fact that equation 2.1 is likely to be a slight under-estimate, the frame would only be capable of dissipating <5W of loss by radiation for a frame temperature of 135°C and an ambient of 70°C, which is considerably lower than the corresponding value of 361W for convection.

2.3 Sources of loss in the stator

An essential pre-requisite for analysing heat transfer within the stator is the calculation of the magnitude and distribution of the losses generated in the stator. Since the effects of fluid losses are largely confined to fluid itself as a result of the insulation provided by the PTFE sleeve, the stator losses are dominated by the copper and iron losses. The copper losses can be relatively straightforwardly calculated for any arbitrary current waveform (providing the winding has been designed such that there is no discernable skin effect within conductors at the frequencies of interest, i.e. the DC resistance provides an adequate representation). However, it is important to recognise that the

magnitude of copper losses are strongly coupled to winding temperature because of the comparatively high temperature coefficient of resistivity of copper (0.00393 parts per °C).

In contrast, the iron losses are considerably more difficult to calculate. Historically, the calculation of iron loss was reliant on a significant degree of empiricism. However, the accuracy with which machine designers have been able to calculate iron losses has improved markedly in recent times with the development of ever-more sophisticated field calculation techniques, particularly finite element models which are increasingly being coupled with models of the power converter and mechanical load. These have enabled flux density waveforms to be derived with greater spatial and temporal refinement (e.g. in each and every element of a finite element mesh of a stator core if necessary).

Having established the flux density variation throughout the machine, a suitable loss model must be employed to calculate the associated loss. A widely employed approach is to consider the net iron losses as consisting of three separate components, viz. hysteresis losses, excess losses and classical eddy current losses. Standard iron loss models have been developed for calculating the contribution from these three components for any arbitrary waveform [BER 85] [LAV 78]. Using one such standard model proposed by Bertotti [BER 85], the overall iron loss for a particular flux density waveform can be derived using equation 2.2, in which the various material coefficients, k_h, k_{exc}, and k_c are derived from standard measurement procedures.

$$P_{Fe} = \frac{\sigma\, d^2}{12\,\delta}\frac{1}{T}\int_T \left(\frac{dB}{dt}\right)^2 . dt + \frac{\sqrt{\sigma\, k_{exc}}}{\delta}\frac{1}{T}\int_T \left(\frac{dB}{dt}\right)^{1.5} . dt + k_h \hat{B}^{a+b\hat{B}}\frac{1}{T} \qquad (2.2)$$

This equation can be applied on an element-by-element basis within a finite element model or to a region of the stator (e.g. tooth body) in which the flux density variation is relatively uniform.

In order to calculate the iron losses in the BLDC machine under representative load conditions at 700rpm and 6000rpm, a magnetostatic finite element model of the machine was employed. Figure 2.3 shows the finite element mesh employed in calculating iron losses in the BLDC machine stator for rms phase currents of 137A and 34.25A respectively, which correspond to the rated load conditions at rotor speeds of 700rpm (55Nm) and 6000rpm (13.75Nm). Figures 2.4 and 2.5 show the predicted iron loss densities throughout the stator iron for these two test conditions. As is evident, there is a considerable variation in the loss density, with particularly high losses in the vicinity of the tooth tips. The total losses in the machine at 700rpm and 6000rpm are 29W and 569W respectively. These losses are significant when compared to the rated power at 6000rpm/13.75Nm but considerably lower than the corresponding copper loss of 300W at 700rpm/55Nm. This illustrates a key issue in developing thermal models which are reliant on a degree of simplification, in that the relative significance of different loss sources and heat transfer mechanisms can vary significantly throughout the operating range.

2.4 Heat transfer modelling techniques

A variety of methods have been applied to the study of heat transfer in electrical machines. Arguably, the most widely employed are those based on lumped parameter analysis in which the machine is divided into a number of regions in which simplifying assumptions regarding the heat transfer are adopted. The resulting heat flow is calculated using equivalent circuits in which the thermal parameters such as temperature, heat flow and thermal resistance are represented by their analogous electrical parameters; voltage, current and resistance respectively. Equivalent T-networks have been used extensively to model conduction heat transfer in rotating electrical machines, firstly by Soderberg in 1931 [SOD 31] who derived equivalent circuits for steady-state heat transfer in large turbine generators with radial cooling ducts. Smaller machines have also been investigated, most notably by Perez and

Kassakian [PER 79] for medium sized induction motors (i.e. tens of kWs) and by Mellor [MEL 91] for on-line temperature monitoring of induction machines. Jokinen [JOK 97] developed this technique further to model the effects of forced air-cooling by including additional temperature sources controlled by the flow of heat.

Another method that has been employed extensively, particularly for modelling conduction heat transfer, is the finite element method. This has been applied for example in large turbo-generators [ARM 76] [ARM 80] and industrial induction machine stators [SAK 91]. Computational Fluid Dynamics (CFD) has been used both in the study of forced convection heat transfer in electrical machines [SHA 02], and in the study of aerodynamic losses in machines with highly salient rotor structures [CAL 02]. However, it is worth noting that the use of ever-more sophisticated models remains reliant on the ability to accurately determine the various input parameters for the model, e.g. solid material properties, tolerances on geometries/fits and fluid properties. Indeed, it is arguable that modelling techniques have evolved to such a level of sophistication, that their ability to accurately represent the behaviour of a practical system is now determined predominantly by the quality of the input data. By way of example, uncertainties in the convection coefficients of a thermal system, sometimes by as much as ±25%, [HOL 90] and more particularly in contact coefficients (±25%) can render elaborate analysis techniques unnecessary. Indeed, there are many examples in published literature [XYP 99] where the detail in which some features are modelled (e.g. localised dissipation within deep rotor bars of induction motors) are difficult to justify, given that other regions which arguably have an equal impact on thermal performance are modelled using only first-order approximations. In formulating an equivalent thermal network for a given machine and external environment, many of the regions are well defined, both geometrically and in terms of thermal properties, e.g. the tooth body region of the stator lamination. Hence, relatively simple analytical equations can be derived to describe the heat transfer in these regions. However, there are other regions where there is a lack of reliable material data and/or a degree of uncertainty in the exact geometries, and modelling is often reliant on published data and / or empirical

guidelines. This is particularly the case for heat transfer within the conductor bundle and slot region, and at the interface between the stator lamination pack and the frame. Since these will have a significant bearing on the thermal behaviour of the machine in fig.2.1, these features were investigated in detail.

2.5 Stator lamination and frame model

Although the vast majority of the stator lamination and the frame itself can be readily modelled as conduction within homogeneous and well-defined regions, one often-problematic feature is the heat transfer between the stator lamination stack and the frame. The heat transfer at this interface is strongly influenced by the processes employed during manufacture, viz. the axial clamping pressure applied to the lamination stack, the surface finishes on the outer diameter of the lamination stack and the bore of the frame, and the radial contact pressure which the frame exerts on the stator lamination pack. There are published experimental studies on heat transfer across representative stack-frame interfaces at a range of pressure conditions [BRI 91], from which the following general conclusions can be drawn:

- The effective thermal resistance of a given interface is essentially independent of temperature over the range 70°C to 130°C.
- Thermal contact resistance decreases as contact pressure increases,
- Corrosion products on a laminated surface increase thermal contact resistance substantially, particularly at low axial clamping pressure and high contact pressure (>1.5Mpa)
- Surface grinding of the lamination pack slightly decreases contact resistance this being most pronounced at high axial clamping pressure.
- The thermal resistance is largely independent of contact pressure for a surface ground finish.

In practice, it is difficult to precisely determine the exact pressure between the stack and frame at the design stage, albeit that some degree of control can be exercised by closely specifying dimensional tolerances. The thermal resistance due to this contact region is very sensitive to the mechanical fit between the surfaces, and consequently, is often measured following assembly of a trial stator in order to provide accurate data for a transient thermal model [MEL 91]. Although there are some published empirical values for contact coefficients [SHL 64], these are restricted to comparatively low contact pressures (up to 1.4MPa). Mellor and Turner [MEL 91] employed these published characteristics, albeit for an extrapolated range of values, and applied a further empirical correction in attempt to provide a better correlation with measured values on an induction motor frame.

For the particular machine considered in this chapter, a contact thermal resistance of 8.5×10^{-4} K.m^2/W was specified between the lamination stack and frame interface. This value is deemed to be representative of a lamination stack that has been seem welded at three equi-circumferentially disposed points along its axis while clamped at a high pressure, machined surface finishes on the stack and frame, and an 'interference' or shrink fit. These manufacturing steps are likely to result in a contact pressure of ~3 MPa (600psi) and a clamping pressure of ~0.8 Mpa (120psi). This value of 8.5×10^{-4} K.m^2/W (equivalent to a contact coefficient of 1200 W/m^{2}K) is comparable with the values in the range 300 to 2500 W/m^{2}K measured in [MEL 91] for an industrial induction motor.

2.6 Thermal properties of electrical machine stator slots and coils

The stator slot region consists of a series of copper conductors (each of which is covered with a thin insulating layer of varnish, a layer of slot liner material to electrically insulate the winding from the stator stack, and a medium between conductors and slot liner (which is often simply air, or in some cases, encapsulants which enhance the heat transfer and/or provide structural support).

This composite region will inevitably present challenges in terms of thermal modelling and property specification, particularly with the lack of repeatability in exact geometry between nominally identical coils. Moreover, the constituent materials have thermal conductivity that vary by several orders of magnitude; e.g. copper has a thermal conductivity of 383W/mK at room temperature, while commonly used commercial slot liner materials such as Nomex 410 have a thermal conductivity of ~0.15W/mK [NOMEX].

One well established method of deriving reliable data for modelling heat transfer within practical coils is to construct a section of the winding and measure its heat transfer capability in a custom test-rig. This enables a net thermal conductivity for the entire bundle to be derived for various packing factors and encapsulants. An alternative approach is to model the region using finite element techniques, although as will be demonstrated in section 2.7, there are a number of factors that must be carefully considered in formulating a finite element model that is capable of representing all the features of practical coils. A further potential source of data is so-called 'handbook results' [GE 69], which endeavour to collate findings drawn from manufacturing trials and measurements. However, although data on conductor bundle thermal conductivity is available in such handbooks, they cover only a small range of conductor geometries. Furthermore, conductor insulation and encapsulant properties have advanced significantly since the original data was collated, and hence it may be somewhat unreliable for modern coil materials and manufacturing processes.

In all electrical machines, the conductors only occupy a proportion of the total slot cross-section. This partial filling is often quantified in terms of a 'fill factor' or 'packing factor', which is the ratio of the copper area to the available slot area. Achievable packing factors in small and medium machines (i.e. up to a few tens of kW) typically range from 0.3 to 0.7 both for hand and automated winding processes. Thus, there is considerable residual space between the conductors, even in machines with comparatively high packing factors. One commonly employed technique for enhancing

heat transfer from the winding region is to fill this residual space with a relatively high thermal conductivity material. Such processes are variously referred to as encapsulating, potting or impregnating the conductor bundle. Although these terms are often used loosely for various processes, for the purposes of this thesis, impregnation is considered to be the application of a varnish (such as a solventless modified alkyd varnish – STERLING 073-1041) by a combination of dipping and/or by a vacuum process, while encapsulation refers to the complete potting of the stator (including the region surrounding the end-windings and coil terminations) with a highly loaded composite under vacuum to form an integrated solid stator module. The vast majority of encapsulants are polymer-based materials that are loaded with an electrically insulating material of a high thermal conductivity, such as alumina oxide or zirconium oxide [EMM]. The thermal conductivities of potting compounds typically range between 0.6 and 1.4 W/mK, [EMM]. However, their maximum operating temperature is typically limited to ~200°C. As well as enhancing heat transfer within the machine, the additional thermal capacity of encapsulants is useful for machines with highly intermittent duty cycles, since the winding is often heated under essentially adiabatic conditions during brief transient overloads. For the particular case of a winding with a packing factor of 0.3, the use of encapsulants such as Stycast 2850 KT (specific heat capacity of 1000 J/kg.K and a density of 2400 kg/m^3) increases the net thermal capacity of the slot region by a factor of 3. An additional benefit of employing encapsulants or varnishes is that they can provide good structural support to the windings (which may endure high forces during operation). However, despite the many advantages of employing encapsulants, it is important to recognise that they are generally expensive; both in terms of the intrinsic material cost and the additional manufacturing steps involved.

As well as heat transfer within the conductor bundle, difficulties are also often encountered in representing heat transfer across material boundaries. A widely used approach for modelling such features is the use of surface-to-surface contact coefficients, in an analogous fashion to a surface convection coefficient. This so-called contact coefficient is a function of both surface finish and the contact pressure between

the two materials. In a model of a typical slot, contact coefficients are required to cater for the interface between the conductor bundle and the slot liner, and the slot liner and stack.

There are some published values of effective thermal conductivity for different slot liner materials at a range of applied pressures [MON 92]. The values were derived from measurements on flat circular test samples in a custom test-rig. Although the published results are representative of commercial slot liner materials and thicknesses, they were measured for the particular case of a uniform applied pressure. Hence, they are not fully representative of a practical conductor bundle, in which some parts of the slot liner are subject to high pressures exerted by the windings, while other parts may have virtually no pressure applied.

2.7 Finite element modelling of stator slots and coils

Due to a relative dearth of published data on thermal modelling of random wound coils, both encapsulated and un-encapsulated, a finite element study was performed to derive reliable data for a lumped parameter model of the entire machine. Moreover, finite element modelling provides a convenient and systematic means of investigating various generic features of practical coils, viz. the significance of convection in a non-encapsulated winding, the influence of the geometry of individual conductors within the bundle on the overall heat transfer capability and the influence of the distribution of the individual conductors.

The initial finite modelling was based on a two-dimensional representation of a cross-section through the machine, i.e. temperature variation in the axial direction was neglected in the slot region due to the axial thermal resistance of the conductors being some 2 orders of magnitude lower than in the radial direction, and therefore giving rise to a correspondingly lower thermal gradient. The heat transfer was modelled using a so-called 'solid' model of the slot region, in which heat transfer is solely a result of

conduction. The periodic geometry of the stator was exploited to reduce the problem domain to one half of a slot pitch. To simplify the geometry somewhat, and allow a systematic approach to be adopted for incrementing the number of conductors within a slot, the curvature of a typical practical machine was neglected, i.e. the slot was 'unravelled' to create a linear representation of the tooth and slot geometry as shown in figure 2.6. Zero heat flux boundary conditions were applied to all exterior surfaces in the model of figure 2.6 except the uppermost surface of the frame section, where a convection coefficient of $30W/m^2K$ was specified (this value being representative of a finned frame).

The model of figure 2.6 includes specific regions for modelling thermal contact coefficients between the slot liner and lamination stack, and between the lamination stack and the frame. As described previously in section 2.5, contact interfaces can be very localised, and it is difficult to rigorously define an equivalent cross-section for a particular contact region, since they are based predominantly on empirical data derived from measurements. Hence, in the finite element models, these contact regions are represented as well defined layers, whose thickness is compatible with the mesh discretisation employed, and whose equivalent thermal conductivity is specified such that they result in the same net thermal resistance. As a consequence, the mesh is not an exact geometrical representation of a stator slot region, as the model is primarily concerned with the heat transfer in the winding region.

The heat generation is assumed to be equal in each conductor and uniformly distributed within each individual conductor. In adopting this assumption, it is recognised that in some machine windings there may be a degree of current re-distribution within a conductor due to eddy currents, i.e. skin and proximity effects and hence additional copper losses (often referred to as 'AC losses'). However, such effects are often minimised in practice by ensuring that the winding is appropriately sub-divided (e.g. by using a number of parallel strands or in extreme cases even Litz wire)

A series of finite element models were analysed, initially with a fixed copper packing factor of 0.6 and a fixed total power dissipation of 20W per slot. Only process 1 (un-encapsulated) and process 3 (encapsulated) coils were considered, as there is no reliable means of formulating a solid finite element model of the process 2 winding (impregnated) given the uncertainty in the location of the impregnating varnish. The number of individual conductors per slot was progressively increased from 1 to 100 with the conductors arranged in a square packed structure of $n \times n$ conductors (as shown in figure 2.6). Figure 2.7 shows the variation in the predicted maximum coil temperature as a function of the number of conductors per slot for process 1 and process 3 coils. In both cases, the maximum temperature increases slightly as the number of conductors is increased, although beyond 16 or so conductors, the maximum temperature remains essentially constant. The benefits of employing encapsulation are clearly evident from figure 2.7, with a reduction in peak temperature from 110°C to 52°C for 1 turn, and 128°C to 57°C for 100 turns (which corresponds to a reduction in temperature difference between the centre of the winding and the inner surface of the slot liner from 58°C to 8°C for 1 turn and 71°C to 8°C for 100 turns, respectively). Figures 2.8 and 2.9 show representations of the temperature distribution in both an un-encapsulated (process 1) and fully encapsulated (process 3) coil for the particular case of 36 conductors per slot.

A series of finite element models were also analysed to establish whether the geometry of the individual conductors has any significant influence on the heat transfer within the reference slot design, particularly for low numbers of turns. To this end, two conductor geometries were compared with the circular conductors, viz. square conductors, and rectangular conductors with an aspect ratio of 3:1 (arranged both vertically and horizontally) as shown in figure 2.10. Figures 2.11 and 2.12 show comparisons of temperature rise for these conductor geometries in both an un-encapsulated and an encapsulated state respectively (in all cases for a copper packing factor of 0.6). As one would expect, the difference between these conductors is only marginal, being most

pronounced for a high number of turns in the case of the horizontal rectangular conductors.

The finite element models up to this point have all been based on a fixed copper packing factor of 0.6. Any variation in this packing factor is likely to influence both the heat transfer capability, and more particularly, the losses generated for a given total ampere turns in the slot. A series of slots having 36 conductors of circular cross section with packing factors between 0.3 and 0.7 (in 0.1 increments) were modelled. The variation in packing factor was simply achieved by varying the diameter of each conductor while maintaining the same square packing arrangement. In order to distinguish between the effects of packing factor and losses on heat transfer, two cases of dissipation were considered, viz. a fixed loss for all packing factors, and a loss that is based on constant ampere turns for a given packing factor. Figures 2.13 and 2.14 show the variation in the maximum temperature with packing factor for these two cases of dissipation. As is evident, although the packing factor influences heat dissipation, particularly for the un-encapsulated coils, the benefits in terms of reduced dissipation with higher packing factors are far more pronounced.

The influence of packing factor was also considered for slots with relatively low numbers of rectangular conductors, as this is often representative of higher power machines such as the BLDC machine for the EHA. Moreover, as is evident by comparing figure 2.7 and 2.11, the difference between circular and rectangular conductors is almost constant above 12 turns. Hence, a series of packing factors from 0.3 to 0.7 (in 0.1 increments) were modelled for the case of 12 turns of rectangular conductors with an aspect ratio of 3:1. Figure 2.15 shows the influence of packing factor on the maximum temperature of process 1 and process 3 windings with 12 rectangular conductors for the same fixed loss of 20W per slot.

Whereas the solid finite element model is able to cater for thermal conduction within the slot, natural convention may also play a role in non-encapsulated windings. In order to

determine the influence of convection in a typical slot, a model with identical dimensions to that considered with the solid model was analysed using a coupled solid finite element /computational fluid dynamic solver. The mesh elements which represent the non-fluid components (i.e. conductors, slot liner, stack and iron have the same degrees of freedom as those used in the standard solid thermal model. The elements that represent the fluid regions surrounding the conductors were assigned the thermodynamic properties of air (these properties being iteratively modified to take account of the air temperature in this non-linear solution) and assigned additional degrees of freedom to allow convection to be modelled. The motion of the air and the resulting heat transfer within these fluid elements was modelled using the Flotran® CFD solver in ANSYS [ANSYS].

The air velocities within the fluid elements are calculated from the principle of conservation of momentum, the pressure from the principle of conservation of mass, and the temperature from the law of conservation of energy. As there is no forced convection within the problem domain, the air movement is solely due to buoyancy forces. The acceleration due to gravity in the problem was set to $9.81 m/s^2$. Zero-slip velocity boundaries are applied to all solid surfaces within the slot.

In a horizontally mounted machine, the orientation of each slot relative to the vertical axis in which gravity acts varies around the periphery of the stator, which in turn will influence the buoyancy effects. In order to establish the limiting values of heat transfer due to natural convection, two reference slots with identical dimensions but different orientations were modelled. These two slots are shown in figure 2.16a and 2.16b and are subsequently referred to as the upper and lower slot respectively. Particular care was taken to ensure that the mesh was finely discretised in regions where abrupt changes in velocity or pressure occur, e.g. at zero-slip boundaries. Moreover, the mesh density was progressively refined for decreasing conductor diameters. The pressure field was solved using the Preconditioned Generalised Minimum Residual (PGMR) method with convergence criteria of 1×10^{-12}, and the temperature and velocity fields were solved

using the Preconditioned Bi-Conjugate Gradient Method (PBCGM) solver with convergence criteria 1×10^{-12} and 1×10^{-6} respectively. This coupled CFD and finite element model was employed to calculate the heat transfer in a series of slots with $n\times n$ conductors, in which the value of n was progressively increased from 1 to 10 in integer increments, i.e. 1 to 100 conductors per slot. Figure 2.17 shows a comparison between the minimum and maximum winding temperature predicted by a solid finite element model and the coupled CFD / finite element model for the particular case of a uniformly distributed power loss of 20W per slot. Since the difference in maximum temperature between the upper and lower slot for the CFD model was found to be <1%, the upper slot only was used for the CFD analyses.

As demonstrated by figure 2.17 the temperatures predicted using the coupled finite element / CFD model are in reasonable agreement with those predicted by the solid model, with a maximum difference of 6.4% (the temperature gradients between the hottest part of the coil and the slot liner is also in good agreement). Thus, the heat transfer in a totally enclosed naturally ventilated machine with un-encapsulated windings surrounded by air, operating at a maximum winding temperature prescribed by the slot liner (<180°C for this case) can be modelled to a practicable degree of accuracy using a solid finite element representation. The correlation between the two models tends to improve at higher numbers of turns, as the air flow pattern around individual conductors become less significant in terms of the overall air flow within the slot. This is illustrated by figure 2.18 and 2.19 which show that convection currents move air over a large proportion of the slot in the case of a single turn (fig 2.18), whereas the convection currents in the 4 turn model are much more localised (fig 2.19).

2.8 Influence of random conductor distribution within a coil

One of the most commonly employed methods for winding electrical machines is to pre-form the windings automatically on a bobbin prior to their insertion into the slot. This technique is capable of rapidly producing coils with good overall dimensional

tolerances, but not necessarily with good repeatability in terms of the relative disposition of individual conductors. For stators which have partially closed slots as a result of wide tooth tips (as is commonplace in BLDC machines) only a relatively low packing factor may be achieved, as tooling must be passed through the slot during the winding process, thus preventing the winding from filling the total available area. Recourse to the more labour intensive method of hand winding is necessary for BLDC machines with large stator tooth tips or large diameter conductors, as pre-formed windings become impractical to insert in such a topology, while the requirement for a high packing factor precludes the use of automatic winding methods used for closed slot designs.

Both methods are capable of generating a formal distribution of conductors in the slot, but in practice, the final position of individual conductors within the slot cannot be predicted with any accuracy. Furthermore, variation in individual conductor position is not only confined to the XY plane, as conductors may also change position from top to bottom of slot, making it very difficult to provide a definitive solution of the temperature distribution in the slot for a given machine. Hence, the effects of random conductor distribution within the slot have been investigated in a finite element study, by generating a large number of solutions based on a simple random distribution of conductors in the XY plane.

Prior to assessing the influence of random conductor disposition on the maximum temperature in the winding, it is useful to consider the limiting cases that are likely to provide the upper and lower limits on temperature distribution, viz. a 'worst-case' model in which the conductors are bunched together in the centre of the slot, and a 'best case' model in which the conductors are packed into the corner of the slot in close proximity to the stator core as illustrated in figure 2.20. The variation in the maximum temperature as a function of the number of turns in the slot for process 1 and 3 windings (in all cases for a packing factor of 0.6) are shown in figure 2.21 and 2.22 respectively.

The maximum temperature within any practical coil distribution is therefore likely to fall within the range of values shown in figures 2.21 and 2.22.

In order to quantify the influence of random conductor placement, a methodology was adopted for defining conductor positions. The basis of this method can be illustrated by reference to figure 2.23, which shows n conductors arranged within the square slot of sides α in an equal number of rows and columns. Having specified n, α and a particular packing factor, the conductor diameter ϕ can be readily calculated. This investigation was concerned only with such 'square packed' arrangements rather than the 'closely packed' arrangement shown in figure 2.24 (these terms being used in an analogous manner to their routine use in describing crystal structure).

As shown in figure 2.25, each individual conductor is restricted to be within a square having sides of $\alpha/\sqrt{n}$. Within this square, the centre of the conductor can be offset from the centre of the square in the x and y-axis by displacements of δ_x and δ_y as shown in figure 2.25, which are given by:

$$\delta_x = \frac{\left(\left(\alpha/\sqrt{n}\right) - \phi\right)}{2} \beta \tag{2.3}$$

$$\delta_y = \frac{\left(\left(\alpha/\sqrt{n}\right) - \phi\right)}{2} \beta \tag{2.4}$$

A degree of constrained randomness can be introduced in the offsetting of each conductor (i.e. each conductor is still constrained to remain within a given square) by assigning random values to β within the range $-0.95<\beta<0.95$. Although not necessarily comprehensive in terms of all possible conductor bundle arrangements (particularly cases where circular conductors adopt a close packed structure in some regions of the slot), this model along with the limiting values derived above, nevertheless serve to demonstrate the sensitivity of the temperature estimation to the exact conductor distribution in a random wound coil.

A series of finite element calculations of heat transfer were performed for all integer values of n between 1 and 10 (i.e. 1 to 100 conductors in a square arrangement). For each value of n, 100 different random conductor arrangements were modelled, with the maximum temperature in each case being noted. Figure 2.26 shows the spread of maximum temperatures in a process 1 winding achieved with a particular number of circular conductors with a packing factor of 0.6, and power loss of 20W. As is evident, slots with a relatively low number of un-encapsulated windings are the most sensitive to the exact conductor position, with a spread of ~20°C for a mean value of ~130°C. However, as one would expect, this spread in temperatures is considerably less than the ~60°C observed between the best and worst case coil arrangements shown previously in fig. 2.21. Although the process 1 winding was seen to be relatively sensitive to conductor position in the case of the randomly placed model, the process 3 winding exhibited a far smaller variation in maximum winding temperature between the worst case and best case conditions as can be seen from figure 2.22. It was therefore deemed unnecessary to employ the random placement model in the determination of maximum winding temperature for the process 3 winding, given that the maximum variation in temperature is ~5°C.

2.9 Summary of conductor bundle modelling

The following general conclusions can be drawn from the findings of the various models described in sections 2.7 to 2.8:

- Fully encapsulating the winding brings benefits of >100% in terms of reduction in maximum temperature.
- The individual geometry of the conductors has a small influence over the maximum temperature rise in the winding region, the most significant variation being noted for the horizontally positioned rectangular conductors.

- The maximum temperature in the winding region showed a high sensitivity to packing factor for a constant Amp-turns (fig 2.13), with a variation of 300°C and 50°C in the process 1 and process 3 winding for packing factors of 0.3 and 0.7 respectively.
- Maximum winding temperature showed a small variation with packing factor at a constant value of power loss; hence the loss density in the region has a greater influence than the packing factor over the maximum winding temperature.

- Heat transfer in the windings of un-encapsulated, naturally ventilated machines, with maximum winding temperatures dictated by conventional slot-liner materials (<180°C) may be accurately represented by solid finite element models, with no recourse to the more time consuming CFD modelling technique.
- Random distribution of the conductors has shown that for a low number of turns in an un-encapsulated machine, the maximum winding temperature may vary by as much as 20% for a low number of turns, whereas high numbers of turns tend to be less affected by the random placement.

2.10 Experimental measurements on conductor bundles

In order to measure the effective thermal conductivity of representative conductor bundles the test rig shown in figures 2.27 and 2.28 was constructed. The conductor bundle under test is located between the two aluminium blocks, one of which contains an electric cartridge heater and the other acts as a heat sink. The DC input power supplied to the cartridge heater is precisely controlled, to a nominal resolution better than 0.2% (Four digit HP 34401A DVM's were employed to measure input current and voltage). The conductor bundle itself is insulated such that the heat flow is a good approximation to being uni-directional. Hence, the net thermal conductivity in a direction perpendicular to the orientation of the conductors can be established. In order to ensure uni-directional heat flow within the test-rig, the thermal conductivity of the surrounding insulation must be at least an order of magnitude less than the thermal

conductivity of the bundle to be measured. To this end, the insulation layer was manufactured from a single cast block of Rescor 740 insulating foam ceramic, which is an alumina/silicon based ceramic with manufacturer's specified thermal conductivity of 0.1 W/mK [COT 99].

In order to ensure that the thermal conductivity was measured under steady-state conditions, temperatures were monitored using K-type thermocouples at the 4 locations shown in figure 2.27. Steady-state conditions were deemed to have been achieved when the temperature change over the period of one hour was less than 1%). The resulting thermal conductivity for a measured temperature difference between the two thermocouples 2 and 3 of $\Delta\theta$ at a particular power q_x is given by:

$$k = \frac{l\, q_x}{\Delta\theta\, A} \tag{2.5}$$

where q_x is the rate of heat flow through the bundle test piece, l is the length of the bundle test piece in the direction of the heat flow, and A is the cross sectional area of the bundle normal to the heat flow path. Given the high precision to which the input power and the thermocouple temperatures can be measured, the principal sources of errors in the measurements are likely to be a result of dimensional tolerances and the departure of the heat flow from a true uni-directional flow. The likely magnitudes of these errors were assessed as being:

- Error in the bundle face area perpendicular to the main heat flow path was assumed to be +/- 0.25mm in each direction, thus giving an error of 1%.
- The separation between the two thermocouples was assumed to be accurate to within +/- 0.25mm, giving rise to a potential error of ±4%.
- Errors attributed to the non-uniformity of the heat path (leakage through the alumina ceramic insulation) were measured by a thermocouple that was attached to the outer wall of the insulation. For an assumed heat transfer coefficient from this wall of 10W/m^{2}K (typical of free convection from a vertical face), the temperature

rise measured by this ancillary thermocouple corresponds to a net loss from the side walls of ~ 1% of the total heat flow.

Assuming as a worst-case condition, in which the various sources of error act in such a way as to compound rather compensate for each other, then the total error in the measured thermal conductivity is ~6%.

Measurements of temperature difference in the test-rig for a fixed input power of 15W were performed for a bundle of 30 conductors with a rectangular cross-section of 10mm x 2mm. (this being representative of the conductor geometry employed in the prototype EHA machine). These measurements were performed on the same conductor bundle for various encapsulation processes, i.e. prior to any encapsulation (process 1) following vacuum pressure impregnation with STERLING 073-1041 varnish (process 2), and finally following complete encapsulation with Stycast 2850kt under vacuum conditions (process 3). A cross-section through the bundle following all encapsulation processes is shown in figure 2.28a, which demonstrates the absence of any significant voids.

The measured temperature differences and inferred thermal conductivities for these 3 encapsulation processes are shown in table 2.2. Also shown in table 2.2 are the corresponding values predicted using a solid finite element model of the test-rig for the particular case of encapsulation processes 1 and 3. As was the case with the solid model of actual slot geometries, there is no reliable means of formulating a solid finite element model of the process 2 encapsulation given the uncertainty in the location of the impregnating varnish. As is evident from table 2.2, considerable benefits can be accrued in terms of heat-transfer from employing a highly loaded encapsulant within the slot.

Thermal conductivity measurements were not performed on the slot liner itself, since the intrinsic material properties of this particular grade of Nomex slot-liner have been measured previously over a range of different uniform pressures [MON 92]. As would be expected, the measured conductivities tend towards the intrinsic value of the material

as the pressure is increased (from 0.86MPa to 9.8MPa), since at low pressures there is a significant contribution from the contact interface of the test-rig heat plates (which were nominally flat machined surfaces) and the slot liner. The value of thermal conductivity measured at low pressure (0.86MPa), viz 0.102W/mK was assumed to be representative of a slot liner and contact interface in an un-encapsulated coil (process 1). In order to cater to some degree for the likely reduction in thermal contact coefficients that would result from the use of an encapsulant, it is assumed that the net thermal conductivity was proportional to the benefit in measured winding thermal conductivity within the coil for a particular encapsulation process. Hence, the slot liner thermal conductivity was corrected using equation 2.6:

$$k_{sl}(n) = k_{P1} - \left(\frac{k_{P1} - k_{P2}}{k_{wdg}(n) / k_{wdg1}} \right) \tag{2.6}$$

where n is the particular encapsulation process employed in the winding (1 to 3), and k_{P1} and k_{P2} are the measured slot liner thermal conductivity at high and low pressures respectively. The resulting thermal resistances derived on the basis of equation 2.6 are shown in table 2.3.

2.11 Lumped parameter model of BLDC machine

Having established representative thermal parameters for slots and windings, a complete thermal model of the BLDC machine was developed. As discussed previously in section 2.4, a lumped parameter thermal network provides a flexible and rapid means of modelling transient thermal behaviour, while having an accuracy which is likely to be sufficient in the context of the uncertainties which are in inherent in any thermal model as a result of dimensional and material property tolerances and repeatability of interfaces etc. The thermal network model of the prototype BLDC machine is divided into a number of geometrically discrete regions, the selection of which was made with due cognisance of the likely temperature gradients throughout the motor and not simply

the size of the particular region. Each region within the network is assigned a lumped thermal capacity, and where appropriate, a heat source, and is connected to other regions via a network of linear (i.e. temperature invariant) thermal impedances. The interconnection of the various elements is based on assumed heat flow paths, which inevitably requires some engineering judgement as to the likely significance of different heat transfer mechanisms.

- The calculation of equivalent thermal parameters for the various lumped regions is based on a number of simplifying assumptions: Heat flow in the radial, axial and circumferential directions is independent of each other.
- A single mean temperature defines the heat flow in all directions within a region.
- The thermal capacity and heat generation within a region are uniformly distributed throughout that region.

The various elements in the thermal model were represented using a standard T-network approach [PER 79]. An example of the derivation of the parameters for such a T-network can be found in [PER 79] and [MEL 91] and is also given in Appendix A for the case of conduction heat transfer through a cylinder.

T-networks for each given direction are connected together at the mean temperature point θm. Lumped thermal storage (capacitance) and internal heat generation are also introduced at the mean temperature node. The resulting thermal network for the BLDC machine is shown in full in Appendix B which caters for heat conduction in three dimensions so that effects such as asymmetrical mounting, shaft coupling, and heat exchange with fluid in the airgap can be accounted for. Figure 2.29 shows how the lumped parameter model is developed from the machine geometry in a simplified form, where it can be seen that one half a stator tooth section is considered. It may be seen from figure 2.29(b) that this is split into five regions; A: winding, B: tooth tip, C: tooth body, D and E: back iron. Each one of these regions is then represented by an equivalent network of thermal resistances and capacitances as shown in figure 2.29(c) where the various regions are coloured according to their materials i.e. thermal resistances

belonging to the winding region are coloured orange, whilst thermal resistances belonging to the stator iron and frame are coloured blue and grey respectively. The utility of this model can be illustrated by considering the particular case of the BLDC machine operating with the duty cycle shown in fig. 2.30(a), which is represenative of its operation in an EHA. The resulting winding and back-iron temperature rise are shown in figure 2.30(b) for this particular duty cycle.

2.12 Experimental measurement to validate stator radial model

In order to validate the thermal model described in section 2.11, a series of thermal measurements were performed on a prototype stator (which included the PTFE sleeve). Measurements were performed during the manufacture of the stator for all 3 encapsulation processes.

The stator was instrumented with 18 thermistors in the back iron, tooth body, tooth tip, windings (including end-windings), and airgap and in the frame. The locations of these thermistors are shown in figure 2.31. In an attempt to mitigate the contact resistance associated with such invasive temperature measurement techniques, the thermistors were held in place by high thermal conductivity aluminium putty. The temperature of each thermistor was measured for the particular case of a heat flow that was restricted to being almost entirely radial in order to evaluate the accuracy of predictions made by the two-dimensional lumped parameter model of Appendix B. This was achieved in practice by insulating both ends and the end-winding cavity of the machine with 200mm of fibreglass as shown in figure 2.32. The fibreglass has thermal conductivity of 0.24 W/m.K, which corresponds to a thermal resistance of 400°C/W for the sections employed. This is some two orders of magnitude greater than the predicted thermal resistance from winding to ambient of 0.26°C/W for this particular stator with a fully encapsulated winding (comparable figure 0.41°C/W for an un-encapsulated winding. Thus, the assumption of essentially radial heat flow is reasonable (with less than 1% leaking axially through the glass fibre).

The stator and frame were suspended horizontally 200mm above the test bench using low thermal conductivity tufnol inserts and rod as shown in figure 2.32. This arrangement allows for sufficient air movement over the frame during the tests and attempts to replicate the proposed orientation of the BLDC machines in the EHA. The thermistors employed to measure the winding temperature were located at the centre of the slot as possible (both axially, and with reference to the slot cross-section). The ambient temperature for a given test was measured by a thermistor located approximately 1.0m away from the machine frame, and was approximately 24°C at the start of all the tests. All the thermistors used in the tests were calibrated in a temperature-controlled oven at 120°C before testing commenced, with a maximum deviation of 0.2°C.

A fixed loss equal to the copper loss of 300W predicted for the steady-state fault condition of 700rpm, 55Nm was introduced to the stator windings. Since the required current of 137A exceeded the capabilities of available DC power supplies, the stator windings were supplied from an existing three-phase inverter. However, in order to achieve near static conditions (i.e. in which negligible iron losses are induced in the stator), the frequency of the inverter was fixed at its minimum value of 10Hz. The measured variation in the temperatures with time at key locations within the stator are shown in figures 2.33, 2.34 and 2.35 for the various winding encapsulation processes. In each case, the ambient temperature was ~ 24 °C and it was necessary to allow a period of some 5-6 hours to elapse before steady-state thermal conditions were achieved. The final steady-state measured temperatures are summarised in table 2.4 along with the corresponding values predicted from the thermal model described in section 2.11 (two measured values are shown for the predicted winding temperature which correspond to minimum and maximum values within the slot). As is evident from table 2.4, good agreement is obtained between measured and predicted temperature throughout the machine for all three encapsulation processes, with a maximum error of 10% arising in the prediction of end-winding temperature.

The benefits of fully encapsulating the winding in Stycast 2850 is clearly apparent, with a reduction in the maximum winding temperature of 33°C and 17°C as compared to the process 1 and process 2 windings respectively. This reduction in winding temperature becomes increasingly important if the ambient temperature is increased beyond the 24°C in the tests. By way of example, for the maximum specified ambient of 70°C (which corresponds to the most onerous ground conditions), the maximum temperature of a process 1 winding would exceed 180°C (which is beyond the service temperature capability of the insulation). This trend in the centre of the winding is also observed in the end-winding regions, albeit that the benefits of encapsulation are marginally less than in the case for the centre of the slot.

It is also interesting to note from figures 2.33 to 2.35, and table 2.5, that the thermal time constant of 60.1 minutes for the fully encapsulated winding is significantly longer than the 43.8 and 48.3 minutes of process 1 and process 2 windings respectively. However, this is achieved at the expense of an additional mass of 2.1kg (which corresponds to a 7% increase in total machine mass from 30.8kg to 32.9kg). However, this increase in mass of 7% compares favourably with the 25% increase that is achieved in the effective thermal capacity of the machine, which is a consequence of the Stycast 2850 being located in the critical slot area.

In assessing the merits of encapsulation, it is interesting to consider the effect of increasing the mass of an un-encapsulated machine by the same 2.1kg. If this additional mass is introduced by increasing the slot area (which also requires an increase in the depth of the stator tooth body) this would result in a 20% increase in slot area and hence a proportional reduction in copper loss. The resulting temperature difference between the original machine design with Stycast encapsulation and the new design would hence be 8°C as compared to the 33°C difference shown in table 2.4. However, it is worth bearing in mind that the thermal capacity of the larger un-encapsulated machine is still 5% lower than the original encapsulated design. Although the larger un-encapsulated

machine and the original encapsulated design have equal mass, the volume of the un-encapsulated machine is larger. Hence, the relative merits of encapsulation are closely coupled to the design constraints imposed by a particular application.

One drawback of encapsulating the stator from a heat transfer point of view is that it precludes the direct cooling of the winding with a fluid. Thus, there may be some scope to increase the cooling in an un-encapsulated or impregnated winding by removing the PTFE sleeve and allowing the hydraulic fluid to flow through the stator slots. However, to derive any net benefit, the available mass flow rate must be high enough to maintain the fluid below its maximum service temperature. This condition is not met in the EHA as the main delivery flow rate of 75 l/min at 6000rpm at 100bar load (27.5Nm), gives rise to a measured leakage flow rate from the pump of 4.0 l/min (equivalent to a mass flow rate of $7x10^{-5}$ kg/s). If this leakage flow passed through the stator windings, the mass flow rate would remain the same ($7x10^{-5}$ kg/s) since this is dominated by the pump leakage characteristics rather than the effective hydraulic resistance of the flow path. However, the increased cross-sectional area through which fluid flows in an open winding would result in a reduction in the axial velocity from 112 mm/s to 12 mm/s. Thus, the fluid would traverse the length of the machine in ~13 seconds, and the fluid temperature would be raised to that of the winding as it will reach effective steady state within this time-frame. However, since the operating temperature limit is likely to be set by the slot liner at ~150°C, this is some 30°C higher than the temperature at which the hydraulic fluid begins to degrade. Hence, there is little scope to employ fluid cooling of the windings unless this is separately forced through the slot regions rather than being reliant on the leakage through flow in the machine.

2.13 Efficiency measurements

Load tests at various pressures have been conducted on a fully encapsulated machine (process 3) with the pump fitted as shown in figure 2.36, and efficiency of each stage of the EHA system has been evaluated from both measurements and predicted losses.

Measurements of DC-link input power to the inverter were measured with a Voltech PM3000 Power analyser, and three-phase output power from the inverter to the BLDC machine was measured with a Norma D600 three phase power analyser. Power developed by the pump was calculated from the measurement of delivery flow and system load pressure, while mechanical shaft power developed by the BLDC machine was estimated from measured copper loss and predicted iron losses using [BER 85]. Figure 2.37 (a to d) shows measured efficiencies of the various stages in the EHA system from electrical 3-phase input to hydraulic output power for pressures of 50, 100, 150 and 200 bar, where a general trend of decreasing efficiency is noted for lower loads. This is attributed to fluid viscous drag loss in the machine that occurs irrespective of load condition, as it is primarily a function of speed and diameter. Hence, as the machine loading is reduced at a given speed, the drag loss becomes an increasingly large fraction of the total mechanical output power of the machine, thereby reducing the overall efficiency (as can be seen in Chapter 3, fig. 3.1). However, the proportion of drag loss that should be attributed to the pump and the machine was unclear from the tests, as there was no means of measuring the respective losses individually. It was decided to manufacture a dummy rotor from mild steel and drive it externally from a dynamometer machine with the pump removed, thus removing any electromagnetic losses, and therefore isolating the fluid friction loss for direct measurement (albeit via a gimbal mounted dynamometer that must be characterised before loss measurements can be taken).

2.14 References

[ANSYS] ANSYS finite element software users guide, revision 6.

[ARM 76] A.F. Armor, M.V.K. Chari. 'Heat flow in the stator core of large turbine-generators by the method of three-dimensional finite elements.' (Parts 1 and 2). IEEE Transactions on power apparatus and systems. Vol. 95, No. 5, Sept/Oct 1976, p. 1648 – 1668.

[ARM 80] A.F. Armor, M.V.K. Chari. 'Transient, three-dimensional, finite element analysis of heat flow in turbine-generator rotors.' IEEE Transactions on power apparatus and systems. Vol. 99, No. 5, May/June 1980, p. 471 – 482.

[BAR 84] A. Bar-Cohen, W.M. Rohsenow. 'Thermally optimum spacing of vertical, natural convection cooled, parallel plates.' Transactions of the ASME, Journal of heat transfer, Vol. 106, Feb 1984. pp. 116 – 123.

[BER 85] G. Bertotti. 'Physical interpretation of eddy current losses in ferromagnetic materials. I. Theoretical considerations.' Journal of Applied Physics, Vol. 57, No. 6, pp. 2110-2117, 1985.

[BOU 95] Bousbaine, A., McCormick, M. and Low, W.F.: 'In-situ determination of thermal coefficients for electrical machines.' IEEE Transactions on Energy Conversion, Vol. 10, N0. 3, September 1995.

[BOU 97] Bousbaine, A., McCormick, M. and Low, W.F.: 'Thermal modelling of permanent-split-capacitor single-phase induction motors based on accurate loss density measurement.' EMD97 1-3 September 1997. Conference publication No. 444.

[BRI 91] European BRITE project report, Sheffield, 1991,
Project No: P-2380-5

[CAL 02] S.D. Calverley. 'Design of a high speed turbo-generator for automotive applications.' PhD thesis, Sheffield University, 2002.

[COT 99] RESCOR 740® ceramic foam data sheet, Cotronics corporation, 3379, Shore Parkway, Brooklyn, NY, 11235.

[DRI 02] J. Driesen, R.J.M. Belmans, H. Kay. 'Methodologies for coupled transient electromagnetic-thermal finite-element modelling of electrical energy transducers.' IEEE Trans. Industry Applications, Vol. 38, No. 5, Sept/Oct 2002.

[EMM] Emmerson and Cumming specialty polymers, National Starch and Chemical, Nijverheidsstraat, B-2260, Wasterio, Belgium.

[GE 69] General Electric. 'Heat transfer and fluid flow data book.' 1969.

[INC 90] F.P. Incropera, D.P. Dewitt. 'Introduction to heat transfer.' 2nd Edition. John Wiley and sons Ltd. 1990.

[JOK 97] T. Jokinen, J. Saari. 'Modelling of the coolant flow with heat flow controlled temperature sources in thermal networks. 1997.

[LAV 78] J.D. Lavers, P.P. Biringer, H. Hollitscher. 'A simple method of estimating the minor loop hysteresis loss in thin laminations.' IEEE Transactions on Magnetics, Vol. 14, No. 5, September 1978, pp. 386 – 388.

[LIU 91] Z.J. Liu, D. Howe, P.H. Mellor, M.K. Jenkins. 'Thermal analysis of permanent magnet machines.' University of Sheffield, U.K. EMD95.138, No. 2, March 1991.

[LIU 95] Z.J. Liu, D. Howe, P.H. Mellor, M.K. Jenkins. 'Coupled thermal and electromagnetic analysis of a permanent magnet brushless DC servo motor.' Electrical Machines and Drives conference, University of Sheffield, U.K, 1995.

[MEL 91] P.H. Mellor, D. Roberts, D.R. Turner. 'Lumped parameter thermal model for electrical machines of TEFC design.' 1991, IEE Proceedings-B, Vol. 138, No. 5, April, pp. 205-218.

[MON 92] P. Monkhouse. 'Design and performance of a high performance brushless DC drive' PhD thesis, Sheffield University, June 1992.

[NOMEX] Nomex type 410 data sheet. Dupont NOMEX, P.O. Box 50, CH – 1218 le Grand Sacannex, Geneva, Switzerland.

[PER 79] I.J. Perez, and J.G. Kassakian. 'A stationary thermal model for smooth air-gap rotating electrical machines. Electric Machines and Electromechanics, 1979, No 3-4, pp. 285-303.

[SAK 91] D. Sarker, P.K. Mukherjee, S.K. Sen. 'Use of 3-dimensional finite elements for computation of temperature distribution in the stator of an induction motor.' IEE proceedings B, Power Applications, Vol. 138, Issue 2, Mar 1991, pp. 75 – 86.

[SAR 95] Saari, J.: 'Thermal Modelling of High-Speed Induction Machines', Acta Polytechnica Scandinavica, Electrical Engineering Series, No.82. 1995.

[SAR 97] Saari, J.: 'Thermal Analysis of High-Speed Induction Machines', Acta Polytechnica Scandinavica, Electrical Engineering Series, No.90. 1997

[SHA 02] S.J. Pickering, D. Lampard, M. Shanel. 'Ventilation and heat transfer in a symmetrically ventilated salient pole synchronous machine.' International conference on Power Electronics Machines and Drives, 2002, Conference No. 487, pp. 462 – 467.

[SHL 64] Y.P. Shlykov, Y.A. Ganin. 'Thermal resistance of metallic contacts.' International Journal of heat and mass transfer, 1964 Vol. 7, pp. 921-929.

[SOD 31] C.R. Soderberg. 'Steady flow of heat in large turbine-generators.' Transactions AIEE, 1931 Vol.50, pp. 782 – 802.

[XYP 99] J. Xypteras, V. Hatziathanassiou. 'Thermal analysis of an electrical machine taking into account the iron losses and the deep bar effect.' IEEE Transactions on Energy Conversion, Vol. 14, No. 4, December 1999.

Table 2.1. Key dimensional data of the BLDC machine with reference to fig. 2.2.

Dimension	**Size (mm)**	**Equivalent parameter from Figure 2.2**
Frame outer radius	95.0	R1
Stator outer radius	90.0	R2
Radius to back of slot	81.7	R3
Stator bore radius	55.5	R4
Airgap sleeve bore radius	54.5	R5
Rotor outer radius	53.0	R6
Magnet outer radius	52.5	R7
Rotor iron outer radius	46.5	R8
Shaft outer radius	37.5	R9
Tooth body height	21.65	th
Tooth body width	14.5	tw
Tooth tip width	6.2	ttw
Tooth tip height	1.0	tth

Table 2.2. Measured and predicted thermal conductivity data from conductor bundle tests and FE models respectively.

Encapsulation process	Packing factor	No. of conductors	Measured temp difference. (K)	Effective thermal conductivity (W/m.K)	Predicted thermal conductivity (W/m.K)
1	0.65	30	50.0	1.07	1.18
2	0.65	30	26.7	2.04	-
3	0.65	30	13.1	4.15	7.23

Table 2.3. Equivalent thermal resistance of NOMEX 410 slot liner for different encapsulation processes from equation 2.6.

Encapsulation process	Equivalent thermal resistance per unit area (°C/W)
1	$2.5\ e^{-3}$
2	$2.0\ e^{-3}$
3	$1.6\ e^{-3}$

Table 2.4. Measured and predicted temperature-rise above ambient at various regions in the stator, for various winding encapsulation processes.

Encapsulation process		Stator back-iron	Tooth body	Tooth tip	Centre of winding	End-winding	Fin tip	Fin centre	Fin Base
1	Predicted	72	71	78	113 /121	114	-	-	69
	Measured	73	75	79	115	118	63	67	68
2	Predicted	70	75	78	95 /99	105	66	67	67
	Measured	72	76	77	98	95	-	-	69
3	Predicted	72	75	77	81/ 83	82	-	-	69
	Measured	75	79	77	83	87	68	74	74

Table 2.5. Thermal time constant for each winding encapsulation process.

Encapsulation process	**Predicted winding thermal time constant (mins)**	**Measured winding thermal time constant (mins)**
Process 1	43.8	47.8
Process 2	48.3	53.0
Process 3	60.1	62.5

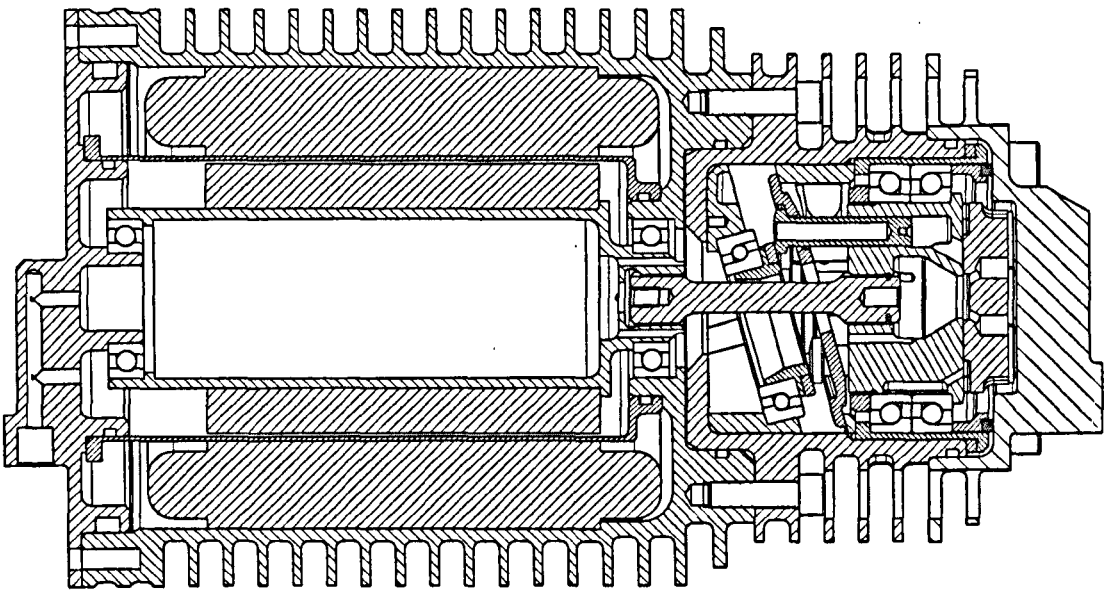

Figure 2.1. BLDC machine and slipperless piston pump combination (pump on right)

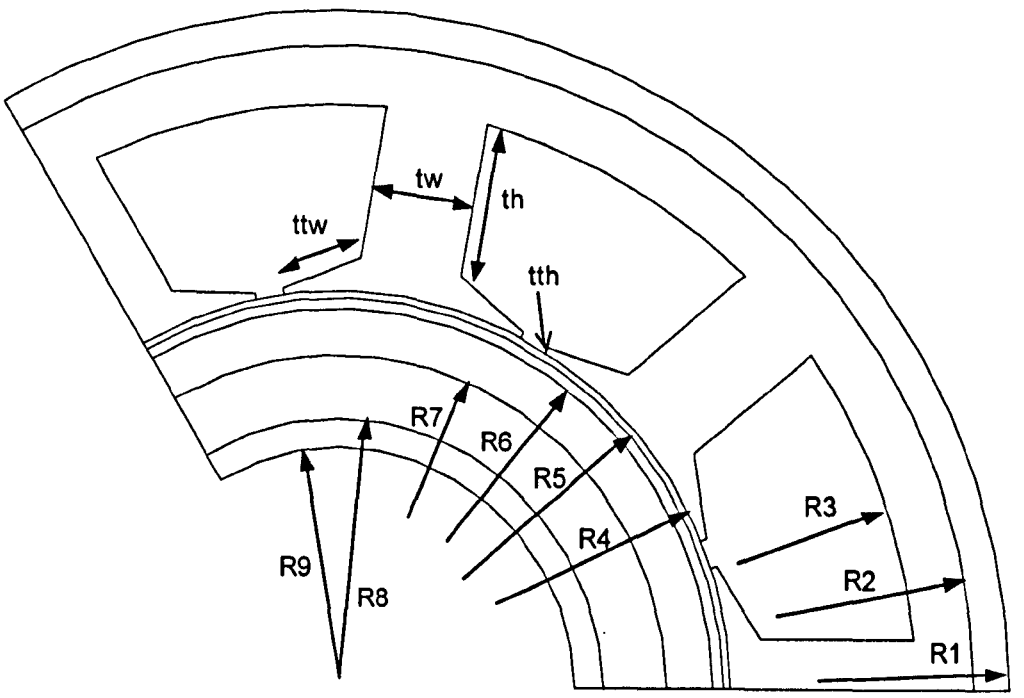

Figure 2.2. Key dimensional parameters of the BLDC machine for the EHA application (actual dimensions are given in Table 2.1).

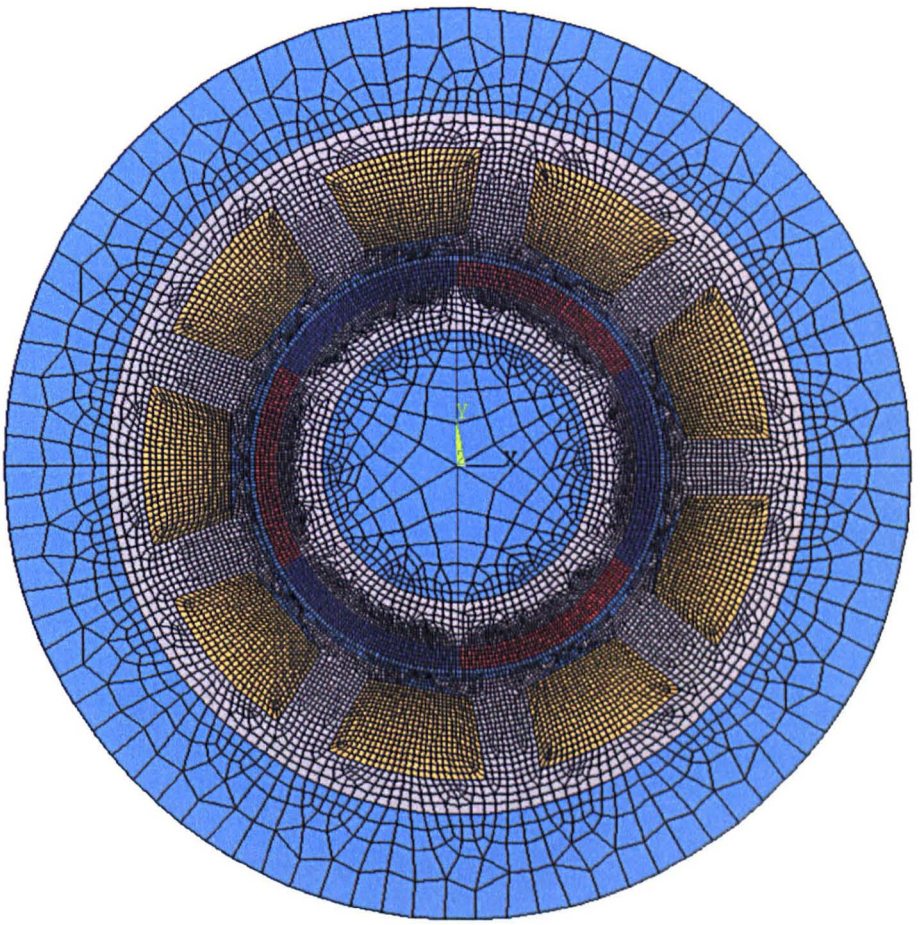

Figure 2.3. Finite element mesh of the BLDC machine used to generate per-element flux density data for the iron loss model.

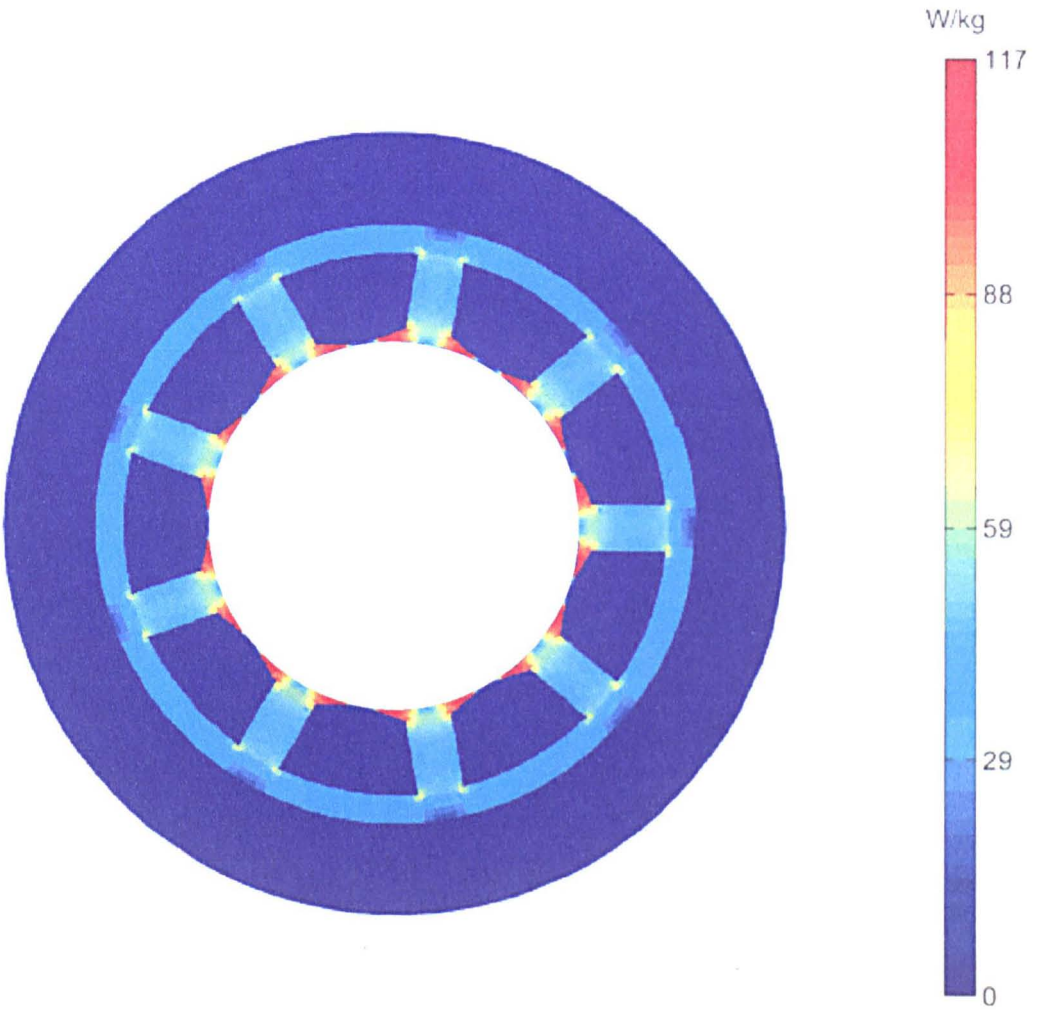

Figure 2.4. Iron loss distribution in the BLDC machine at 6000 rpm, 13.75 Nm.

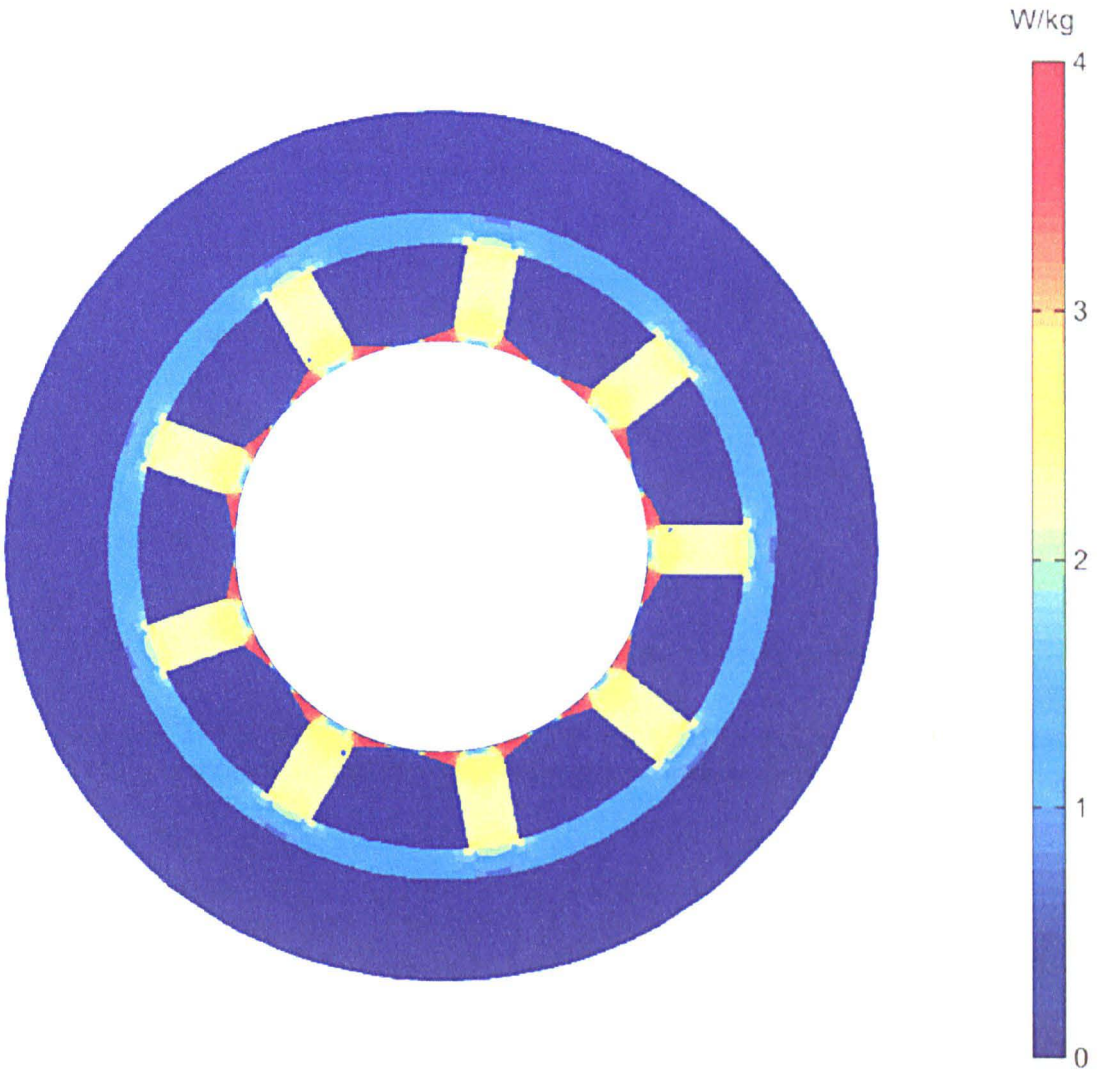

Figure 2.5. Iron loss distribution in the BLDC machine at 700 rpm, 55 Nm.

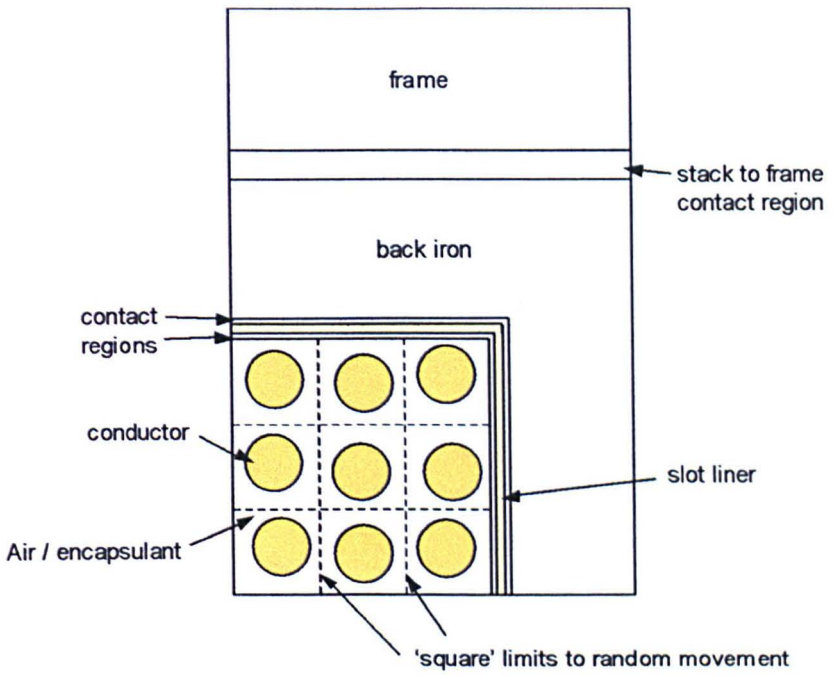

Figure 2.6. Diagram of stator section used in the FE model, showing the various contact regions modelled, and the limits of conductor placement within the slot region.

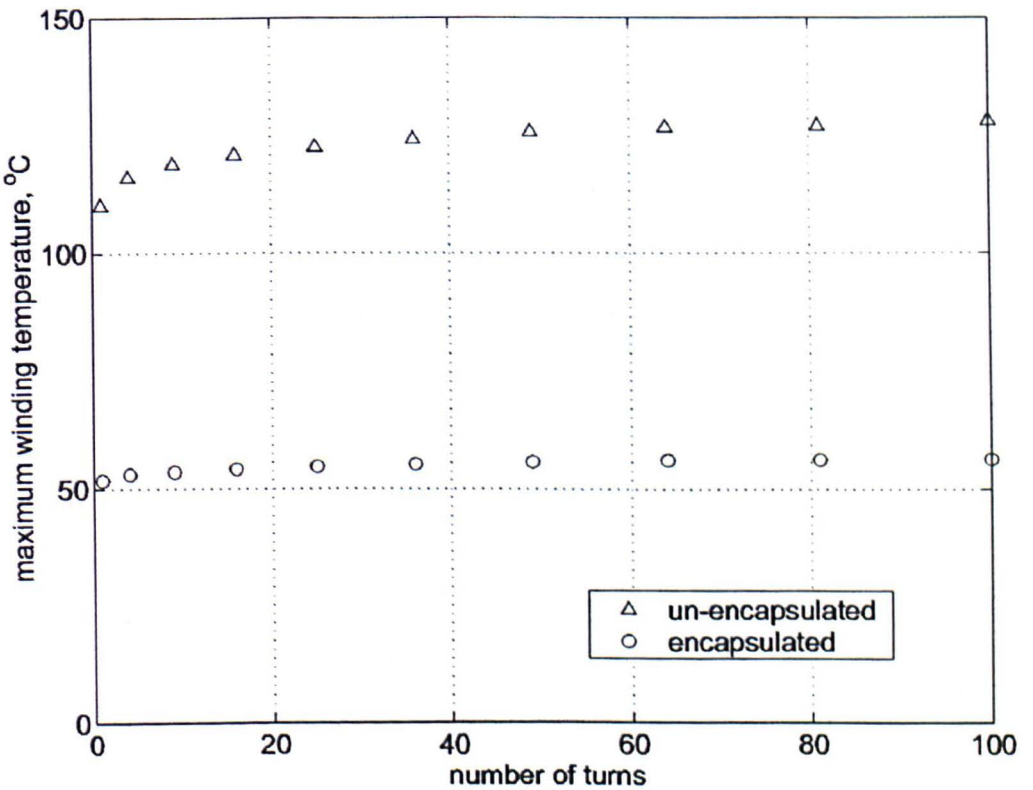

Figure 2.7. Maximum winding temperature as a function of number of turns for an un-encapsulated (stage 1) winding and an encapsulated (stage 3) winding at a fixed power loss of 20W.

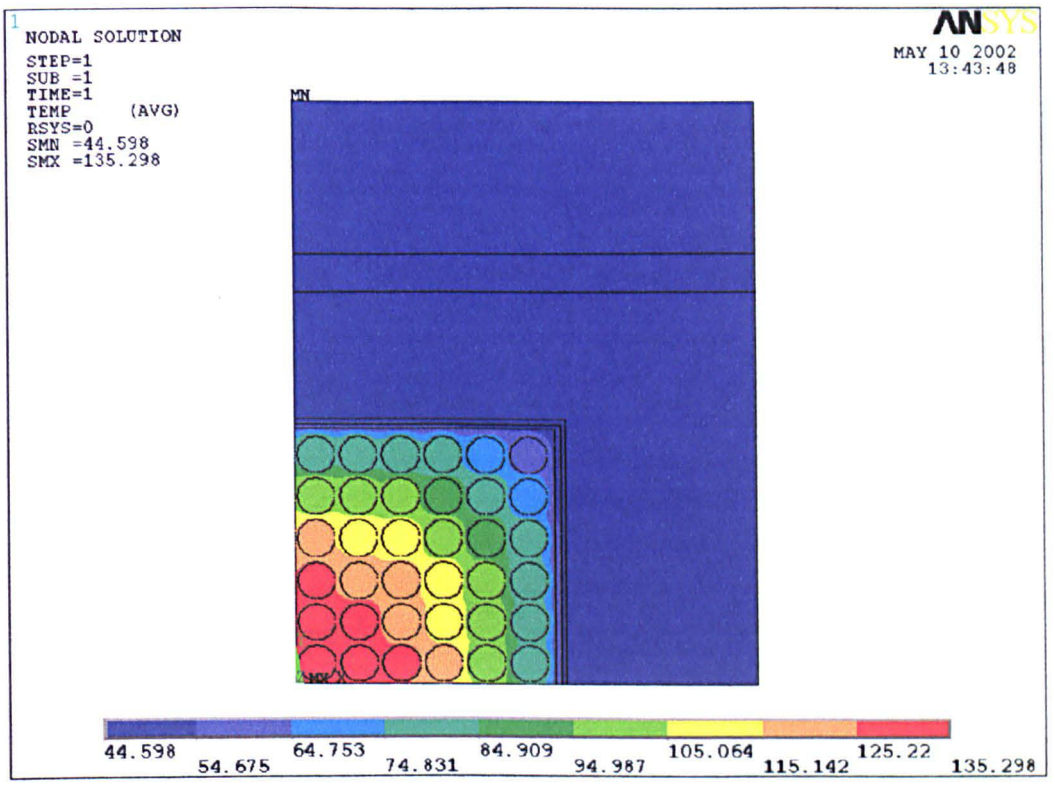

Figure 2.8. Temperature distribution in an un-encapsulated slot for a packing factor of 0.6, a power loss of 20W, with 36 conductors of circular cross-section.

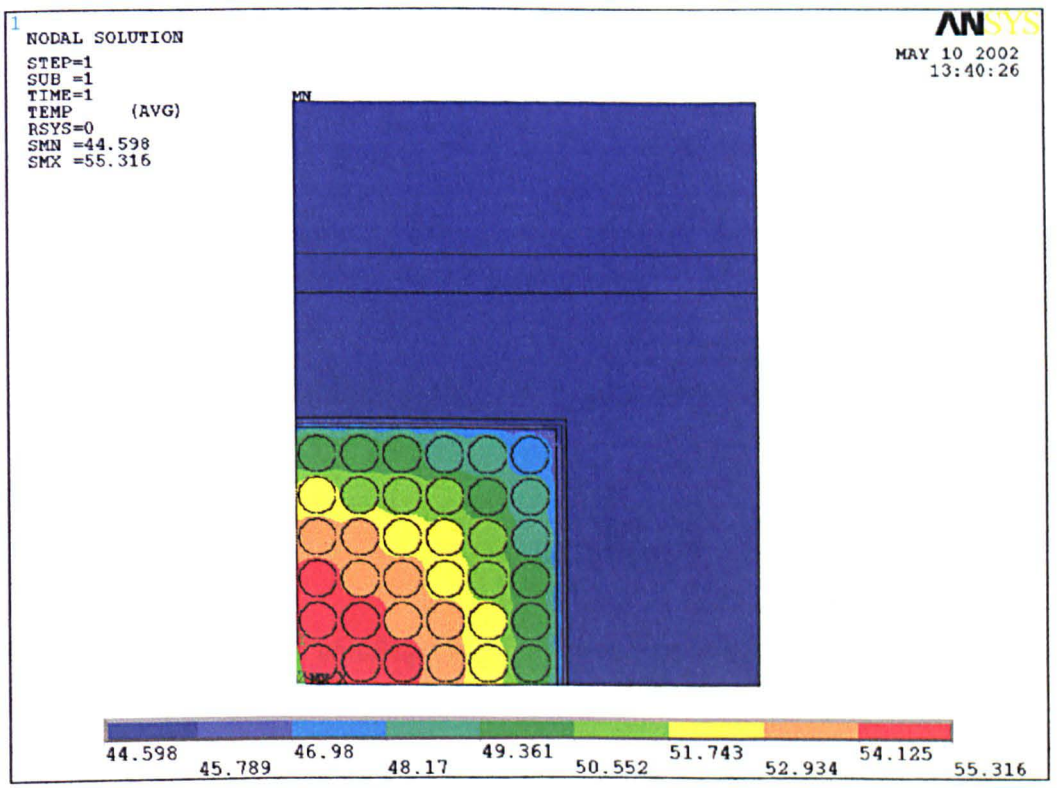

Figure 2.9. Temperature distribution in a fully encapsulated slot for a packing factor of 0.6, a power loss of 20W, with 36 conductors of circular cross-section.

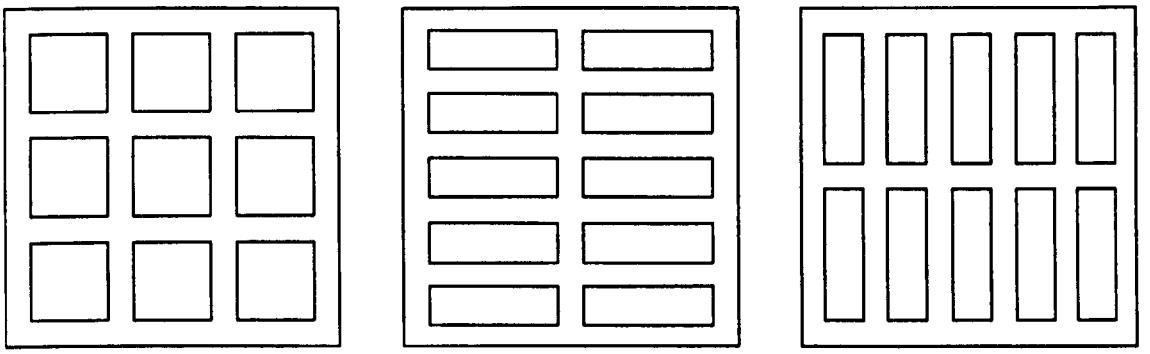

Figure 2.10. Various conductor geometries considered: (a) square conductors, (b) horizontal rectangular conductors, (c) vertical rectangular conductors.

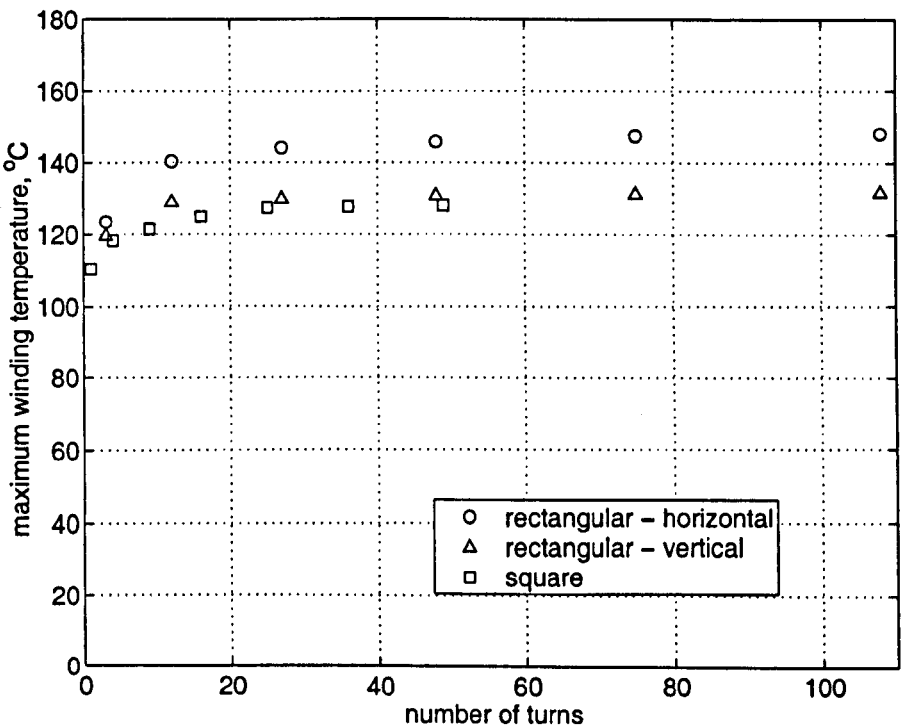

Figure 2.11. Maximum winding temperature as a function of the number of turns; for an un-encapsulated winding; with three different conductor geometries.

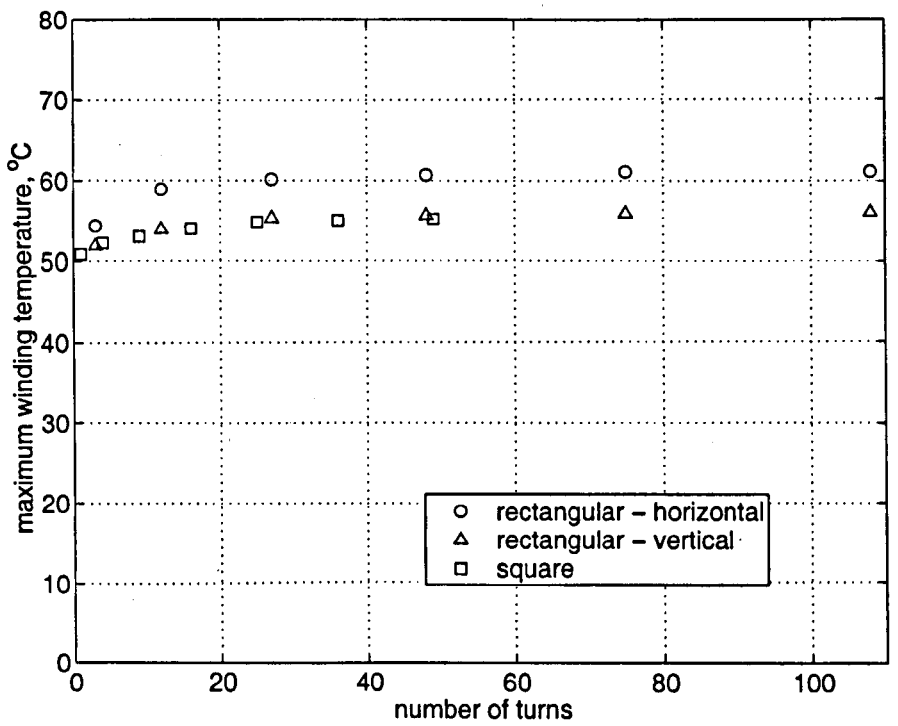

Figure 2.12. Maximum winding temperature as a function of the number of turns; for an encapsulated winding; with three different conductor geometries.

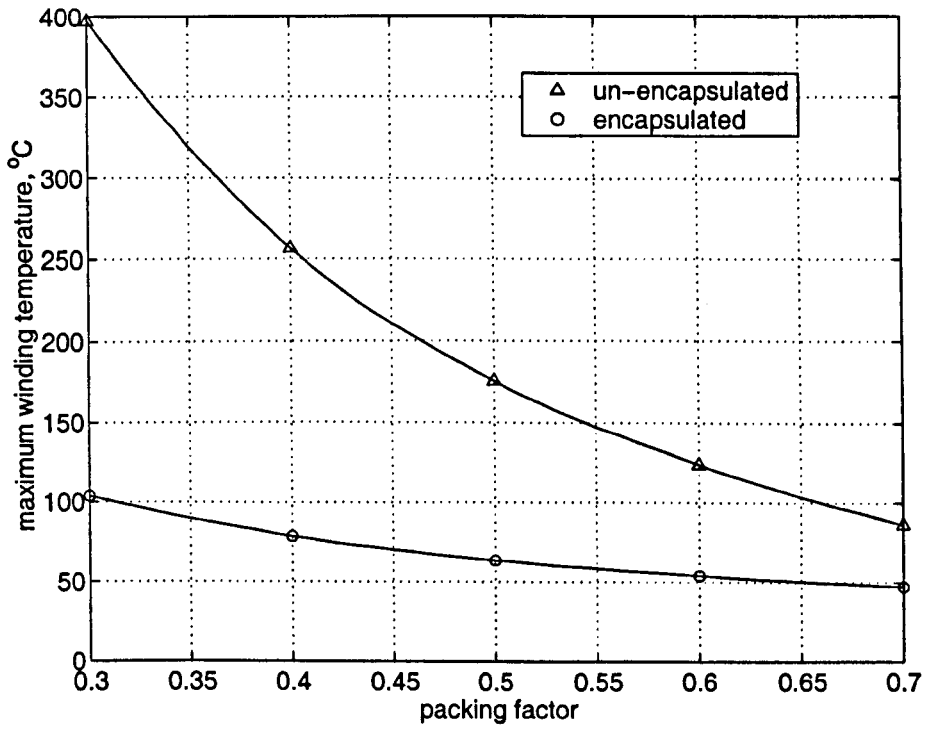

Figure 2.13. Maximum and minimum winding temperature as a function of the packing factor for a fixed mmf of 500 A.turns.

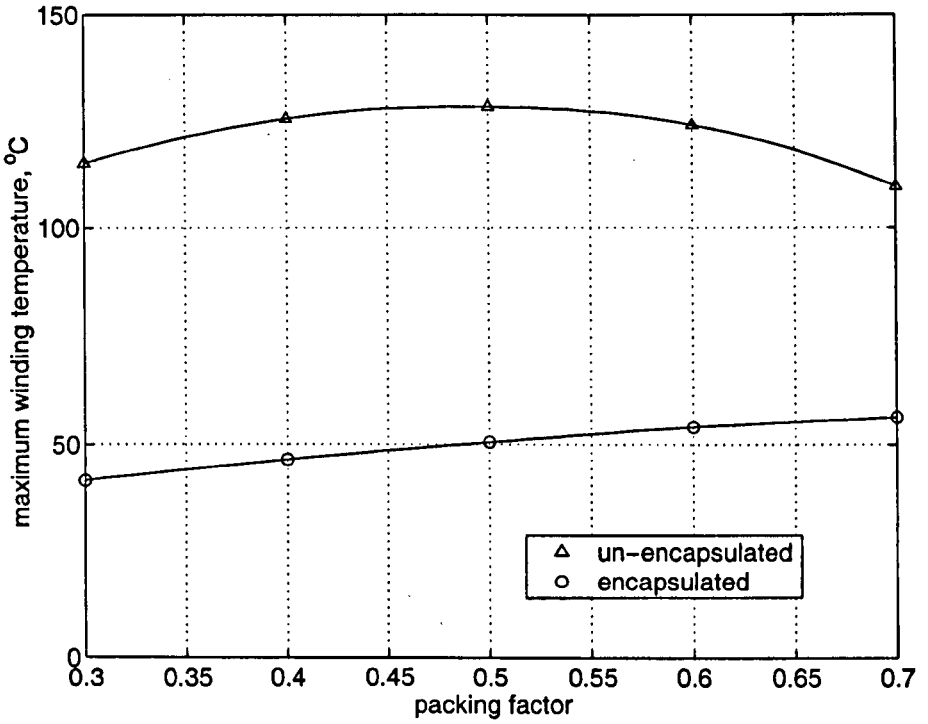

Figure 2.14. Maximum and minimum winding temperature as a function of the packing factor for a fixed power loss of 20W (corresponding to the power loss obtained with a packing factor of 0.6 and mmf = 500A.turns)

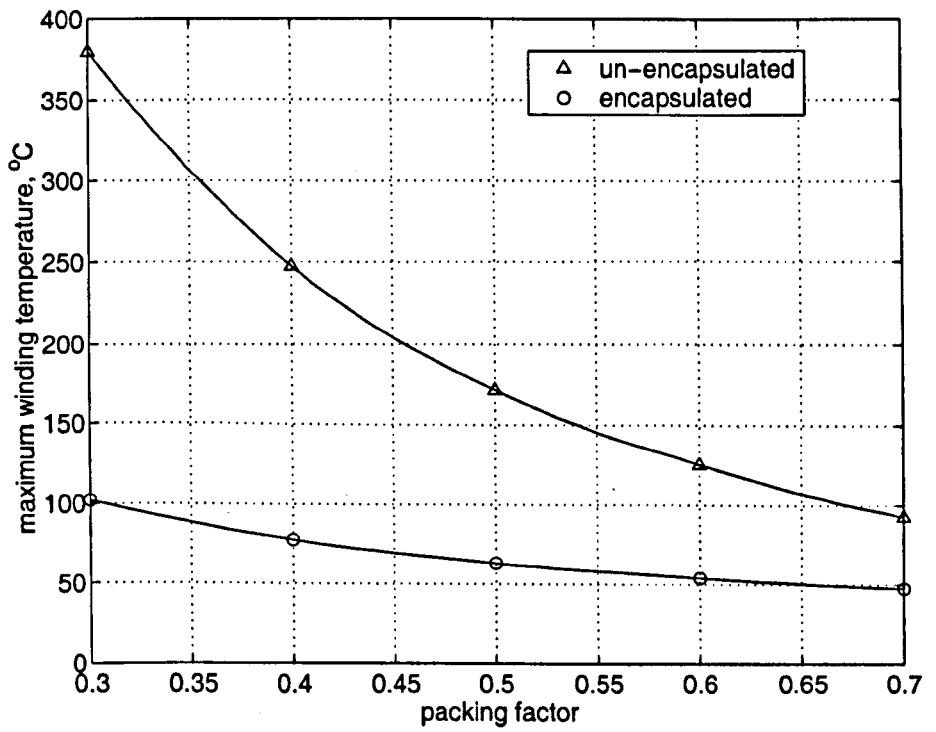

Figure 2.15. Variation in maximum winding temperature with packing factor for 12 horizontally arranged rectangular conductors. Constant power loss of 20W.

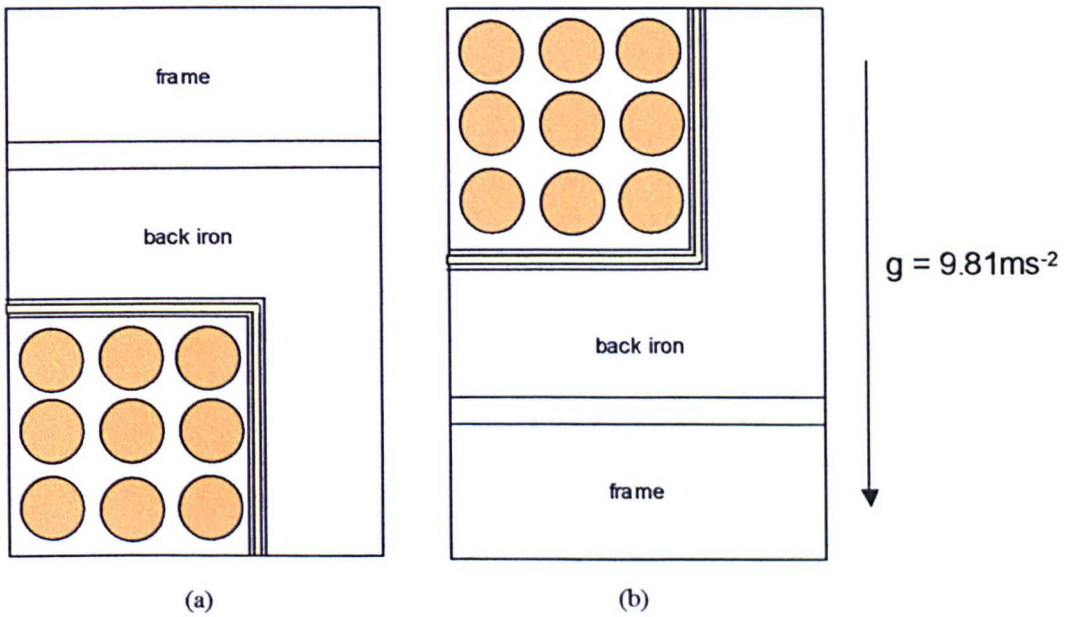

Figure 2.16. Reference slots for CFD model with different orientations with respect to gravitational forces. (a) upper slot, (b) lower slot.

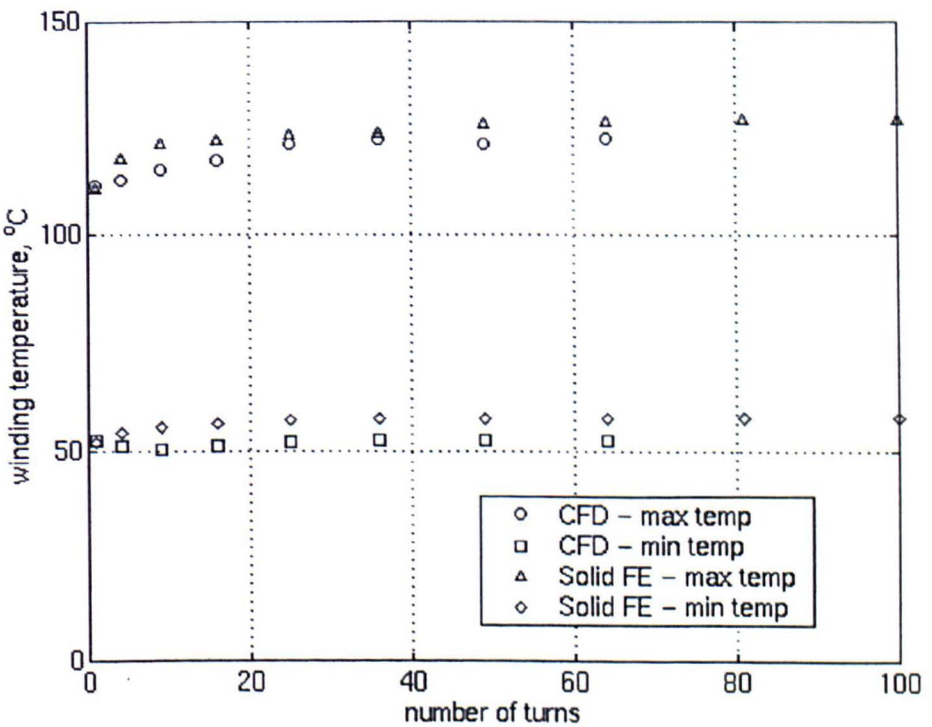

Figure 2.17. Solid finite element and CFD predicted maximum and minimum winding temperatures for the particular case of a uniformly distributed power loss of 20W per slot.

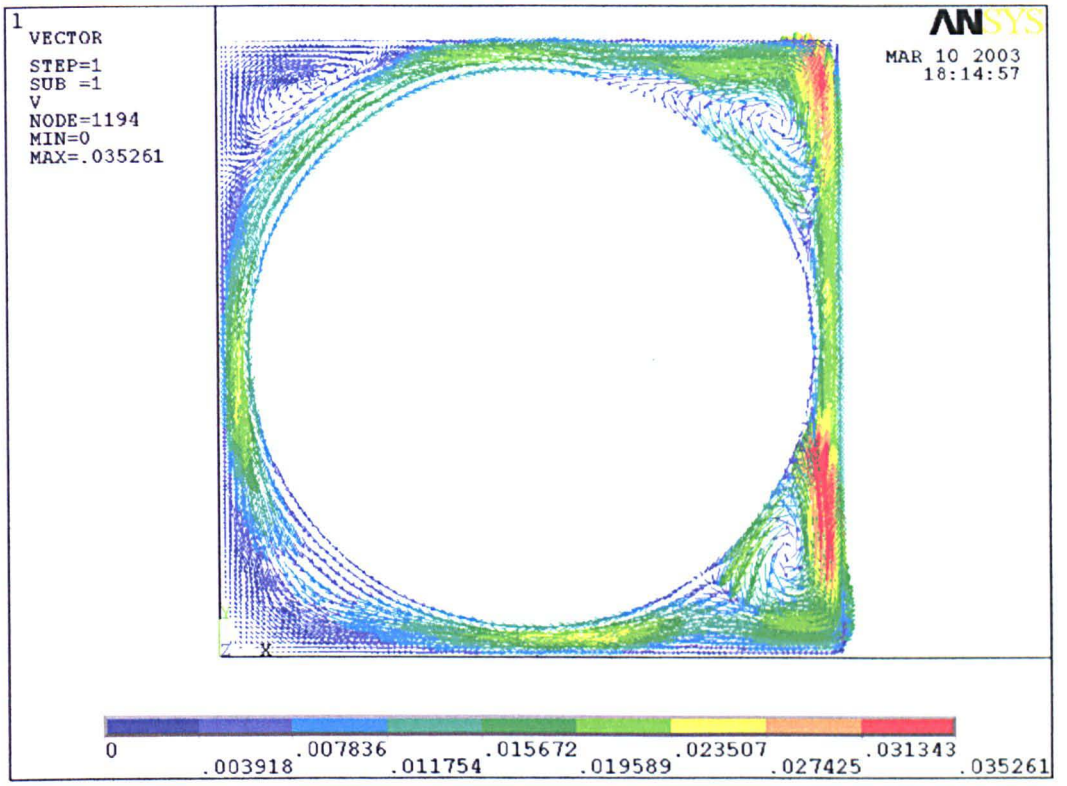

Figure 2.18. Velocity vectors computed from the CFD model for a single circular turn.

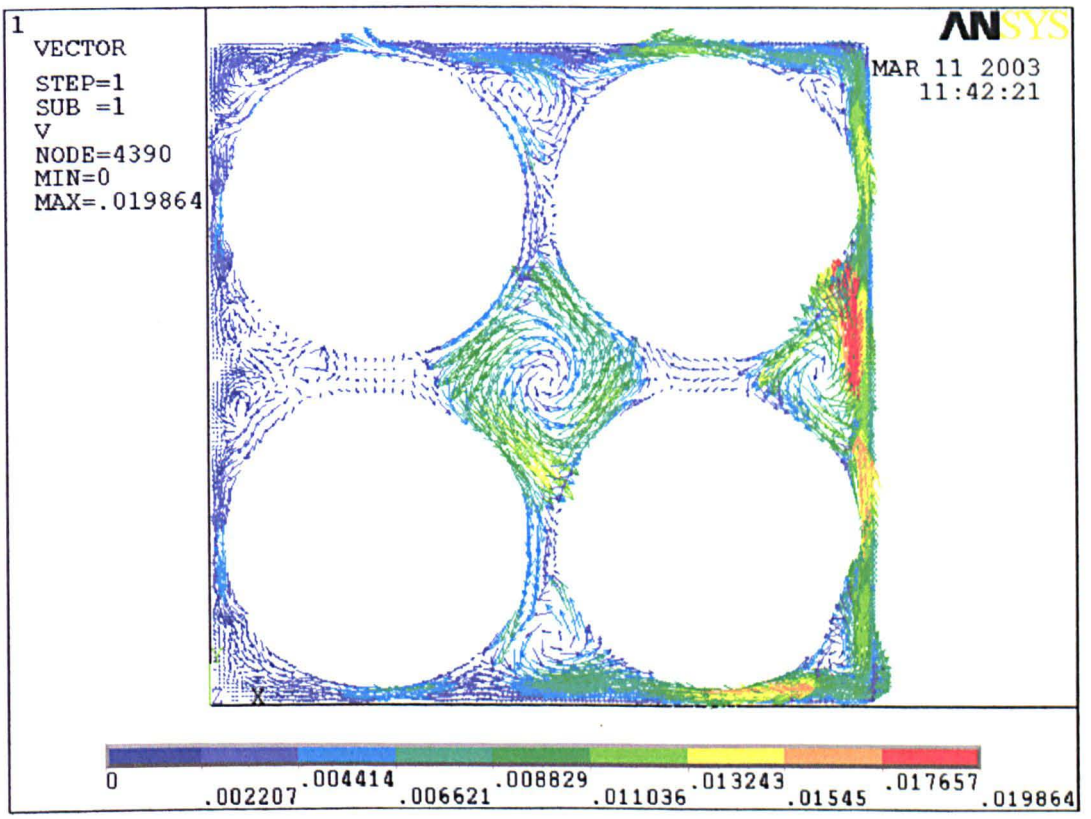

Figure 2.19. Velocity vectors computed from the CFD model for 4 circular turns.

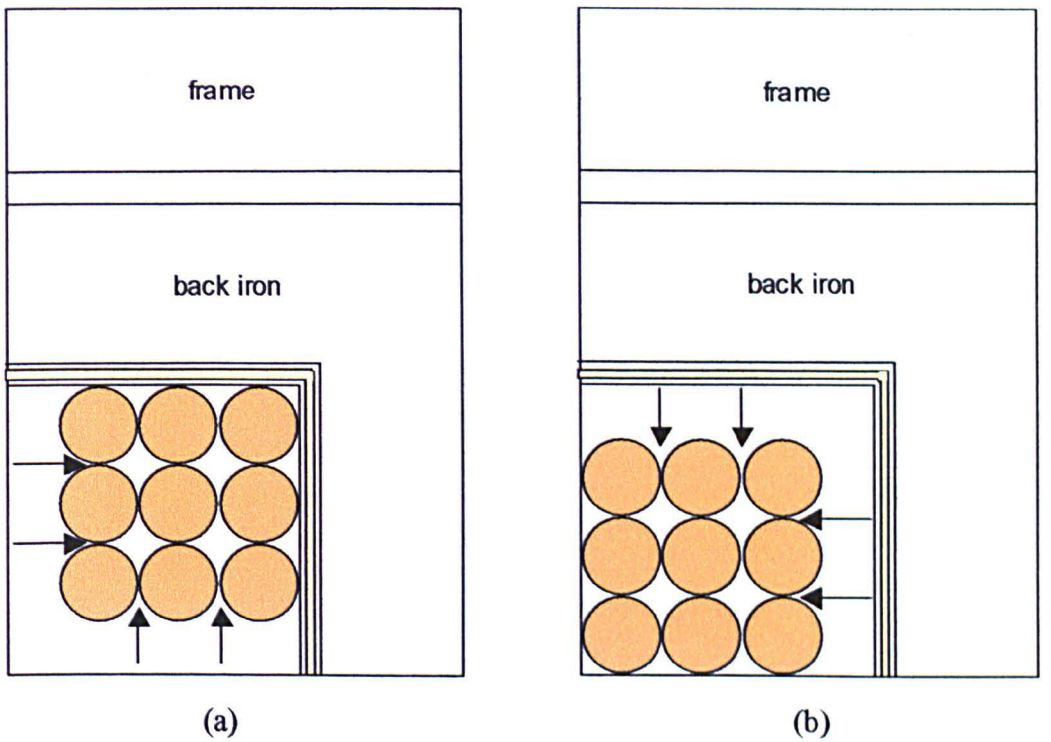

Figure 2.20. (a) Best case, and (b) worst case conductor positioning for heat transfer from the winding to the stack.

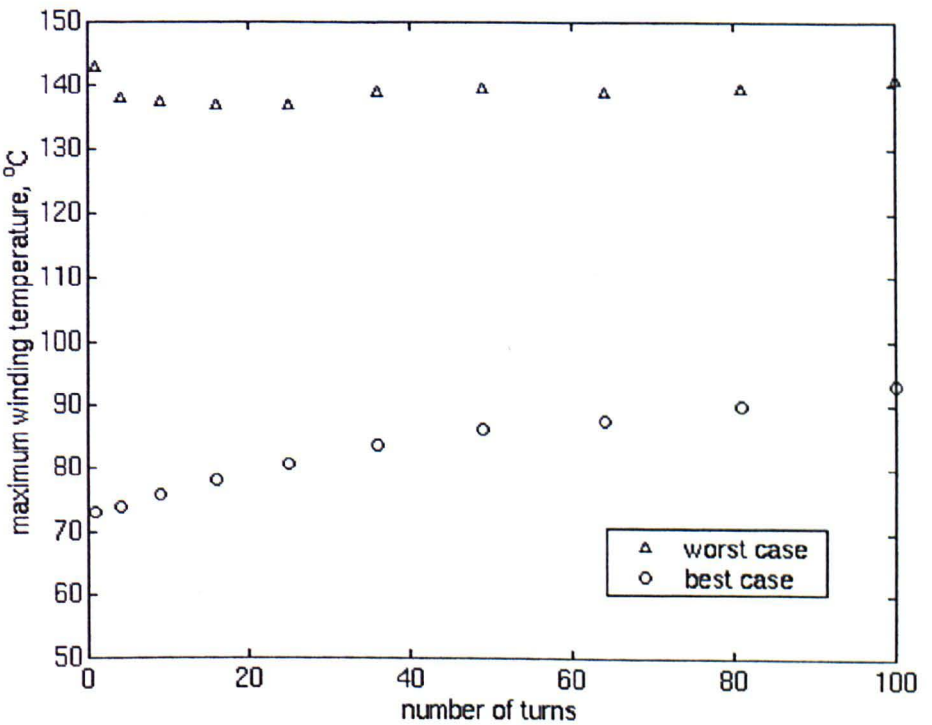

Figure 2.21. Maximum winding temperature as a function of the number of turns for the worst and best-case conductor positions in an un-encapsulated winding (with reference to fig 2.23 (a) and (b).

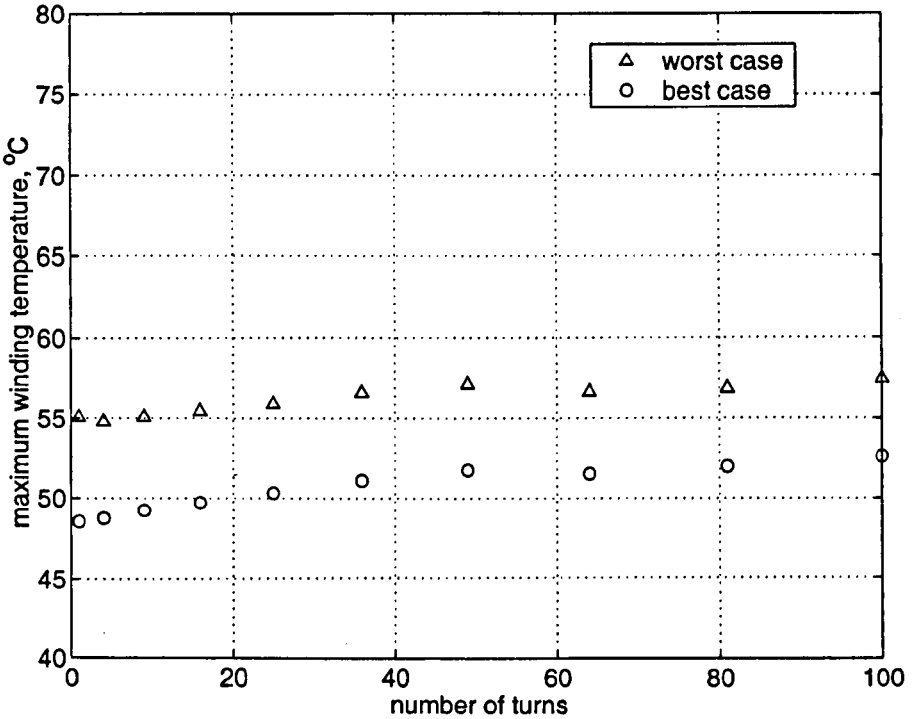

Figure 2.22. Maximum winding temperature as a function of the number of turns for the worst and best-case conductor positions in an encapsulated winding (with reference to fig 2.23 (a) and (b).

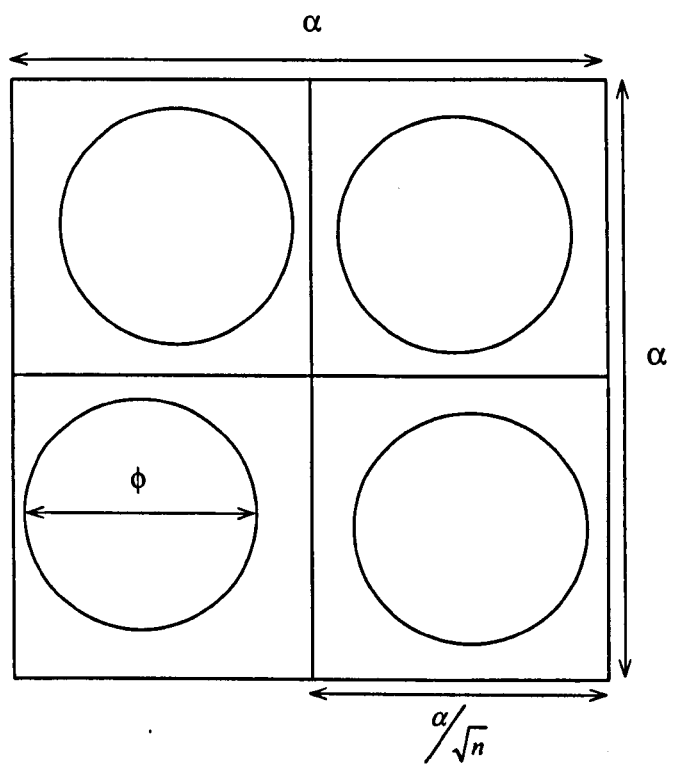

Figure 2.23. Geometric definition of the random conductor position model

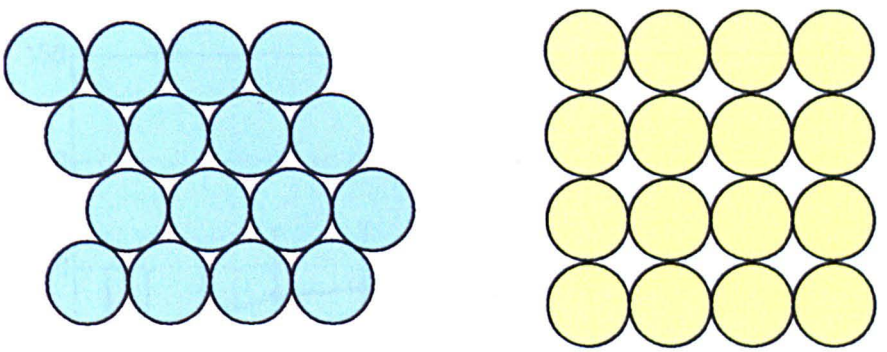

(a) (b)

Figure 2.24. (a) Close packed geometry, (b) Square packed conductor geometry

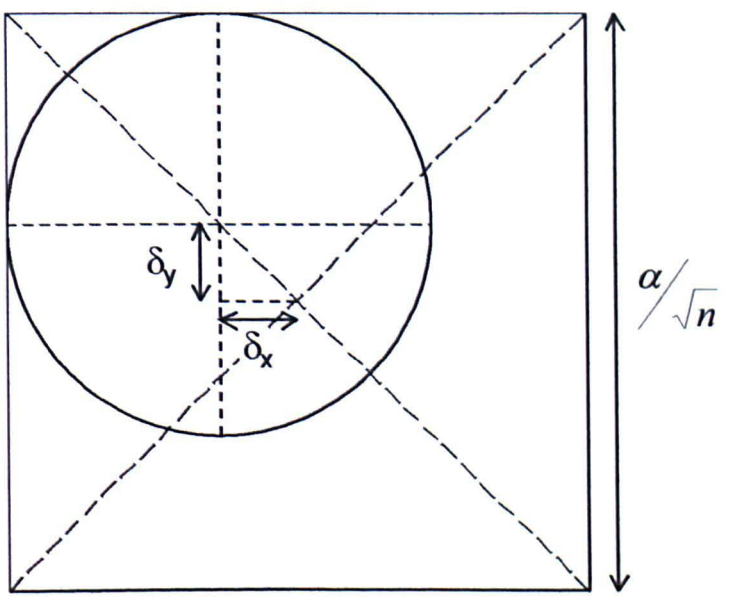

Figure 2.25. Definition of the maximum conductor displacement from the centre position of the square with reference to equation 2.3 and 2.4.

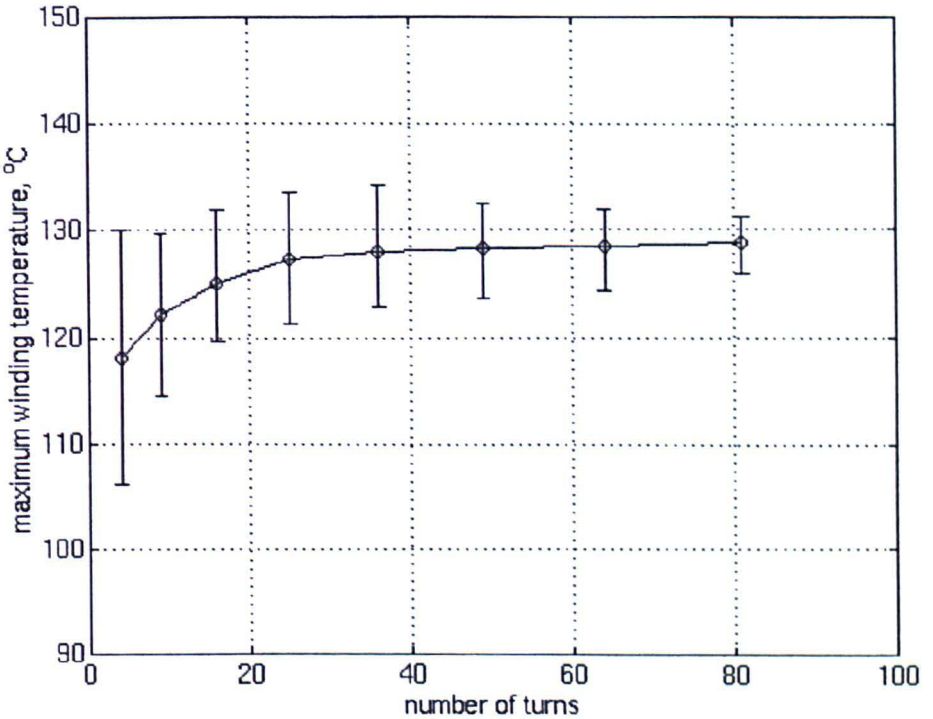

Figure 2.26. Variation in maximum winding temperature with increasing numbers of turns for randomly positioned, stage 1 conductors of circular cross section. Power loss = 20W.

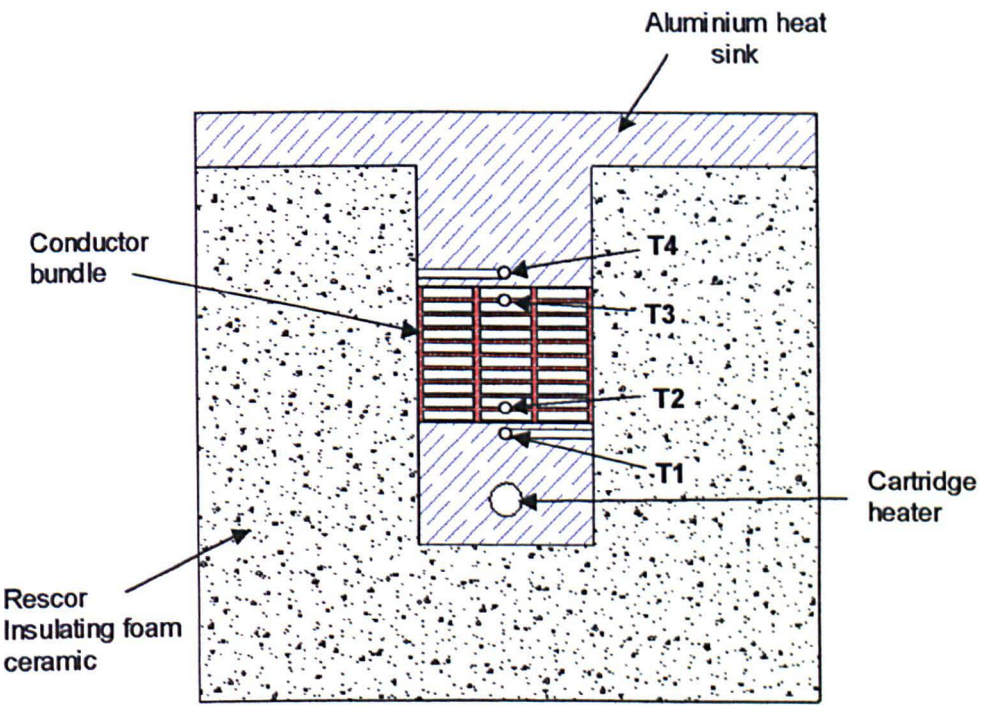

Figure 2.27. Cross section of bundle thermal conductivity test fixture

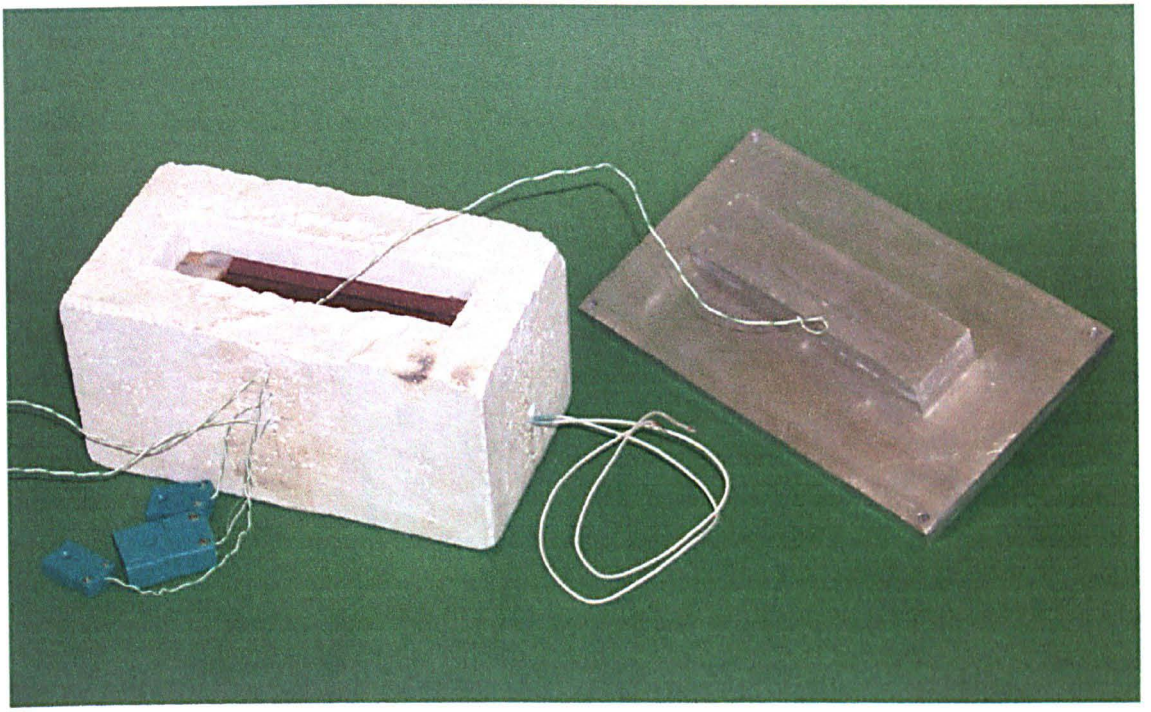

Figure 2.28. Conductor Bundle test fixture with aluminium heat-sink removed.

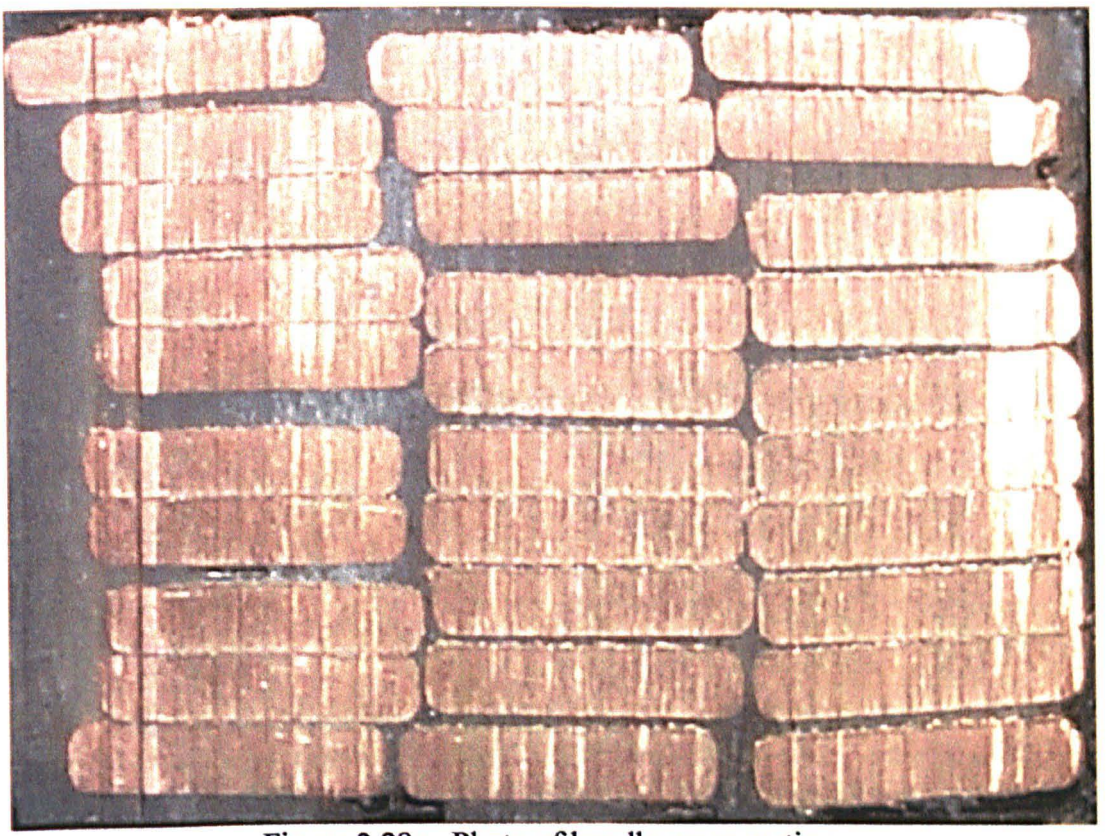

Figure 2.28a. Photo of bundle cross section.

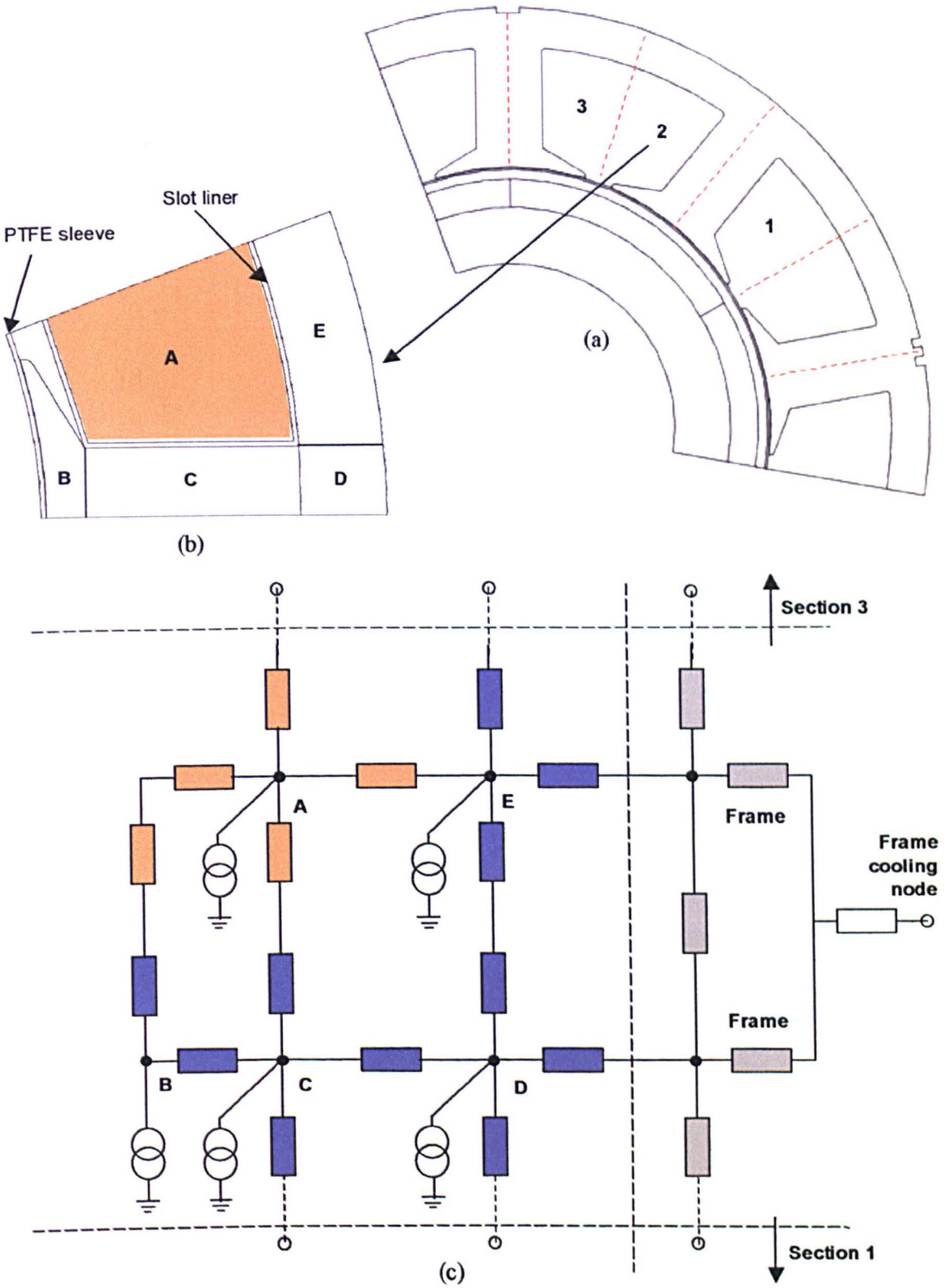

Fig. 2.29 BLDC machine showing stator section considered in the thermal model. (b) Subdivision of the section into A: winding, B: tooth tip, C: tooth body, D and E: back iron. (c) Simplified thermal network of resistances showing connection with adjacent sections 1 and 3, and the frame. Although thermal capacitances have been neglected for clarity, these would be situated at points A through E.

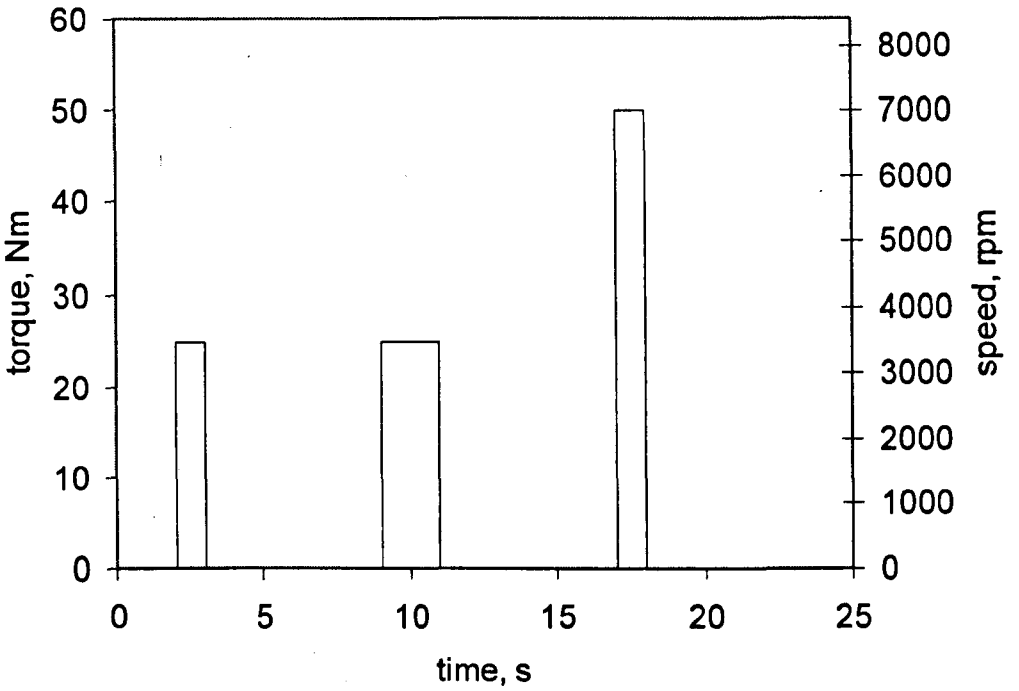

Figure 2.30(a). Representative duty cycle for a rudder primary flight surface actuator during take off/ landing.

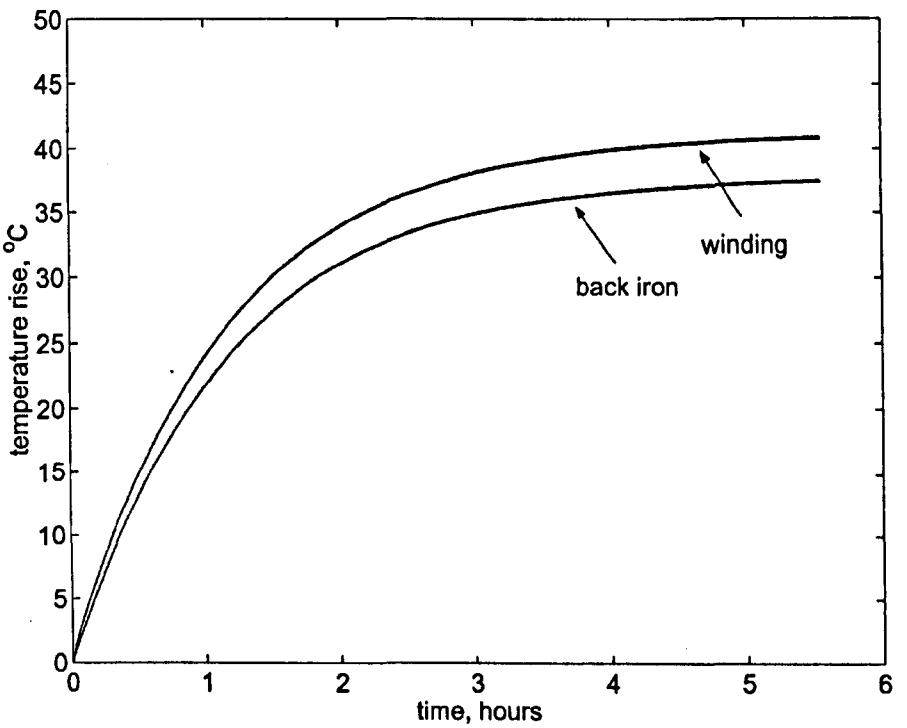

Figure 2.30(b). Winding and back iron transient temperature rise for the BLDC machine operating on the duty cycle of fig 2.30(a).

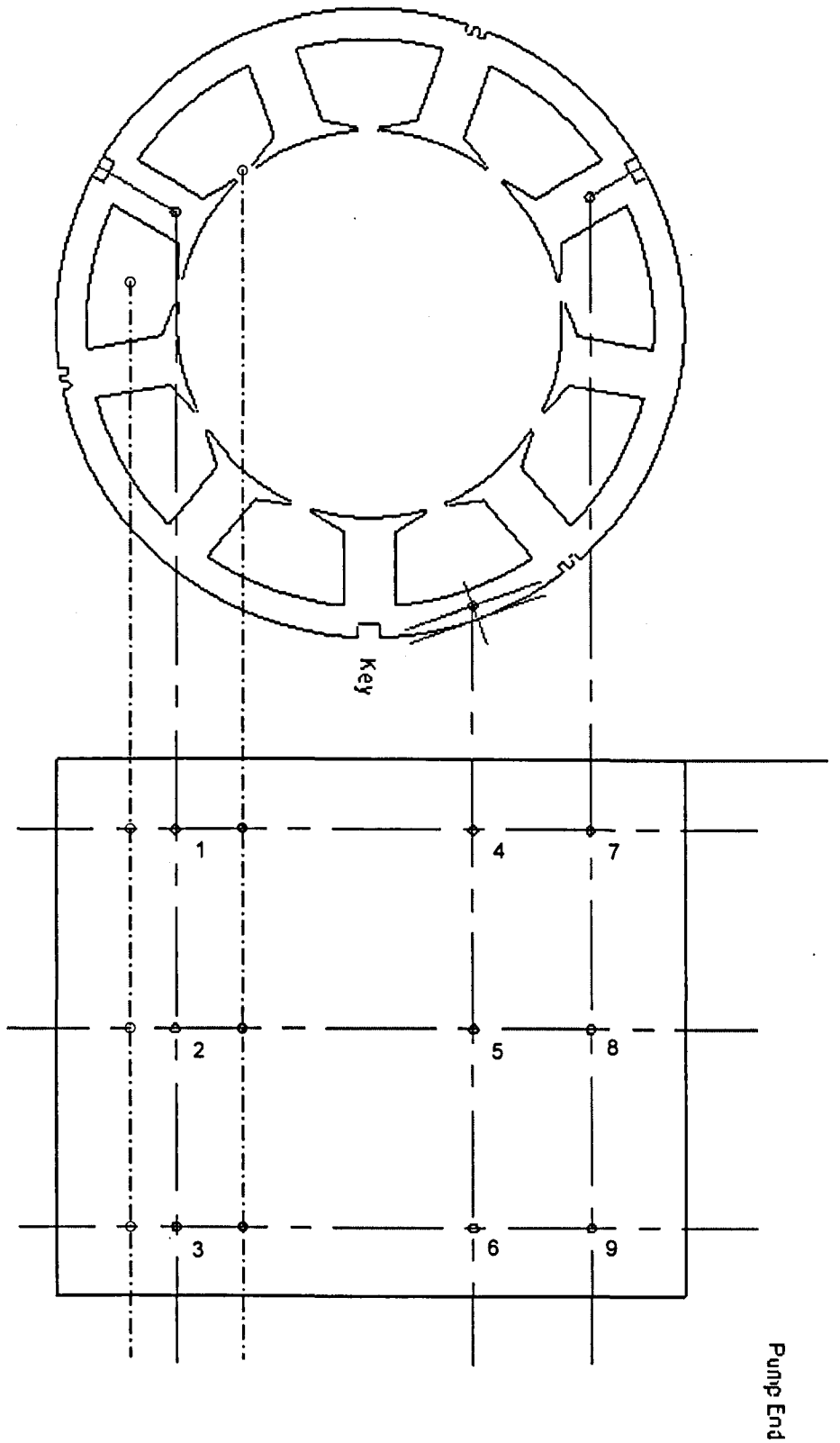

Figure 2.31. Location of the 15 thermistors in the stator iron and windings. (3 additional thermistors are placed in the end-windings).

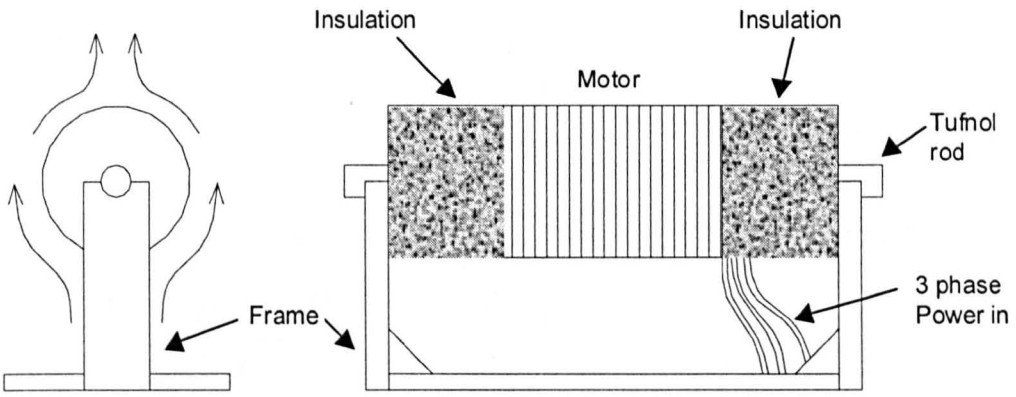

Figure 2.32. Test arrangement for BLDC stator thermal tests during different stages of encapsulation.

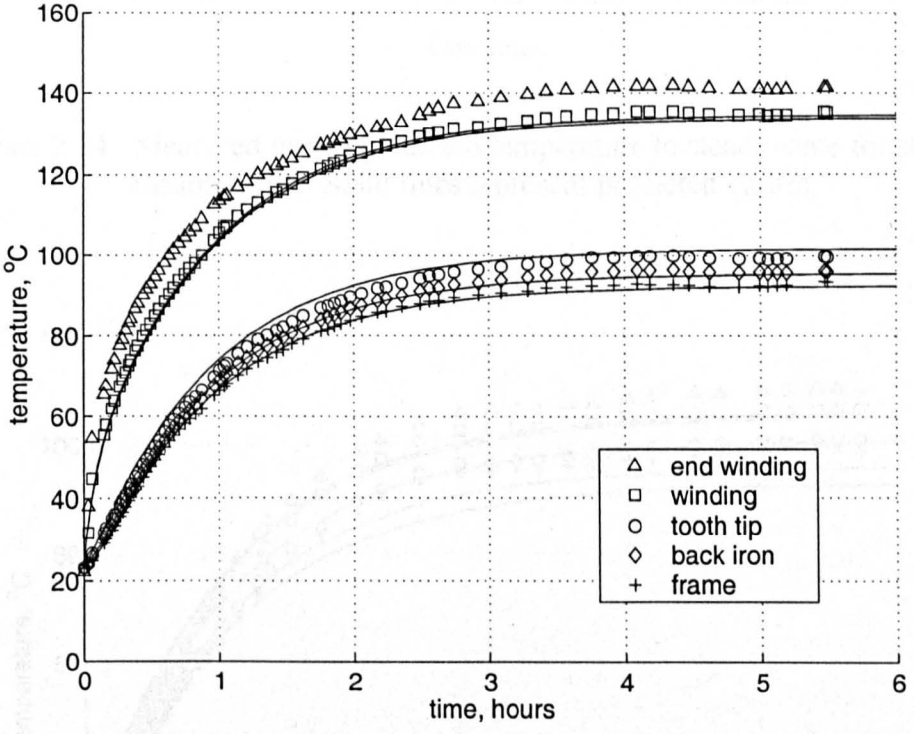

Figure 2.33. Measured versus predicted temperature to steady-state for stage 1 encapsulation. Solid lines represent predicted values.

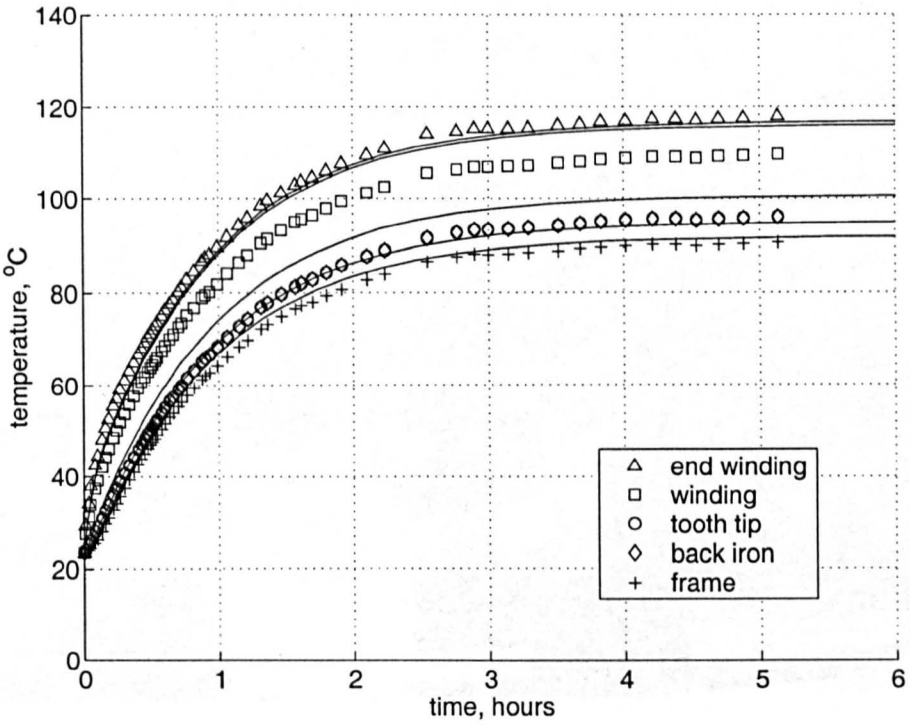

Figure 2.34. Measured versus predicted temperature to steady-state for stage 2 encapsulation. Solid lines represent predicted values.

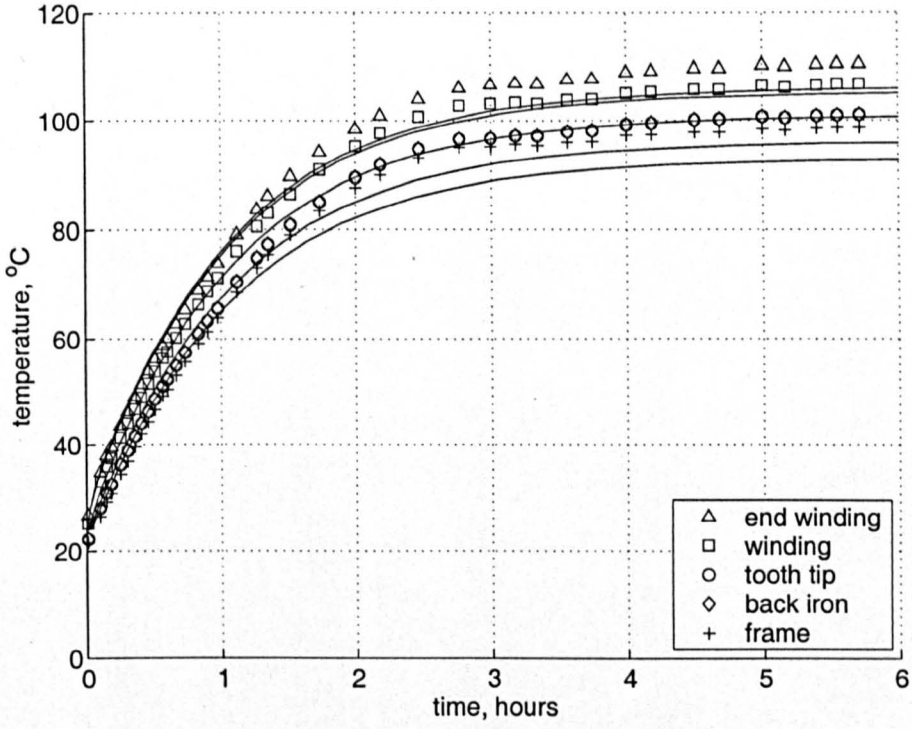

Figure 2.35. Measured versus predicted temperature to steady-state for stage 3 encapsulation. Solid lines represent predicted values.

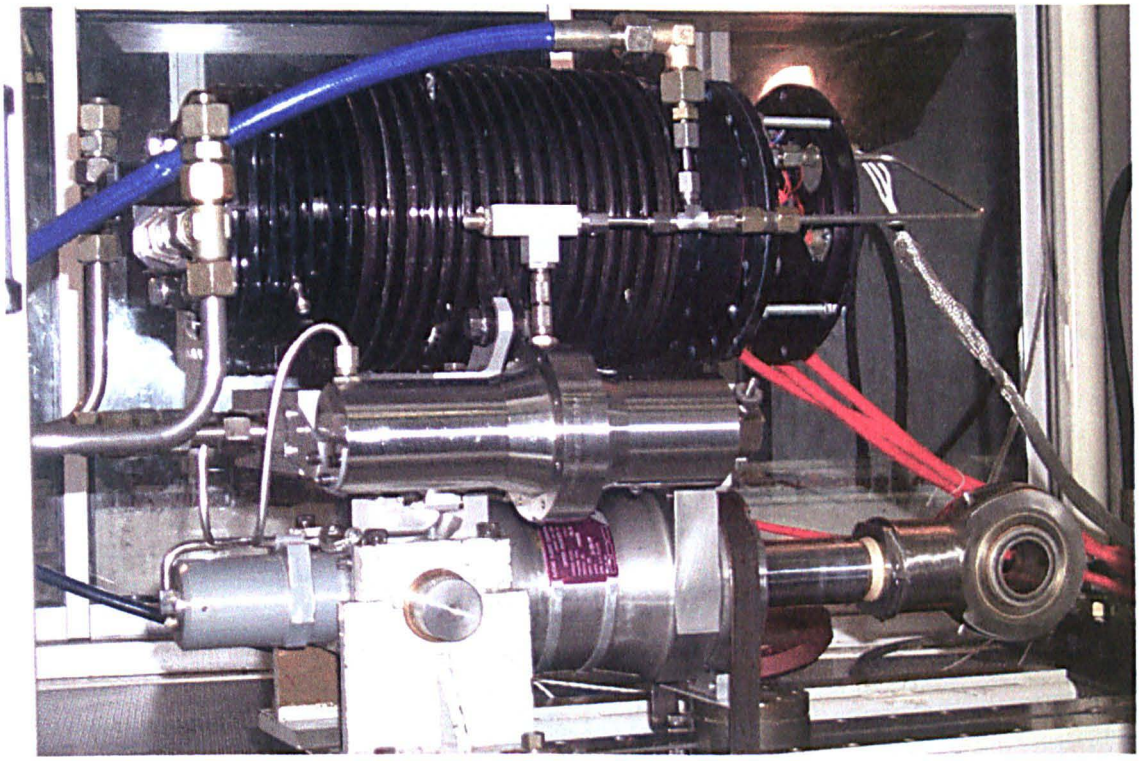

Figure 2.36. EHA system load testing. The BLDC machine is top centre with the pump mounted on the left hand end. The hydraulic ram shown at the bottom is not in circuit.

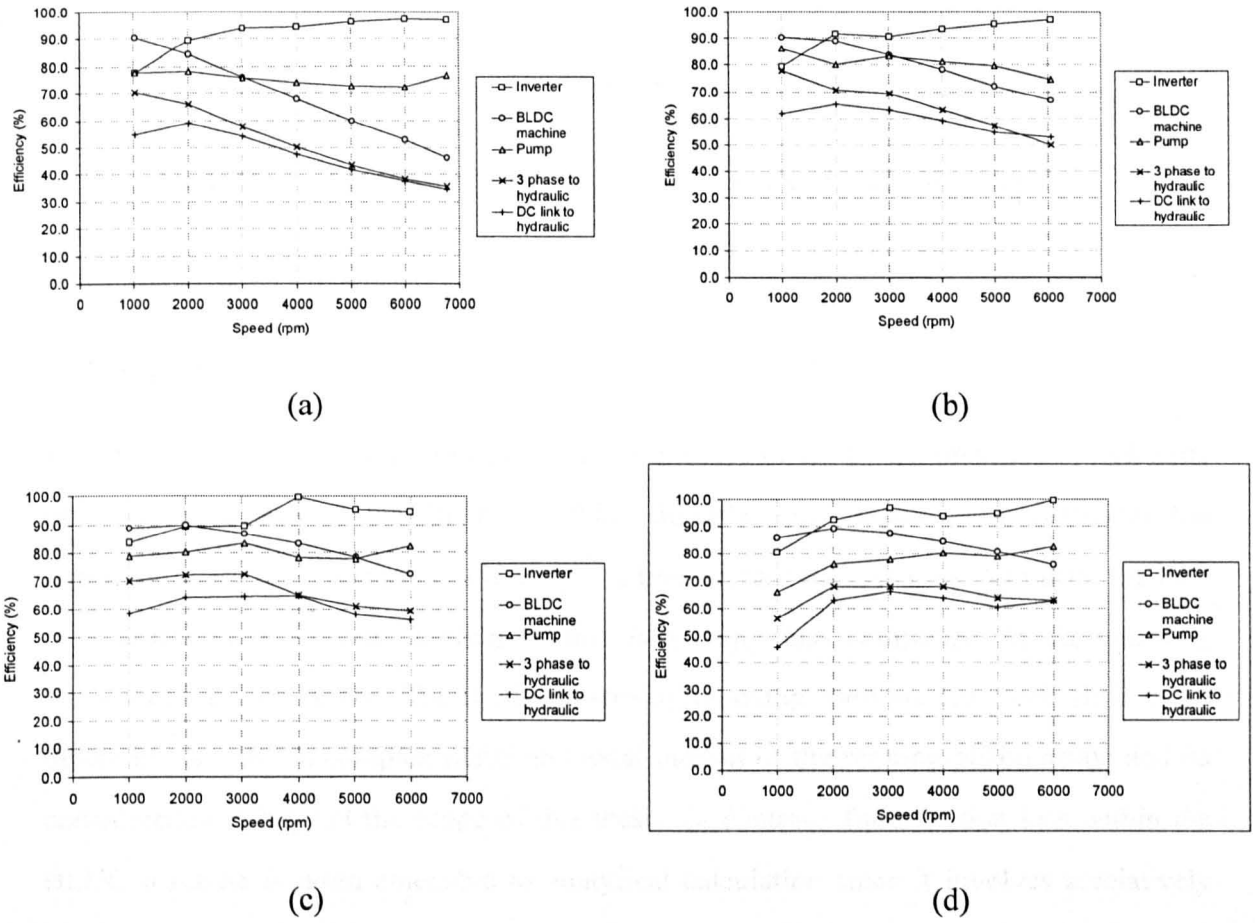

Figure 2.37. Measured efficiency of the various stages in the EHA system at various loads. (a) 50 bar, (b) 100 bar, (c) 150 bar, (d) 200 bar.

CHAPTER 3

FLUID LOSSES IN THE EHA ELECTRICAL MACHINE

3.1 Introduction

This chapter addresses the design and modelling issues raised by the presence of hydraulic fluid in the airgap of the BLDC machine described in chapter 2, in particular the implications for overall system efficiency and temperature rise. As is evident from the load tests described in Chapter 2, fluid friction is a major loss component in the machine, particularly at high speeds. The friction losses in the pump itself are extremely difficult to determine due to the complex radial and axial motion of the rotating piston array, and its consideration is beyond the scope of this thesis. In contrast, fluid friction loss within the BLDC machine is more amenable to analytical calculation since it involves a relatively simple geometry comprising two concentric cylinders (with the inner cylinder rotating). In terms of calculating the overall drag losses, it is useful to consider the net losses as consisting of two contributions, friction losses and acceleration losses. The friction losses are a result of circumferential flow and subsequent shear in the airgap, while the acceleration losses are a consequence of the axial flow from the inlet to the outlet and the need to accelerate the fluid at the inlet since it has no tangential component of velocity on entry.

As is evident from the measurements presented in chapter 2, the overall efficiency of the EHA unit diminishes markedly for a combination of low load and high rotor speed, since the parasitic fluid friction losses in the pump and in the airgap of the BLDC machine form an large fraction of the total output power. For the particular case of a load demand of 50 bar (equivalent to 13.75Nm of motor torque), as can be seen in figure 3.1, the efficiency falls from 70.4% at 1020rpm to 35.6% at 6870 rpm.

Fluid friction loss in the machine is investigated in this chapter, with particular emphasis on establishing the influence of the radial airgap length (i.e. the mechanical clearance between the surface of the rotor and the inner bore of the stator). This in turn provides a methodology for selecting an airgap that provides the best balance between the conflicting requirements of reducing fluid friction losses (which would tend to require a larger airgap) and enhancing the magnetic loading of the machine (which is best achieved by reducing the airgap). The development of this methodology is supported by measurements of fluid friction losses at various speeds, axial flow rates, and radial airgap lengths on a dummy rotor.

3.2 Slipper-less pump leakage characteristics

The slipper-less piston pump has an inherent leakage path that flows through the BLDC machine airgap annulus because of the absence of a dynamic seal. The leakage flow rate is a function of both rotor speed and pump load. In order to quantify this leakage, measurements were performed with a flow-meter during load tests of the motor and pump. The measured characteristics are shown in figure 3.2, from which it is apparent that the leakage flow rate exhibits a non-linear relationship with both speed and load pressure. These complex characteristics are largely determined by specific design features of this slipper-less pump, with the nature of flow in the airgap of the machine having little effect. Since the leakage characteristics of slipperless pumps are beyond the scope of this research, the measured values of figure 3.2 were adopted in subsequent analyses.

3.3 Fluid physical properties

Aerospace hydraulic fluids such as Skydrol 500B have a highly non-linear viscosity versus temperature characteristic, and hence fluid friction loss (which is strongly influenced by the viscosity) will inevitably be highly sensitive to the fluid temperature. By way of example,

as is evident from table 3.1, the kinematic viscosity of Skydrol 500B drops from 1100 mm^2/s, to 9.6 mm^2/s between –55°C and +50°C. All hydraulic oils have a maximum recommended continuous service temperature, beyond which significant changes in chemical composition can occur. This in turn, reduces the active working life and diminishes its fire retardant qualities. In the case of Skydrol 500B hydraulic fluid, the operating temperature must be maintained below 120°C so at to avoid the possibility of oil degradation, which in turn will adversely affect the reliability, and thus MTBF of the EHA. Although it would be desirable to perform experimental measurements using Skydrol 500B, it is unfortunately a chemically hazardous phosphate-esther and cannot be used in a laboratory test-rig. Hence, the fluid friction loss measurements undertaken in this research programme have been performed with Castrol HF-18, a mineral oil which has similar physical properties to Skydrol 500B, but is considerably less hazardous. The physical properties of both Skydrol 500B and Castrol HF-18 are shown in tables 3.1 and 3.2 and in figure 3.3.

3.4 Calculation of fluid friction losses

Despite the relative simplicity of the airgap geometry, the nature of the fluid flow requires consideration of the tangential flow due to the rotation of the rotor, the axial flow provided by the pump leakage path, and Taylor vortices [TAY 36] due to centrifugal forces in the airgap of the machine. Moreover, the fluid properties (particularly its viscosity) vary significantly over the operating temperature range of the machine.

The nature of the flow can be determined by firstly considering a cylinder rotating in an infinite volume of fluid. A useful guide to the type of flow (i.e. whether it is turbulent or laminar) can be derived from the so-called Reynolds number, which is a dimensionless number that expresses the ratio between inertial forces and viscous forces in the flow. For a given combination of fluid density (ρ), kinematic viscosity (μ) and angular velocity (ω_r) the tip Reynolds number for an isolated rotating cylinder is given by

$$\mathrm{Re} = \frac{\rho \omega r^2}{\mu} \tag{3.1}$$

If a comparatively large diameter stationary outer cylinder is now introduced into the fluid volume, the flow in the region between the cylinders becomes influenced by the interaction of the two surfaces. As the radial distance between the two cylinders (δ) is continually reduced, the flow pattern increasingly approaches that of Couette flow between parallel plates. For this particular case, the Couette-Reynolds number is given by

$$\mathrm{Re} = \frac{\rho \omega r \delta}{\mu} \tag{3.2}$$

where the presence of turbulent flow is now influenced by the radial airgap length, δ.
When the Couette-Reynolds number is below ~2300, the flow is a reasonable approximation to laminar flow (i.e. the fluid particles nominally flow in a single direction). However, if the rotor speed is increased, such that the Reynolds number exceeds ~2300, fluctuations in velocity occur as the fluid particles move randomly in small 'packets' (although they still exhibit a net flow in the same direction). In this case, the flow is said to be turbulent. The onset of turbulence may in turn be influenced by a number of factors, occurring at lower velocities than indicated by equation 3.2, if for example there is significant surface roughness and/or obstructions in the flow path.

There is an extensive body of published literature concerned with fluid friction losses in concentric cylinders. Measurements have been reported for numerous different fluids with a wide variety of surfaces, airgap lengths, cross-flow velocities and Reynolds numbers [GAZ 58] [KAY 58] [DOR 63]. Measurements of fluid friction losses on rotating cylinders date back to experiments conducted by Theodorsen and Regier [THE 44] who made a detailed study of friction torque on rotating cylinders in free space i.e. with no outer cylinder

present. The tests were carried out in air, kerosene, oil and water, while in half the experiments the surface of the cylinder was roughened with sand. They found that the friction coefficient of rough cylinders was significantly higher than those of smooth cylinders at high Reynolds numbers.

The effects of surface roughness of the rotor and stator must therefore be considered, as it influences both the frictional losses and the surface heat transfer. Such 'rough' rotor surfaces also increase heat transfer between stator and rotor, as firstly, the area available for heat transfer is larger, and secondly, the onset of turbulence occurs at lower rotational speeds as described previously in this chapter, thus increasing surface heat transfer.

However, the stator of the BLDC machine shown in figure 3.4 is sealed from the rotor by a smooth machined PTFE sleeve which has a very low friction coefficient and was machined to a high quality surface finish, while the rotor surface has a carbon fibre/epoxy overwrap that has been surface ground to a high surface finish. It is therefore reasonable to assume that the rotor and stator surface in the BLDC machine are reasonable approximations to ideal smooth surfaces.

As shown previously by equation 3.2, the Couette-Reynolds number is proportional to the airgap radial length, δ and the peripheral surface speed of the rotor. Figure 3.5 shows the Reynolds number at the inlet and the outlet of the airgap over the operating speed range of the machine for temperatures of –50°C and 100°C and a radial airgap length of 1.5mm (the effective viscosity of the fluid at a given temperature taking the values shown in fig.3.3). It can be seen from figure 3.5 that the flow is predominantly turbulent above ~750rpm for the high inlet temperature, whereas the flow only becomes turbulent after ~3000rpm for the low inlet temperature (although the Reynolds number is seen to rise sharply after this point due to the greater losses dictating a high temperature, and thus lower viscosity). In the subsequent analysis, the correlating equations developed by Bilgen and Boulos [BIL 73] have been employed to describe the effective friction coefficient of the machine airgap annulus over a wide range of Couette-Reynolds numbers. Approximations to the effective

surface friction coefficient as a function of the Couette-Reynolds numbers between zero and $>1x10^4$ are given below.

$$Cf = 10\frac{(\delta/r)^{0.3}}{\mathrm{Re}} \qquad \mathrm{Re} < 64 \qquad (3.3)$$

$$Cf = 2\frac{(\delta/r)^{0.3}}{\mathrm{Re}^{0.6}} \qquad 64 < \mathrm{Re} < 5\,x10^2 \qquad (3.4)$$

$$Cf = 1.03\frac{(\delta/r)^{0.3}}{\mathrm{Re}^{0.5}} \qquad 5\,x10^2 < \mathrm{Re} < 1\,x10^4 \qquad (3.5)$$

$$Cf = 0.065\frac{(\delta/r)^{0.3}}{\mathrm{Re}^{0.2}} \qquad 1x10^4 < \mathrm{Re} \qquad (3.6)$$

Figure 3.5a shows the variation in friction coefficient, C_f with airgap height. It can be seen from figure 3.5a that the friction coefficient decreases with airgap length below a Reynolds number of $1x10^4$, whereas beyond a Reynolds number of $1x10^4$, the friction coefficient increases with airgap length. Having established a value for the friction coefficient, the associated power loss generated by a rotating cylindrical body due to fluid friction can be estimated:

$$P_{drag} = \frac{1}{2} Cf\, \pi\, \rho\, \omega^3 r^4 L \qquad (3.7)$$

3.5 Acceleration losses

On entering the end space of the stator cavity, the fluid is accelerated from zero tangential flow to its terminal tangential flow rate over an axial length which is governed by the ratio of the two flow rates. The kinetic energy gained by the fluid as it is accelerated on entry is ultimately dissipated as heat in the fluid on exit. The losses generated by such fluid acceleration have been investigated by Polkowski [POL 84] by applying the momentum equation to a rotor-stator system. By adopting this approach, the friction torque associated with the entry effects in the airgap region can be approximated by:

$$T = \frac{2}{3}\pi\rho\left(r_2^3 - r_1^3\right)v_t v_a \tag{3.8}$$

where v_t is determined by the final velocity distribution in the airgap:

$$v_t = C_v \omega_r \tag{3.9}$$

C_v is a velocity coefficient defining the relationship between tangential flow and rotor peripheral speed. The findings of Polkowski [POL 84] and Dorfman [DOR 63] suggested that a suitable value for C_v is 0.48 for theoretically smooth surfaces. Measurements by Saari [SAR 95] suggest that this parameter varies significantly for the case of high-speed axial flow in induction machines, with values as low as 0.12 being derived from experimental measurements. However, since the flow in the EHA is closer to the conditions studied by Polkowski, a value of 0.48 was adopted for the analysis.

3.6 Heat transfer in the airgap

Since both Skydrol 500B and Castrol HF-18 exhibit a highly non-linear viscosity characteristic over the likely operating temperature range, it is important to reliably

establish the variation of fluid temperature within the airgap in order to avoid any large errors in the prediction of fluid friction loss. Moreover, in order to avoid premature degradation of the hydraulic oil, care must be taken at the design stage to ensure that its temperature is maintained below 120°C in service.

The PTFE sleeve which separates the stator from the airgap, and the carbon-fibre over-wrap on the rotor dictate that the heat transfer capability from fluid to both stator and rotor is relatively poor (the equivalent thermal resistances being 1.8°C/W and 0.5°C/W respectively). Hence the vast majority of the loss generated in the airgap by friction and acceleration losses directly heats the fluid as it passes through the airgap. The net heat transfer capability of the airgap is influenced strongly by fluid physical properties, axial flow rate, rotational speed, and radial airgap length. The flow in the annulus can be approximated by a channel flow for heat transfer purposes. The nature of this flow can be determined by reference to the so-called Nusselt number that is given by [BEJ 95].

$$Nu = \frac{h\delta}{k} \tag{3.10}$$

At low speeds, the fluid around the rotor surface is forced to flow tangentially, and hence resembles the flow between a moving and a stationary parallel plate, i.e. classical Couette flow. However, as the speed is increased, and centrifugal forces begin to play a greater role in determining the flow pattern, toroidal vortices known as Taylor vortices develop in the airgap. This flow regime (known as Taylor-Couette flow) increases the heat transfer in the airgap, and development of these vortices can be described by the Taylor number [TAY 36]

$$Ta = \frac{\rho^2 \omega^2 r_m \delta^3}{\mu^2} \tag{3.11}$$

A modified Taylor number can also be derived which takes into account the actual rotor radius and airgap length, however, since the ratio of airgap length to rotor radius is

sufficiently small in this case (0.028), the modified Taylor number tends towards the classical Taylor number. Average Nusselt numbers have been measured by [GAZ 58], [BJK 59], [BEC 62] over a range of Taylor numbers, and have been expressed for three different flow regimes by Becker [BEC 62]:

$$Nu = 2 \qquad \text{Ta} < 1700 \qquad (3.12)$$

$$Nu = 0.128 Ta^{0.367} \qquad 1700 < \text{Ta} < 1\text{x}10^4 \qquad (3.13)$$

$$Nu = 0.409 Ta^{0.241} \qquad 1\text{x}10^4 < \text{Ta} < 1\text{x}10^7 \qquad (3.14)$$

Thus the overall heat transfer coefficient, h, of a rotating concentric cylinder can be derived by rearranging equation 3.10, which results in an equivalent thermal resistance of 1/hA.

For a rotor speed of 6000rpm and a bulk fluid temperature of 50°C, the average heat transfer coefficient calculated from equation 3.10 is 224 W/m^2K, corresponding to an equivalent thermal resistance for the particular dimensions of this machine of 2×10^{-5} °C/W. This value of heat transfer coefficient is very high in comparison to the corresponding values for the natural convection heat transfer from the frame (30 W/m^2K). However, due to the relatively high thermal resistance of the PTFE sleeve and carbon fibre, it is reasonable to bound the problem at the inner bore of the PTFE sleeve and the outer surface of the rotor carbon-fibre and assume zero heat transfer into both the stator and rotor.

In order to cater for any axial temperature increase between the inlet and outlet, and the consequent impact on drag losses, it is necessary to divide the airgap into a number of axial sections, in which the viscosity is assumed to be essentially constant within each section. The number of axial sections must be sufficient to ensure that the variation in viscosity between successive sections is sufficiently small so as to provide a reasonable approximation to a continuous variation in the context of the characteristics of fig. 3.3.

The temperature rise of the fluid in the airgap is a function of the drag loss, the axial mass flow rate, and the specific heat capacity of the fluid. The temperature rise can be evaluated for successive axial sections in the airgap annulus starting at the inlet (pump end), in turn allowing the appropriate material viscosity to be established for calculating the contribution to the fluid losses. This process can be repeated along the length of the machine to calculate the maximum temperature that occurs at the outlet end. This procedure can be illustrated by considering n axial sections, in which the temperature in the i^{th} section can be calculated using equation 3.15:

$$\Delta\theta(i)=\frac{q_{drag}(i)}{mC_p} \tag{3.15}$$

Establishing an appropriate value for n for a given set of operating conditions requires an iterative process in which a series of calculations are performed for increasing n until successive values of calculated drag loss converge within a pre-specified tolerance. In order to determine the values of n required for a range of representative conditions, a series of such iterative calculations were performed for a rotor speed of 6000rpm and an axial flow rate of 3 l/min. The inlet temperature of the Skydrol 500B was varied between –50°C and +100°C, for 3 values of airgap, viz. 0.5mm (which is at the lower limit of a practical gap in this application), 1.5mm and 3.0mm. In all cases, the value of n was increased until the convergence between successive values of drag loss was better than 2%. Table 3.3 shows the resulting values of n required and the corresponding drag losses for these combinations of conditions. As would be expected, the highest values of n are required when the axial gradient of the viscosity is highest, conditions which are achieved with a high loss (and hence high temperature gradient) and for temperatures which correspond to regions of the viscosity characteristics of fig.3.3 where the rate of change of viscosity with temperature is greatest.

Figure. 3.6 shows the predicted variation in the fluid friction loss, acceleration loss and hence total drag loss as a function of speed for 4 specific conditions, viz. all inclusive combinations of inlet temperatures of –50°C and +100°C and zero axial flow and 5 l/min. As is evident, even with a high axial flow rate, the losses are dominated by the fluid friction loss for both temperatures and all speeds.

3.7 Drag loss measurements on a dummy rotor

An experimental test rig was constructed in order to measure the drag loss, which comprises the fluid friction loss, and acceleration loss. A mild steel dummy rotor with identical dimensions was used during these measurements, to eliminate any electromagnetic losses induced by the rotating field of the permanent magnets. The hydraulic fluid circuit used to control the axial flow rate is shown in the schematic of Figure 3.7 and the photograph of figure 3.8. An axial flow rate was enforced by pumping the hydraulic oil around the closed circuit at a predetermined flow rate (this value increased during the test due to the increase in temperature, and hence reduction in viscosity of the oil). Various flow rates corresponding to those measured during load tests on the motor/pump unit were investigated at rotor speeds between 0 and 6000rpm (this upper limit being imposed by the rating of the available dynamometer machine). The oil was passed through a water-cooled heat exchanger during the tests to provide some level of control over the oil inlet temperature. Two dummy rotors which resulted in two radial airgap lengths, δ = 1.5mm and δ = 3.0mm were employed to investigate the influence of radial airgap length on the losses. The overall drag loss, which is the sum of the fluid friction and acceleration losses, was measured using the gimbal mounted dynamometer machine with a 2kg torque cell mounted on the test bench. The average axial flow rate was measured with a flow meter mounted in the oil circuit in the return path to the header tank, while oil temperature was measured at the inlet and the outlet of the machine with K-type thermocouples inserted directly into the flow stream. A series of thermistors were mounted behind the PTFE sleeve in an attempt to measure the airgap temperature along the axis of

the machine. However, these proved to be of limited use for the dynamic tests as the effective thermal time constant of the PTFE sleeve was considerably longer than the rapid change in fluid temperature (and hence drag losses) in the airgap. Indeed, given the strong coupling between the magnitude of the drag losses and oil temperature, it is difficult to realise a pre-defined steady-state condition in practice. However, the trend observed in the thermocouple readings did show a linear temperature rise axially through the annulus of the machine as was assumed.

In order to measure the drag caused by the fluid using the test-rig shown in fig 3.7, it was necessary to quantify and account for the various other sources of losses that contribute to the net torque measured by the load cell. The variation of the measured friction and windage losses for the dynamometer drive machine alone are shown in figure 3.9 together with the corresponding characteristics for the dynamometer machine when coupled to the dummy rotor BLDC machine, but without hydraulic fluid in the airgap. This enables an estimate to be derived of the net drag loss of the dry BLDC machine. This characteristic is also shown in figure 3.9, where it is evident that the nature of variation in drag loss with speed is dominated by friction rather than windage. Hence, the overall drag loss characteristic for the coupled machines is representative of the parasitic losses that will be encountered during testing with a flooded rotor (in which the BLDC windage losses are not present).

For each of the two dummy rotors, a series of drag loss measurements were performed for speeds up to 6000rpm with two different nominal axial flow rates, viz. zero net axial flow and a high flow rate of 2.6 l/min. Whereas zero flow can be reliably controlled, it was not possible using the test-rig to provide closed loop control of the high flow rate condition (the hydraulic pump that was used simply provided a given flow-rate for a particular viscosity). Hence, although a nominal starting flow rate of 2.6l/min was set, this inevitably drifted upwards as the tests progressed, particularly at high speeds (and hence high loss) due to heating of the fluid. Full control could not be exercised over the inlet temperature to avoid

this drift because of the limited capacity of the heat-exchanger and the limited volume of oil in the system.

Tables 3.4 and 3.5 summarise the measurements of drag loss for 3 speeds (2000rpm, 4200rpm and 5400rpm) at the two nominal flow rates for both 1.5mm and 3mm airgaps. Also shown in tables 3.4 and 3.5 are the measured axial flow rates and the inlet and outlet temperatures which correspond to these particular measured losses. Although the axial flow rate has some influence on drag losses, the variation in loss is more sensitive to rotor speed than axial flow rate. Indeed, the maximum acceleration losses were found to be < 50W at a rotor speed of 5400rpm, and a fluid flow rate of 4 l/min for the worst case condition of δ = 1.5mm (the equivalent value of fluid friction loss for these conditions being 2042W).
Also shown in table 3.4 are the corresponding drag losses predicted using equations 3.7 and 3.8 in which the flow rate and inlet/outlet temperatures are based on the measured results. There is good agreement between measured and predicted losses, with a maximum error of ~18% occurring for the tests at low speed. As is evident from tables 3.4 and 3.5 the measured and predicted drag losses show good correlation for both airgap lengths.

3.8 Optimisation of mechanical airgap in the machine

A first-order estimate of the electromagnetic torque produced by an electrical machine can be derived from equation 3.16

$$T = \tfrac{1}{2}\pi D_{ro}^{2} L B_g Q \tag{3.16}$$

The electric loading, Q, in equation 3.16 describes the stator ampere-turns per unit of active airgap periphery of the machine:

$$Q = \frac{\alpha\, Nph\, Nt\, Nc\, I_{ph}}{\pi\, D_{si}} \tag{3.17}$$

where α describes the fraction of the coils contributing to torque production at any instant, e.g. 2/3 for the case of a conventionally commutated, 3 phase BLDC machine. The average airgap flux density, B, can be approximated using

$$Bg = \frac{Br}{1 + \mu_o\left(\frac{\mathrm{lg}}{lm}\right)} \tag{3.18}$$

In order to maintain a constant airgap flux density, it is evident from equation 3.18 that the ratio of the magnet length to the airgap length (l_m/l_g) must remain fixed. However, it is recognised that equation 3.18 involves some simplifications as its neglects interpolar leakage [ZHU 91] and flux de-focussing [ATT 94], both of which tend to reduce the magnitude of the airgap flux density. However, these additional factors only have a marked influence when the magnet thickness is significant with respect to the pole pitch and the rotor diameter respectively. However, neither of these conditions is met in the BLDC motor considered in the chapter. Hence, from equation 3.18 it is reasonable to assume that any increase in the net magnetic airgap due to an increase in the mechanical clearance between the rotor outer surface and the PTFE sleeve can be compensated for by an appropriate increase in the magnet thickness. The magnetic loading can therefore be regarded as being independent of the mechanical airgap (δ). However, since any increase in the mechanical airgap necessitates a corresponding decrease in the rotor diameter, an increase in electrical loading (and hence the copper loss) is required to maintain a given output. However, the increase in electric loading required is marginal in rotors of the size considered in this chapter, when the airgap is varied by only a few millimetres (particularly since the value of the effective magnetic airgap has a small offset associated with the 0.5mm thick rotor containment and the 1.0mm thick stator PTFE sleeve).

The EHA machine operates on a highly transient duty cycle, typically between 1000 and 9000rpm, while the fluid temperature and hence viscosity can vary over a wide range. The flight duty cycle of modern large civil aircraft involves a number of high power transients during take-off and landing (followed by relatively low speed manoeuvres at cruising altitude). During take off and landing, the aircraft electrical power generation system may be required to deliver maximum power to flight control surfaces, undercarriage, radar, and the various cabin systems. Thus, any improvements in the efficiency of the electric drives of the flight control systems will yield dividends in terms of down-sizing the components of the power generation system. Hence, it is important to consider a variety of operating conditions and fluid temperatures when establishing the value of airgap that results in the best overall efficiency.

As is evident from the predicted drag losses shown previously in fig. 3.6 for the worst-case conditions of start-up at an ambient operating temperature (and hence fluid temperature) of –50°C, the losses are extremely large in relation to the rated power of the machine. By way of example, for 6000rpm and a load of 50bar (a typical load and speed requirement during positioning of the rudder flight control surface during take-off), the drag losses are 12kW at –50°C for a mechanical airgap of 1.5mm. Although this level of initial loss at –50°C may be tolerable from a thermal point, it will have severe implications for the inverter rating and the required installed capacity of the power generation system. However, as is evident from the temperature-viscosity characteristic of Skydrol 500B shown in figure 3.3, there is a large reduction in viscosity between –50°C and 0°C. Hence, in terms of reducing the peak power rating, considerable benefits are likely to be derived by pre-heating the hydraulic fluid prior to take-off. This could be achieved using a variety of means, e.g. an electric cartridge heater in the small fluid reservoir, gentle controlled slewing of the control surfaces when the aircraft is grounded to gradually increase the fluid temperature. Since

fluid pre-heating yields such large benefits and is likely to be adopted in future systems, for the purposes of this study, a minimum starting temperature of 0°C was assumed.

The method used in calculating copper loss from the various input parameters is best explained with reference to Figure 3.10. Firstly, the input parameters are defined; torque demand (which is derived from the load pressure); airgap height; rotor speed; axial flow rate and fluid inlet temperature. The Couette-Reynolds number of the flow is calculated from equation 3.2, and the drag losses (P_{drag}) from equations 3.3 to 3.9. This loss represents the total fluid friction loss and acceleration loss in the airgap calculated over one axial section in the airgap (n = 1). The convergence test to determine the number of axial sections required (n) is carried out in a while loop as shown in figure 3.10, where the outlet temperature of each successive axial section (calculated from equation 3.15) provides the inlet temperature of the next section. Once the criteria has been reached, the final value of drag loss is used to determine the electromagnetic power required based on a given torque demand i.e.:

$$T_{drag} = P_{drag} / \omega \tag{3.19}$$

$$T_{em} = T_{demand} + T_{drag} \tag{3.20}$$

$$P_{em} = T_{em} \cdot \omega \tag{3.21}$$

Where T_{drag} is the torque associated with the drag losses (P_{drag}) and ω is the speed ($rads^{-1}$). T_{em} and P_{em} are the electromagnetic torque and power that must be supplied by the BLDC machine for a given torque demand. The electric loading, Q, is then calculated from the electromagnetic torque requirements (as described in equation 3.16), and in turn the phase current is calculated from equation 3.17. The copper losses may then be established from the phase resistance. This approach is repeated over a speed range of 300 to 10000rpm, and

airgap lengths from 0.25 to 10mm to generate the copper loss contours of figures 3.11 to 3.14.

Hence, for a given mechanical airgap, δ, the drag loss for a particular rotor speed, load pressure and fluid inlet temperature can be readily calculated, along with the resulting copper losses for this particular operating point. By way of example, figure 3.11 shows contours of constant copper loss for airgap lengths between 0.25mm and 10mm, and for rotor speeds between 200rpm and 10000rpm, for the particular operating conditions of an inlet fluid temperature of 0°C and a load pressure of 20 bar. For a given combination of rotor speed and airgap, the axial flow rate (which influences the temperature rise and hence the loss) has been derived from the measured pump-leakage characteristics shown previously in figure 3.1.

The dashed line in figure 3.11 shows the locus of airgap length that gives the maximum speed for a given copper loss. This point constitutes the lowest copper loss for a given operating speed. In the particular case shown in figure 3.11 that corresponds to a low pressure and low temperature, the drag losses form a comparatively large proportion (~67% at 6000rpm) of the total torque requirement. Hence, considerable reductions in copper losses can be achieved by increasing the airgap (e.g. 4.5mm gives the lowest copper loss at 6000rpm). The reduction in the optimal airgap beyond 6000rpm is a consequence of the non-linear pump leakage characteristics in that the axial flow rate almost saturates, and hence the temperature of the fluid increases markedly (with a consequent reduction in viscosity and hence drag losses).

However, for the extreme case of load pressure, viz. 200 bar, the drag losses only constitute a very small proportion of the required electromagnetic torque (the vast majority of which is required to provide the high pressure at the output of the pump). As shown by the corresponding copper loss contours of figure 3.12, for this case, the optimal airgap remains comparatively small (< 1mm) over the entire speed range, since the penalty in electrical

loading associated with increasing the airgap (due to the consequent reduction in rotor diameter) outweighs any benefits in reduced drag losses with larger airgaps.

Any increase in the fluid temperature favours a reduction in airgap since the magnitudes of the drag losses relative to the pump output power diminishes even further. This is clearly illustrated by the copper loss contours of figures 3.13 and 3.14 for the case of a 100°C fluid temperature and loads of 20 bar and 200 bar respectively. Hence, the best system level compromise will be achieved with small airgaps of the order of 1mm, providing pre-heating is employed (a larger airgap would be preferred if operation with a fluid temperature of –50°C was required).

3.9 Discussion of results

At low inlet temperatures and low load pressure, the desired radial airgap length was in general found to be larger than for high temperatures and high load pressures, as can be seen by inspection of figures 3.11 and 3.13. Specifically, for a speed of 6000rpm, the minimum copper loss in figure 3.11 is found to be at an airgap length of 4.5mm, whereas for the same speed at high temperature and high load pressure (fig 3.13) optimum δ is found to be 0.3mm. Therefore, a trade-off between the two operating extremes must be sought. Efficiency of the BLDC machine must be maximised for the higher values of drag loss and copper loss experienced under take-off conditions in order to minimise the maximum inverter VA rating, and also relax the maximum aircraft power generation system requirements during take-off as this has been shown to be the most onerous operating condition for such embedded machines (Chapter 6). Hence a mechanical airgap clearance of between 1.0 and 2.0 mm, corresponding to the minimum copper loss at 6000rpm, 150bar with a fluid inlet temperature of 50°C and 6000rpm, 50bar, 0°C respectively, would be most suitable for a BLDC machine with a flooded rotor operating under these conditions.

3.10 Conclusions

Fluid friction loss has been shown to play a key role in determining the rating of the BLDC machine and associated inverter for an EHA application, with significant implications on the total system efficiency under the combination of high speed and light load operation. Established fluid friction loss coefficients for rotating concentric cylinders together with acceleration losses have been successfully applied to the solution of fluid friction losses in the airgap, and good agreement is shown with measured data. The iterative solution of the fluid friction loss necessary for such widely varying physical properties has shown to deliver very accurate results. Good correlation is shown for two airgap lengths with zero axial flow rate, and at high axial flow rate. The method has also been extended to the selection of a sub-optimal airgap length in terms of providing a maximum average efficiency over envisaged speed and load characteristics during take off and landing, and to provide a lower VA rating of the inverter. The selection of an appropriate airgap length has proved a very complex task due to the highly variable duty cycle in terms of speed and load, and the wide range of fluid inlet temperatures.

3.11 References

[ATT 94] K.A. Attalah, Z.Q. Zhu, J.K. Mitchell, D.Howe. 'Curvature effects in radial-field permanent magnet machines'. Electrical machines and Power systems, Vol. 22, No. 4, pp. 511-520, July-Aug 1994

[BEC 62] K.M. Becker, J. Kaye. 'Measurements of diabatic flow in an annulus with an inner rotating cylinder. Transactions of the ASME, Journal of heat transfer, Vol. 84, 1962, May, pp. 97-105.

[BEJ 95] A. Bejan. 'Convection heat transfer'. Second Edition, 1995, ISBN 0-471-57972-6.

[BIL 73] E. Bilgen, R. Boulos. 'Functional dependency of torque coefficient of coaxial cylinders on gap width and Reynolds numbers.' Transactions of the American Society of Mechanical Engineers, Journal of fluids engineering, March, 1973, pp.122-126

[BJK 59] I.S. Bjorkland, J. Kaye. 'Heat transfer between concentric rotating cylinders.' Journal of heat transfer, Vol. 81, 1959, August, pp. 175-186.

[CAL 00] S.D. Calverley, G.W. Jewell, R.J. Saunders. 'Aerodynamic Losses in Switched Reluctance Machines', IEE Proceedings – Electric Power Applications, Vol 147, No.6, 2000, pp 443-448

[DOR 63] L.A. Dorfman. 'Hydrodynamic resistance and the heat loss of rotating solids.' Translated from Russian. Oliver and Boyd Ltd, London, 1963.

[GAZ 58] C. Gazley. 'Heat transfer characteristics of the rotational and axial flow between concentric cylinders.' Transactions of the ASME, Vol. 80, January, 1958 pp. 79-90.

[JOK 97] T. Jokinen, J. Saari. 'Modelling of the coolant flow with heat flow controlled temperature sources in thermal networks.' IEE proceedings of electrical power applications, 1997, Vol. 144, No. 5, pp. 338-342.

[KAY 58] J. Kaye, E.C. Elgar. 'Modes of adiabatic and diabatic fluid flow in an annulus with an inner rotating cylinder'. Transactoins of the ASME, 1958, Vol. 80, pp. 753 – 765.

[LAM 97] D. Lampard, S.J. Pickering, J. Mugglestone – The use of computational fluid dynamics to model the airflow in the end region of a TEFC induction motor'. IEE colloquium on modeeling the performance of electrical machines (Digest No. 1997/166). 15th April 1997. pp. 2/1 – 2/5.

[POL 84] J.W. Polkowski. 'Turbulent flow between coaxial cylinders with the inner cylinder rotating.' Transactions of the ASME, Journal of Engineering for Gas Turbines and Power, 1984, Vol. 106, No. 1, pp. 128-135.

[SAR 95] J. Saari. 'Thermal modelling of high-speed induction machines.' Acta polytechnica Scandinavica electrical engineering series, No. 82.

[THE 44] T. Theodorsen, A. Regier. 'Experiments of drag of revolving disks, cylinders, and streamline rods at high speeds.' Thirtieth annual report of the National Advisory Committee for Aeronautics (NACA), 1944, Technical report No. 793, pp. 367-384.

[YAM 62] Y. Yamada. 'Resistance of a flow through an annulus with an inner rotating cylinder.' Bulletin of Japanese Society of Mechanical Engineers, 1962, Vol. 5, No. 18, pp. 302-310.

[ZHU 91] Z.Q. Zhu, D. Howe. 'Analytical determination of the instantaneous airgap field in a brushless permanent magnet DC motor.' International conference on computation in electromagnetics, Nov 1991, pp. 268 – 271

TAY 36] G. I. Taylor. 'Fluid friction between rotating cylinders – torque measurements'. Proceedings of the Royal Society, London, Series A, Vol. 223, 1936, pp. 546 – 578.

Table 3.1. Skydrol 500B hydraulic fluid physical properties.

Temperature (°C)	Kinematic viscosity (mm^2/s)	Specific Gravity
-55	1100	1.072
-17.8	147	1.036
50	9.6	0.9768
100	4	0.938

Table 3.2. Castrol HF-18 hydraulic fluid physical properties.

Temperature (°C)	Kinematic viscosity (mm^2/s)	Specific Gravity
-40	2200	1.03
0	108	-
40	14	-
70	5.9	-
100	3.5	0.965

Table 3.3. Convergence in fluid friction loss with number of sections, n, at 6000rpm.

Fluid inlet temperature (°C)	δ = 0.5mm		δ = 1.5mm		δ = 3.0mm	
	Number of axial sections, n	Total loss (kW)	Number of axial sections, n	Total loss (kW)	Number of axial sections, n	Total loss (kW)
-50	31	13.99	21	10.69	15	9.32
-25	12	8.53	8	7.12	7	6.26
0	6	5.80	6	4.65	5	3.95
25	5	3.87	4	3.10	4	2.54
50	4	2.76	4	2.14	3	1.80
75	3	2.13	3	1.63	2	1.57
100	2	1.83	2	1.51	2	1.46

Table 3.4. Predicted and measured drag losses for δ = 1.5 mm (high flow rate corresponds to 2.6 l/min at the start of the tests.

	Rotor speed of 2000rpm		Rotor speed of 4200rpm		Rotor speed of 5400rpm	
	Zero flow rate	High flow rate	Zero flow rate	High flow rate	Zero flow rate	High flow rate
Measured drag loss (W)	271	277	1185	1491	2287	2603
Flow rate (l/min)	0	2.6	0	2.9	0	3.3
Fluid inlet temperature (°C)	20.7	18	21.5	19.0	34.3	21.8
Fluid outlet temperature (°C)	22.8	21.6	29.4	28.1	57.7	36.3
Predicted drag losses for measured flow rate and inlet/outlet temperatures (W)	130	189	1240	1522	2179	2711

Table 3.5. Predicted and measured drag losses for $\delta = 3.0$ mm (high flow rate corresponds to 2.6 l/min at the start of the tests.

	Rotor speed of 2000rpm		Rotor speed of 4200rpm		Rotor speed of 5400rpm	
	Zero flow rate	High flow rate	Zero flow rate	High flow rate	Zero flow rate	High flow rate
Measured drag loss (W)	121	212	901	1236	1624	2085
Flow rate (l/min)	0	3.6	0	3.8	0	4.1
Fluid inlet temperature (°C)	19.5	18.8	19.3	19.4	20.3	20.5
Fluid outlet temperature (°C)	22.1	23.0	36.8	32.0	53.1	43.6
Predicted drag losses for measured flow rate and inlet/outlet temperatures (W)	93	134	934	1337	1798	2286

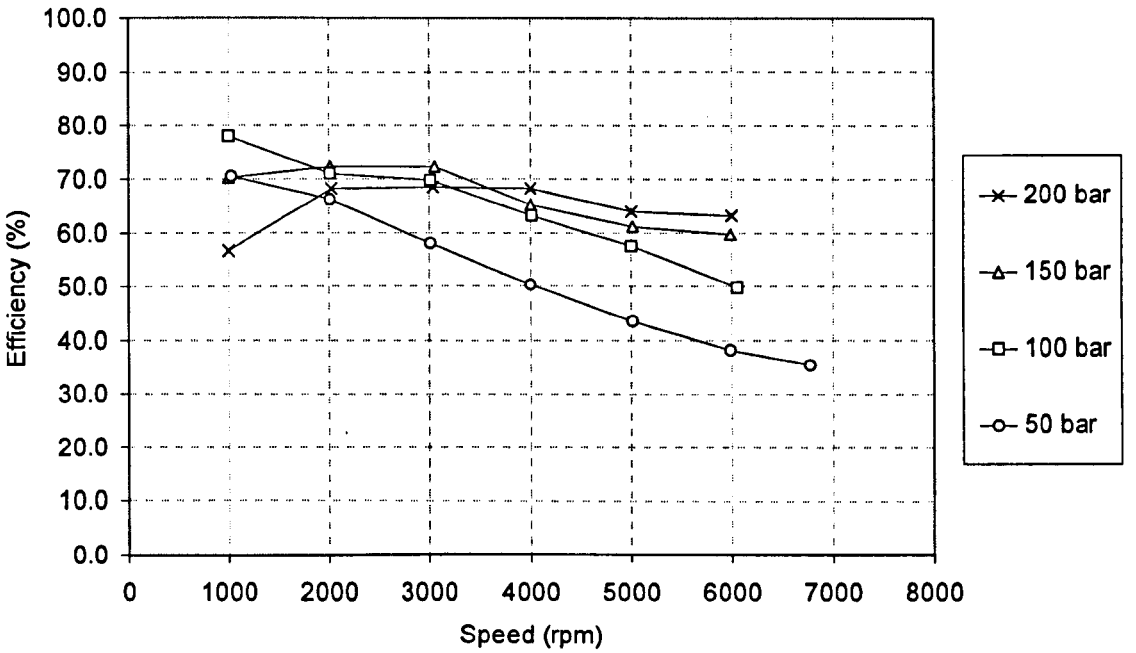

Figure 3.1. Three-phase electrical input power to hydraulic power efficiency for the EHA system at various levels of loading.

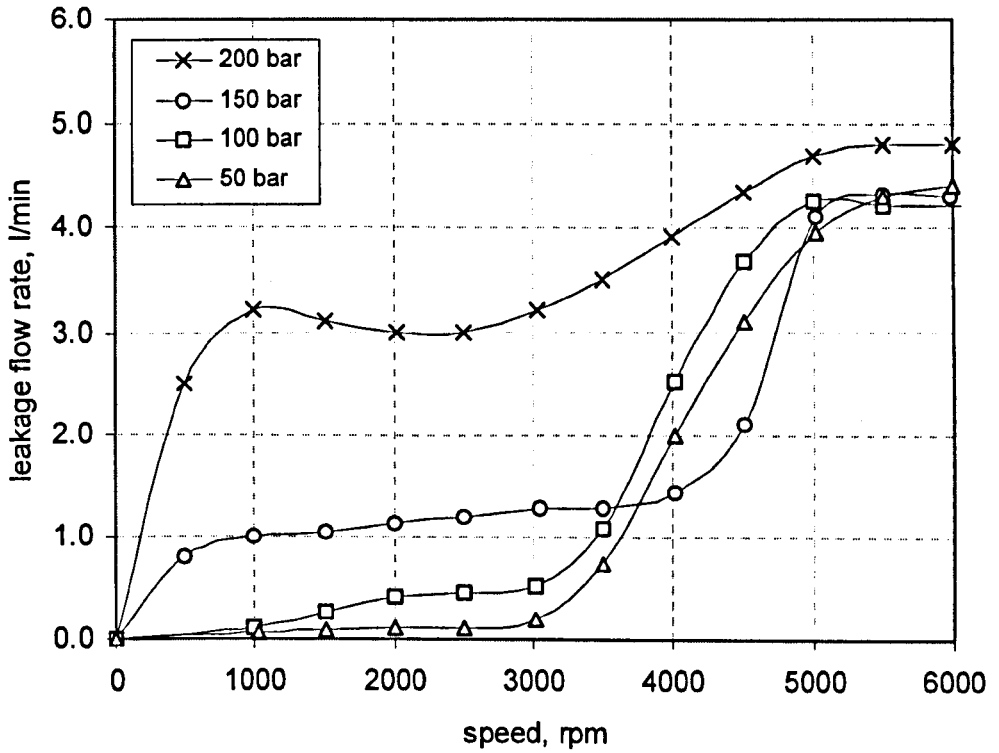

Figure 3.2. Measured pump leakage flow rate with speed at various load pressures.

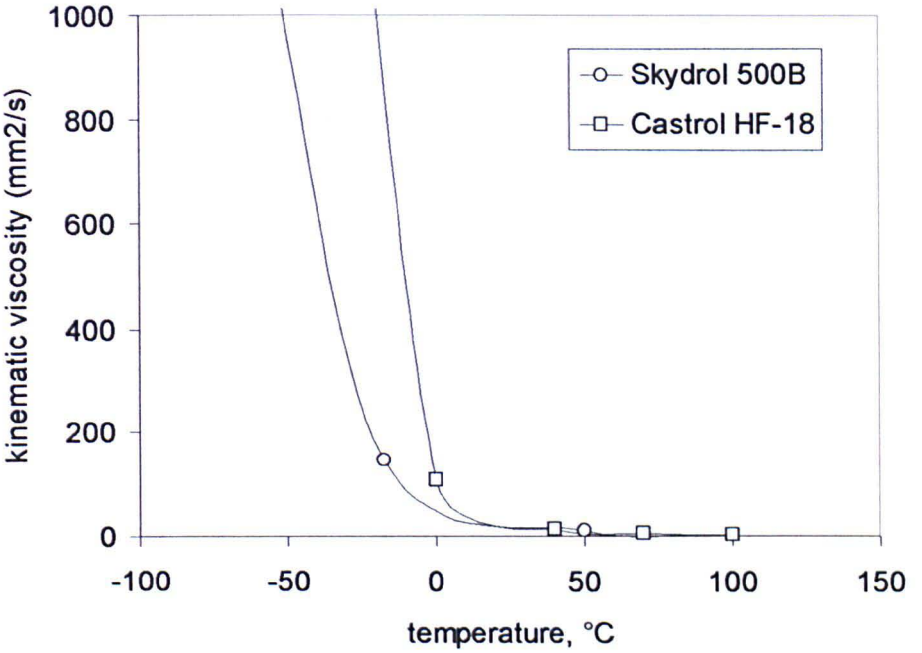

Figure 3.3. Viscosity of Skydrol and Castrol HF 18.

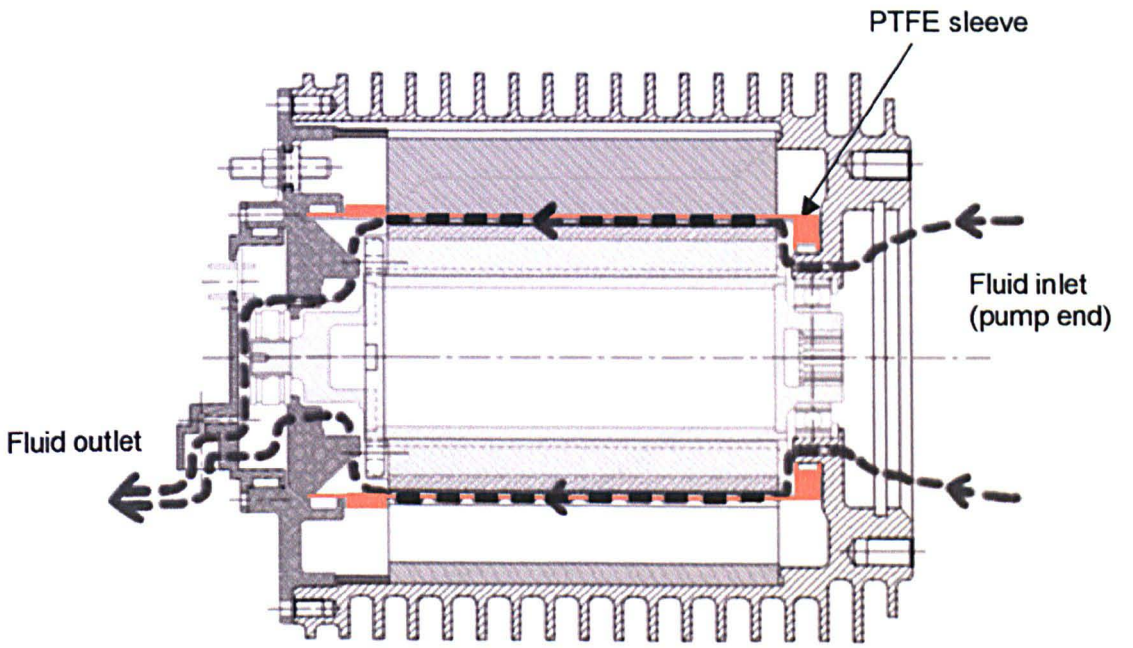

Figure 3.4. Diagram of BLDC machine showing PTFE sleeve and fluid flow path.

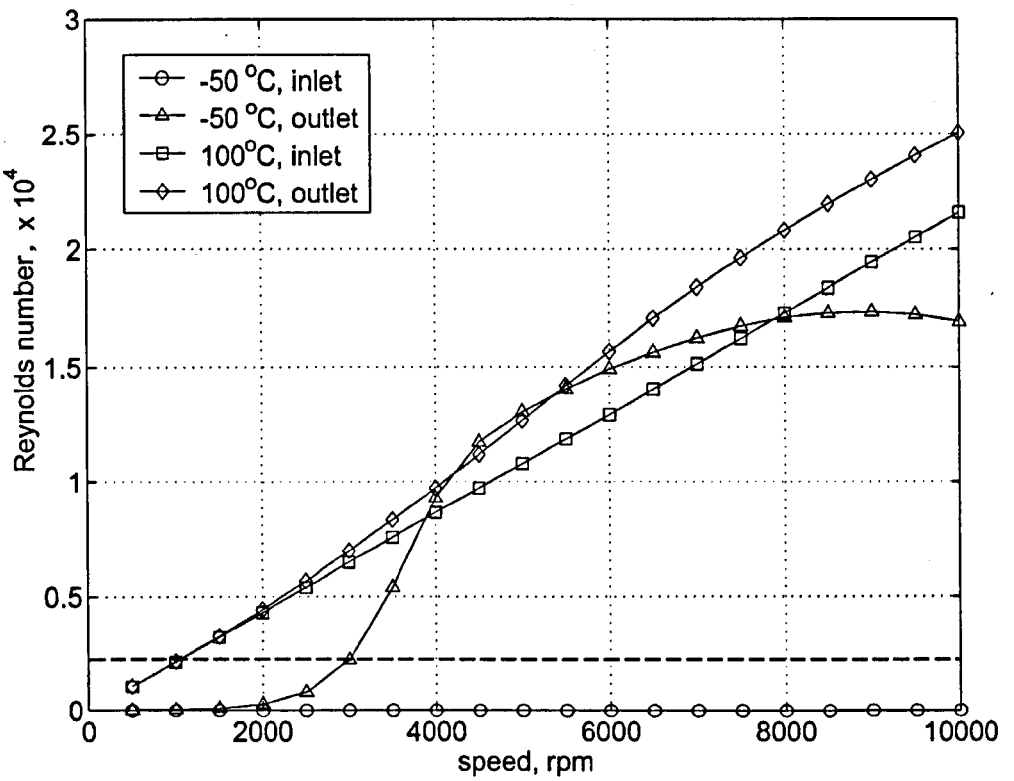

Figure 3.5. Reynolds number for inlet temperatures of -50°C and 100°C for a radial airgap length of 1.5mm from zero to 6000rpm. Values are presented for the Reynolds number at the inlet and the outlet. Dashed line shows onset of turbulence (Re = 2300).

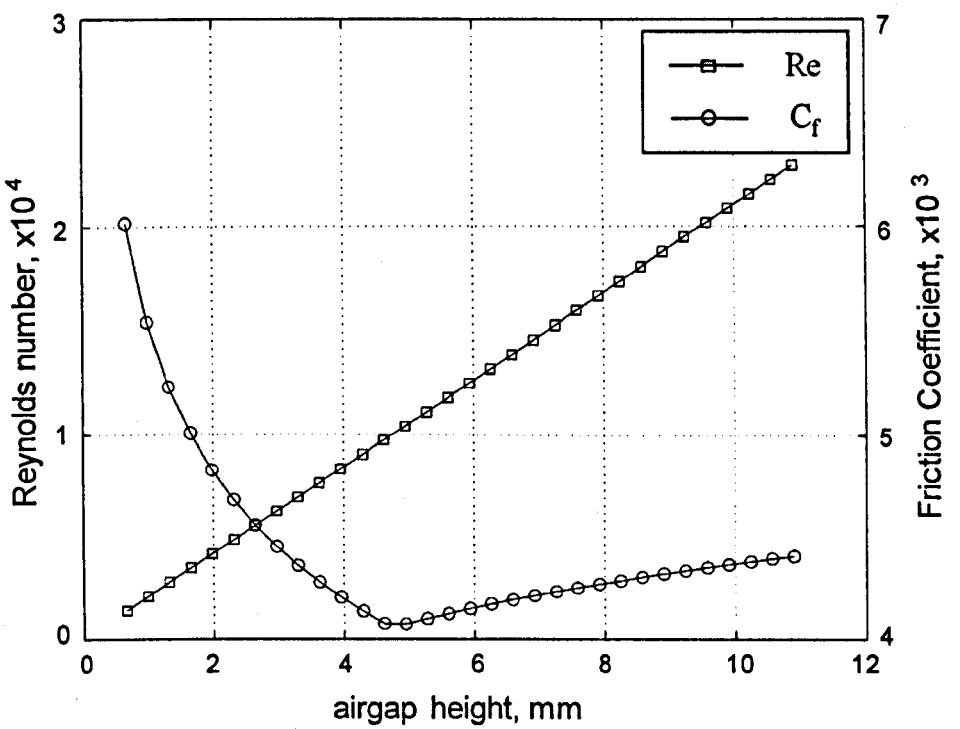

Figure 3.5a. Variation in friction coefficient with airgap height at constant speed. It can be seen that the friction coefficient decreases with airgap height up to a Reynolds number of $1x10^4$, and increases with airgap height thereafter.

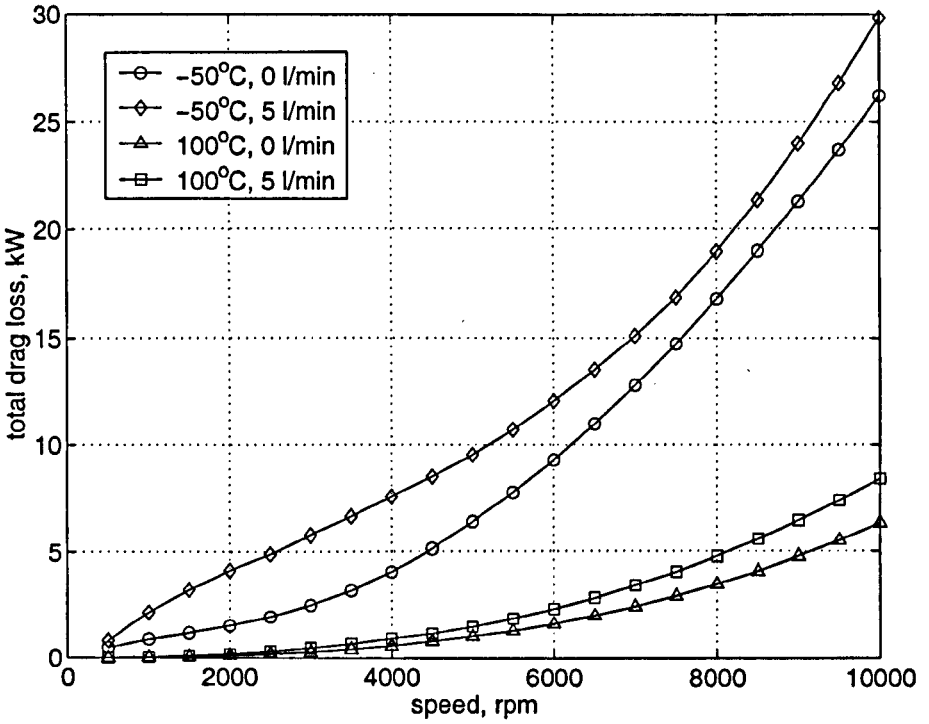

Figure 3.6. Predicted variation in the total drag loss as a function of speed for δ = 1.5mm, and inlet temperatures of -50°C and +100°C, each at zero axial flow and 5 l/min respectively.

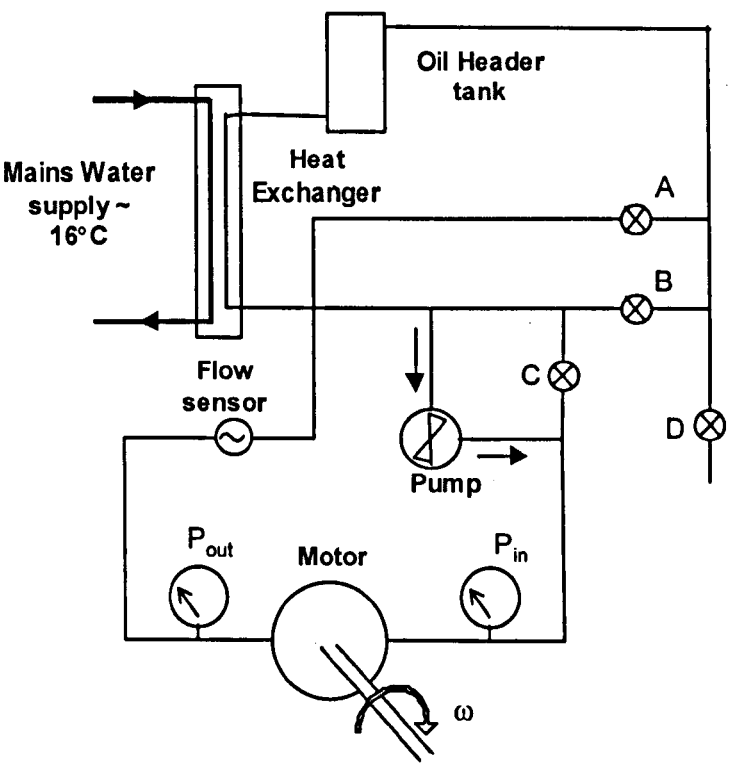

Figure 3.7. Schematic of oil system for drag loss tests.

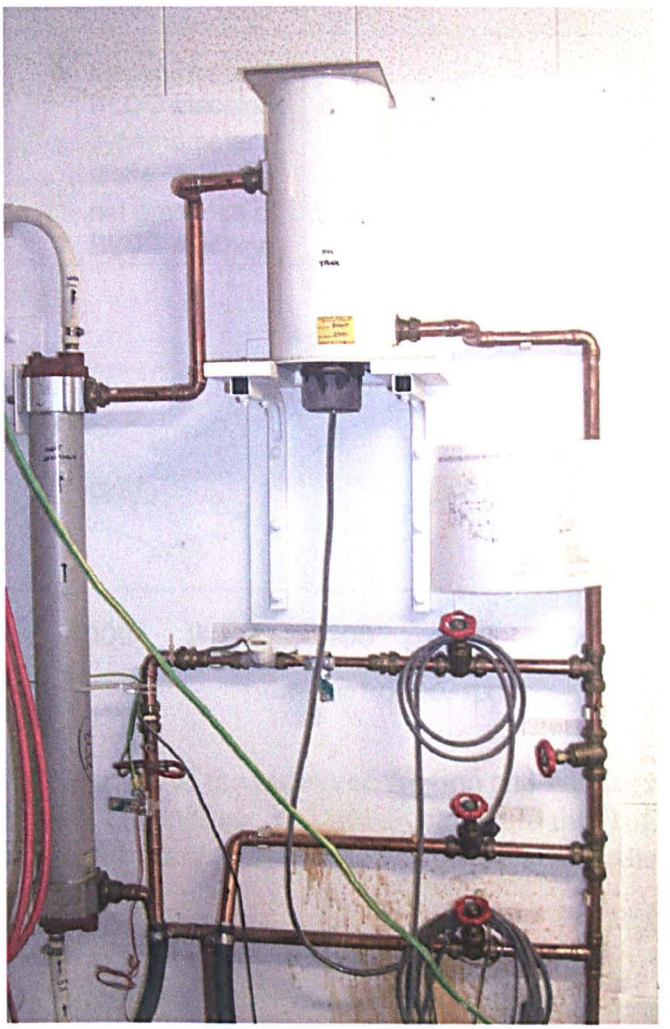

Figure 3.8. Hydraulic fluid closed circuit cooling for axial flow tests.

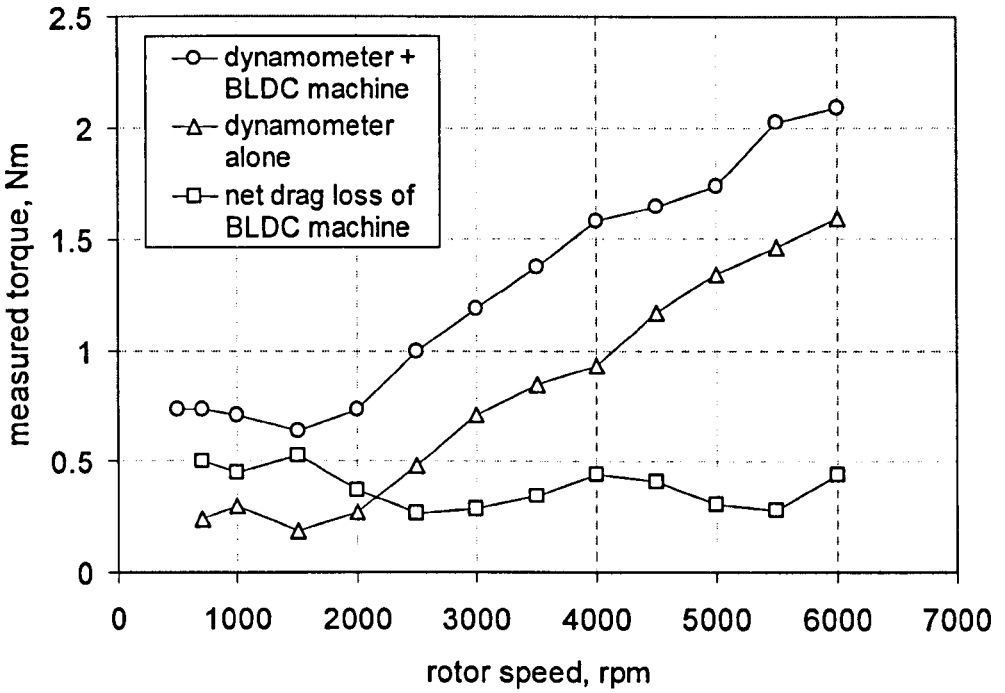

Figure 3.9. Variation of the measured friction and windage torque for the dynamometer drive machine alone, and when coupled to the BLDC machine with the dummy rotor fitted. (No hydraulic fluid present in the airgap).

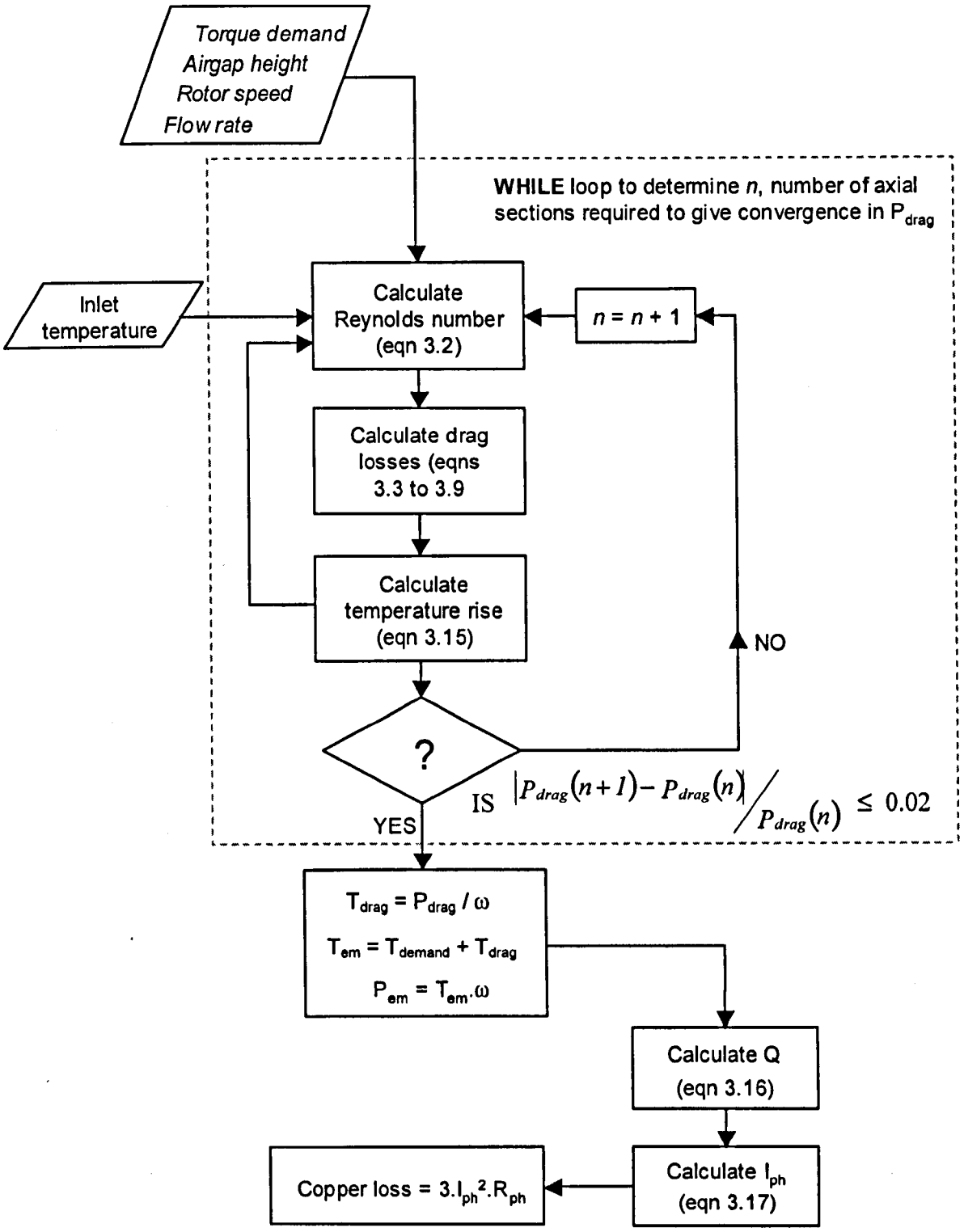

Figure 3.10. Flow diagram describing the method of calculating the BLDC machine copper loss from fluid physical properties, speed and load. The method includes a convergence criteria in determining the minimum number of axial sections to calculate drag losses to a sufficient level of accuracy (see table 3.3).

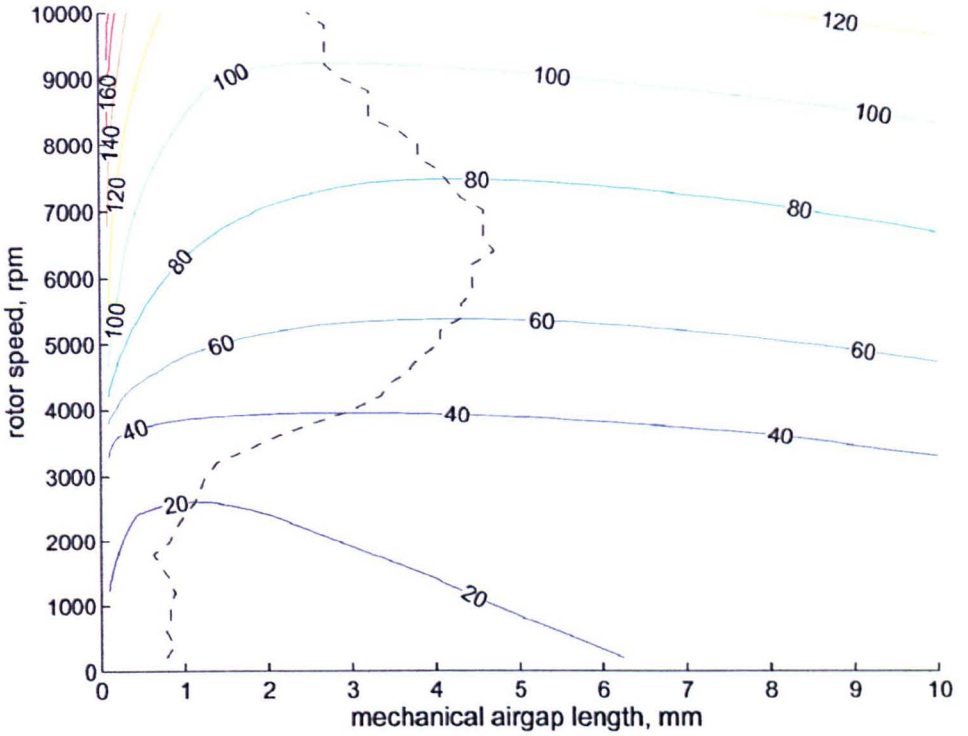

Figure 3.11. Contours of constant copper loss (W) for a fluid inlet temperature of 0°C, and a load pressure of 20 bar. Dashed line shows the locus of minimum copper loss.

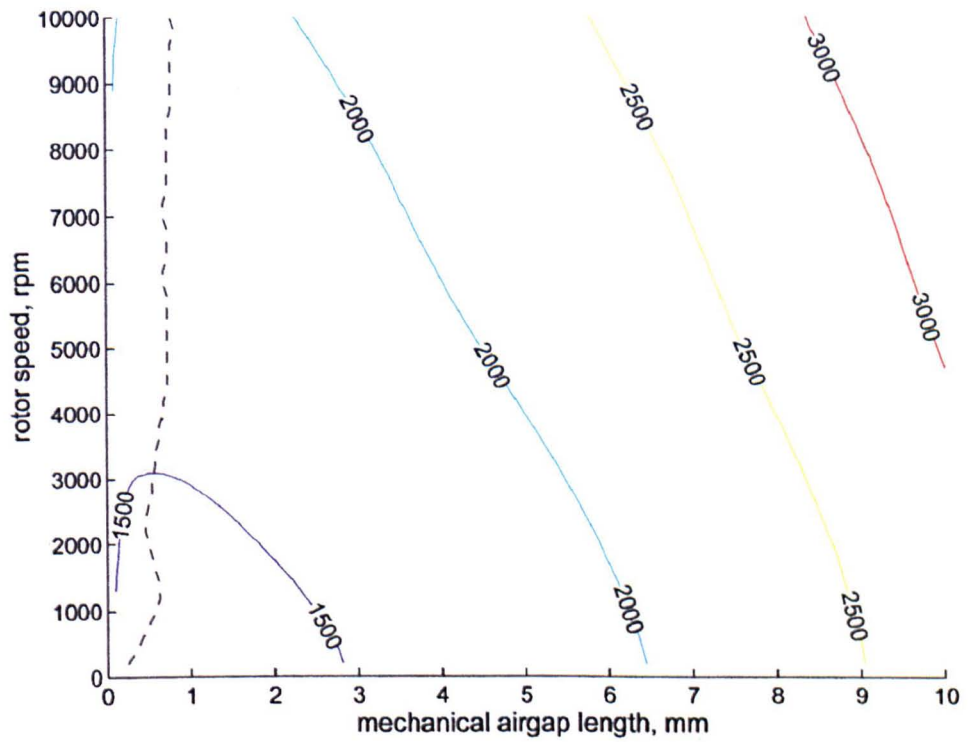

Figure 3.12. Contours of constant copper loss (W) for a fluid inlet temperature of 0°C, and a load pressure of 200 bar. Dashed line shows the locus of minimum copper loss.

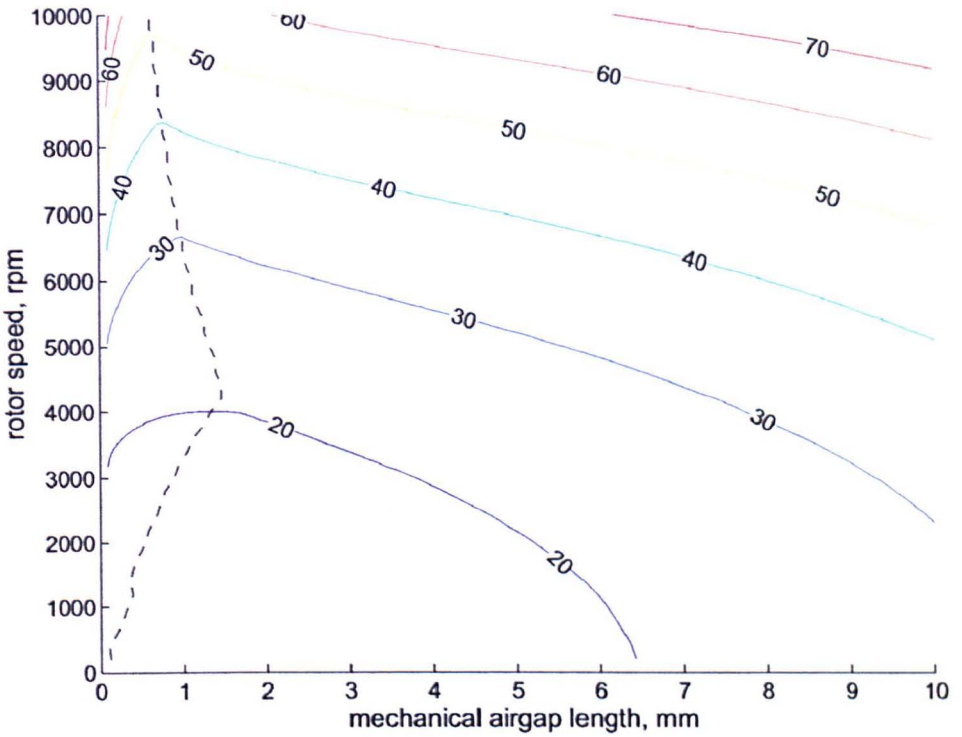

Figure 3.13. Contours of constant copper loss (W) for a fluid inlet temperature of 100°C, and a load pressure of 20 bar. The dashed line shows the locus of minimum copper loss.

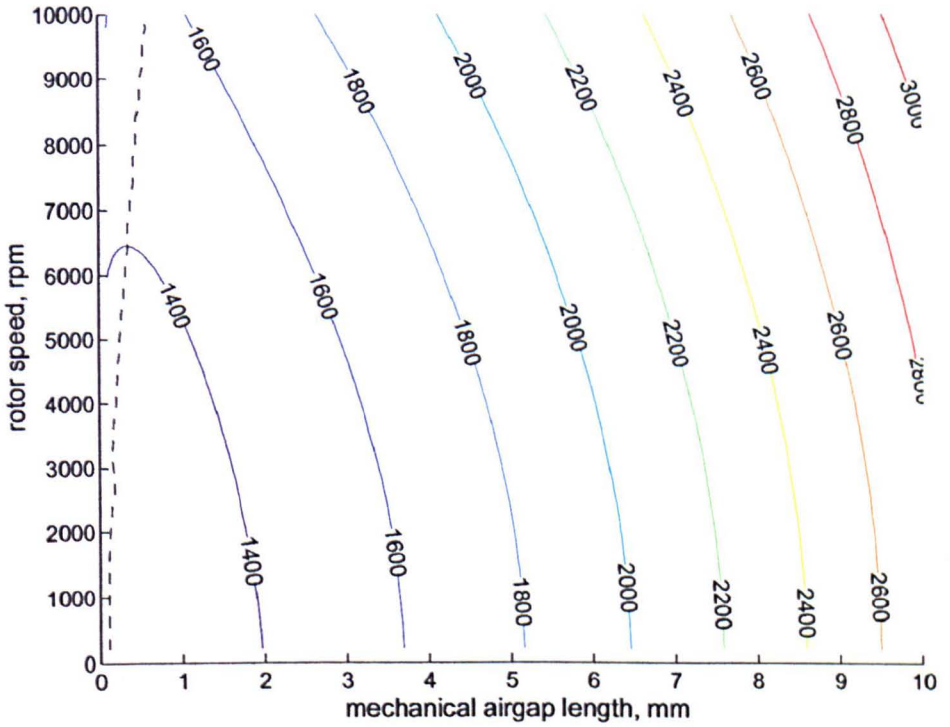

Figure 3.14. Contours of constant copper loss (W) for a fluid inlet temperature of 100°C, and a load pressure of 200 bar. The dashed line shows the locus of minimum copper loss.

CHAPTER 4

HP SPOOL EMBEDDED MACHINE DESIGN

4.1. Introduction

This chapter investigates the design of a switched reluctance starter/generator machine that is to be embedded within the high-pressure (HP) region of a civil aircraft turbo-fan engine as shown in Chapter 1, figure 1.10. The high-pressure spool of a typical large turbo-fan engine rotates at speeds of up to 13500 rpm on a typical flight duty cycle, and up to 15000rpm in an over-speed condition. It is disposed concentrically as the outer of the three rotating spools, hence having the largest diameter. Due to the close concentric arrangement of the spools, it is unpractical to embed a machine inside the HP spool, thus necessitating a large rotor bore diameter. At this early stage in the move toward the 'more electric' engine, turbo-fan engine designers seek to employ embedded electric generation without the obligation to make any major changes to the existing engine design. Hence the HP starter/generator machine must be incorporated within the same axial section of the engine that is presently occupied by the radial take-off shaft, while the maximum diameter is constrained by the aerodynamic requirements of the turbo-fan engine. The combination of a large rotor bore diameter, and the high rotational speeds of the HP spool dictates that the rotor will potentially be subject to high mechanical stresses. The constraints imposed by conventional rotor designs due to the limited mechanical strength of the laminations are highlighted by finite element analysis of the stress distribution. A modular rotor structure is proposed which facilitates a significant reduction in the mechanical stress in rotor laminations, and thereby an increase in the diameters. Both two and three-dimensional finite element analyses are employed to compare the static electromagnetic performance of a switched reluctance machine with a modular rotor against two machines having conventional rotors.

Many modern turbo-fan engines employ a three-shaft design that affords greater fuel economy than a double or single shaft configuration as described in Chapter 1, section 6. The shafts or 'spools' are classified by their operating pressure, viz. the low-pressure (LP), intermediate-pressure (IP), and high-pressure (HP) spools. The 'more-electric' aircraft engine concept envisages electrical machines integrated co-axially with the spools, and supplying electrical power directly to the aircraft system loads, thus negating the large accessory gearbox and take-off shaft. However, although the potential advantages in terms of functionality, reliability, efficiency and weight saving in civil aircraft are well recognised [PRO 02], significant technical challenges must be overcome before such highly integrated engines enter service. Many of these challenges are related to the harsh operating environment and the demanding performance specifications. In civil aircraft, the most onerous conditions are for electrical machines which are to be integrated with high-pressure (HP) spools, where the ambient temperature may reach as high as ~350-400°C, the rotational speed is ~15,000-20,000 rpm and the required power rating is in excess of 100kW [GAR 99], [FIN 00].

Of the various candidate machine technologies, the switched reluctance (SR) machine has been identified as a leading, if not the leading, candidate for this application due to its ability to operate in high temperature environments and its high specific power capability [RIC 88], [MAC 89A], [MAC 89B]. Other machine topologies have been considered for this role, including the singly-fed and doubly-fed induction machines [ELB 97], albeit much of the development of such VSCF systems being aimed at lower speed wind generators. Permanent magnet machines have so far received little attention for application as an aircraft starter/generator due mainly to the poor high temperature performance of permanent magnet materials. Various grades of Samarium Cobalt magnets have been developed for high temperature operation (>350°C) [TAN 99, LIU 99] but offer vastly diminished performance in terms of remanent flux density (typically ~0.6 Tesla at 400°C) and lower intrinsic coercivity, ultimately resulting in a machine with a very poor specific torque density.

Cooling of the machine may be augmented by forced oil cooling (as is presently the case with the externally mounted CSD) or forced air-cooling. Forced oil cooling provides a higher heat transfer rate than that of forced air cooling, but as the long-term aim of the 'more-electric' engine is to operate with an oil-less engine as discussed in Chapter 1, section 6, the machine has been designed to operate with forced air cooling in mind, thus enabling incorporation in future engine designs. However, the high pressure differential required to generate forced air cooling necessitates the use of bleed air from the intermediate compressor region, where air temperatures may reach as high as 300°C. Hence, dissipation within an air-cooled machine operating in an ambient temperature of ~350°C with cooling air at 300°C is likely to raise the internal temperature to ~400°C. This will have a significant impact on the copper loss, since the winding resistance at 400°C is ~2.5 times greater than that at room temperature. In order to increase the winding area, so as to partially mitigate the increased winding resistance, the 'split-ratio' (the ratio of the rotor outer diameter to the stator outer diameter) may be reduced.

In terms of the magnetic properties of soft magnetic lamination materials, such as cobalt iron and silicon steel, elevated temperature operation does not pose any significant difficulties, since their magnetisation characteristics degrade only slightly with temperature up to 400°C. Indeed, some benefit may accrue in terms of a reduction in iron loss due to the increase in electrical resistivity [SIM 96]. In contrast however, the mechanical properties of soft magnetic laminations are a major consideration at such elevated temperatures since the high rotational speed and power (and by implication the large rotor diameter) will inevitably result in high stress levels within the rotor. The problems associated with stresses in the rotor are compounded by the particular space envelope constraints, since in order to integrate an SR machine in an HP spool, its rotor must have a large central bore, typically of 200mm diameter which compares with a maximum outer stator diameter of 400mm. Table 4.1 outlines the dimensional and electromechanical requirements for the HP spool starter/generator.

In order to quantify the minimum number of rotor teeth required to achieve an acceptable value of aligned to unaligned inductance within the given space envelope, a study has been carried out using a simple criteria proposed by Radun [RAD 95] based on the minimum height of a rotor tooth, viz. little benefit will be derived in increasing the rotor tooth height beyond 1.5 to 2 times the circumferential distance between the edges of the stator and rotor teeth when in the un-aligned position. For this particular study, the lower value of 1.5 was used. The shaft diameter and stator outer diameter were fixed at 200mm and 400mm respectively, and the minimum rotor outer diameter fulfilling this criterion was determined for each viable combination of stator and rotor poles. Table 4.2 shows the minimum rotor outer diameter for each combination. It is also interesting to note that the 6-4 and 8-6 designs are geometrically unfeasible for such a shaft diameter and stator outer diameter, as the stator tooth length is defined to have a negative value imposed by the large back iron width requirement. Therefore, as a consequence of this space envelope constraint, a comparatively high pole number machine must be employed so as to reduce the thickness of the rotor and stator back iron, whereas in general, a high speed machine would be designated a low number of poles in order to reduce the electrical frequency, and hence the iron losses.

A conventional SR rotor employs a single-piece lamination, and is hence relatively simple and robust. However, high levels of hoop stress can occur in the laminations, particularly at high rotational speeds. Generally, there is little scope to employ any form of containment around the laminated rotor, e.g. a carbon-fibre over-wrap or a high-strength steel sleeve, since the performance of SR machines degrades markedly when the effective magnetic airgap is increased. Additionally, the high ambient temperature precludes the use of epoxy resins used in carbon-fibre over-wraps, which typically have a maximum operating temperature of <200°C. Although high-strength rotor cages have been proposed as a means of providing additional mechanical support to SR rotors [PAT 96], these can pose significant problems in terms of axial stiffness, increased weight, and induced eddy currents in the case of a metallic cage.

Hence, for a given speed rating and with a single-piece lamination, the maximum rotor diameter is generally limited by the mechanical properties of the rotor lamination material. Of the candidate lamination materials for high performance SR rotors, the various grades of cobalt iron offer significant advantages over silicon iron in terms of mechanical properties, typical room temperature 0.2% yield strengths being 680MPa and 400MPa respectively, as well as having superior magnetic properties [HIP 50] [CK 26]. Thus, cobalt iron laminations are likely to be preferred for the rotors of SR machines for integration in the HP spool, albeit at a considerable cost premium compared to silicon iron.

The mechanical properties of cobalt iron can be tailored to some degree to suit the requirements of a particular application by control of the heat treatment, albeit an increase in mechanical strength being achieved at the expense of compromising the magnetic properties. Both the mechanical and magnetic properties of these cobalt alloys have been found to be very sensitive to the heat treatment schedule and temperature [KON 00].

By way of example, the room temperature yield strength of Hiperco 50HS (a commercially available grade of 49% cobalt iron whose composition is optimised for mechanical strength [HIP 50]), can be increased from 441 MPa to 665 MPa by reducing the heat-treatment temperature from 800°C (which gives optimal magnetic properties) to 720°C. However, even after being heat treated to optimise the mechanical strength, subsequent exposure to elevated temperatures results in a marked reduction in the mechanical strength, e.g. at 400°C, the yield strength of Hiperco 50HS is 580MPa, which compares to 665MPa at 20°C [FIN 99]. This difficulty in employing cobalt iron laminations when they are exposed to high stress levels and elevated temperatures is further compounded by concerns regarding their stability under long-term and cyclical operation, in particular their high-temperature creep behaviour [FIN 99].

4.2. Limitations of conventional rotor topologies

In order to establish the consequent constraints which the lamination material imposes on the dimensions of a rotor, it is first necessary to specify an appropriate safety factor which relates the operational design limits to the nominal material properties. One widely employed criteria for accommodating long-term factors such as fatigue in metals is to limit the maximum stress to 50% of the yield strength [GER 01], which for Hiperco 50HS at a temperature of 400°C corresponds to a maximum stress in the rotor of 290 MPa. A useful first-order estimate of the constraint which this imposes on the rotor diameter can be obtained by considering the analytical expression for hoop stress in a thick-walled cylindrical disk [FEN 90].

$$\sigma_\theta = \frac{(3+\nu)}{8}\rho\omega^2\left(R_1{}^2 + R_2{}^2 + \frac{R_1{}^2 R_2{}^2}{r^2} - \frac{1+3\nu}{3+\nu} r^2 \right) \tag{4.1}$$

where σ_θ is the circumferential stress, ρ is the density, ω is the angular velocity, and ν is Young's modulus. R1 and R2 are the outer and inner radius of the disk respectively, and r is the radius at which σ_θ is evaluated. For a disk having an inner bore of 200mm and rotating at 15,000 rpm, a maximum stress criterion of 290MPa would limit the maximum outer diameter to 248mm. With reference to table 4.2, it can be seen that this mechanically determined maximum rotor diameter would place a lower limit on the number of rotor poles to be 16, as combinations with lower pole numbers require a larger diameter to achieve the electromagnetic saliency criteria.

However, whilst this simple analysis provides a useful starting point, it is important to consider the actual stress distribution within the SR rotor. In this respect, a rotor that is constrained to have a large bore diameter relative to its outer diameter, and is required to incorporate a degree of magnetic saliency, usually results in an increase in the peak stress as compared to that which exists in a uniform disk of the same outer diameter

[CAL 03]. For the uniform disk, the maximum stress always exists at the bore. For a salient structure however, when the bore diameter tends towards the rotor outer diameter, the tooth height becomes a greater proportion of the total rotor annulus, thus decreasing the back iron width. This increases stress at the bore, with a greater focusing under the pole faces as can be seen from figure 4.1. Further increase in bore diameter moves the region of maximum stress to the inter-pole region on the outer surface of the rotor, while stress levels continue to rise. An investigation of the stress distribution in a four-pole switched reluctance rotor has been reported by Calverley [CAL 03] arguing that the most efficient use of the rotor material is achieved when the stress in the fillet is equal to the stress in the bore.

Thus, an iterative design approach, using two-dimensional linear finite element stress analysis was employed to establish the maximum dimensions of an 18-pole rotor having a bore of 200mm and a localised peak stress of 290MPa at 15,000 rpm (assuming that no pre-stress is induced during assembly of the rotor laminations onto the central shaft). One pole of the resultant rotor design, which has an outer diameter of 229mm (c.f. 248mm for a cylindrical disk having the same peak stress of 290 MPa) is shown in figure 4.1. As will be evident however, this limiting rotor design has a very poor saliency ratio, which severely compromises the specific torque capability of the SR machine. In order to achieve an acceptable level of rotor saliency, whilst maintaining a 200mm rotor bore diameter and rotating at 15,000 rpm, it is necessary to operate the Hiperco 50HS laminations at stress levels that exceed 50% of its yield strength at 400°C.

In order to establish the extent to which the rotor laminations must be stressed so as to realise viable electromagnetic SR machine designs, a linear structural finite element study was undertaken on a series of 12- and 18-pole SR rotors, whose outer diameters were varied up to 350mm. In each case the rotor bore diameter was maintained constant at 200mm, and the following design guidelines were adopted to establish the rotor geometry for each outer diameter:

- The rotor pole-arcs for the 12- and 18-pole rotors were fixed at 11.3° and 7.4°, respectively, these values being typical of those employed in practical machines, and consistent with the values proposed by Lawrenson for achieving a high torque density [LAW 80].

- The height of the rotor teeth was based on the criteria proposed by Radun [RAD 95], viz. little benefit will be derived in increasing the rotor tooth height beyond 1.5 to 2 times the circumferential distance between the edges of the stator and rotor teeth when in the un-aligned position. For this particular study, the lower value of 1.5 was used.

- The thickness of the rotor back-iron was assumed to be 2/3 of the width of a rotor pole to accommodate flux from more than one phase during phase overlap operation.

- A fillet, based on a B-spline curve, was incorporated at the base of the teeth in order to alleviate any localised stress concentration (which is predominantly radial in these regions).

To ensure a satisfactory degree of accuracy in the finite element solutions, a convergence study was carried out on the maximum Von-Mises stress and the maximum deflection in the problem. Due to the nature of the toothed structure, there is a large stress concentration at the knee-point of the tooth fillet; hence the mesh in this region should ideally be assigned smaller elements than the remaining regions, where stress concentrations are lower. Two different meshing approaches were investigated, the first with a generic global element size, and the second with a locally refined mesh in the regions of high stress concentration. For the global mesh, the element size was gradually reduced by a normalised scaling factor, κ, until a convergence of <0.1% was achieved for both the maximum Von-Mises stress, and the maximum deflection. The element size is defined to be:

$$d_{xy} = \frac{r_1 \kappa}{Nrt} \tag{4.2}$$

where r_l is the rotor outer radius and Nrt the number of rotor teeth. Figure 4.2 shows one pole of the rotor, showing the key dimensions used to determine the element size, and the applied boundary conditions. Table 4.3 shows the convergence in maximum deflection, ξ, convergence in maximum Von-Mises stress, ε, and the normalised computational requirement, with normalised element scaling factor, κ. The problem is first discretised with the minimum number of elements returning a solution, while each subsequent solution reduces the element size by 50% until the convergence tolerance of <0.1% is met. It can be seen by inspection of table 4.3 that both the global and local mesh achieve the convergence tolerance for Von-Mises stress with $\kappa = 0.071$, whereas the maximum deflection converges at a much faster rate ($\kappa = 0.25$ and $\kappa = 0.20$ for global and local meshes respectively).

It is also interesting to note from table 4.3 the relative computational requirement for each solution, as a large number of iterations were required in determining the most appropriate fillet shape for each value of outer radius, and thus the solution time should be kept to a minimum. The relative computational requirement is shown to be considerably less for the local mesh at $\kappa = 0.071$, with values of 19.1 and 8.3 for global and local discretisation respectively, showing that the locally refined mesh converged in under half the time taken with the globally refined mesh. Increasing the mesh density in the problem beyond that which satisfies the convergence tolerance is a law of diminishing returns, with relative computational requirement increasing as a function of the total number of elements in the mesh, while the value of ε beyond $\kappa = 0.071$ only changes by some 0.01% for the local mesh.

Adopting the electromagnetic design criteria set out for the finite element solutions (and using $\kappa = 0.071$) imposed a lower limit on the outer diameter of the 12- and 18-pole rotors of 261mm and 248mm, respectively, the maximum associated localised stresses being 389 MPa and 345 MPa, respectively (which correspond to 67% and 60%, respectively, of the yield strength of Hiperco 50HS at 400°C). Fig. 4.3 shows the variation in the predicted maximum localised Von-Mises stress levels for the 12- and 18-pole rotor designs as their outer diameters are varied between these lower limits and

350mm, the rotor bore diameter being 200mm in all cases. Fig.4.3 also shows the variation of the peak stress that would result in a thick-walled cylindrical disk of the same density. As will be seen, the adoption of a higher pole number has benefits in terms of a reduction in the maximum stress for a given rotor outer diameter, owing to the more acute pole arc angle affording a reduced tooth height. Thus the back iron becomes a greater proportion of the total rotor annulus, and is able to carry the hoop stress over a greater diameter. Figs. 4.4 and 4.5 show Von-Mises stress contours for a 261mm diameter 12-pole rotor, and a 248mm diameter 18-pole rotor respectively, the peak stress being essentially circumferential and occurring at both the inner bore and inter-pole / slot regions. Electro-magnetically induced radial forces have been shown to be very high for the switched reluctance machine topology [GAR 99], leading to unbalanced magnetic pull, and hence raising concern over its operation as a fault tolerant machine in many applications. However, electromagnetically induced radial stresses due to in the rotor were assumed to be negligible for the purpose of analysis, since for the particular rotor geometries considered, even with an airgap flux density of 2.0T, they represent less than 0.01% of the maximum Von-Mises stress due to rotation.

In summary, the combination of a large rotor bore diameter, a high rotational speed and a high ambient temperature cause the rotor lamination material to operate at the limits, or indeed beyond the limits of their long-term mechanical capabilities, e.g. at 60% of their 400°C yield strength for an 18-pole rotor. Further, even when operating at these stress levels, there are severe constraints on the rotor diameter that, in turn, will limit the achievable power capability, given that the axial length of the machine is also severely constrained by the available space envelope in the engine.

4.3. Modular rotor topologies

One means of overcoming the limitations imposed by the use of a single-piece rotor lamination and the mechanical strength of the lamination material is to employ a modular rotor construction, in which separate laminated pole modules are attached to a

high strength, non-magnetic, annular hub. Such a modular rotor is illustrated schematically in Fig.4.6. It has 9 laminated modules each consisting of two poles, resulting in 18 rotor poles. The hoop-stress in such a rotor structure is borne predominately by the non-magnetic hub, which can be manufactured from a high strength material having the required fatigue, corrosion and high temperature creep properties, e.g. Nickel super-alloys such as Inconel 718 which have a 0.2% yield stress of 1100 MPa at 400°C [BOY 89]. Figure 4.7 shows the variation in 0.2% yield strength with operating temperature for Inconel 718 following typical heat treatment for high strength.

SR machines equipped with modular rotors of the type shown in fig. 4.6 appear to have received relatively little attention in the published literature, although patents exist for rotors fabricated from a series of individual poles [PAT 92] (although the motivation was to reduce the volume of soft magnetic material). The apparent lack of interest in SR machines with modular rotors may be due to the fact that their construction conflicts with one of the major perceived benefits of conventional SR machines, viz. the relative simplicity of the rotor.

Various technologies could be employed for attaching the individual laminated pole modules onto the rotor hub. For example, by using a 'fir-tree' arrangement that is commonly used in the retention of turbine blades in aircraft engines (shown in fig 4.8), or dovetailing the modules into the hub with a suitable degree of pre-compression, as illustrated in fig. 4.9. A structural finite element study has been undertaken using non-linear contact elements in order to determine the feasibility of attaching such modules using different techniques. The contact element approach allows the module to act as a dead weight in the problem, with the relative displacement of the two interfaces (hub and module) determining the degree of constraint imposed on the module and hub. Fig 4.10 shows the approach taken in developing the problem for analysis using contact elements, with the hub and module first being created separately with surface-to-surface contact elements formed along the interfacing surfaces. The two components are then brought together with the mesh nodes at the interface overlapping. The contact elements

are nonlinear, and thus require a full Newton iterative solution. The load (angular velocity) is applied in discrete steps in order to stabilise the solution. [ANS 01]. Figure 4.11 shows finite element results for the Von-Mises stress distribution in a 'fir-tree' type fixing arrangement for an 18-pole rotor (9 modules) with an outer diameter of 300mm, and a rotor bore diameter of 200mm rotating at 15000 rpm. The module material is Hiperco 50HS and the hub material is Inconel 718. It can be seen from Fig 4.11 that the maximum stress is highly localised around the fir-tree lobes, reaching a maximum of 3100 MPa. Plastic deformation would normally occur in the Hiperco 50HS at these very high levels of stress, and indeed, may serve to alleviate the stress concentration to some degree. However, the linear analysis has shown that the Hiperco 50HS would be taken into the plastic region of the stress-strain characteristic, thus increasing the likelihood that it will suffer from fatigue. Figure 4.12 shows the stress distribution for a dovetailed arrangement with the same loads and limiting dimensions, which again suffers from high stress concentrations at the contact points. Pre-compression of the dovetailed module has also been investigated. An overlap of 0.4mm was determined from the coefficient of thermal expansion of Inconel 718 ($13.5e^{-6}$/°C) at 200°C, resulting in a pre-compression of 250 MPa. Table 4.4 summarises finite element results for the maximum deflection, maximum Von-Mises stress, and maximum stress at the hub inner radius for the various arrangements.

In summary, the methods of attachment do not mitigate the maximum stress experienced by the cobalt iron, which may be subject to fretting fatigue in service due to the high stress concentrations, and hence reduce the mean time between failures of the rotor. However, one potentially attractive technique in terms of avoiding any localised stress concentrations is to friction weld the lamination modules to the hub [KAL 99]. As the modules have a non-cylindrical geometry, the parts would have to be linear friction welded, a method for joining materials that is finding increasing application in the attachment and repair of turbine blades. Other techniques are available for joining the two materials such as induction welding and induction brazing technologies. Indeed,

induction brazing technologies [WU 00] have been successfully used in the joining of Inconel X-750 and stainless steel 304, achieving a joint strength of 483MPa.

In order to assess the stress levels that would result in the laminated rotor pole, in the high strength non-magnetic hub, and at their interface, iterative finite element analysis was employed to predict the stress distribution in an 18-pole SR modular rotor (i.e. 9 modules each having 2 poles) with an outer diameter of 300mm and a bore diameter of 200mm when rotating at 15,000 rpm. A convergence study of maximum stress and displacement has been carried out in the same way as that for the conventional machine, with the radius r_1 in this case being replaced by the hub maximum outer radius. A value of $\kappa = 0.057$ gave convergence to within 0.1%.

Fig. 4.13 and fig. 4.14 shows the resulting Von-Mises stress distribution and radial displacement respectively, with the interface between the laminated modules and the hub being modelled as an idealised rigid bond. The Von-Mises stress at the interface is less than 250MPa, which compares with a maximum value of 658MPa in the hub, corresponding to 60% of the yield strength of Inconel 718 at 400°C [BOY 89]. By way of comparison, a single-piece rotor lamination with the same dimensions would have a maximum stress of 406MPa, which is 70% of the 400°C yield strength of Hiperco 50HS alloy. During the iterative finite element analysis of the modular rotor, it was noted that the fillet radius between the two teeth had little influence on the stress distribution within the module, as centripetal acceleration is manifested predominantly as radial forces in the module teeth. Hence the tooth fillet radius has been reduced to zero, affording a lighter module with subsequent lower stress in the hub, and a greater degree of magnetic saliency.

The basic operation of an SR machine equipped with a modular rotor can be illustrated with reference to the 8-phase machine having an 18-pole rotor (configured as 9 modules, each with two poles) and a 24-pole stator shown in fig.4.6. In order to facilitate operation with uni-polar currents, the coils would be wound such that adjacent

stator poles are of opposite polarity. In terms of its electromagnetic performance, two key features distinguish the modular rotor machine from a conventional SR machine.

Firstly, the poles of each rotor module have the same pitch as the stator poles, the required difference in the total number of stator and rotor poles that is necessary for continuous torque production being achieved by appropriately separating adjacent modules. Secondly, whereas every region of the rotor back-iron of a conventional SR machine is fluxed at some stage during each revolution, since the rotor back-iron in a modular rotor machine is not continuous, a different excitation sequence must be employed to realise continuous rotation, viz. two phases on adjacent teeth are excited. By way of example, for the machine shown in fig.4.6, the required excitation sequence to produce clockwise motoring torque from the position which is shown would be GF – DC – AH - FE – CB – HG – ED – BA – GF, etc. This mode of operation results in the utilisation of ¼ of the stator poles and 1/3 of the rotor poles (assuming no overlap), which is the same as for conventional four-phase 16-12 and 24-18 pole SR machines. No phase overlap was assumed in order to establish a comparison of machine utilisation factors, whereas in practice, phase overlap may be fully realised by either machine topology. The modular rotor machine achieves phase overlap with negligible super-imposition of flux-paths as compared to machines with conventional rotor designs, in which overlapping phases share the same flux path.

As a consequence of its mode of operation, the possible combinations of rotor poles, stator poles and number of phases that are capable of producing continuous torque are more limited than for conventional SR machines, particularly for low rotor and/or stator pole numbers. Simple relationships defining the viable combinations of stator poles, rotor poles and number of phases for conventional SR machine topologies have been presented by Lawrenson [LAW 80], However, for the modular arrangement, the viable designs are seen to be more limited, and are satisfied by the following:

The number of stator teeth, Ns and number of rotor teeth, Nr, must be even numbers, and Ns > Nr. (whereas Ns may be less than Nr in a conventional SR machine, albeit at

the expense of available stator winding area). The minimum number of phases required for correct excitation of the modular machine is given by the minimum value of N_{ph} satisfying:

$$N_{ph} = \frac{\alpha_r \lambda}{\alpha_s} \tag{4.3}$$

where λ is an integer value between 1 and $N_r/2$, and N_{ph} is the number of phases, also an integer value. α_r is defined to be the angle subtended by one half of the rotor pole pitch, and α_s is defined to be the angle subtended by one stator pole pitch i.e.

$$\alpha_r = \frac{4\pi}{N_r} \qquad \alpha_s = \frac{2\pi}{N_s} \tag{4.4}$$

$$N_{ph} \neq N_s \tag{4.5}$$

$$2\alpha_r \neq \alpha_s (\beta_n) \tag{4.6}$$

where β_n describes integer values between 1 and Ns.

Relationship 4.5 defines those designs that produce nominally balanced radial forces, and relationship 4.6 defines those designs that are capable of self starting and producing continuous torque over one revolution in either direction. The former criterion precludes low-pole number combinations such as a machine with 8 stator poles and 6 rotor poles, since only one of the 3 rotor modules produces torque during a particular commutation interval.

Table 4.5 lists all viable combinations of SR machines with modular rotors having up to 30 stator poles and 28 rotor poles. Also shown in Table 4.5 are the number of steps per revolution (that is related to the fundamental electrical frequency and hence the iron loss) and the 'utilisation factor' of the stator, i.e. the proportion of the stator poles that are active during a particular interval (assuming no overlap). Further combinations with even higher pole numbers can be derived, although they are unlikely to be suitable for high-speed applications.

As is evident from Table 4.5 there are numerous viable combinations, albeit that they all require a relatively high number of separate phases. In terms of minimising iron losses, the combinations with the lowest number of rotor and stator poles would appear to be the most attractive for this particular high-speed application. Further, in terms of drive complexity there is likely to be a preference for minimising the number of separate phases.

However, the first combination in Table 4.5, viz. a 7-phase machine with 14 stator poles and 12 rotor poles, has the disadvantage of still requiring a relatively thick rotor back-iron. Given the space envelope constraints, this has an adverse impact on the radial force at the interface between the laminated rotor pole modules and the non-magnetic hub, and, for a given bore diameter, limits the thickness of the hub, thereby increasing the level of hoop stress for a given rotor outer diameter. Indeed, for a rotor having an outer diameter of 300mm and a bore diameter of 200mm, it is necessary to employ at least 16 rotor poles (i.e. 8 modules) in order to realise a viable design from both electromagnetic and mechanical points of view at 15,000rpm. Of the remaining combinations in Table 4.5, a machine with 24 stator poles and 18 rotor poles provides a good compromise between enhancing the 'utilisation factor' and minimising both the phase number and number of steps per revolution.

4.4. Performance Comparison

In order to quantify the merits of a modular rotor SR machine relative to that of conventional SR machines, the performance of a modular rotor SR machine has been compared to that of two conventional SR machines, details of all three machines being given in table 4.6. In the conventional SR machine design number 2, the rotor diameter of 248mm is the largest diameter that can be employed while limiting the peak stress to 345MPa at 15,000 rpm, i.e. 60% of the yield stress of Hiperco 50HS at 400°C. As regards the conventional SR machine design number 3, although its rotor would not be capable of running at 15,000 rpm within the specified maximum stress limit of 345MPa

(the peak stress being 406MPa), it enables a comparison to be made of the static torque capability of a conventional SR machine with that of a modular rotor SR machine of the same rotor dimensions. The axial length of the stator core and the rotor for all 3 machine designs was 50mm, which given the need to accommodate end-windings, terminals etc, is likely to be typical of the available space envelope in civil aircraft engines.

Although a significant increase in the rotor diameter will occur in running up from standstill to 15,000 rpm, e.g. the rotor diameter of motor design number 2 will increase by 0.28mm, the finite element analyses assumed a nominal airgap length of 1.0mm for all 3 machines (i.e. the value at standstill). This provides a worst-case estimate of their torque capability. The magnetisation curve for the rotor and stator lamination material, Hiperco 50HS, is shown in fig.4.15. In this initial analysis, the influence of stress on the magnetisation curve was neglected. However, it is recognised that the magnetic properties will be modified to some degree in operation, particularly in terms of iron loss.

The initial finite element analyses were performed using a two-dimensional, magneto-static model. Fig. 4.16 shows representative two-dimensional field distributions in the modular machine, whilst fig. 4.17 shows the resulting flux-linkage versus current characteristics (per unit length) for machine design numbers 1 and 3.

Two dimensional finite element analysis has also been employed to investigate the effects of various rotor tooth heights on the aligned to unaligned inductance ratio for designs 1 and 3. While it is obvious that a conventional rotor would have zero saliency if the rotor teeth were removed (and hence a unity ratio of aligned to unaligned inductance) the modular rotor is seen to exhibit a degree of saliency even when the rotor tooth height is reduced to zero. Figure 4.18 shows results from two-dimensional finite element magnetostatic analysis of designs 1 and 3 with a low excitation mmf of 7 A-turns (to preclude any saturation effects) for rotor tooth heights between zero and 20mm. It can be seen that little benefit is derived in increasing the rotor tooth height

above 12 mm for the conventional rotor (design 3), whereas, for the modular rotor this value is around 6 mm. This is primarily due to the modular rotor deriving much of its saliency from the large airgap afforded by the discontinuous rotor back iron as it is brought into alignment, hence allowing a much shorter rotor tooth, which in turn affords a thicker retaining hub. The maximum aligned to unaligned inductance ratio for design 1 is ultimately limited by the definition of the unaligned position, as the rotor and stator have the same pole pitch, causing a significant amount of flux linkage. The maximum achievable ratio is hence lower, and as can be seen by inspecting Fig. 4.18 this relates to ~75% of that achievable with design 3. It is also interesting to note that the two designs return the same inductance ratio for a rotor tooth height of 6mm, and that for rotor tooth heights below this value (as may be required in high stress applications) the modular rotor shows consistently higher inductance ratios, where the discontinuous back iron dominates the value of unaligned inductance.

Fig. 4.19 shows the static torque-angle characteristics (per unit length) for all 3 machine designs, calculated by Maxwell Stress integration from a series of two-dimensional finite element field analyses for 2000 A-turns excitation (a rotor angle of 0° corresponding to the fully aligned position).

It is evident that machine design number 1 with the modular rotor is competitive with the machine design number 3 in terms of its static torque capability, and has a considerable advantage over machine design number 2. An interesting feature of the torque-angle characteristic for the modular rotor SR machine is that it exhibits a region of negative torque from -8.2° to –10° (the extent of this negative torque region tending to reduce under conditions of extreme magnetic saturation). Although the negative torque region lies outside the normal angular interval during which this particular combination of coils would be excited to generate motoring torque (typically from –7° to –2°), it may cause a reduction in the net torque if the commutation is advanced to such an extent that current flows during this angular interval. Further, it may limit the scope for employing overlap of the phases (as is often the case in conventional SR machines for high speed operation), although it does not preclude it entirely.

Two-dimensional analysis is useful in terms of comparing the relative performance of 3 machine designs on a per unit length basis. However, due to the short axial length relative to the outer diameter, 'end-effects' will inevitably have a significant influence on performance. Although correction factors have been proposed for conventional SR machines to enable results deduced from two-dimensional finite element analyses to be scaled to account for end-effects [TOR 95], these are not necessarily applicable to modular rotor machines. Hence, three-dimensional, magneto-static, non-linear finite element analysis was employed in the analysis of the three machines to establish the significance of end-effects. The three-dimensional analysis was limited to consideration of the aligned and unaligned positions only. For each position, two excitation levels were modelled, viz. 7 A.turns and 2000 A.turns per coil, which for a rotor in the aligned position correspond to un-saturated and saturated conditions respectively (2000 A.turns being equivalent to an effective current density in the winding of 11.7 A/mm^2).

An important system level consideration when comparing alternative machine designs is their inductive impedance, and hence their power factor, since this has a significant influence on the VA rating of the converter. However, the different number of phases and the different operating mode of the modular SR machine make it difficult to form direct comparisons with conventional machines. Nevertheless, in terms of the influence on the power factor, it is useful to compare the self-inductance per phase of the conventional 24-18 pole machine (i.e. having 6 stator poles excited simultaneously), with the inductance of a pair of adjacent phases in the modular SR machine (i.e. again having 6 stator poles excited). The resulting values of inductance per turn, calculated from both two- and three-dimensional finite element analyses, are given in table 4.7. As is evident, there is no penalty in employing a modular rotor in terms of the inductance per turn. Further, a comparison between the values of inductance calculated using two- and three-dimensional analyses shows that the relative contribution of the end-windings is very similar irrespective of whether the machine has a modular rotor or a conventional rotor.

4.5. Conclusions

This chapter has highlighted the fact that the mechanical strength of the lamination materials is likely to be a critical issue in realising SR machines which are capable of meeting demanding performance requirements in the harsh environment of the HP spool of an aircraft engine. Although commercially available grades of cobalt iron are capable of meeting the application requirements to some degree, they will necessarily have to be operated at higher stress levels than would normally be desired (particularly given concerns regarding high temperature creep). Further, the heat treatment which is employed to achieve the required mechanical properties inevitably compromises the magnetic properties, and in particular, increases the specific iron loss. Thus, conventional SR rotor designs are likely to be fairly severely constrained by the combination of mechanical and magnetic properties that can be obtained from current cobalt iron laminations.

A modular rotor structure has been described which potentially offers a means of alleviating the stress in the rotor laminations, albeit many practical issues in relation to the reliable attachment of the laminated rotor modules to a high-strength, non-magnetic hub remain to be resolved. Nevertheless, such a modular rotor provides an opportunity to increase the rotor diameter and/or to modify the heat-treatment in order to enhance the magnetic properties of the cobalt iron laminations. The static performance of a modular rotor SR machine has been compared with that of two conventional SR machines, using a combination of two- and three-dimensional finite element analyses. The modular rotor machine has been shown to be competitive in terms of its average torque capability, and would not seem to be at a disadvantage as regards power factor (which is a critical issue from a system level point of view when assessing the viability of embedded SR machines). Further, the unbalanced magnetic pull which results in a symmetrically disposed modular rotor SR machine is likely to be similar to that which results in a comparably sized conventional 'short-flux' path SR machine, such as machine design number 3.

However, it is pertinent to emphasise that given their relatively complex construction and the associated higher manufacturing cost, their relatively high number of poles and phases, it is unlikely that modular rotor SR machines will be preferred to conventional SR machine designs for the vast majority of applications. However, they may be an attractive option for an embedded machine in the HP spool of a gas-turbine, for which mechanical strength and long-term stability of the rotor at elevated temperatures are limiting design factors, and which necessarily requires a machine with a high pole number in order to accommodate a large rotor bore.

4.6. References

[ANS 01] ANSYS® users guide, Procedures, Volume 1, Chapter 3.8.

[BOY 89] H.E. Boyer, T.L. Gall. 'Metals Handbook.' Published by American Society for Metals, 1989, ISBN 0-87170-188.

[CAL 03] S.D, Calverley, G.W. Jewell, R.J. Saunders. 'The calculation of centrifugal stress in four pole switched reluctance rotors', IEE Proceedings, Electrical Power Applications, 2003, Vol. 150, No.1, pp.97-105.

[CK 26] Ck26 Physical Properties Data Sheet – Surahammars Bruk Non-Oriented Electrical Steels Catalogue, published by European Electrical Steels Ltd.

[ELB 97] M.E. Elbuluk, D. Kankam, 'Potential starter/generator technologies for future aerospace applications.' IEEE AES systems magazine, May 1997, pp. 24-31.

[FEN 90] R.T. Fenner. 'Mechanics of Solids', Blackwell Scientific Publications, 1990, ISBN 0-632-02018-0

[FIN 00] R.T. Fingers, C.S. Rubertus. 'Application of High Temperature Magnetic Materials', IEEE Transactions on Magnetics, Vol.36, No.5, Sept. 2000, pp.3373-3375.

[FIN 99] R.T. Fingers, J.E. Coate, N.E. Dowling. 'Creep deformation of a soft magnetic iron-cobalt alloy', Journal of Applied Physics, vol.85, no.8; 15 April 1999; p.6037-9.

[GAR 99] N.R. Garrigan, W.L. Soong, C.M. Stephens, A. Storace, TA.Lipo. 'Radial force characteristics of a switched reluctance machine' Conference Record of the 1990 IEEE Industry Applications Conference (Cat. No.99CH36370), 1999, Vol.4, p.2250-2258.

[GER 01] J.M. Gere, S.P. Timoshenko. 'Mechanics of Materials – 5th Edition', Chapman and Hall, 2001, ISBN 0534371337.

[HIP 50] Hiperco Alloy 50HS Data sheet, Carpenter Speciality Alloys.

[KAL 99] S. Kallee, D. Nicholas. 'Friction and forge welding processes for the automotive industry.' International Body Engineering Conference, Detroit, USA, 28-30 September 1999 (Paper No. 99-IBECC-13)

[KON 00] A. Kondoleon, W.P. Kelleher. 'Soft Magnetic alloys for high temperature radial magnetic bearings.' 7th international symposium on magnetic bearings, August 23-25, 2000, ETH Zurich.

[LAW 80] P.J. Lawrenson, J.M. Stephenson, P.T. Blenkinsop, J. Corda, N.N. Fulton. 'Variable-speed switched reluctance motors,' IEE Proceedings B. Electric Power Applications, Vol. 127, Part B, No. 4, July 1980, p.253-265.

[LIU 99] S. Liu, J. Yang, G. Doyle, E. Kuhl, C. Chen, M. Walmer, 'New sintered high temperature SM2(Co, Fe, Cu, Zr)17 permanent magnet materials.' Proceedings of the 1999 IEEE International Magnetics Conference, 18-21 May 1999.

[MAC 89A] S.R. MacMinn, W.D. Jones. 'A very high speed switched-reluctance starter-generator for aircraft engine applications' IEEE Proceedings of the National Aerospace and Electronics Conference, Vol. 4, 1989, pp 1758-1764.

[MAC 89B] S.R. MacMinn, J.W. Sember. 'Control of a switched-reluctance aircraft engine starter-generator over a very wide speed range.' Proceedings of the Intersociety Energy Conversion Engineering Conference, Vol 1, 1989, pp 631-638.

[MEC 02] B.C. Mecrow, J.W. Finch, E.A. El-Kharashi, A.G. Jack. 'Switched reluctance motor with segmental rotors.' IEE proceedings Electrical Power Applications, Vol. 149, No. 4, July 2002, pp. 245-254

[PAT 92] Patent Number EP 0504093. 'Isolated segmental switch reluctance motor.' 16th September 1992.

[PAT 96] European Patent Number EP 0736952. 'Rotor for reluctance machines.' 9th October 1996.

[PRO 02] M.J. Provost. 'The more electric aero-engine: a general overview from an engine manufacturer', Proceedings of the IEE Conference on Power Electronics, Machines and Drives, Bath, April 2002, Publication No: 487, pp.246-251.

[RAD 95] A.V. Radun. 'Design Considerations for the Switched Reluctance Motor', IEEE Transactions on Industry Applications, Vol.31, No.5, September/October 1995; p.1079-1087.

[RIC 88] E. Richter. 'High temperature, lightweight, switched reluctance motors and generators for future aircraft engine applications.' Proceedings of the 1988 American Control Conference. Atlanta, USA, Jun 15-17, 1988, Vol. 88, p.1846-1851.

[SIM 96] G.K. Simon, R.E. Perrin, M.C. Ohmer, T.L. Peterson, 'Resistivity of Fe,Co,V. High strength laminates from –73°C to +650°C.' Wright Laboratories report number: AD-A325086, Nov 1996

[TAN 99] W. Tang, Y.Zhang, G.C. Hadjipanayis. 'High-temperature magnetic properties of $Sm(Co_{bal}\ Fe_{0.1}\ Cu_{0.088}\ Zr_x)_{8.5}$ magnets.' Journal of Magnetism and Magnetic Materials Vol. 212, 2000, p.138-144.

[TOR 95] D.A. Torrey, X.-M Niu, E.J Unkauf. 'Analytical modelling of variable-reluctance machine magnetisation characteristics', IEE Proceedings. Electric Power Applications, Vol. 142, No. 1, January 1995, p.14-22.

[WU 00] X. Wu, R.S. Chandel, S.H. Pheow, H. Li. 'Brazing of Inconel X-750 to stainless steel 304 using induction process.' Materials Science and Engineering A: Structural Materials: Properties, Microstructure and Processing, Vol. 288, No. 1, Aug, 2000, p 84-90.

Table 4.1. Dimensional and electromechanical requirements for the HP spool starter/generator.

	Motoring	**Generating**
Max Stator OD	400mm	
Min rotor bore diameter	200mm	
Max overall length	100mm	
Speed range	0 – 4500rpm	7000 – 13500rpm
Max torque	200Nm	135Nm
Rated Power	100kW	100kW

Table 4.2. Minimum rotor outer diameter based on defined inductance ratio criteria, with a fixed shaft diameter of 200mm for various combinations of stator and rotor pole numbers.

Number of stator poles	Number of rotor poles	Minimum rotor outer diameter	Steps per revolution
6	4	653	12
8	6	367	24
10	8	301	40
12	8	315	48
12	10	273	30
14	12	257	84
16	12	261	48
18	12	266	36
20	16	241	80
20	18	235	180
24	16	245	48
24	18	237	72
24	20	231	60
30	24	225	120

Table 4.3. Convergence in maximum displacement and maximum stress with normalised element size. Relative computational requirement for each level of discretisation is also shown.

Normalised element scaling factor, κ	Convergence in maximum displacement, ξ (%)		Convergence in maximum Von-Mises stress, ε (%)		Relative Computational Requirement	
	Global	Local	Global	Local	Global	Local
1.000	-	-	-	-	-	-
0.500	0.507	1.011	3.054	4.066	1.0	1.0
0.333	0.221	0.355	2.245	3.070	1.7	1.1
0.250	0.069	0.194	1.027	0.311	2.4	1.5
0.200	0.055	0.062	0.492	1.144	3.2	1.9
0.167	0.041	0.090	0.601	0.565	4.4	2.6
0.143	0.028	-0.007	0.372	0.326	6.2	3.3
0.125	0.021	0.159	0.383	0.230	7.3	3.8
0.111	0.014	0.041	0.170	0.250	9.5	4.3
0.100	0.014	0.062	0.250	0.217	10.3	5.2
0.091	0.014	-0.028	0.199	0.166	12.2	6.1
0.083	0.007	-0.021	0.104	0.130	15.0	6.1
0.077	0.007	-0.007	0.139	0.118	18.4	7.1
0.071	0.007	0.090	0.089	0.088	19.1	8.3
0.067	0.007	0.000	0.106	0.077	22.0	9.4
0.063	0.007	-0.041	0.059	0.085	25.0	9.6
0.059	0.000	0.007	0.088	0.056	27.6	10.4
0.056	0.007	0.021	0.050	0.056	29.3	11.4
0.053	0.000	0.034	0.068	0.050	32.1	12.8
0.050	0.007	-0.014	0.041	0.050	36.3	13.4

Table 4.4. Maximum Von-Mises stress and deflection for the various rotor module fixing arrangements.

Method of attachment	Maximum Deflection, mm	Maximum Von-Mises stress, MPa	Maximum Von-Mises stress at the hub inner radius, MPa
Fir tree	0.5	3110	997
Dovetail	0.83	3150	1510
Dovetail with pre-compression	0.76	3240	1570

Table 4.5. Viable combinations of SR machines with modular rotors.

Number of Stator poles	Number of Rotor poles	Number of Phases	Steps per revolution	Utilisation factor
14	12	7	42	0.286
16	12	8	48	0.250
18	16	9	72	0.222
20	12	10	60	0.200
22	12	11	66	0.182
22	16	11	88	0.182
22	20	11	110	0.182
24	18	8	72	0.250
24	20	12	120	0.167
26	12	13	78	0.154
26	16	13	104	0.154
26	20	13	130	0.154
26	24	13	156	0.154
28	12	14	84	0.143
28	20	14	140	0.143
28	24	7	84	0.286
30	16	15	120	0.133
30	18	10	90	0.200
30	28	15	210	0.133

Table 4.6 Design parameters of the 3 machines modelled

	Machine Designs		
	1	2	3
Rotor Topology	Modular	Conventional	Conventional
Phases	8	4	4
Rotor poles	18	18	18
Stator poles	24	24	24
Rotor inner diameter (mm)	200	200	200
Rotor outer diameter (mm)	300	248	300
Stator outer diameter (mm)	400	336	400
Axial length of stator stack and rotor (mm)	50	50	50
Airgap (mm)	1.0	1.0	1.0
Rotor pole arc (° mech)	6.9	7.4	6.9
Stator pole arc (° mech)	6.9	6.9	6.9
Stator slot depth (mm)	31	31	31
Cross-sectional area of coil (mm^2) assuming $k_p = 0.6$	171	135	171
Step angle (° mech)	5	5	5
Rotor material	Hiperco 50HS	Hiperco 50HS	Hiperco 50HS
Stator material	Hiperco 50	Hiperco 50	Hiperco 50
Fundamental electrical frequency @15000rpm (Hz)	4500	4500	4500
Peak Von-Mises stress in rotor (MPa)	658 (hub) 230 (module)	345	406

Table 4.7 Values of inductance calculated by two and three-dimensional magneto-static finite element analysis

	Machine Design					
	1		2		3	
	2D	3D	2D	3D	2D	3D
Aligned inductance per turn (μH) (7 A turns)	53.02	61.55	45.70	50.53	51.35	61.79
Unaligned inductance per turn (μH) (7 A turns)	13.83	20.28	12.46	15.66	10.96	15.72
	3.83	3.04	3.67	3.22	4.69	3.93
Aligned inductance per turn (μH) (2000 A turns)	42.46	43.21	35.59	35.62	42.42	43.22
Unaligned inductance per turn (μH) (2000 A turns)	13.84	20.26	12.46	15.71	10.97	15.26
Inductance ratio at 2000 A turns	3.07	2.13	2.86	2.27	3.87	2.83

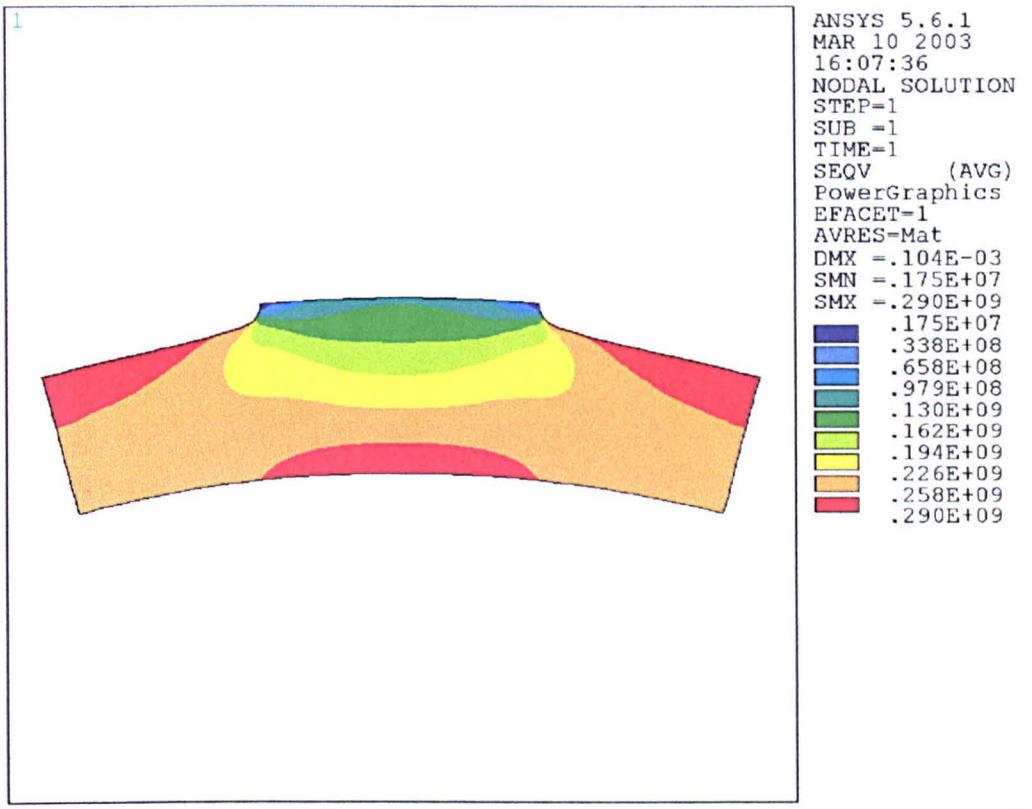

Figure 4.1. Finite element predicted Von-Mises stress at 15000 rpm in one pole of a 12-pole rotor with a bore diameter of 200mm and maximum stress limited to 290MPa.

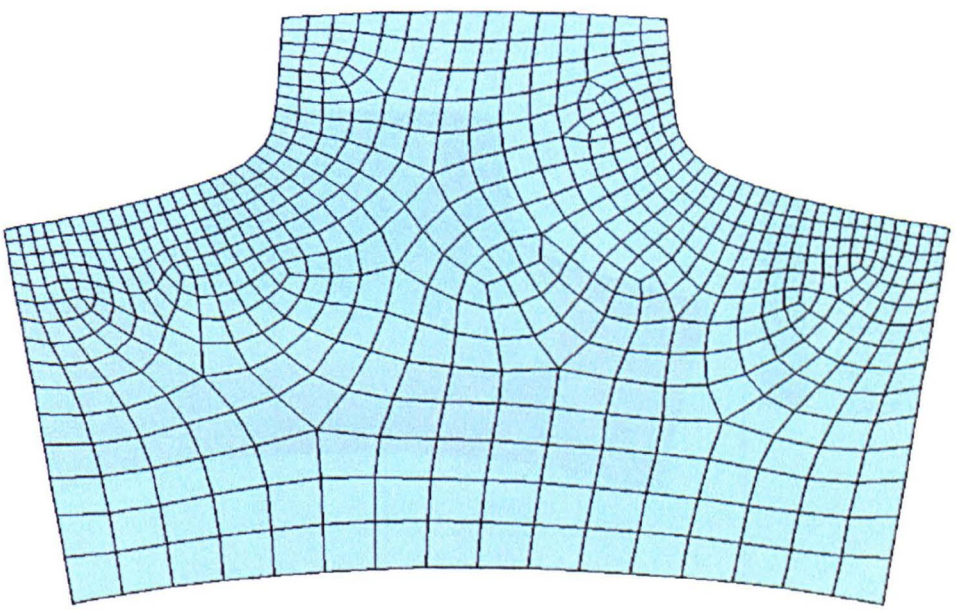

Figure 4.2. Locally refined finite element mesh of the 18-pole SR rotor.

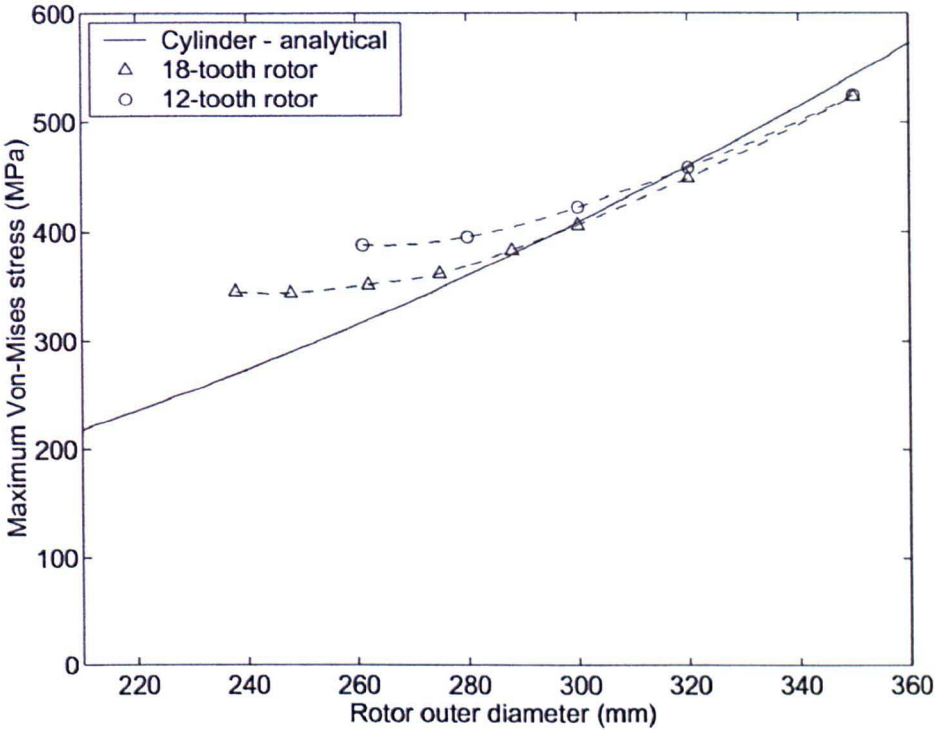

Figure 4.3. Predicted variation of the maximum stress at 15,000 rpm with rotor outer diameter (rotor bore diameter = 200mm)

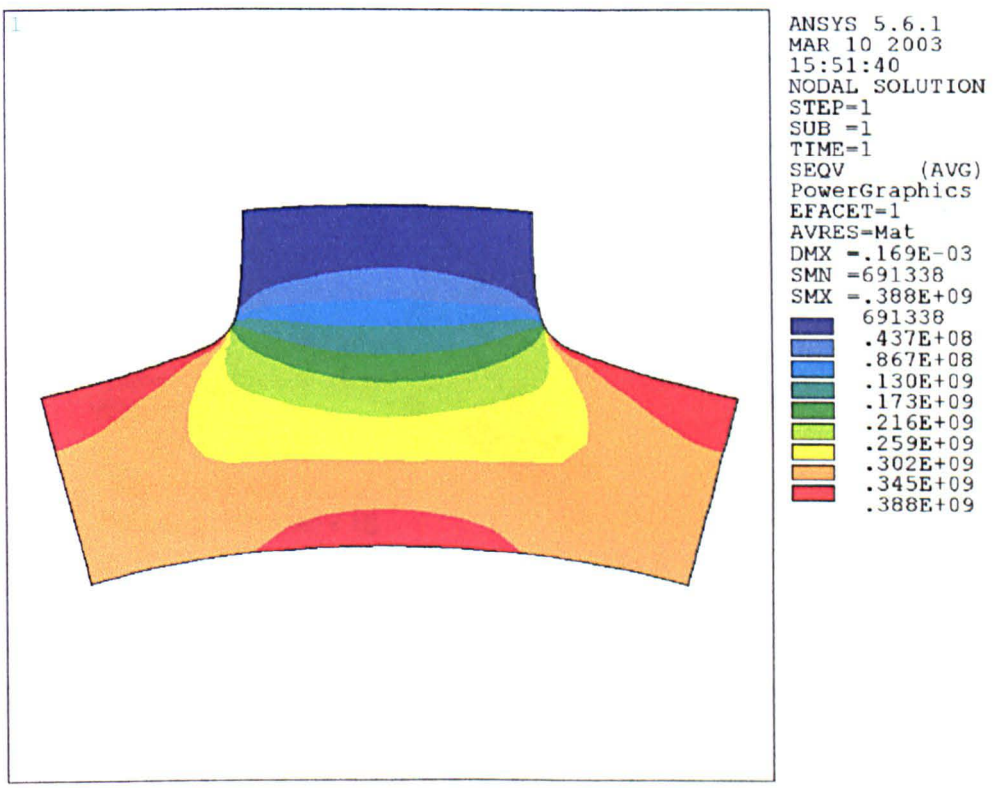

Figure 4.4. Finite element predicted Von-Mises stress at 15000 rpm in one pole of a 12-pole rotor with an outer diameter of 262mm and a bore diameter of 200mm.

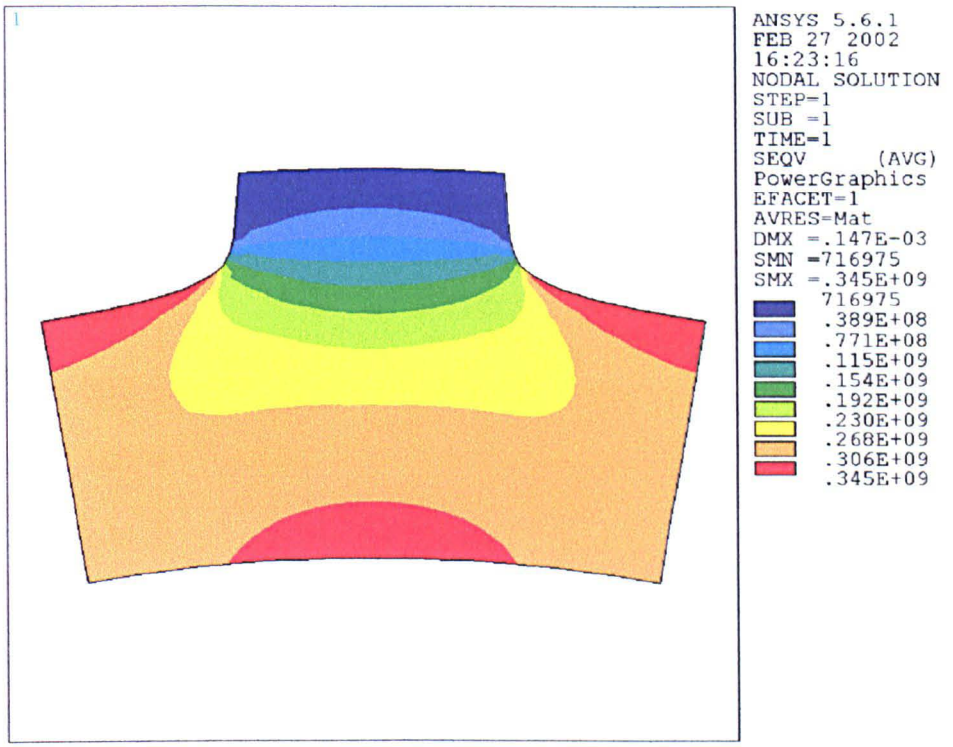

Figure 4.5. Finite element predicted Von-Mises stress at 15,000 rpm in one pole of an 18-pole SR rotor with an outer diameter of 248mm and a bore diameter of 200mm.

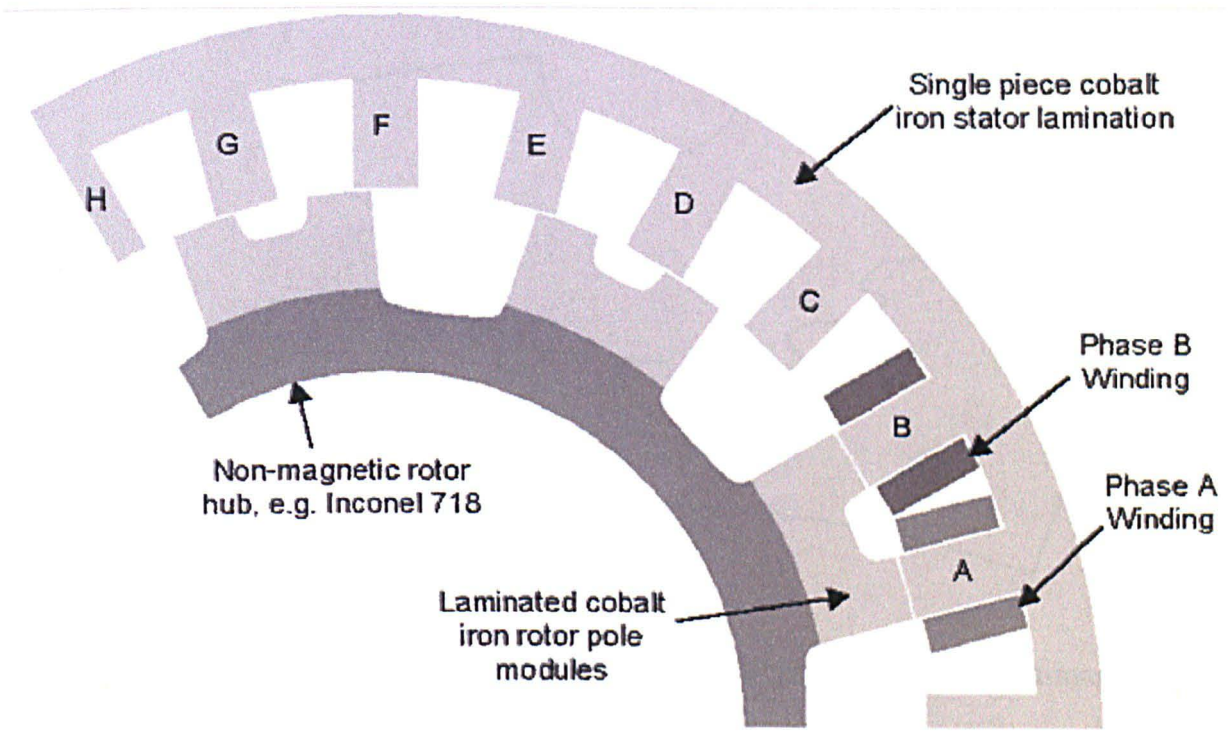

Figure 4.6. Schematic of a 120° section of an SR machine with a modular rotor (24 stator poles and 18 rotor poles).

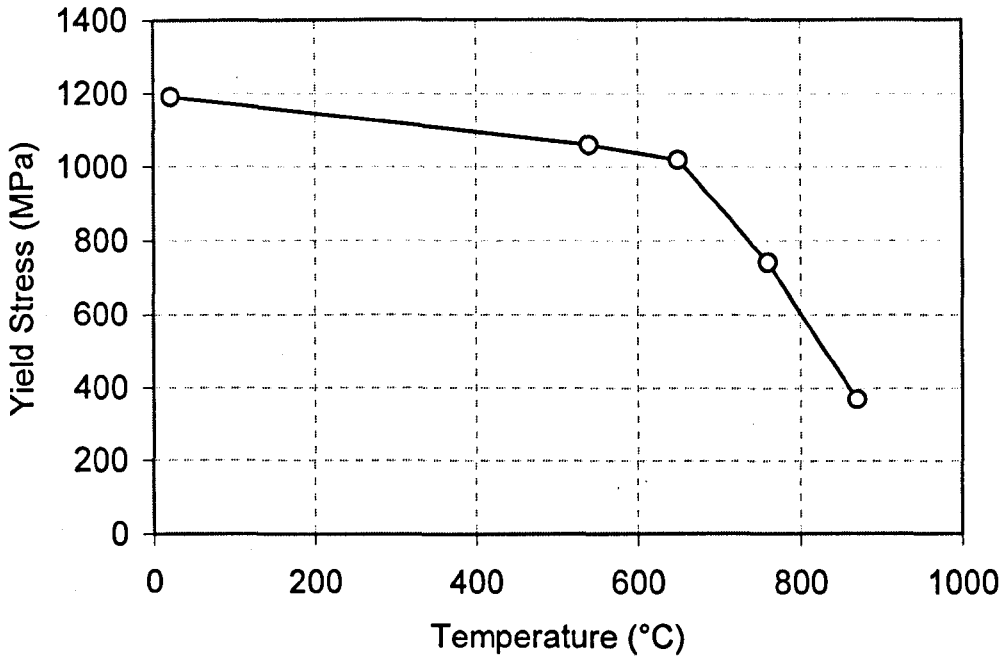

Figure 4.7. Inconel 718 0.2%Yield strength vs. temperature [BOY 89].

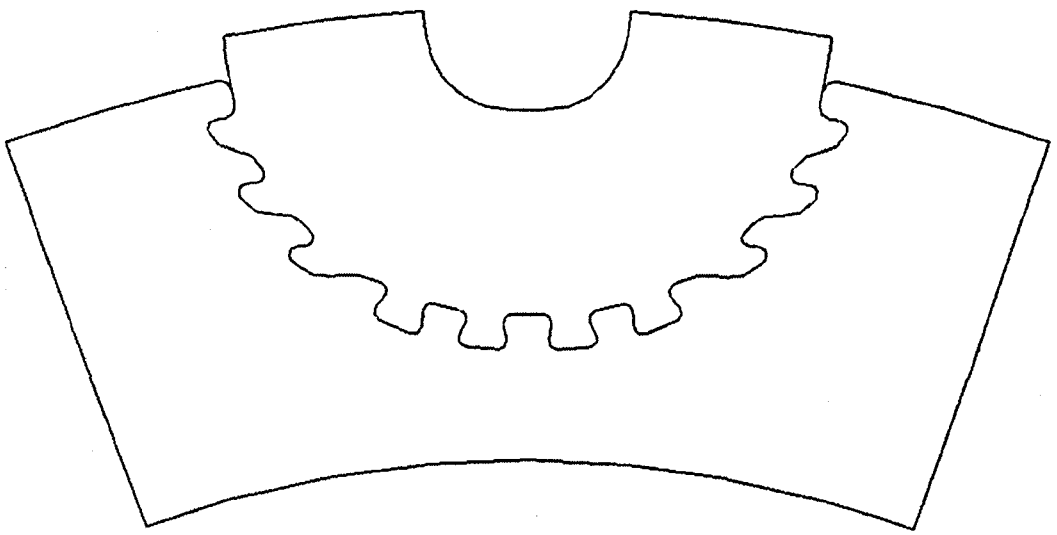

Figure 4.8. 'Fir-tree' technique for attaching laminated pole modules to non-magnetic hub

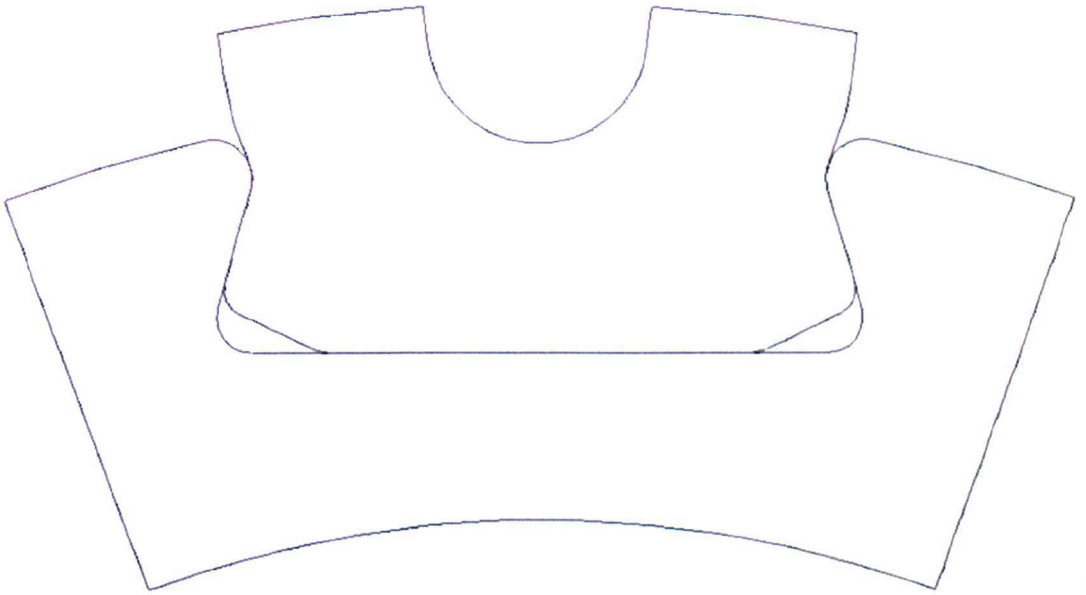

Figure 4.9. 'Dovetail' arrangement for attaching laminated pole modules to non-magnetic hub

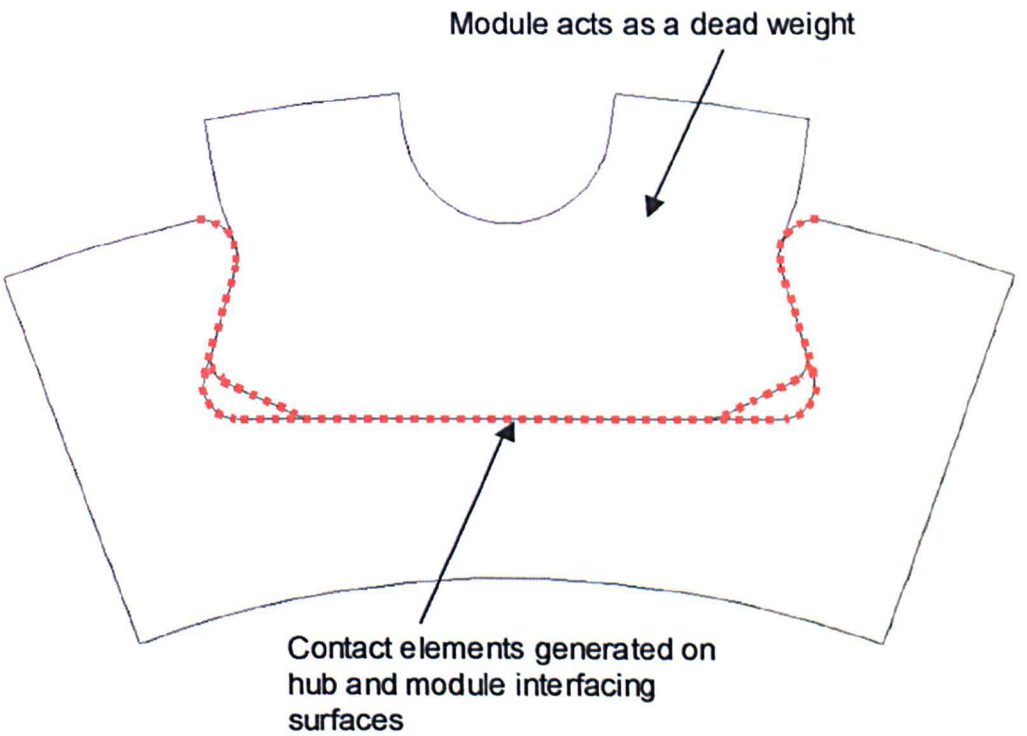

Figure 4.10. Location of contact elements at the interface between the non-magnetic hub and the rotor module.

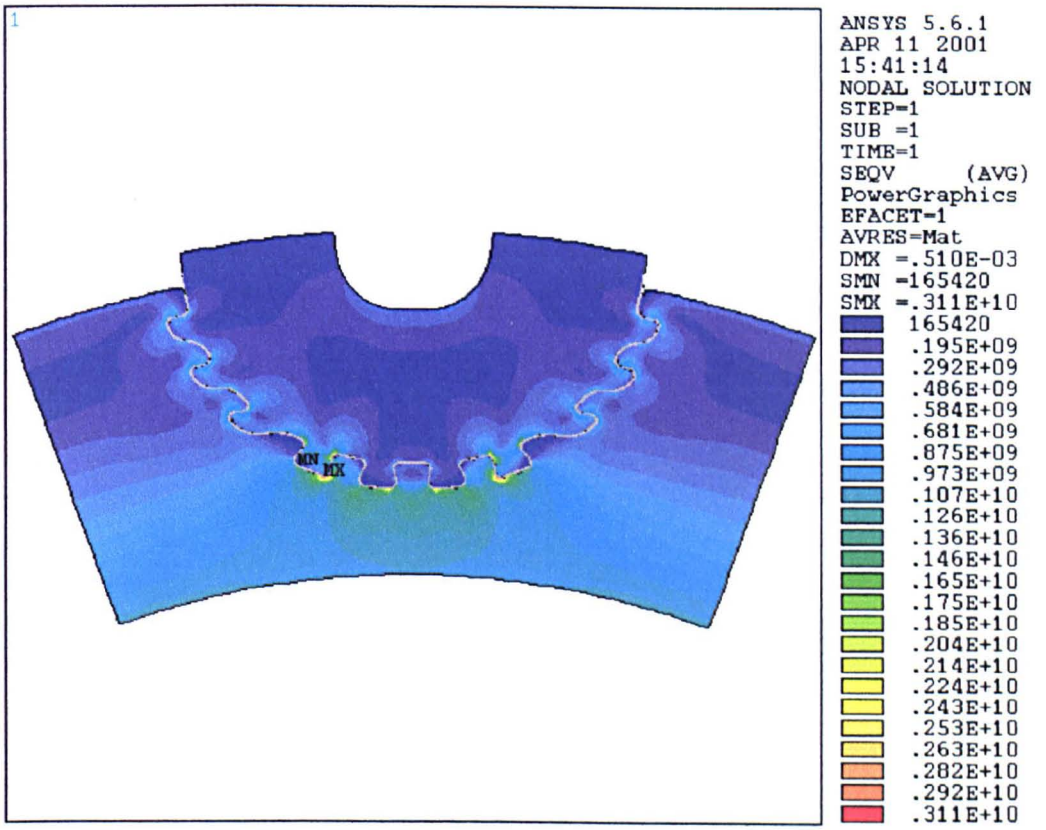

Figure 4.11. Finite element predicted Von-Mises stress distribution in the 'fir-tree' type attachment at 15000 rpm.

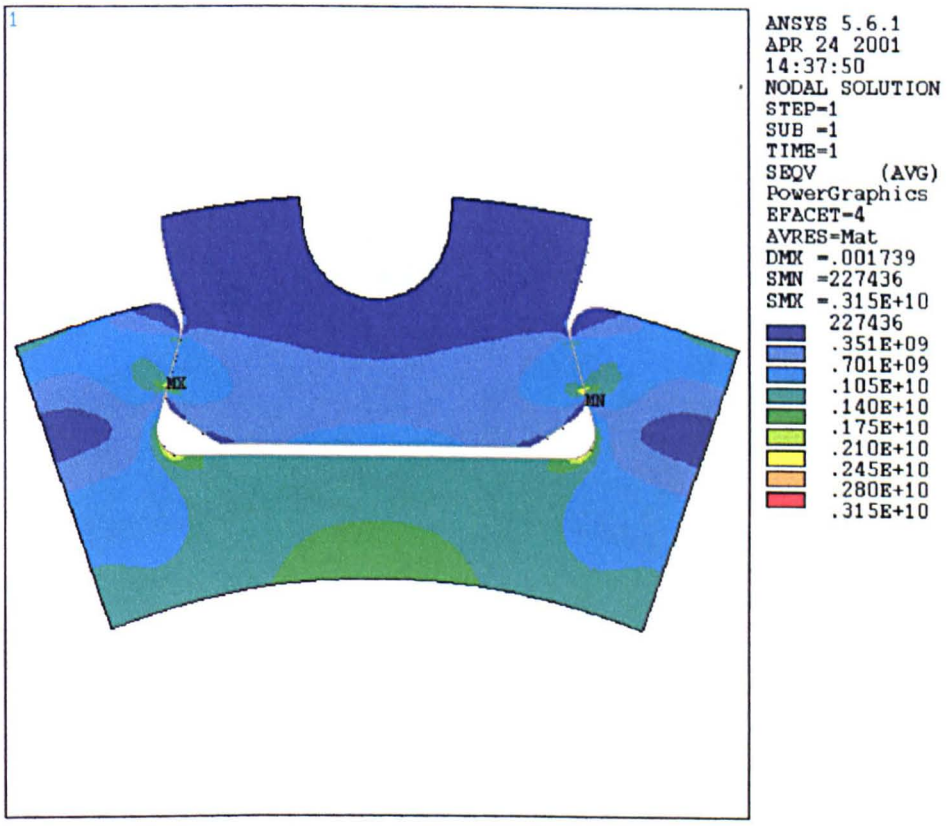

Figure 4.12. Finite element predicted Von-Mises stress distribution in the dovetailed module attachment at 15000 rpm.

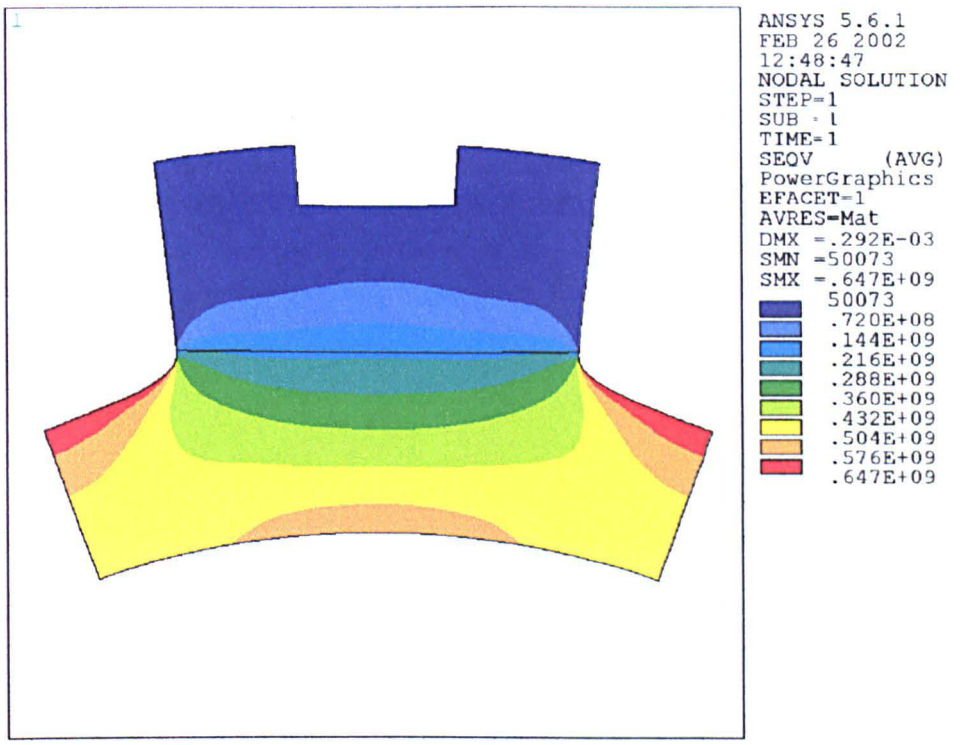

Figure 4.13. Finite element predicted Von-Mises stress at 15000 rpm in one pole of a welded modular rotor with an outer diameter of 300mm and a bore diameter of 200mm.

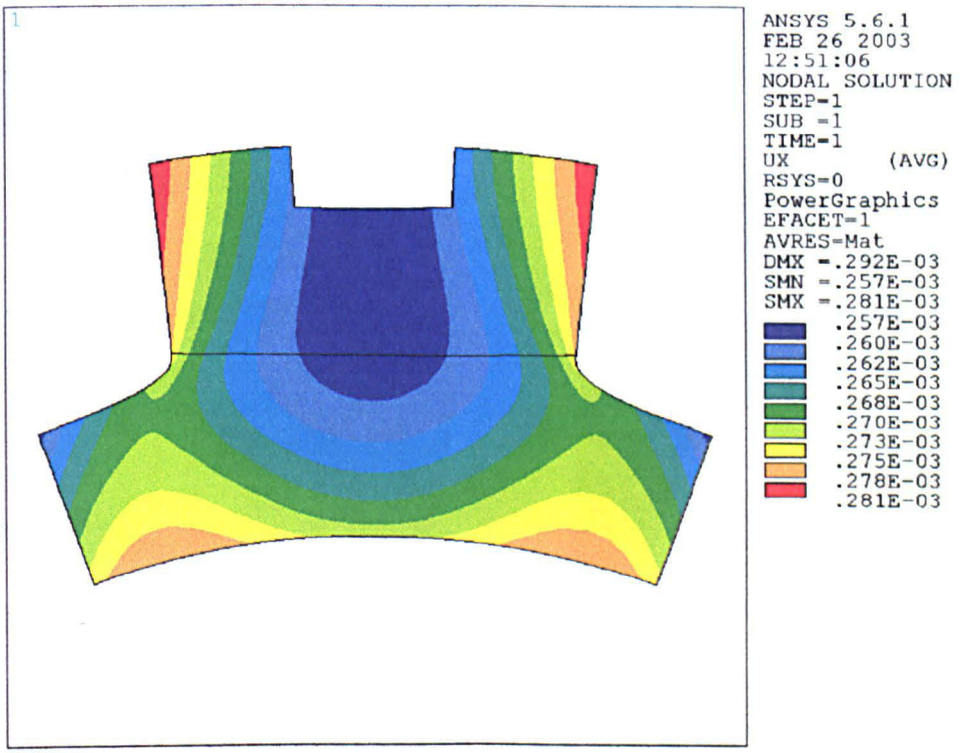

Figure 4.14. Finite element predicted radial displacement at 15000 rpm in one pole of welded modular rotor with an outer diameter of 300mm and a bore diameter of 200mm

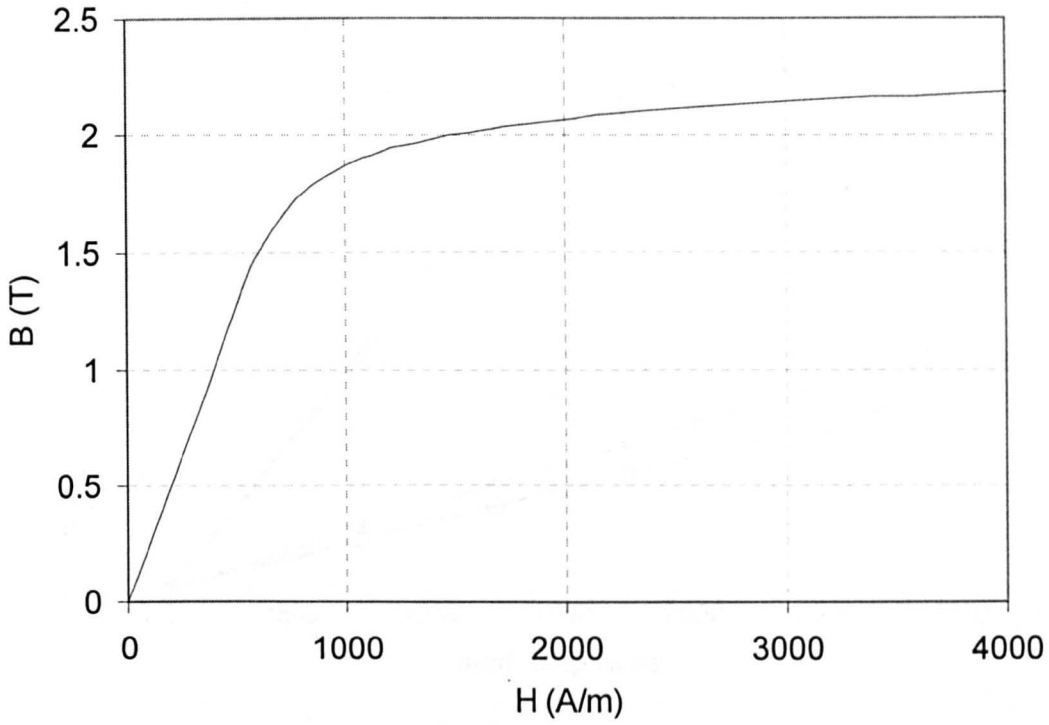

Figure 4.15. Initial DC magnetisation curve of Hiperco 50HS cobalt iron heat-treated for 1 hour at 720°C (680MPa 0.2% yield strength).

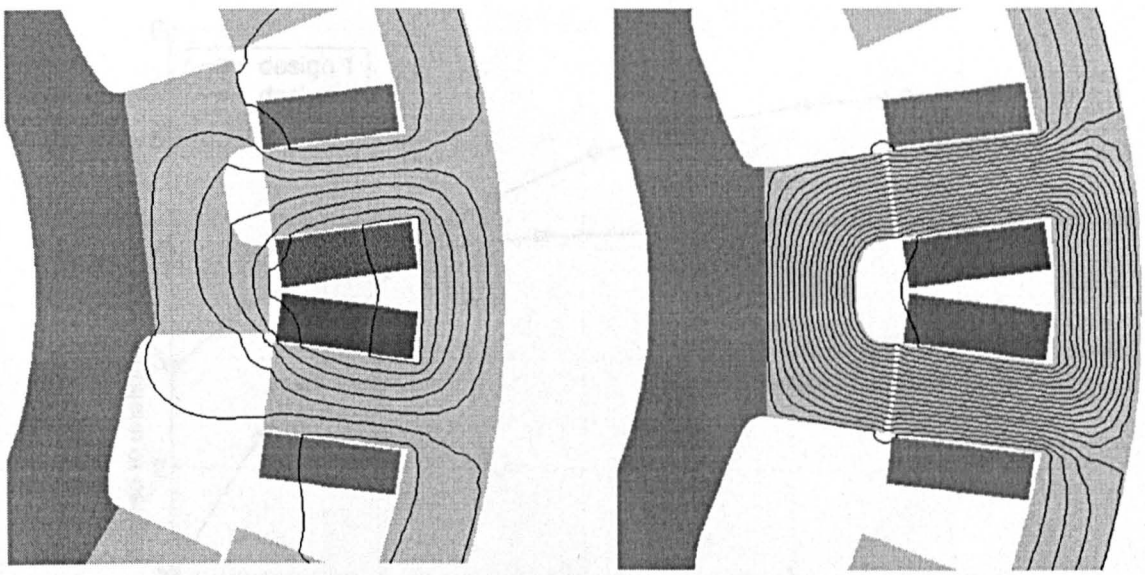

Un-aligned position (corresponds to -7.5° in fig.5.19)

Aligned position (corresponds to 0° in fig.5.19)

Figure 4.16. Finite element predicted field distributions in a 24-18 pole modular rotor SR machine for an mmf of 2000A turns per coil.
Increments between contours = 2.21×10^{-3} Wbm^{-1} in both cases.

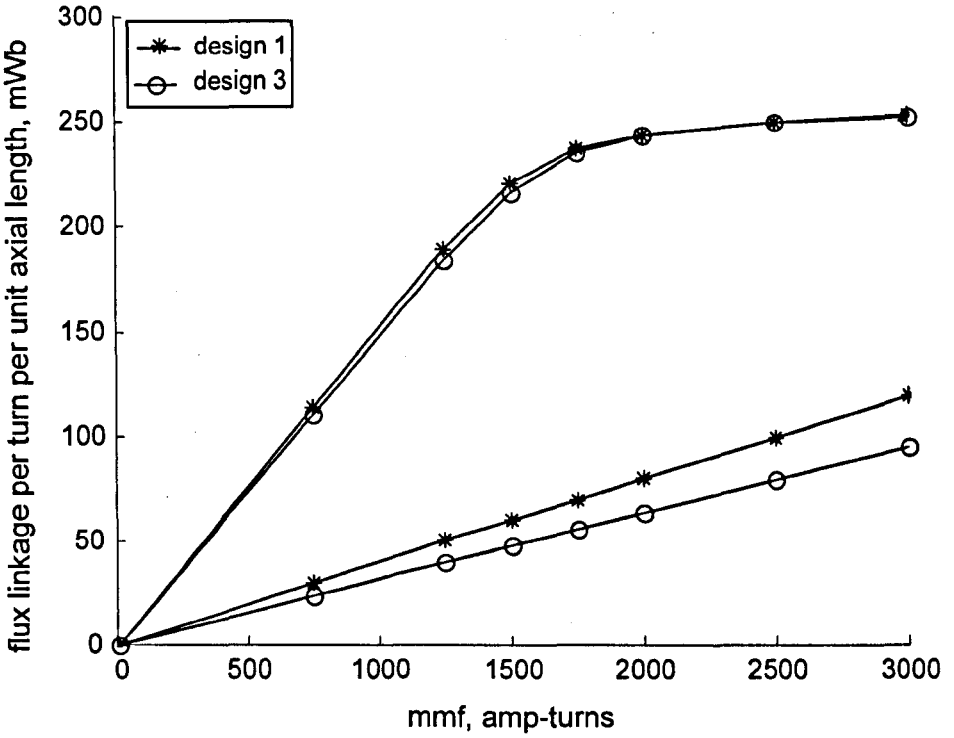

Figure 4.17. Finite element predicted flux-linkage versus mmf characteristics for machine designs 1 and 3

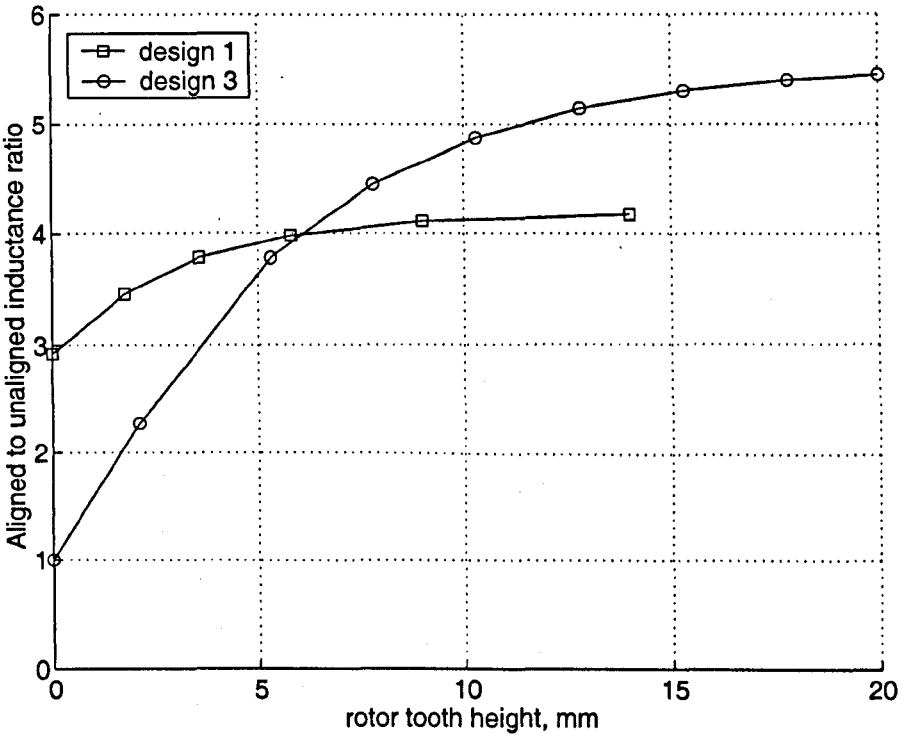

Figure 4.18. Aligned to unaligned inductance ratio as a function of rotor tooth height for designs 1 and 3.

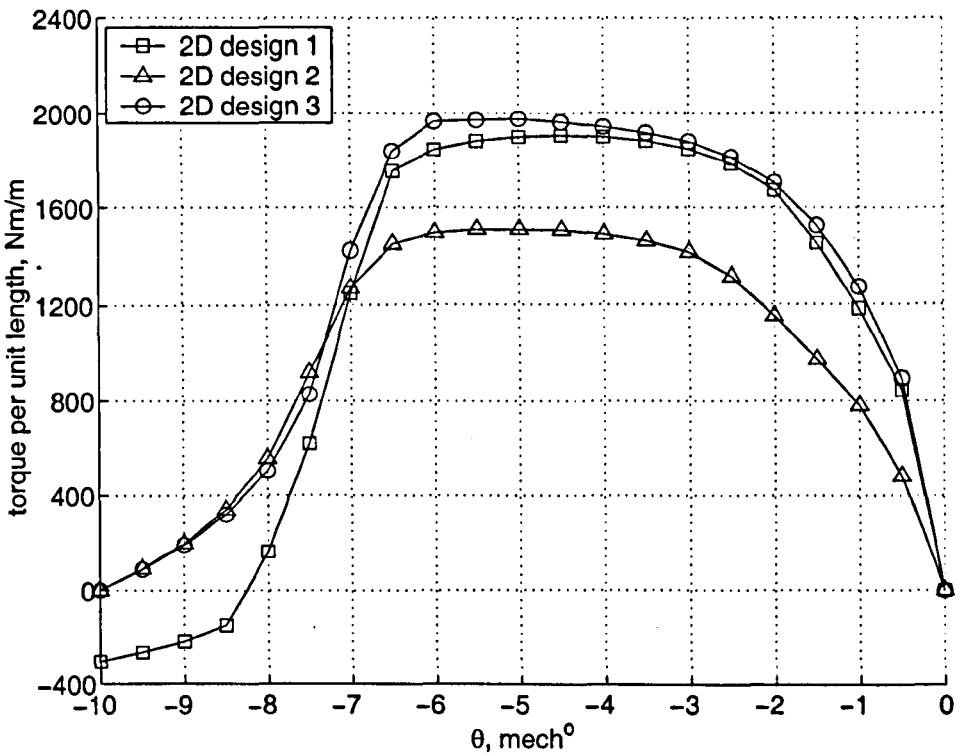

Figure 4.19. Two-dimensional, finite-element predicted static torque versus rotor position characteristics for an mmf of 2000A turns per coil (-10° corresponds to un-aligned position and 0° to aligned position)

CHAPTER 5

DYNAMIC MODELLING

5.1 Introduction

Although an SR machine with a modular rotor has a number of potential advantages over a conventional rotor for the particular case of a HP-spool machine, its ultimate viability is dependant on realising a practical and reliable means of attaching the rotor modules. As a consequence, a conventional rotor topology may well be favoured as the near-term solution, albeit that the rotor diameter and hence torque capability is lower. Hence, a conventional SR machine was selected for further investigation. This chapter describes the dynamic modelling of the HP spool SR starter/generator with a conventional rotor (i.e. design 2 in table 4.6).

5.2 Selection of the number of turns for the stator winding

By virtue of being singly excited machines, a given SR machine can accommodate a wide range of winding designs, since they are to some degree self-compensating. However, in any practical system with a particular DC link voltage, there is likely to be a preferred number of turns which provides the best compromise between minimising the converter VA rating and copper loss while providing the maximum power capability. As well as selecting the appropriate number of turns during the design synthesis, the so-called 'commutation angles' employed during operation provide an additional useful degree of freedom in optimising the converter VA rating and the copper loss for a given output power [MES 00].

In most PM machines, a reasonable estimate of the number of turns required can be derived simply from matching the induced emf to the DC link voltage with due allowance for reactive and resistive voltage drops at rated load and speed. However, the behaviour of SR machines is considerably more non-linear, and hence a combination of

finite element analysis and circuit simulation play a key role in determining the most appropriate number of turns in the machine to meet a given performance specification.

For the particular case of the SR machine for an HP-spool, the difficulties in selecting the preferred number of turns are compounded by the need to meet the requirements of two contrasting and conflicting operating points, a high starting torque of 200Nm, and a high speed generating requirement of 100kW at 13500rpm. The power requirement at high speed imposes an upper limit on the number of turns due to the effects of inductance (which varies as the square of the number of turns) limiting the rate of rise of current in the windings, whereas the high torque required for starting requires a high number of turns to reduce the phase current, and hence the VA rating of the converter. Thus the selection of the number of turns requires consideration of the various operating points and the weightings associated to various performance features [COR 97].

5.3 Basic dynamic operation of SR machine and converter

Most SR machines are operated in conjunction with voltage source converter, in which a series of nominally square wave voltage pulses are applied to the various phases in turn. A number of converter topologies have been developed for SR machines, ranging in complexity from a single switching device per phase and a chopper which controls the DC link voltage (which are often favoured in low-power and cost-sensitive applications [KRI 88] through to the full bi-polar H-bridge (which has been employed for SR machines with fully-pitched windings [MEC 95]). However, the most commonly employed topology is a so-called asymmetric H-bridge, which is shown in fig. 5.1. The governing voltage equation for one phase during the application of such a voltage pulse is:

$$V_{dc} = iR + \frac{d\psi}{dt} \tag{5.1}$$

This equation can be re-arranged to calculate the evolution of flux linkage in a phase:

$$\psi = \int (Vdc - iR)\, dt \tag{5.2}$$

This period in which the flux-linkage rises is often referred to as 'fluxing' of the machine. At some point during one electrical cycle of the machine, the particular phase must be 'de-fluxed' following each voltage pulse, which in turn results in a significant stored magnetic energy being returned to the supply (this would be realised in the converter shown in figure 5.1 by currents flowing through the free-wheeling diodes of the half H-bridge.

The net direction of energy transfer between the machine and the supply is controlled by the relative phasing of the voltage pulses with respect to the rotor position. Figure 5.2 shows a schematic representation of the commutation intervals required for both motoring and generating for the idealised case of a machine with a linear variation in inductance between the un-aligned and aligned positions. In order to produce motoring power the machine is fluxed when the rotor is in the un-aligned position and a torque is produced by the machine as the rotor tooth is drawn into the aligned position. In order to generate net electrical power, the phase is initially fluxed when the rotor is in the aligned position, and the prime-mover provides the necessary input torque to pull the rotor tooth away from this preferred position into the un-aligned position (hence generating a net current flow into the supply).

Figure 5.3 shows the specified torque-speed characteristic for the HP spool embedded machine, where a motoring torque of 200Nm is required up to 4000rpm in order to start the engine, and operation as a generator is required from 7000 to 13500rpm. As well as controlling the commutation intervals to achieve the desired characteristics, it is also necessary to exercise a close degree of control over the current waveforms, particularly at low speeds. To this end, most SR converters employ closed loop current control schemes.

The most common strategy for machines operating with a low fundamental electrical frequency is to employ a switching frequency significantly higher than the fundamental

electrical frequency. These techniques, such as pulse-width-modulation (PWM), hysteresis, and bang-bang control are well suited to very accurate control of the current waveform, as they are able to provide many switching cycles during one machine electrical cycle. They are used extensively in drives for low and medium speed applications.

For the case of the HP starter/generator, the fundamental electrical frequency is 4.05 kHz at 13500rpm, and techniques such as PWM become severely compromised at such high fundamental electrical frequencies, as the number of switching intervals per cycle reduces to such an extent that only limited control can be exercised over the current waveform. Hence, at high speeds it is common practice to reduce the number of pulses per electrical cycle to just one, and rely on the switching angles to control the average value of current and hence the power flow. By controlling the turn-on and dwell angles accurately, the average current can be controlled to a reasonable accuracy, however, this technique gives rise to increased copper loss due to the high peak to rms current ratio encountered in the very 'peaky' single-pulse operating mode. This operating mode also increases the torque-ripple due to the single pulse operation, but owing to the lower switching frequency, the eddy losses are reduced. This technique provides no control over the shape of the current waveform during the pulse, and indeed, current may rise even after the supply voltage has been removed in a generating situation, due to the negative inductance profile. Control is therefore only provided in an open-loop approach during the current pulse, which limits the accuracy of which a given power output may be achieved.

The practical implementation of such a control method is very difficult with no prior knowledge of the effect that switching angles have on output power. One way of achieving this is to generate a map of turn-on and dwell angles with respect to speed and power, which form the basis of look-up tables in the controller. The only method available in generating such a look-up table is to conduct a series of numerical simulations. This mapping approach, which could also in principle be performed by repeated testing of a prototype, is a similar procedure to that employed for mapping control parameters for internal combustion engines.

5.4 Description of the non-linear dynamic model

Although SR machines have a very simple mechanical geometry, their performance is often highly nonlinear and essentially consists of a series of transient pulses. The non-linear dynamic model employed to calculate current waveforms, and hence torque in the SR machine is shown in figure 5.4.

The non-linear magnetic behaviour of an SR machine can be conveniently represented in a system model by pre-calculating the variation of both the flux-linkage and static torque with stator current and rotor position from a large number of magneto-static finite element solutions. Although the torque produced by the machine for a given current could in principle also be derived from the flux-linkage characteristic [DPA 00] [SOA 01] [CAO 00], the approach in figure 5.4 with a separate torque characteristic greatly simplifies the operation of the model.

A two-dimensional flux-linkage characteristic for SR machine design 2 was shown previously in figure 4.16. However, the very confined space envelope that is available within a typical aero-engine to integrate an electrical machine dictates that the axial length of the stator iron is necessarily much smaller than its outer diameter, for this particular specification being 50mm and 336mm respectively. Hence, end-effects may have a significant influence on the flux-linkage characteristics of the machine, which in turn would require recourse to three-dimensional finite element analysis, despite the significant increase in computation time. In order to establish whether three-dimensional analysis was necessary, the limiting cases of the un-aligned and aligned positions were modelled using both two- and three-dimensional analysis. Figure 5.5 compares the resulting predicted flux-linkage characteristics for these two positions, from which the significant influence of end effects, particularly in the un-aligned position, is apparent. Hence, to provide an accurate representation of the machine behaviour for the dynamic model, a series of 110 three-dimensional finite element calculations were performed for all-inclusive combinations of rotor position between the aligned and unaligned positions (in 10 increments) and coil mmfs from 500A.turns to 7000A.turns, which corresponds to a highly saturated machine. In each case, only single-phase excitation was considered, i.e. no overlap of phase currents was considered at this stage of the modelling. However,

the mutual flux linkage of the adjacent phase was calculated. The static torque at each angular position and current was calculated using the principle of virtual work. Fig 5.6 shows a typical finite element mesh (in this case for the aligned position), while fig. 5.7 shows the corresponding flux densities in the rotor and stator core for the particular case of an mmf of 2800A.turns.

The resulting flux-linkage characteristics for SR machine design 2 are shown in figure 5.8, while fig 5.9 shows the torque characteristics. In both cases, these characteristics are based on a total ampere-turns per phase, and hence can be scaled appropriately for any number of turns. These characteristics are incorporated into the dynamic model as two-dimensional look-up tables with cubic-spline interpolation. However, since the finite element solutions were performed for a specified value of current rather than for a specified value of flux-linkage, it is necessary to re-arrange and curve fit the data of figure 5.8 such that the modified characteristic provides the current for a given combination of input flux-linkage and angular position.

The electrical resistance of one phase can be calculated for a given number of turns using the idealised model shown in fig 5.10. The resistance for a phase with N_c coils, each having *n* turns is given by:

$$R_{ph} = \frac{((N_c . n\ (2 L_{stk} + \pi(r_1 + r_2))) + L_p)\rho}{h_c (r_1 - r_2) k_p} \tag{5.3}$$

where L_p is the total length of the interconnecting conductors between coils around the machine periphery, k_p is the packing factor, and ρ the resistivity of copper. Equation 5.3 calculates the DC resistance of the winding. Although this value neglects the influence of any eddy currents in the windings (which is a particular concern given the high frequencies involved), this assumption is valid providing due care is taken during the design of the machine to sub-divide the conductors into an appropriate number of parallel

strands (or in extreme cases the use of Litz wire). An estimate of the conductor diameter required can be derived from the classical expression for skin depth:

$$\delta = \frac{1}{\sqrt{\pi f \mu \sigma}} \tag{5.4}$$

For a sinusoidal current with a frequency of 4.0kHz, the skin depth predicted using equation 5.4 is ~1.0mm. Wire diameters greater than twice this skin depth will therefore yield little benefit in terms of current density reduction in the conductor cross-section.

It is worth noting that in common with many large machines, the resistive volts drop corresponds to a very small proportion of the DC link voltage. Hence the calculated value of current is relatively insensitive to any errors in the calculated resistance (due for example to over-simplified representations of the end-winding). Indeed, even for a 50% increase in phase resistance the rms phase current changes by less than 0.4%.

An important consideration when calculating dynamic current waveforms in SR machines, is the extent to which mutual coupling between phases must be accounted for. Although SR machines are generally regarded as operating on essentially phase-by-phase basis, there is often considerable overlap of the currents in different phases (either deliberately so as to minimise ripple torque for example, or as a natural consequence of the decay period of the currents at high speeds). However, the rigorous inclusion of mutual effects would require many more field calculations to be performed to cater for all-inclusive combinations of currents in the remaining phases at each rotor angular displacement. For the case of a 4-phase machine, this would increase the number of degrees-of-freedom in the flux-linkage characteristic from 2 to 5, which in turn is prohibitive in terms of computational time. For this machine design, a series of test calculations demonstrated that the mutual inductance does not exceed 5% of the corresponding value of self-inductance in any position or with any of the values of mmf considered. Hence, it is reasonable to neglect mutual inductance given the dramatic reduction in computational effort that this allows.

5.5 Winding design

By performing dynamic simulation for increasing numbers of turns, it is possible to establish a maximum number of turns that allows 100kW of generating power to be derived at 13,500 rpm from a 270V DC link. This in turn will determine the minimum starting current which is required if the high-speed power specification is to be met. For each particular number of turns, the commutation angles θ_{on} and θ_{off} were optimised by repeated simulation in order to generate the maximum power. Table 5.1 summarises the maximum achievable power at 13,500rpm, the corresponding commutation angles, the peak and rms currents at 13,500rpm and the starting current, for increasing number of turns from 1 to 5. As is evident, the power requirement of 100kW is only exceeded for machines with up to 4 turns per coil, which in turn gives a minimum starting current of 1200A. However, 4 turns per coil is on the limit of being able to produce 100kW and requires almost continuous current as shown in figure 5.11 which shows the predicted current waveform for the commutation angles listed in table 5.1 (the resulting dwell angle being 179° and a phase extinguish angle of 356°). The difficulties in satisfying the two conflicting performance requirements are clearly apparent in that even following careful optimisation, the rating of the converter is ~143kVA, i.e. some 1.4 times the maximum power rating of the machine.

A further series of simulations were performed for values of N up to 5 to establish commutation angles that would generate 100kW at 13,500rpm. In all cases apart from N=4, there are several combinations of commutation angles which would allow 100kW to be produced. Hence, in each case the commutation angles that give rise to the minimum copper loss were determined. Table 5.1 lists the resulting commutation angles and peak currents required to generate 100kW at 13,500rpm.

On the basis of the findings of the dynamic simulation, 4 turns per coil would appear to offer the best viable compromise in terms of converter VA rating. However, given that the predicted power only exceeds the 100kW specification by less than 2% and that there is little scope to improve on this value given that the current is close to being continuous, it is important to consider the sensitivity of the dynamic simulation results to variations in the ambient temperature.

The DC magnetisation curve of Hiperco 50HS is influenced to a degree by operating temperature. However, discernable changes in permeability, and more particularly saturation flux density, only occur for temperatures in excess of 500°C [LI 96] the magnetisation characteristic being essentially constant for temperatures up to 400°C. Hence, finite element flux linkage versus current characteristics generated with room temperature magnetisation data can be used with negligible error for temperature up to at least 400°C. The other potential impact of elevated temperatures on the prediction of current waveforms and hence torque is the variation in copper resistivity (which increases by a factor of 2.5 between room temperature and 400°C). However, as discussed previously in section 4 of this chapter, the resistive volts drop in this high power machine is very small in relation to the induced emf and the DC link voltage, e.g. for a 250% increase in resistivity for a machine with 4 turns, the rms current reduces from 316A to 314A (i.e. by less than 1%). Hence, temperature effects can be neglected in the dynamic model from the point of view of calculating current and torque, although it is critical to use an appropriately compensated value of resistance to calculate the resulting copper loss. Having established the preferred number of turns and the resulting current waveform at the rated point, the iron losses in the machine can be determined.

5.6 Calculation of iron losses

In order to quantify both the overall efficiency, and the likely temperature rise of the machine imposed by the iron losses, a detailed study of iron loss in the 4-phase SR machine was undertaken. As was highlighted in section 2 of Chapter 4, the combination of high speed and high pole number (electrical frequency of 4.05kHz at 13500rpm) will inevitably result in high levels of iron loss.

An important consideration in calculating the iron losses in this SR machine is the influence of the temperature employed for heat-treating the Cobalt Iron on the losses in the rotor. As discussed previously in section 2 of chapter 4, there is considerable scope to tailor the mechanical properties of a particular composition of Cobalt Iron by varying the heat treatment temperature. However, any benefits in enhanced mechanical strength are

gained at the expense of the magnetic properties, in particular the coercivity and hence the iron loss.

For Hiperco 50HS, the iron loss increases markedly with increasing yield strength as shown by the measured characteristics published by Masteller which are shown in figure 5.12 [MAS 98]. The increase in iron loss observed in figure 5.12 can be explained by reference to the grain size produced with different heat treatment schedules (i.e. Hall-Petch relationship) whereby the yield strength increases in inverse proportion to the square root of the grain size. For heat treatment which produces a high strength of 680MPa (i.e. 720°C) the resulting small grain size causes a significant increase in the coercivity and hence the hysteresis losses. By way of example, for mechanical strengths of 500MPa and 680Mpa, the hysteresis loss for a maximum flux density of 2.25T is 0.253 and 0.441 J/kg/cycle respectively [CAR 95]. This represents a 76% increase in hysteresis loss for a 36% increase in mechanical strength. However it is worth noting that the coercivity of the material reduces with operating temperature while the electrical resistivity increases, both of which tend to result in a reduction in losses at elevated temperatures.

Whereas material specific iron loss coefficients can be readily derived from manufacturer's data and/or measurements for room temperature operation, there is little available data for higher temperatures. However, it is well documented that up to 400°C, the change in coercivity losses is small in comparison to the change in electrical resistivity [LI 96]. Moreover, in view of the fact that eddy current losses are dominant at such high frequencies, it was deemed to be reasonable to account for the influence of temperature on the iron losses by solely scaling the electrical resistivity in line with published data [SIM 96]. The resulting coefficients for use in equation 2.2 are shown in Table 5.2.

5.7 Procedure for calculating iron loss in the SR machine

In many respects, the procedure for calculating iron losses in the SR machine is very similar to that described for the BLDC machine in chapter 2, i.e. the flux density waveforms throughout the machine are calculated from a series of magneto-static finite element solutions with the appropriate current waveform, following which, an iron loss model is used to calculate the losses for each of these waveforms. However, for SR machines, it is necessary to extend the model for calculating the hysteresis component of the loss since many regions of the stator and rotor are exposed to either unidirectional flux density variations or asymmetric variation with large DC offsets (c.f. BLDC machines where the flux density variations are symmetrical – although not necessarily sinusoidal). To cater for these uni-polar variations, the method proposed by Calverley for calculating minor-loop losses has been implemented [CAL 02]. This method, which extends the basic methodologies proposed by Lavers [LAV 78] employs a non-linear correction factor with a conventional hysteresis model.

In order to calculate flux density waveforms throughout the machine, a series of two-dimensional magnetostatic finite element solutions were performed using the current waveform shown in figure 5.11, which corresponds to generating 100kW at 13,500rpm, a condition that will yield the worst-case losses. Two-dimensional finite elements were deemed to be adequate for calculating flux density variations within the core, since although end effects will have some influence on the flux-density waveforms, this is likely to be considerably less significant than the influence of the flux-linkage characteristics.

Since SR machines operate with uni-polar currents and largely on a phase-phase basis, there is scope to vary the sense in which the various phase coils are wound without having a significant impact on torque production. For the case of a 24-18, 4-phase machine, the coils can be connected as either NNNN-SSSS or NSNS-SNSN as shown in figures 5.13(a) and 5.13(b) respectively. The main difference in operation is in the flux waveforms in the stator back-iron as shown, which in turn will influence the iron losses. As is apparent from fig. 5.13, the NNNN-SSSS configuration is likely to yield the lowest losses, a conclusion which is consistent with that observed by Calverley for the case of a

6-4 machine [CAL 02] Given the benefits of a NNNN-SSSS connection, this was adopted for the HP spool machine and formed the basis of the finite element modelling

A series of field solutions were performed at 0.5° increments in rotor angle using the ANSYS electromagnetic package. Representative field distributions in the aligned position and at the end of overlap between the rotor tooth and the main excited stator tooth (i.e. 0° and 5.5°) are shown in figure 5.14(a) and (b). As is evident from figure 5.14(b) as the teeth become increasingly un-aligned, very highly localised values of flux density occur near the edges of both the stator and the rotor teeth. Figure 5.16 shows a series of resulting flux density waveforms at key locations within the stator and rotor that are defined in fig 5.15.

The resulting total iron loss for this particular operating condition was calculated to be 2780W (1220W in the rotor and 1560W in the stator) using the model described in chapter 2 with modifications to cater for uni-polar flux density variations. This corresponds to a very high average loss density of 192W/kg. However, there are very high loss densities in the trailing tips of the rotor teeth and the leading tips of the stator teeth as is evident in the predicted distribution of loss density within the machine which is shown in figure 5.17. Of the three contributors to the overall iron loss, the classical eddy current component is dominant, as would be expected given the high frequency. The relative magnitudes of the hysteresis, excess, and classical eddy current losses being 1110.8, 138.8 and 1527.3 W respectively.

5.8 Consideration of alternative soft magnetic materials

In view of the high iron loss densities predicted for a machine with a Hiperco 50HS rotor and Hiperco 50 stator, the scope for employing alternative soft magnetic materials was considered. Of the various candidate materials that might offer some advantages over 49% cobalt-iron alloys in this particular application (in which classical eddy current losses are dominant) arguably the most interesting is 6.5% Silicon Iron (specifically 0.1mm thick laminations of NKK10ex900) because of its significantly higher electrical

resistivity, viz. 4.53×10^{-7} Ωm and 8.2×10^{-7} Ωm respectively. However, as demonstrated by figure 5.18, it has a considerably lower saturation flux density as compared to Hiperco 50 (viz. ~1.3T and ~2.3T respectively).

An alternative machine with the same dimensions as the original design, but employing NKK 10ex900 in both the stator and rotor was modelled. The dynamic current waveforms (and the subsequent selection of the most appropriate number of turns) and calculation of the iron losses were performed using an identical procedure to that employed for the Hiperco 50HS/ Hiperco 50 machine. The flux-linkage characteristics derived from three-dimensional FE analysis for the NKK 10ex900 machine is shown in figure 5.19, whilst the resulting dynamic phase current waveform at 13500rpm, 100kW, for the particular case of 3 turns, is shown in figure 5.20. Table 5.3 compares the performance of the NKK machine with that of the Hiperco 50 / 50HS machine. Although the iron losses are reduced by some 40% at this particular operating point, the NKK machine is only capable of meeting the 100kW output torque if the machine is highly saturated, which in turn requires an rms phase current of 893A (equivalent to an mmf of 2680 A-turns) and a peak phase current of 2900A. The resulting copper losses at 100kW are 12.4 kW and the starting current is 5800 A to produce 200Nm (as compared to 1200 A for the Hiperco 50/ 50HS machine). Hence, any benefits accrued in reducing iron losses are offset by the substantially increased converter rating (and associated converter losses) and a large increase in copper loss, which, as will be demonstrated in Chapter 6, is more difficult to remove due to the poor thermal path from the winding to the coolant.

A third design variant was considered with an NKK stator and a Hiperco 50HS rotor. However, the resulting flux linkage characteristics showed little deviation from those of the machine with both an NKK stator and rotor, and hence little improvement was gained in terms of torque capability, since saturation of the stator teeth limits any advantage that could be gained from the higher saturation flux density of the rotor. Given that the losses in this mixed material machine would inevitably be higher than the full NKK machine, while the significant penalties in copper loss and converter rating would be similar, it is unlikely to provide a preferred option to the original Hiperco 50 / 50HS machine.

5.9 References:

[CAL 02] S.D. Calverley. 'Design of a high speed turbo-generator for automotive applications.' PhD thesis, Sheffield University, 2002.

[CAO 00] S. Cao, K.J. Tseng. 'Dynamic modelling of SRM including neighbouring phase coupling effects' Electrical machines and power systems, 2000, Vol. 28, p.1141-1163. © 2000 Taylor and Francis.

[CAR 95] Carpenter Specialty Alloys manufacturers data, Hiperco 50HS, 1995

[COR 97] J. Corda. 'Effect of changing the number of turns on the performance of a switched reluctance motor'. EPE '97, Trondheim, p. 586-590.

[DPA 00] P.P. de Paula, W.M. da Silva, S.I. Nabeta W.M. da Silva, J.R. Cardoso. 'Modelling a switched reluctance motor/generator by using the finite-element method coupled with circuit equations'. ICEM 2000, Espoo, Finland. P.1752-1756.

[IND 00] R. B. Inderka, M. Menne, S. Schroder, R.W. De Doncker. 'Modelling of Switched Reluctance Drives with Commercial Simulation Software'. ICEM 2000, Espoo, Finland, p.1757-1761.

[KON 00] A. Kondoleon, W.P. Kelleher. 'Soft Magnetic alloys for high temperature radial magnetic bearings.' 7th international symposium on magnetic bearings, August 23-25, 2000, ETH Zurich.

[KRI 88] R. Krishnan, P. Materu. 'Design of a single switch per phase converter for switched reluctance motor drives.' Industrial electronics society, IECON 1988 proceedings. Vol. 3. p. 773 – 779.

[LAV 78] J.D. Lavers, P.P. Biringer, H. Hollitscher. 'A simple method of estimating the minor loop hysteresis loss in thin laminations.' IEEE Transactions on Magnetics, Vol. 14, No. 5, September 1978, pp. 386 – 388.

[LI 96] L. Li. 'High temperature magnetic properties of 49%Co-2%V-Fe alloy.' Journal of Applied Physics, Vol. 79, No. 8, 15th April 1996.

[MAS 98] M.S. Masteller. 'Soft magnetic materials for hostile environments.' Soft Magnetic Materials Conference, April 21, 1998, Barcelona, Spain.

[MEC 95] P. G. Barrass, B.C. Mecrow, A.C. Clothier. 'Bipolar operation of fully-pitched winding switched reluctance drives.' Electrical machines and drives conference 1995. Conference publication No. 412,1995, pp 252-256

[MES 00] E. Mese, Y. Sozer, J.M. Kokernak, D.A. Torrey. 'Optimal excitation of a high speed switched reluctance generator.' IEEE Applied Power Electronics Conference, Vol. 1, 2000, p 362-368.

[SIM 96] 'Resistivity of Fe,Co,V. High strength laminates from -73°C to +650°C.' NASA Final Report, 1st Dec 1995 -30th Nov 1996 Wright Laboratories Report number: AD-A325086.

[SOA 01] F. Soares, P.J. Costa Branco. 'Simulation of a 6/4 Switched Reluctance Motor Based on Matlab/Simulink Environment. IEEE Transactions on Aerospace and Electronic Systems, vol. 37, No. 3, July 2001, p.989-1009.

Table 5.1. Hiperco 50 stator / Hiperco 50HS rotor results from dynamic modelling.

Number of turns		1	2	3	4	5
Max power at 13,500 rpm	Power (kW)	116	300	142	102	61
	Peak Current (A)	>30000	>10000	1910	540	307
	RMS current	>10000	3774	802	323	185
	θ_{on} / θ_{off} (°elec)	170 / 240	120 / 250	100 / 270	78 / 259	60 / 240
100kW at 13,500	Peak Current (A)	>10000	2620	710	527.4	-
	RMS current (A)	1861	630	373	316	-
	θ_{on} / θ_{off} (°elec)	170 / 236	120 / 233	100 / 254	78 / 258	-
Current for 200Nm starting torque (A)		5100	3440	2410	1200	950

Table 5.2. Loss coefficients for Hiperco cobalt iron materials at 400°C.

Constant	Hiperco 50	Hiperco 50HS
k_h	0.0159	0.073
mv	8120	8120
τ	$0.15e^{-3}$	$0.15e^{-3}$
k_{exc}	$3.708e^{-5}$	$5.910e^{-5}$
a	1.405	2.213
b	0.075	-0.410
sigma	$1.79e^{6}$	$1.79e^{6}$

Table 5.3. Comparison of Hiperco 50/50HS and NKK 10ex900 machines.

Number of turns		Hiperco50/50HS (4 turns per coil)	NKK 10ex900 (3 turns per coil)
Max power at 13,500 rpm	Power (kW)	102	160
	Peak Current (A)	540	5230
	RMS current	323	1782
	θ_{on} / θ_{off} (°elec)	78 / 259	105 / 275
100kW at 13,500	Peak Current (A)	527.4	2900
	RMS current (A)	316	893
	θ_{on} / θ_{off} (°elec)	78 / 258	105 / 235
Current for 200Nm starting torque (A)		1200	5800

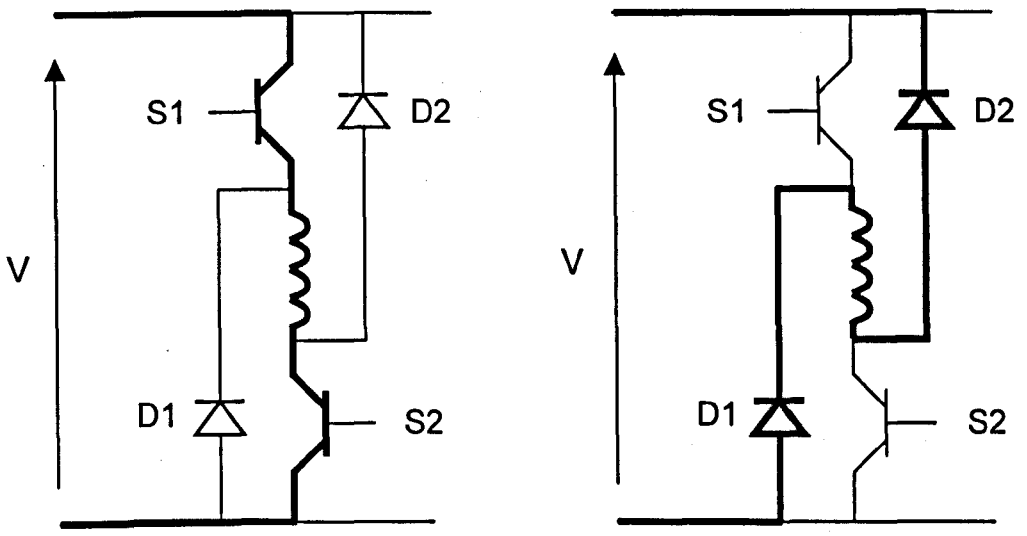

Figure 5.1. Typical asymmetric half H-bridge converter for an SR machine with the phase winding in series with the devices, hence removing the possibility of shoot-through.

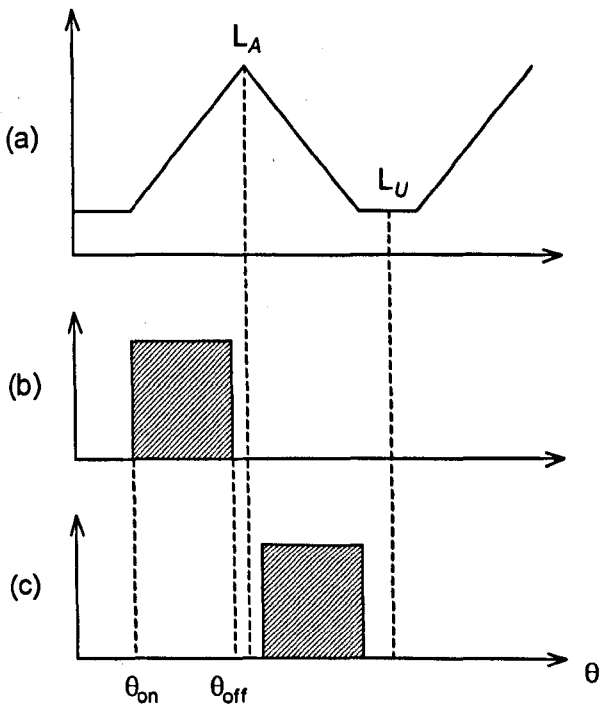

Figure 5.2. Commutation intervals, θ_{on} and θ_{off} for motoring and generating operation. (a) Idealised inductance profile, (b) Motoring operation, (c) Generating operation.

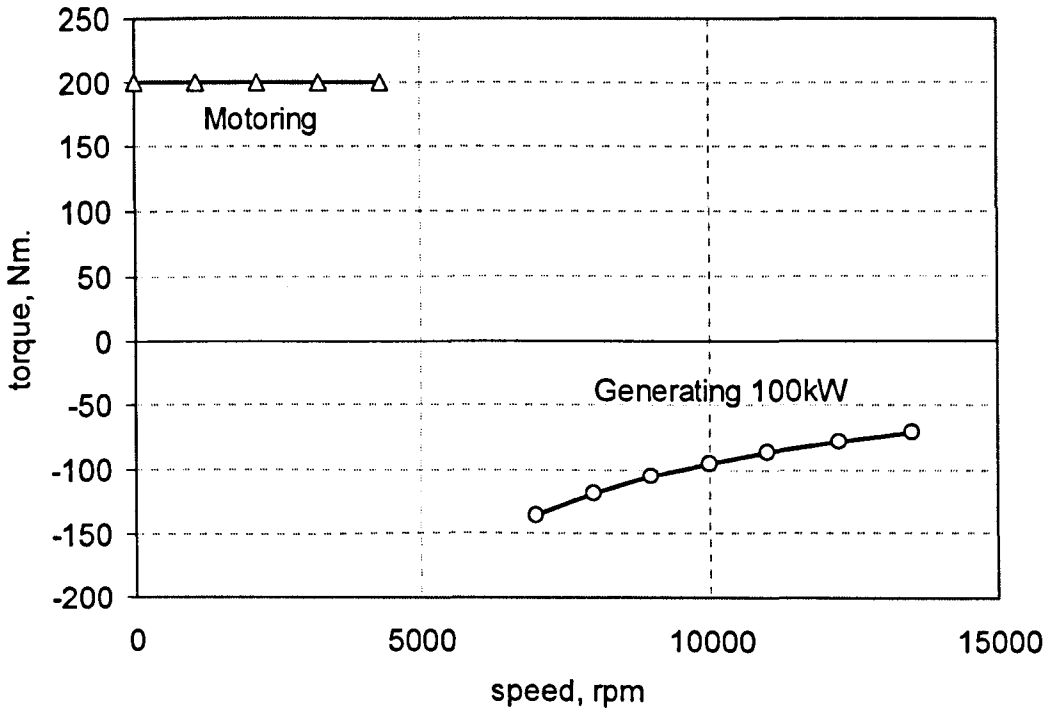

Figure 5.3. Torque versus speed profile for the HP spool machine under motoring and generating conditions.

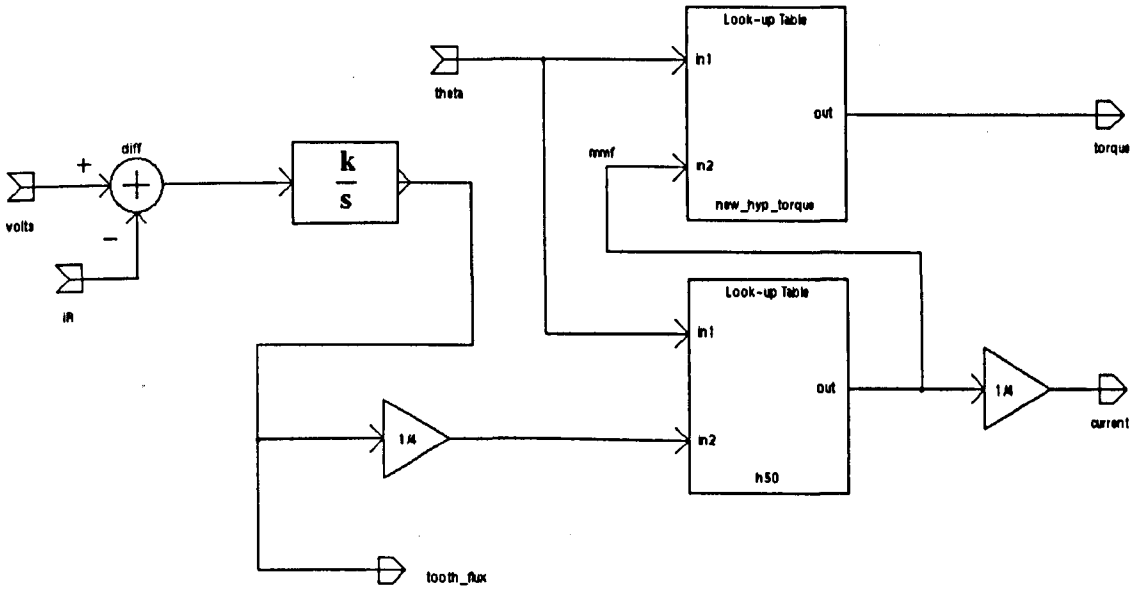

Figure 5.4. Schematic of dynamic model developed in SABER, showing the two 2D lookup table approach to calculate phase current and torque.

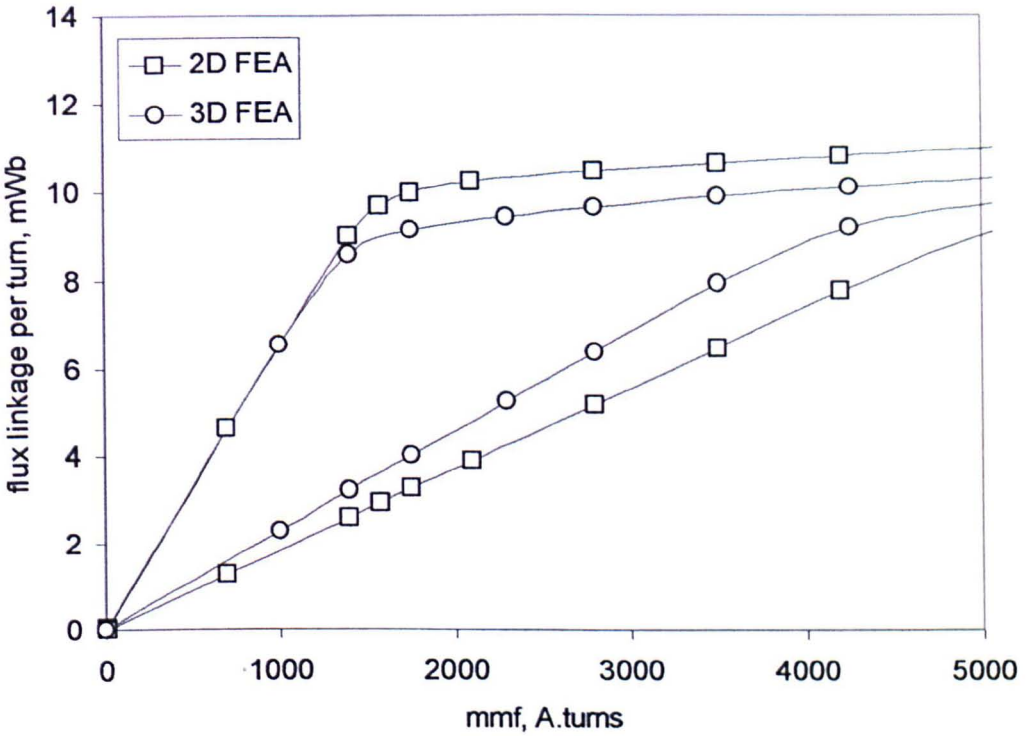

Figure 5.5. Flux linkage versus current from 2D and 3D finite element models

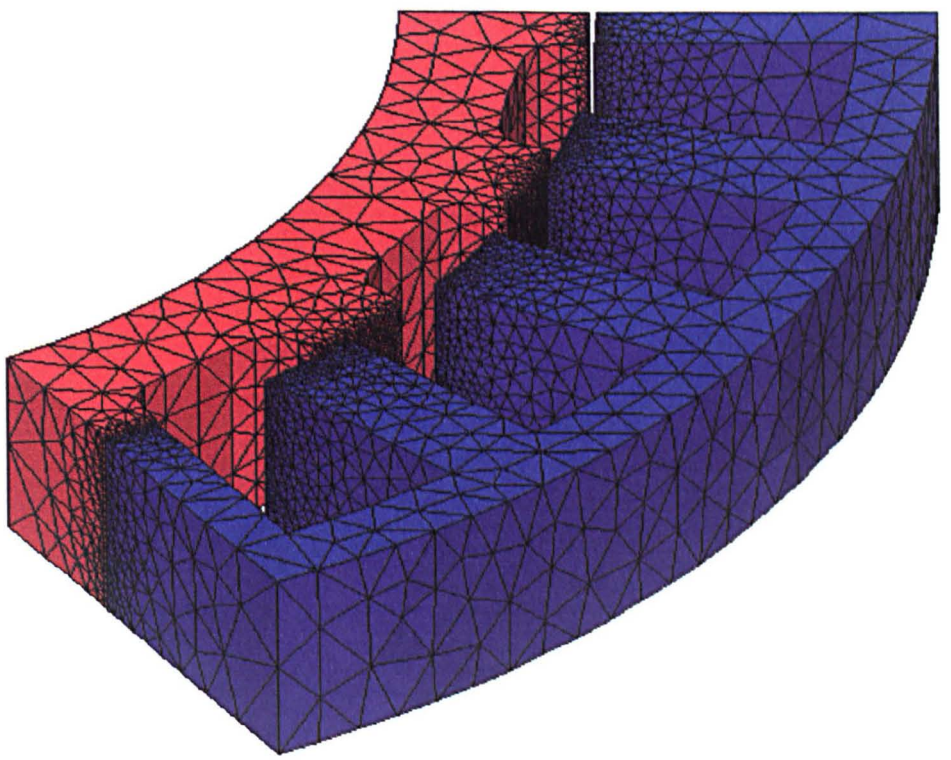

Figure 5.6. Three-dimensional finite element mesh of the SR machine with axial symmetry, and 60° cyclic symmetry.

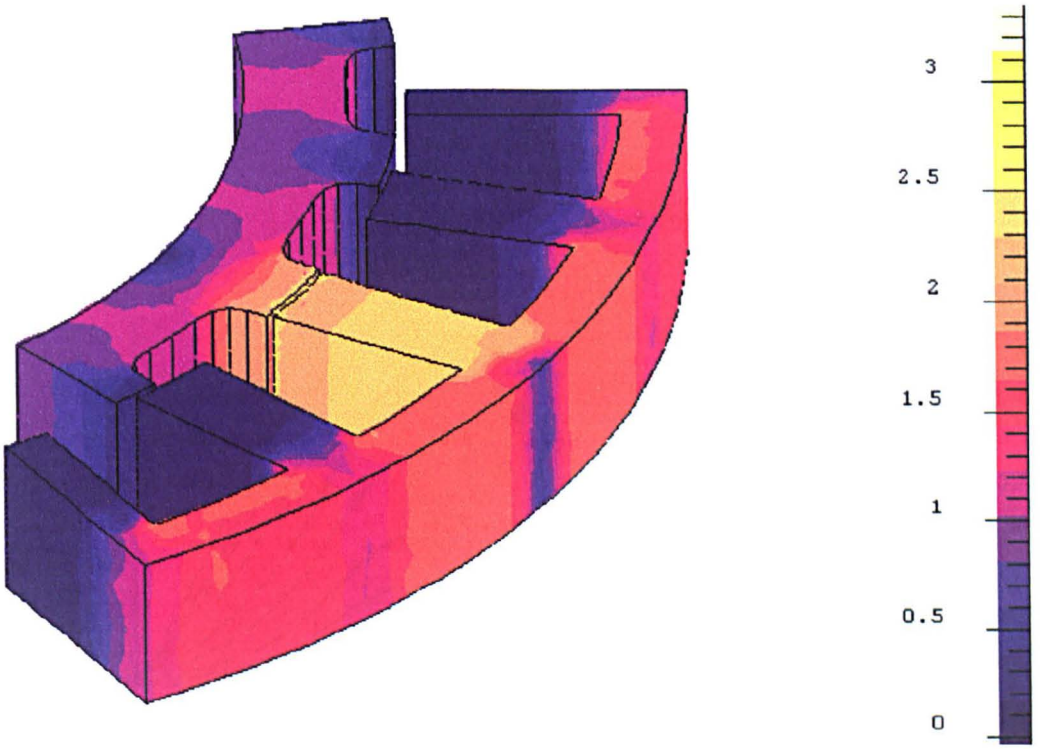

Figure 5.7. Flux density in the SR machine in the aligned position, for a winding mmf of 2800 A.turns.

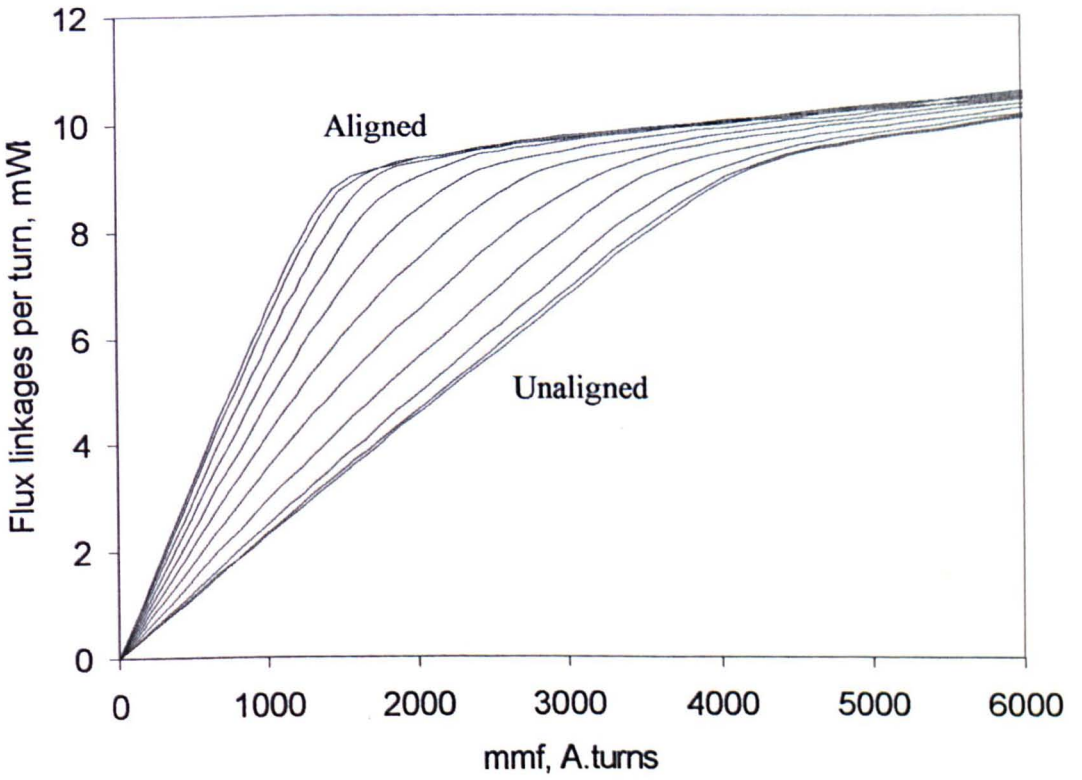

Figure 5.8. Three-dimensional finite element derived flux linkage characteristics for machine design 2.

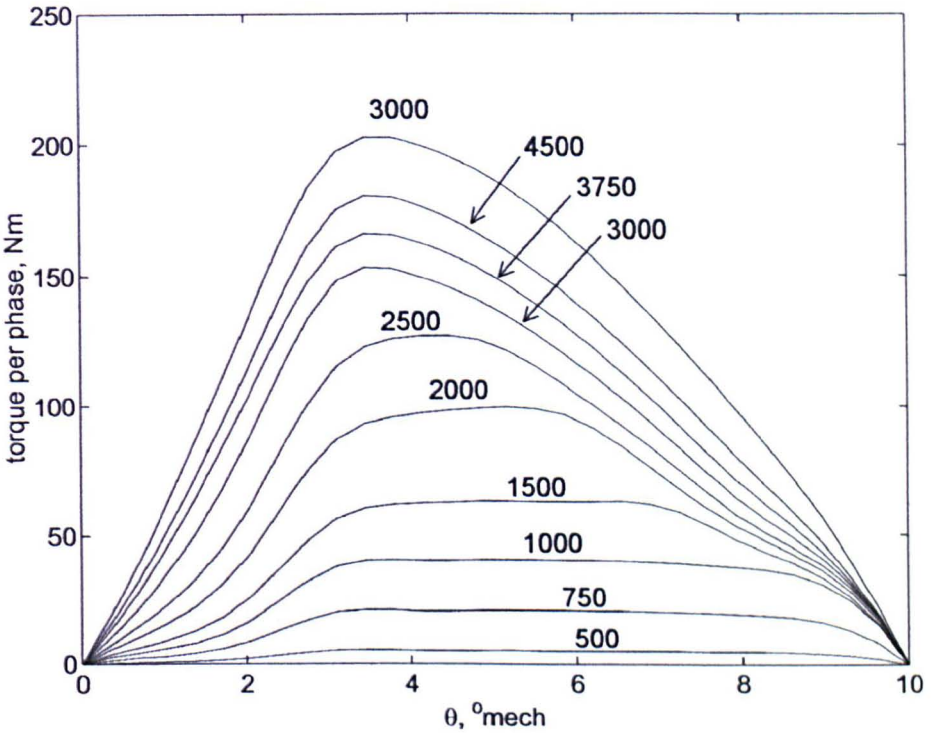

Figure 5.9. Three-dimensional finite element derived torque for machine design 2 for increasing values of phase mmf (A-turns shown in figure)

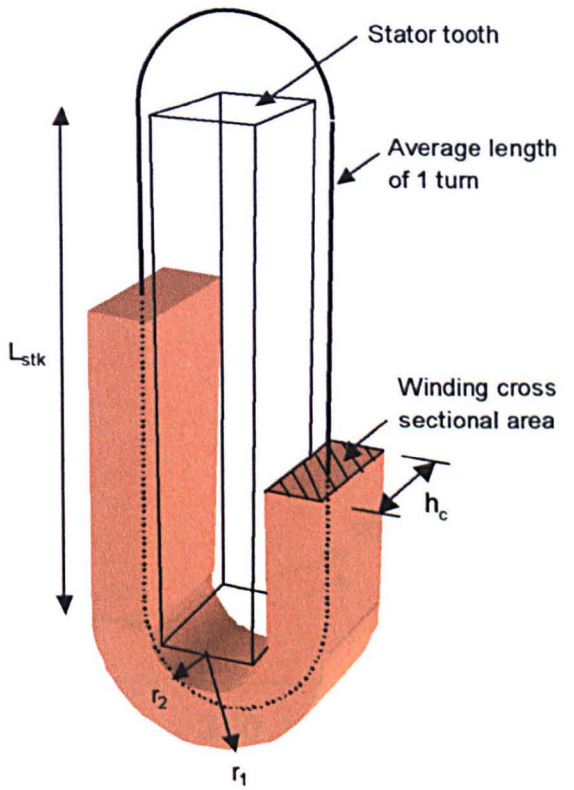

Figure 5.10. Definition of key winding dimensions for the calculation of phase resistance.

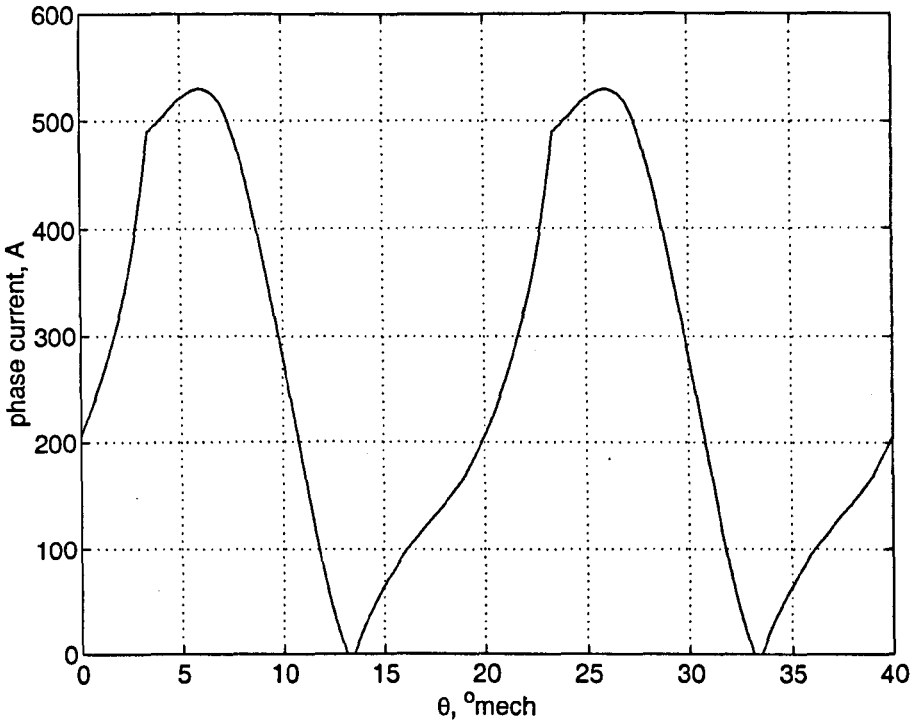

Figure 5.11. Predicted current waveforms for all four phases, showing the large degree of overlap, and almost continuous current required to achieve 100kW at 13500rpm. Vdc = 270v, θ_{on} = 78°, θ_{off} = 258°.

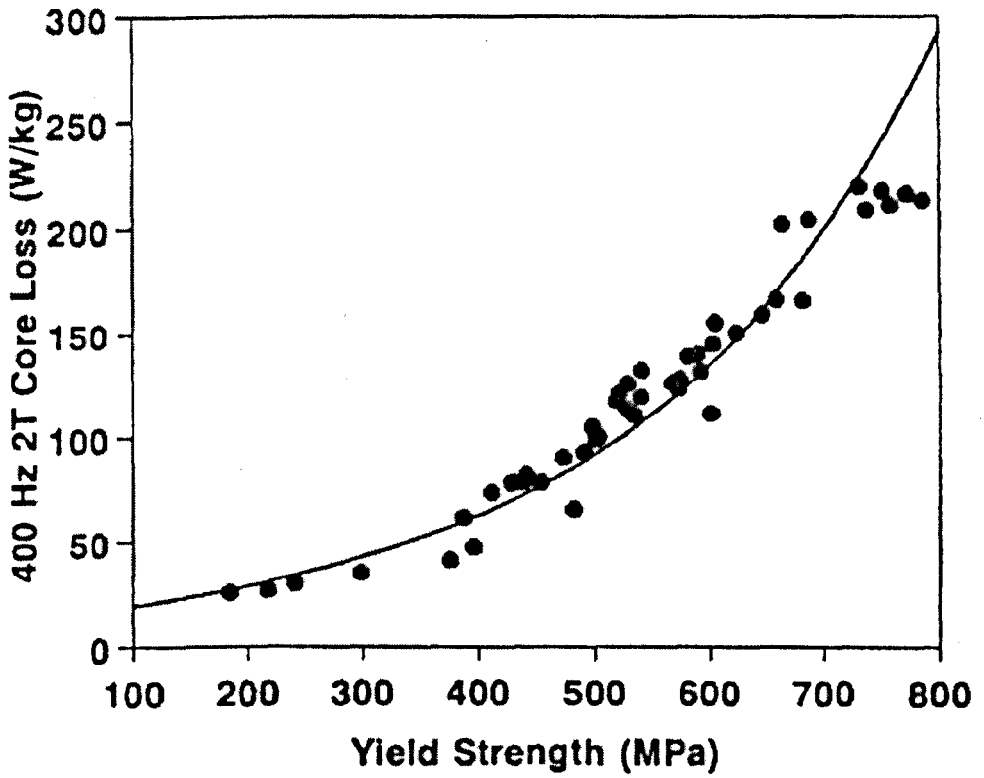

Figure 5.12. Core loss as a function of yield strength in Hiperco 50HS, for sinusoidal flux at 400Hz, 2T. Source: S.D. Masteller [MAS 98].

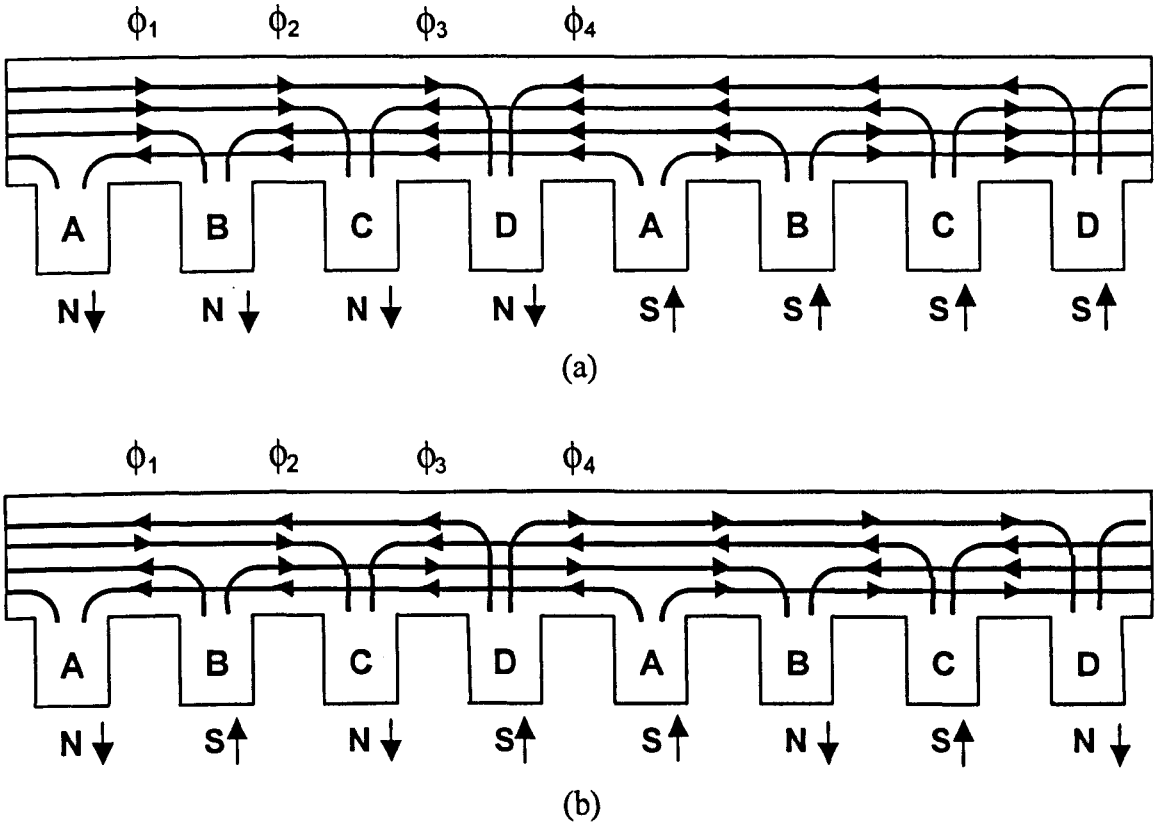

Fig 5.13 (a) Stator iron showing direction of flux paths for a NNNN-SSSS winding connection in a 24-18 SR machine. (b) NSNS-SNSN connection.

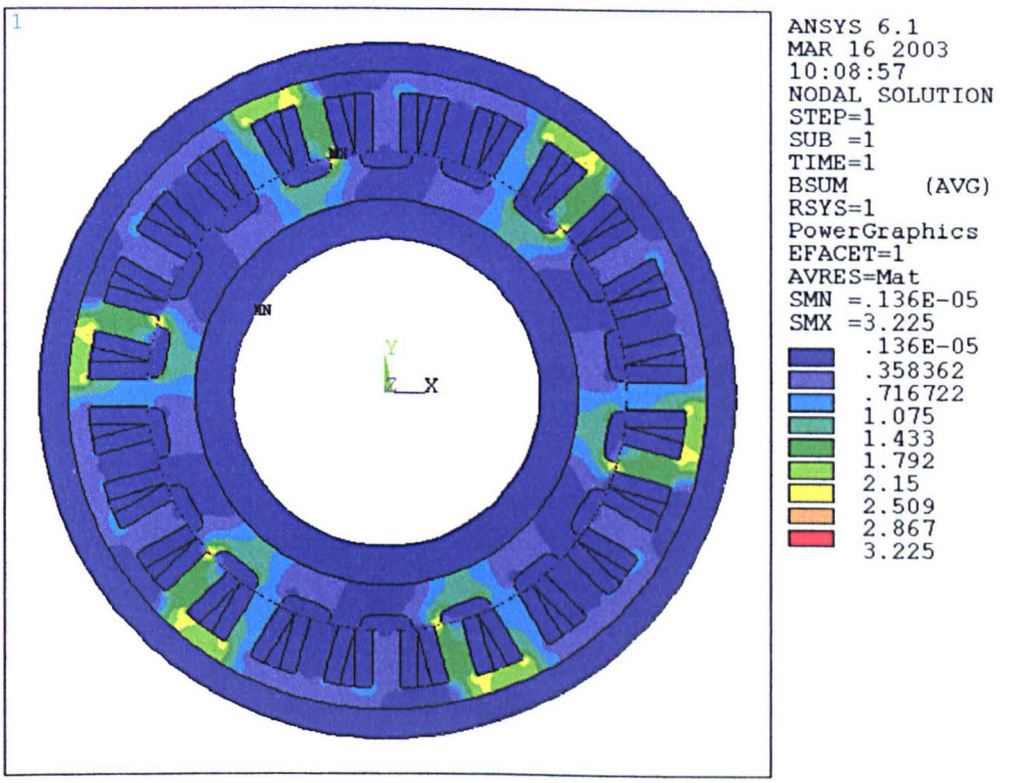

Fig 5.14(a) Flux distribution in the machine in the aligned position for phase A.

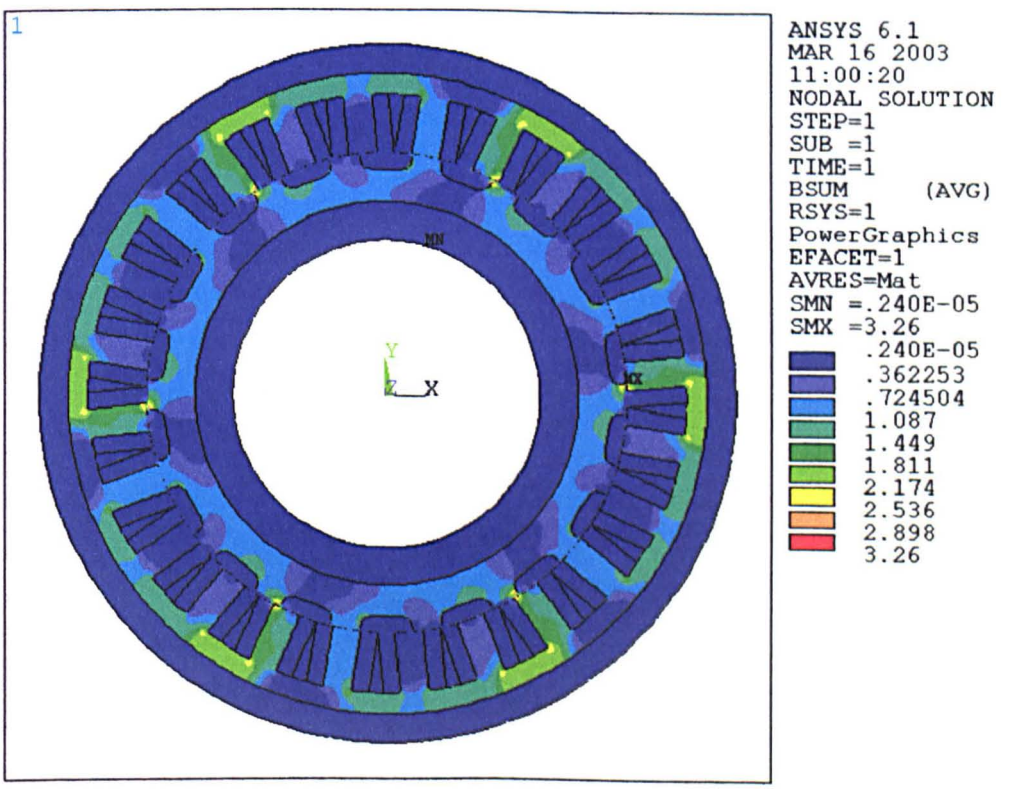

Fig 5.14(b) Flux distribution in the machine at 5.5° clockwise rotation from the aligned position for phase A. (Unaligned position = 10°)

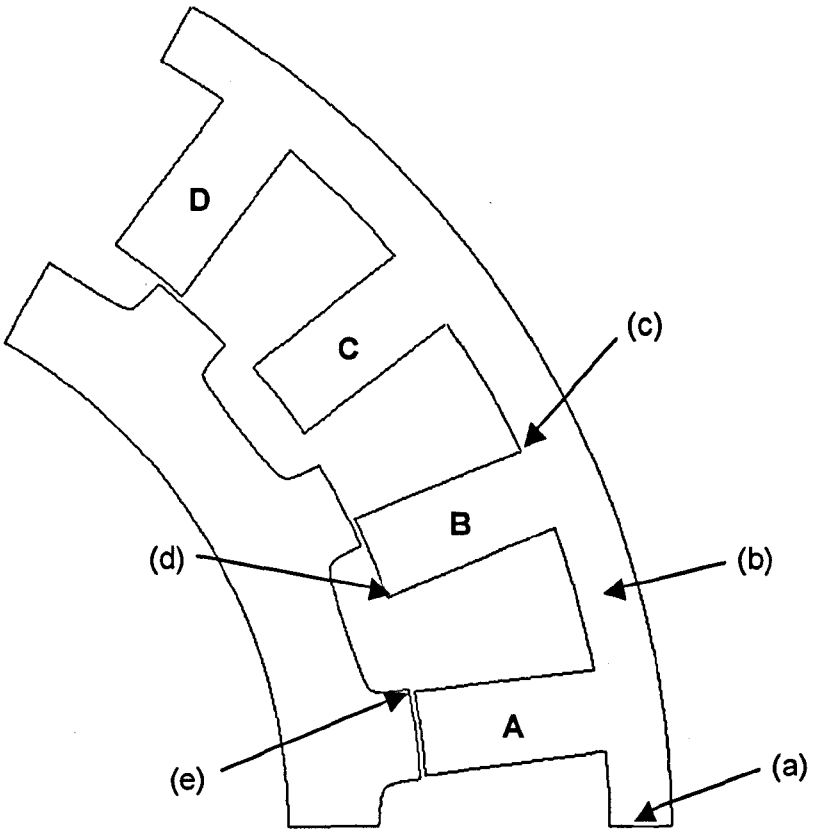

Figure 5.15. Key locations in the stator and rotor for determination of the flux density waveforms shown in figure 5.16.

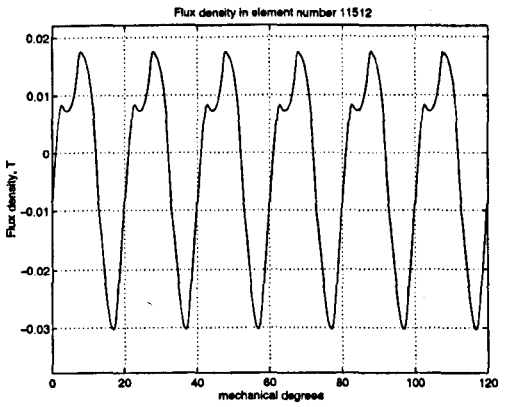

(a)

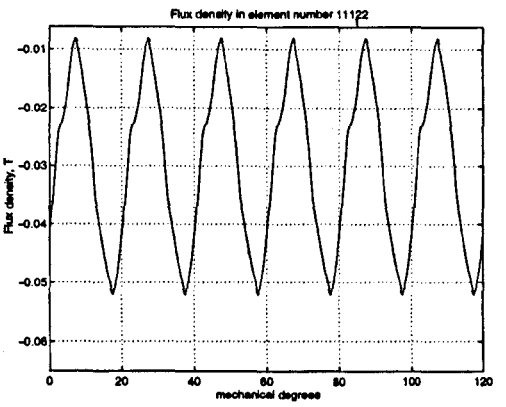

(b)

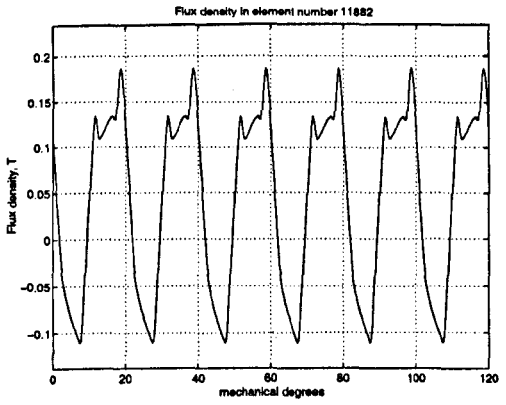

(c)

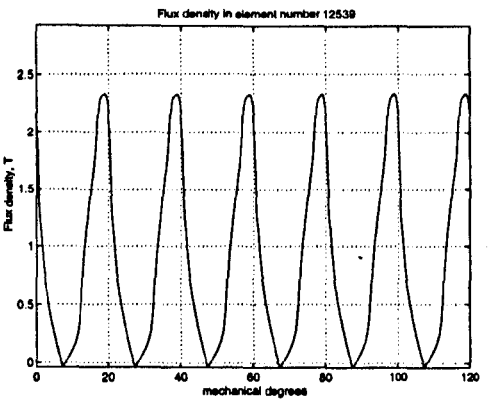

(d)

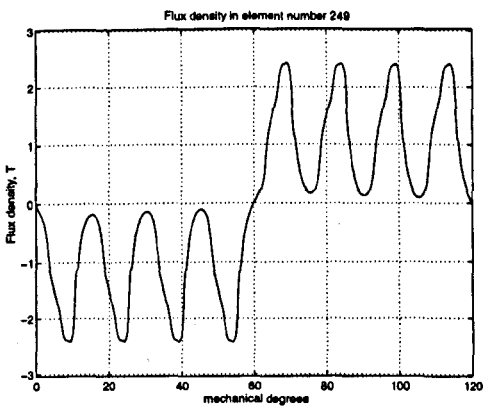

(e)

Figure 5.16. Flux density waveforms at the locations defined in figure 5.15.

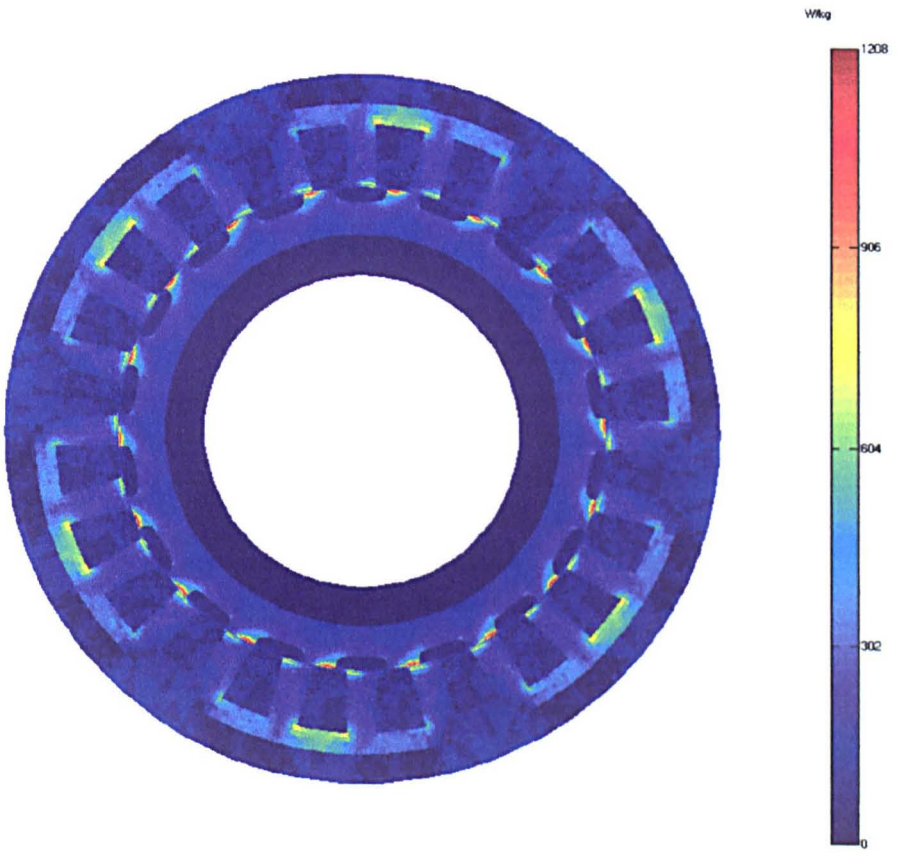

Figure 5.17. Local iron loss density calculated on an element-by-element basis at 13500rpm, 100kW.

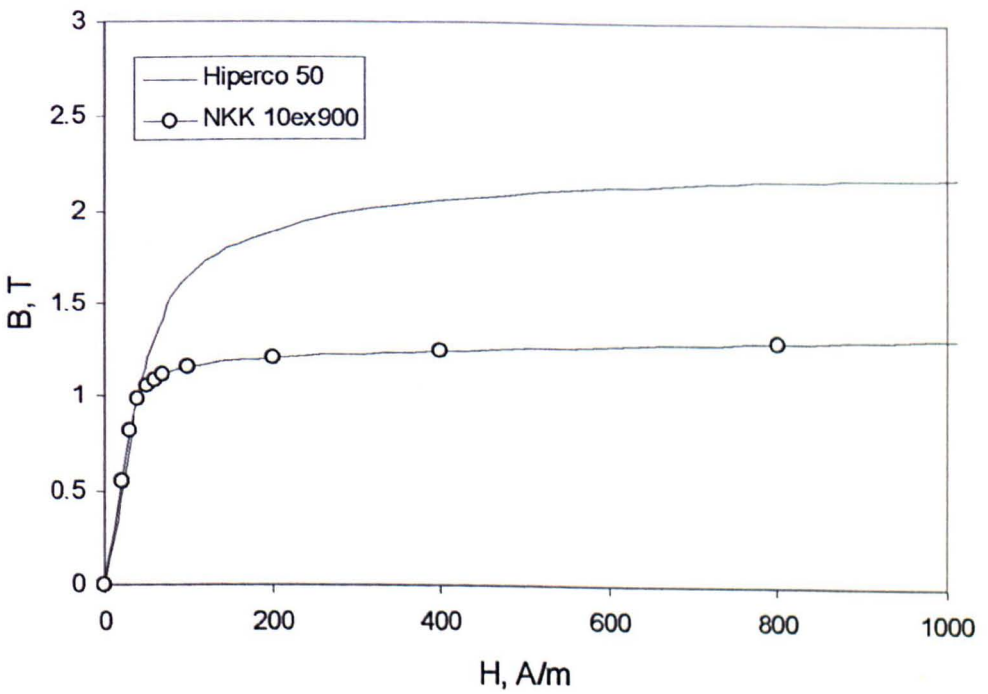

Figure 5.18. Comparison of Hiperco 50 and NKK 10ex900 magnetisation curves.

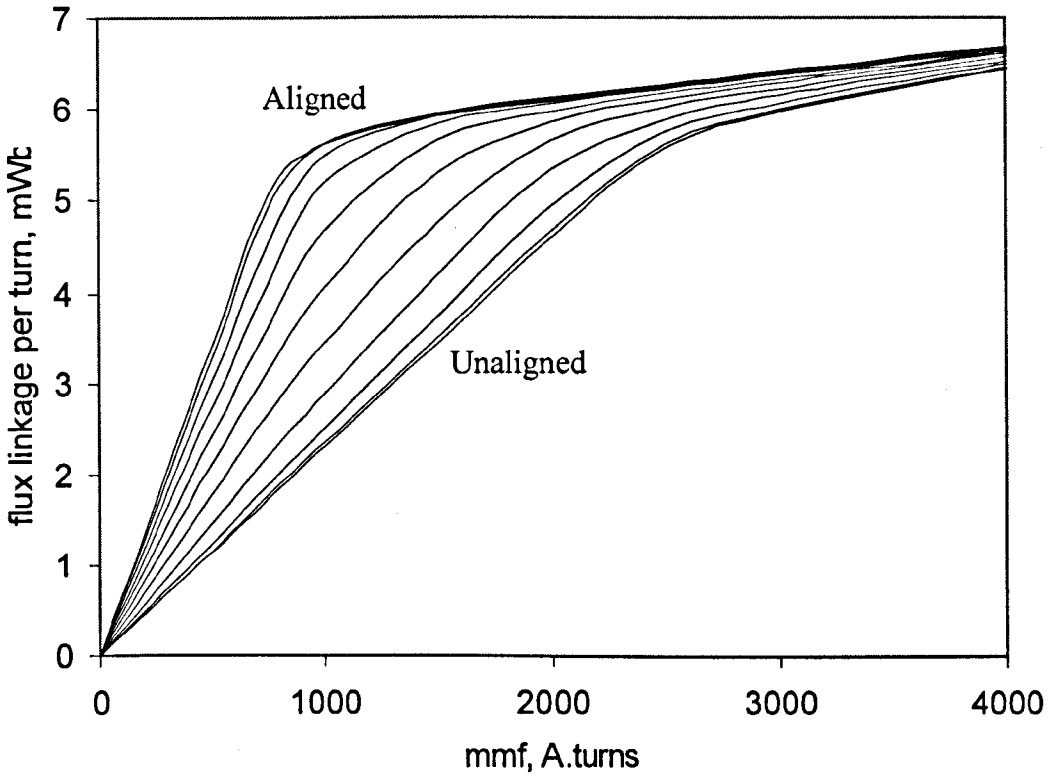

Figure 5.19. Flux linkage characteristics for the full NKK machine derived from three-dimensional FE analysis.

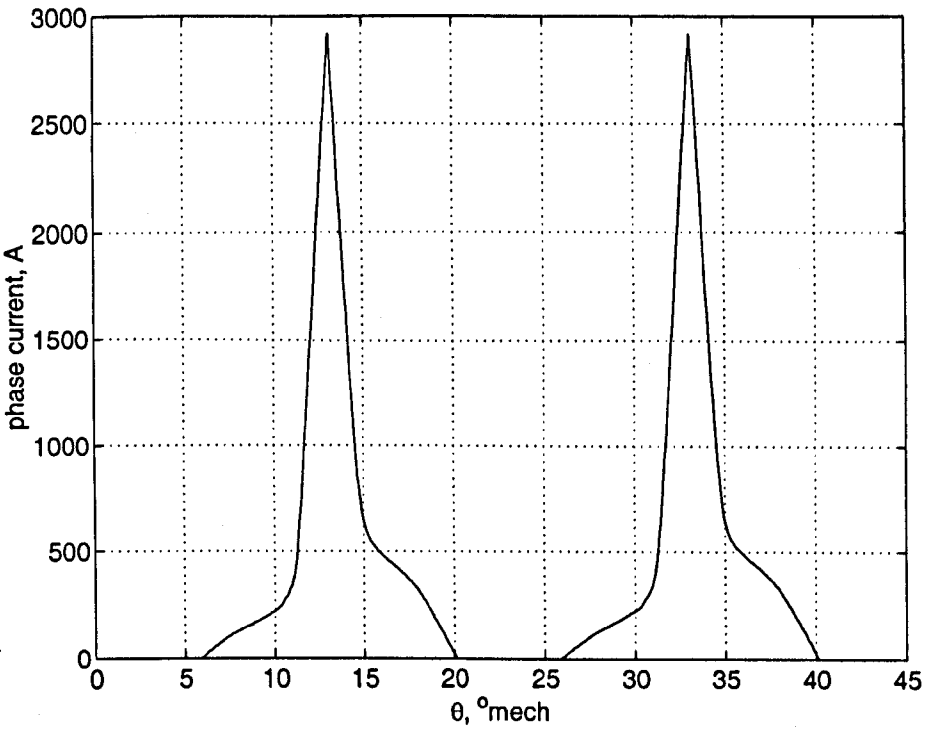

Figure 5.20. Dynamic phase current waveform for the full NKK machine at 13500rpm, 100kW with 3 turns.

CHAPTER 6

THERMAL MODELLING OF THE SWITCHED RELUCTANCE STARTER/GENERATOR

6.1 Introduction

The high-pressure spool of an aircraft-engine provides arguably one of the most hostile environments in which the deployment of electrical machines is being proposed. The potential difficulties posed by the operating environment, particularly the elevated temperature, are compounded by the fact that this application is also extremely demanding in terms of reliability. Many established and well proven electrical machine technologies are incapable of operating at such elevated temperatures, which in turn necessitates the use of materials and processes for which there is often a dearth of data (both quantitative and empirical / historical). Hence, particular attention must be given to minimising any additional thermal stresses on components as a result of excessive internal heat generation and/or poor heat transfer.

As was demonstrated in chapter 5, the HP spool machine is subject to very high levels of internal power dissipation (approx 140 W/kg) as a consequence of the demanding power density (3.6 kW/kg) and operating speed specifications. Given the combination of a harsh temperature environment and the desire for minimal ancillaries for cooling, the thermal behaviour of the machine (particularly over extended periods of operation) is likely to have a significant bearing of the viability of embedding a machine within the engine.

A variety of different cooling strategies are employed in high power density aerospace electrical machines. Such machines require very high specific heat transfer rates, and hence, tend to use either forced oil cooling or oil-spray cooling [RAD97, RIC94]. Indeed existing published design studies on HP spool machines have been based on oil-cooling, although it is recognised that this is unlikely to be a long-term solution since

they require complex ancillary systems comprising filters, pumps and heat-exchangers (which could be either fuel/oil or air/oil), which in turn necessitate demanding and costly maintenance schedules. Hence, in the longer term, forced air cooling is likely to emerge as the preferred option, providing the required heat transfer rates can be achieved. This is particularly the case for the more-electric engine, where a long-term objective is the removal of oil systems from the engine (i.e. the so-called 'oil-less' engine). In a large civil aircraft engine, high-pressure cooling air is readily available via existing bleed ducts in the IP compressor. Figure 6.1a and b show one proposed configuration for an HP spool machine, in which high pressure cooling air is fed into the machine casing. This forced air then flows through a series of circular ducts in the stator frame and via a series of triangular ducts within the stator slots.

An accurate thermal model of the HP spool starter/generator is therefore an essential pre-requisite for assessing its viability and establishing the features that would need to be integrated into an engine to provide the necessary cooling. Moreover, detailed temperature distributions within the machine are essential in order to reliably predict the lifetime of various components (e.g. the high temperature creep behaviour of cobalt iron materials [FIN 02], the premature ageing of insulation materials).

In some respects, the thermal modelling of an SR machine located on the HP spool has many features in common with the modelling of the BLDC machine in the EHA, which was described in chapter 2. However, the external environment, in particular the degree to which purpose-designed forced cooling features will be employed has yet to be established for the more-electric engine. Although some useful data can be garnered from temperatures and air flow-rate data measured on conventional engines, these only provide typical ambient temperature values. Moreover, the detailed architecture of an electric engine has yet to be definitively specified. Hence, in the absence of a well defined description of the operating environment, the approach adopted in this chapter is based on modelling internal heat transfer within the machine using the loss data generated in chapter 5 in order to establish the likely external cooling requirements. This in turn will provide quantitative data to assess the feasibility of air-cooling an

embedded machine on a HP spool and provide an initial design specification for a cooling system. Although the external environment in which the electrical machine resides is greatly simplified (in effect it is represented by a few lumped thermal resistances), it provides a convenient means of establishing the sensitivity of the machine performance to the external cooling, and hence a quantitative means by which the trade-offs between electrical machine power density and cooling requirements can be determined.

6.2 Thermal properties of the HP spool machine

The maximum ambient temperature encountered in the region between the IP and HP compressors of a typical large three-spool turbo-fan engine is ~350°C, while the available cooling air is at 300°C and ~8 bar. For the purposes of the design synthesis described in Chapter 4, it was assumed that the combination of losses and cooling strategy would result in a bulk operating temperature in the machine of ~400°C. Although this approach provided a basis for establishing the mechanical constraints of the rotor, an improved calculation of internal temperatures within the stator and rotor is required to establish the properties and the integrity of the materials. In the case of the soft magnetic materials, although Hiperco 50HS exhibits useful saturation flux density levels at operating temperatures up to 500°C [FIN 02] there is a degree of aging if the temperature is maintained beyond 450°C for a significant period of time. By way of example, the Hiperco 50HS alloy considered for the rotor has been shown by Li to be relatively unstable at operating temperatures of 500°C in terms of its magnetic properties, showing an irreversible increase in coercivity of 34% after 2000 hours aging in an argon atmosphere with little sign of reaching a plateau; thus raising obvious concerns over its long term stability [LI 96]. The resulting increase in total iron loss at 400°C for 1.8T and 1kHZ excitation is 49% and 21% for Hiperco 50HS and Hiperco 50 respectively. Consequently, the effects of aging at high temperatures may result in higher temperatures in the machine after long periods of operating time, causing the soft iron material to become 'harder' magnetically, and may eventually result in excessive temperature rises after long periods of service.

The high temperatures which are likely to be encountered within the slot preclude the use of conventional polymeric insulation systems such as Polyimide based materials which have a maximum continuous temperature rating of 240°C, fibre based slot lining materials such as Nomex 410 (typically 180°C) and epoxy potting compounds such as Stycast® 2850 (max. 200°C). For example, un-encapsulated copper windings are susceptible to corrosion over a temperature of ~350°C, and must therefore either be adequately shielded from the ambient environment using an appropriate high temperature ceramic encapsulant, or manufactured from nickel clad copper. One candidate material that could be used for lining the slots in a high temperature machine is Aluminium Nitride. This ceramic is widely used in the electronics packaging industry, by virtue of its combination of a high thermal conductivity (170W/mK - c.f 0.15 W/mK for Nomex 410 slot liner material) and excellent electrical insulation properties (volume electrical resistivity in excess of $1x10^{15}\Omega m$ and dielectric strength of 40kV/mm). It is capable of stable operation in temperatures up to 700°C with minimal change in electrical, mechanical or thermal properties. Moreover, it can be readily machined, albeit that very thin sections can pose manufacturing problems because of their inherent brittleness.

6.3 Thermal model

In order to predict internal temperatures within the SR machine, a lumped parameter thermal network was developed, using a similar approach to that described in chapter 2 for the BLDC machine. In defining the problem domain for the thermal model it is useful to consider the likely extent of the heat transfer between the stator and rotor across the airgap. Given the high axial air flow rates through the airgap which are likely to be required to cater for the high specific dissipation, the radial convection heat transfer is likely to be very small in comparison with the heat transfer to the cooling air. Hence, the thermal models of the stator and rotor can be de-coupled and analysed separately.

In order to establish the cooling requirements using the thermal model of the stator, the frame of the machine was assigned an effective heat transfer coefficient to ambient. A

series of solutions were then performed for progressively increasing values of this heat transfer coefficient.

As demonstrated by the predicted iron loss contours shown previously in figure 5.17, for a 'NNNN-SSSS' winding arrangement, the iron loss is periodic over an 8 pole section of the stator and over one pole pitch of the rotor. This periodicity can be exploited to reduce the thermal model to a 60° section of the stator and a 20° section of the rotor. It is worth noting that this reduction in the problem domain is based on the assumption that the heat transfer from the frame is dominated by forced air cooling rather than buoyancy effects (which vary between successive 60° sections).

Figure 6.2(a) shows the stator region that is represented in the thermal model. It comprises 8 half tooth-pitch sections (labelled 1 to 8), with zero heat flux boundaries applied on faces P and Q. Each of the sections of the stator lamination is further divided into 4 sub-regions (labelled B-E in figure 6.2(b)). This level of discretisation was selected as it provides a practicable balance between network complexity and catering for the significant variation in loss density within the stator lamination. Within each of these 4 sub-regions, a mean loss is calculated by integrating the loss of each individual finite element within that region. The copper loss is equal for each coil and is uniformly distributed over the cross-section of the coil (labelled as region A in figure 6.2(b)).

The stator slot liner of the thermal model is based on representing the actual Aluminium Nitride slot inserts by their bulk thermal properties together with the same thermal contact resistances as were used for the Nomex slot liner described in chapter 2 (although it is recognised that the high precision to which an Aluminium insert can be machined may result in the contact resistance at slot insert / stack interface being lower in practice). It is interesting to note that by virtue of its high thermal conductivity, the thickness of an Aluminium Nitride slot liner only has a marginal effect on the net thermal resistance between the winding and stack, since this is dominated by the contact coefficients.

Figure 6.2(c) shows a simplified equivalent network for section 4 of the stator lamination, in which various thermal resistances have been combined for the purposes of aiding clarity. The networks for each successive section of the stator are simply connected by means of circumferential nodes that allow heat transfer between sections. The equivalent thermal resistance values for the network of figure 6.2(c) are derived using the same approach as that described in chapter 2 for the stator of the BLDC machine in the EHA, and indeed there is much commonality between many elements of both models. A detailed network diagram for the SR machine stator thermal model, together with a table of values for the various thermal resistances and loss sources are contained in Appendix C.

The regions employed to discretise a 20° section of the rotor are shown in figure 6.3(a), with the corresponding thermal network shown in figure 6.3(b). Zero heat flux boundaries are applied at faces X and Y, while face Z is assumed to be at a constant temperature of 350°C, since the large HP shaft can be reasonably approximated as having a fixed temperature with respect to any variation in the heat dissipated in the machine (although it is important to recognise that it may vary to some degree with changes in ambient environment and/or the duty cycle of the engine). The outer surface of the rotor is subject to a degree of forced convection heat transfer due to a combination of its own rotation and the axial flow of cooling air. This is represented in the thermal model by a lumped equivalent thermal resistance R_{rot}.

Rotor aerodynamic losses will inevitably influence the heat transfer in the airgap region. The nature of air-flow due to rotation in the airgap of an SR machine is extremely complex as a result of the highly salient structure of the rotor. It has been demonstrated by Yamada [YAM 62] that standard expressions for rotating cylinders are of little utility for SR machines. The complex interaction of tangential and axial flows in a 4-pole SR rotor has been studied by Calverley using a three-dimensional computational fluid dynamics model [CAL 00]. However, this technique is computationally very expensive, and requires detailed knowledge of the flow path entering and leaving the rotor air space, and of the axial pressure differential. Given the complex nature of the flow in the

end-regions of the machine, and its comparatively short axial length (which will give rise to significant entry and exit effects), an accurate calculation of rotor losses and the degree to which these losses enter the rotor and stator rather than being removed by the cooling air was deemed to be outside the scope of this thesis. It was therefore assumed that the cooling strategy that would ultimately be employed in a practical machine would be specified such that the aerodynamic rotor losses would not cause a discernable rise in the rotor and stator temperature, and hence could be neglected in the models of heat transfer.

6.4 Procedure for determining cooling requirements

The equivalent thermal network of the stator was initially employed to model heat transfer for the particular case in which forced air cooling from the IP compressor (which is at 300°C) was applied to the stator frame only. In this case, the thermal resistance R_{wdg} in figure 6.2(c) was assumed to be infinite, i.e. the heat transfer within the slot region was assumed to be solely a result of conduction into the stator and the frame. The effective thermal resistance due to forced air cooling of the frame, i.e. R_{fr} in figure 6.2(c), was assigned a series of values between 0.017 K/W and 2.33 K/W. Figure 6.4 shows the calculated variation in the maximum temperature of the winding and back iron for values of R_{fr} up to 2.33 K/W, for the particular operating point of 100kW at 13,500rpm (the total copper and stator iron losses being 1710W and 1560W respectively). It can also be seen from figure 6.4 that a limiting value of temperature is achieved by setting a value for R_{fr} of 0.005 K/W (which in effect is equivalent to an infinite heat sink with respect to the internal thermal resistances). The maximum winding temperature approaches an asymptotic value of ~570°C for this condition, as the heat transfer capability from the frame is continually increased. Thus, additional direct cooling of the windings is necessary if the maximum winding temperature is to be limited to more acceptable levels, i.e. ~400°C. In order to quantify the benefits of direct forced cooling of the winding, the heat transfer was calculated at the same 100kW, 13500rpm operating points for all inclusive combinations of R_{fr} between 0.017 and 2.3 K/W and R_{wdg} values between 0.6 and 31 K/W. The resulting variation in the maximum winding temperature as a function of R_{fr} and R_{wdg} is shown in the contour plot of fig 6.5.

It is apparent from figure 6.5 that various combinations of R_{fr} and R_{wdg} will result in a winding temperature of ~400°C, although many of these combinations may not be achievable in practice for forced air cooling. In selecting the most suitable combination of thermal resistances from figure 6.5, it is important to recognise that the area available for heat transfer from the winding is highly constrained whereas, within limits, the number of ducts in the stator frame can be increased to provide the desired effective area. In practice, the ease with which air can be forced into the winding and frame ducts will influence the best combination from figure 6.5. By way of illustration, from the point of view of minimising the overall cooling requirements, the best balance would arguably be achieved by selecting a combination of thermal resistances on the basis that they require the same heat transfer coefficient (i.e. the same heat transfer per unit area) in both the stator frame and the winding slots. Using this criterion, it is necessary to achieve a heat transfer coefficient of ~110W/m^{2}K in both regions to limit the maximum winding temperature to ~400°C (which in turn corresponds to a required stator frame duct surface area of 0.056m^2, and hence values of R_{fr} and R_{wdg} of 0.75 K/W as shown in figure 6.5). In order to minimise the overall mass of the HP-spool machine, a relatively thin frame would be desirable. This in turn favours the use of a relatively large number of ducts of small cross-section. Assuming that a frame thickness of ~10mm would be sufficient for mechanical purposes, then one possible duct arrangement would be a series of 48 circular ducts having a diameter of 7.5mm.

Although a value of heat transfer coefficient of 110W/m^{2}K lies within the range of values that have been achieved in practice for some high performance forced air cooling schemes [SARI 95], it is important to consider the mass flow rates required, and the subsequent aerodynamic losses associated with the cooling air for the particular ducts shown in figure 6.1. Indeed, 'cooling losses' can result in the benefits that are accrued by increasing the mass flow being gained at a much diminished rate of return, and indeed may ultimately cause the net heat transfer to decrease.

The mass flow rate required to achieve a given heat transfer coefficient through a particular cooling duct can be estimated from published correlation equations for fully

developed turbulent flow in ducts [GNI 76] In the case of the winding duct, the effective cross-section of the duct is assumed to be the area A_{wdg} in figure 6.6(a). The flow within the duct is assumed to be fully developed and uniform along its entire length (i.e. there are no entry or exit effects), which is a reasonable approximation given that the flow is likely to be highly turbulent on entry after flowing through the external ducting and across the end windings. Therefore, the Nusselt number required to achieve a specified heat transfer coefficient can be calculated from:

$$Nu = \frac{h D_h}{k} \tag{6.1}$$

where D_h is the effective hydraulic diameter of the duct, and can be approximated in the case of a triangular duct as: [CAR 61]

$$D_h = \frac{L_t \sin 2\phi}{1+\sin\phi} \tag{6.2}$$

where the angle 2ϕ and the length L_t are defined in figure 6.6(a). The corresponding axial Reynolds number can then be evaluated by rearranging the heat transfer equation for turbulent flow in a duct, i.e.

$$Nu = 0.0214\left(\mathrm{Re}^{0.8} - 100\right)\mathrm{Pr}^{0.4} \tag{6.3}$$

where Pr is the dimensionless Prandtl number and is given by:

$$\mathrm{Pr} = \frac{C_p \mu}{k} \tag{6.4}$$

where C_p is the specific heat of air at constant pressure, μ is the dynamic viscosity, and k the thermal conductivity of air. In order to calculate heat transfer within the duct, the physical properties of air were evaluated at 400°C. Given an estimate of the Reynolds number required, the corresponding mean axial velocity, U, can then be calculated for the given hydraulic diameter

$$U = \frac{\mathrm{Re}\nu}{D_h} \tag{6.5}$$

where ν is the kinematic viscosity of air at 400°C. This axial velocity can be related to the mass flow rate by:

$$m = \rho U A_{wdg} \tag{6.6}$$

where ρ is the density of air at 400°C. By using equations 6.1 to 6.6, for the particular case of air at 400°C, the mass flow rate required to achieve a heat transfer coefficient of 110 W/m^2K in the winding duct is $1.9e^{-3}$ kg/s. The resulting cooling losses that are generated by this flow rate can be estimated from standard expressions for pressure drops in ducts. Standard expressions for circular ducts can be corrected for non-circular ducts by using shape factors such as those measured by Carlson and Irvine [CAR 61] for triangular ducts. For the particular triangular duct geometry employed in the stator winding (i.e. $2\phi = 15°$), the shape factor, f_s, is 0.865 (c.f. 1.0 for a circular duct). The corresponding friction factor, f can then be determined by scaling the Reynolds number with respect to the shape factor:

$$f = \frac{16}{\mathrm{Re}} f_s \tag{6.7}$$

The corresponding pressure drop is evaluated from

$$\Delta P = L\left(\frac{4f}{D_h}\right)\frac{1}{2}\rho U^2 \tag{6.8}$$

and hence, the power loss associated with this pressure drop is given by

$$P_f = \Delta P m \tag{6.9}$$

Figure 6.7 shows the predicted variations in heat transfer as a function of mass flow

rate, both with and without allowance for the pressure drop. It can be seen from figure 6.7 that for the required mass flow rate of 0.0019 kg/s in the winding duct, there is negligible reduction in the effective heat transfer from the winding to the air as a result of parasitic friction losses.

The mass flow rate through the frame cooling ducts is calculated using the same method as for the winding ducts, albeit with circular ducts, while mass flow rate over the end windings is calculated from correlating equations for turbulent flow over a flat plate considering the areas 2 and 3 in figure 6.6(b) [INC 90]. The total mass flow required through the machine to maintain a 400°C operating temperature, for the most arduous ambient conditions and highest values of iron loss is therefore 0.28 kg/s. It is useful to compare this value with mass flow rates that are envisaged for the more electric engine. A typical large 3-spool aero-engine can supply up to ~1% of the main engine airflow for bleed air purposes, which equates to approximately 1 kg/s at a maximum air temperature of 300°C. Hence, a significant proportion of the available bleed air from the IP compressor (which also has to perform various other functions such as climate control) would be required to cool the HP spool machine.

Whereas the thermal model predicts that the existing machine design can be cooled with acceptable levels of mass flow rate, it is interesting to consider the degree to which the cooling requirements (i.e. the mass flow rate) can be alleviated by increasing the size of the machine, specifically by increasing the depth of the stator slots. An increased slot depth will yield two benefits, viz. a reduced copper loss for a given total ampere turns per slot and an increasing cooling area, and need not necessarily compromise the electromagnetic torque capability. The relative insensitivity of the torque capability to variations in slot depth is shown in figure 6.8 which shows a comparison between un-aligned and aligned flux-linkage characteristics (predicted from 2D magneto-static finite element analysis) for the original machine design and a design with essentially the same parameters but 50% deeper stator slots, i.e. 31mm and 46mm deep slots respectively.

Although increasing the slot depth reduces the copper loss and increases the surface area available for heat transfer (albeit at the expense of an increased mass), the larger

cross-sectional area of the triangular duct dictates that a lower air velocity will exist for a given mass flow rate, hence reducing the turbulent heat transfer per unit area from the winding. In order to investigate the influence of winding duct geometry on heat transfer, the mass flow required to limit the winding temperature to 400°C was calculated for increased slot depths for an operating point of 100kW at 13,500rpm. As was demonstrated in figure 6.4, direct forced air cooling of the winding is responsible for ~90% of the heat transferred from the winding (the remainder being conducted into the frame). Hence a reasonable approximation as to mass flow required for increasing slot depths can be derived by neglecting conducted heat transfer. The resulting heat transfer coefficients required to maintain the winding temperature at 400°C is shown in figure 6.9 for slot depths between 31mm and 61mm, while the corresponding increase in the available duct area is shown in figure 6.10. Equations 6.1 to 6.6 have been employed to calculate the mass flow rate required in these ducts to achieve the desired heat transfer coefficient. The predicted variations in the copper loss and required mass flow rate as a function of slot depths between 31mm and 61mm are shown in figures 6.11 and 6.12 respectively. The corresponding increase in overall mass and stator outer diameter of the machine as a function of slot depth are shown in figure 6.13 and 6.14 respectively.

It is interesting to note from figure 6.12, that the mass flow rate required does not reduce proportionally with the reduction in copper loss for increasing slot depth, since little cooling is provided by air-flow in the centre of the duct (the cross-section of which increases with the square of the slot depth). Hence, the required mass flow rate could be reduced significantly from the value shown in figure 6.12 without unduly affecting the velocity on the cooling surface by locating a triangular flow restrictor in the centre of the slot, although the pressure drop will inevitably increase. In this regard, it is worth noting that as shown by figure 6.7, there remains a considerable remaining margin for increasing the pressure drop.

Another key operating condition that will have a marked influence on temperature rise within the machine is its thermal behaviour during the starting of the engine, where the copper loss is 11.98kW. The transient thermal model of the stator shown previously in figure 6.2(c) was used to calculate the transient temperature rise in the machine. It was

assumed that the iron loss was negligible in comparison with respect to the copper loss, and that no cooling was available. As a worst case condition, it was assumed no cooling air is provided by the IP compressor during the starting phase, and that heat loss from the machine is solely a result of natural convection from the frame. The transient thermal response of the machine was predicted for two starting temperature, viz. 25°C and 70°C, the latter corresponding to the worst case ground conditions. The resulting variations in the winding temperature for these two starting conditions are shown in figure 6.15. As is evident, the stator winding and its immediate environment has sufficient thermal capacity to sustain this large copper loss for a period of some 90 seconds before the winding temperature reaches 400°C. This is likely to be sufficient for a typical starting cycle, which typically has a duration of 30-60 seconds. Moreover, some bleed air for cooling will be available during this interval.

6.5 References

[CAL 00] S.D. Calverley, G.W Jewell, R.J Saunders, 'Aerodynamic Losses in Switched Reluctance Machines', IEE Proceedings - Electric Power Applications, Vol 147, No.6, 2000, pp 443-448

[CAR 61] L.W. Carlson, T.F. Irvine. 'Fully developed pressure drop in triangular shaped ducts.' Transactoins of the ASME, Series C, Vol. 83, pp 441-444.

[FIN 02] R.T. Fingers, R.P. Carr, Z. Turgut. 'Effect of aging on magnetic properties of Hiperco 27, Hiperco 50, and Hiperco 50 HS alloys.' Journal of Applied Physics, Vol. 91, No. 10. 15th May 2002.

[GNI 76] V. Gnielinski. 'New equations for heat and mass transfer in turbulent pipe and channel flow.' International Chemical Engineering, Vol.16, 1976, pp. 359-368.

[INC 90] F.P. Incropera, D.P. Dewitt. 'Introduction to heat transfer.' 2nd Edition. John Wiley and sons Ltd, 1990.

[LI 96] L. Li. 'High temperature magnetic properties of 49%Co-2%V-Fe alloy.' Journal of Applied Physics, Vol. 79, No. 8, April 1996.

[RAD 97] A.V Radun, C.A Ferreira, E.Richter, 'Two channel switched-reluctance starter / generator results', IEEE Transactions on Industry Applications, Vol. 34, No. 5, 1997, pp.1026-1034.

[RIC 94] E. Richter, A.V Radun, C.Ferreira, Ruckstadter, 'An integrated electrical starter/generator system for a gas turbine application, design and test results, Proceedings of ICEM 1994, Vol. 3, pp. 286-291.

[SARI 95] J. Saari, 'Thermal modelling of high-speed induction machines', PhD Thesis, Acta Polytechnic Scandinavica, Helsinki, 1995.

[YAM 62] Y. Yamada, 'Torque resistance of a flow between rotating co-axial cylinders having axial flow, Bulletin of JSME, Vol.5, No.20, 1962, pp.634-642.

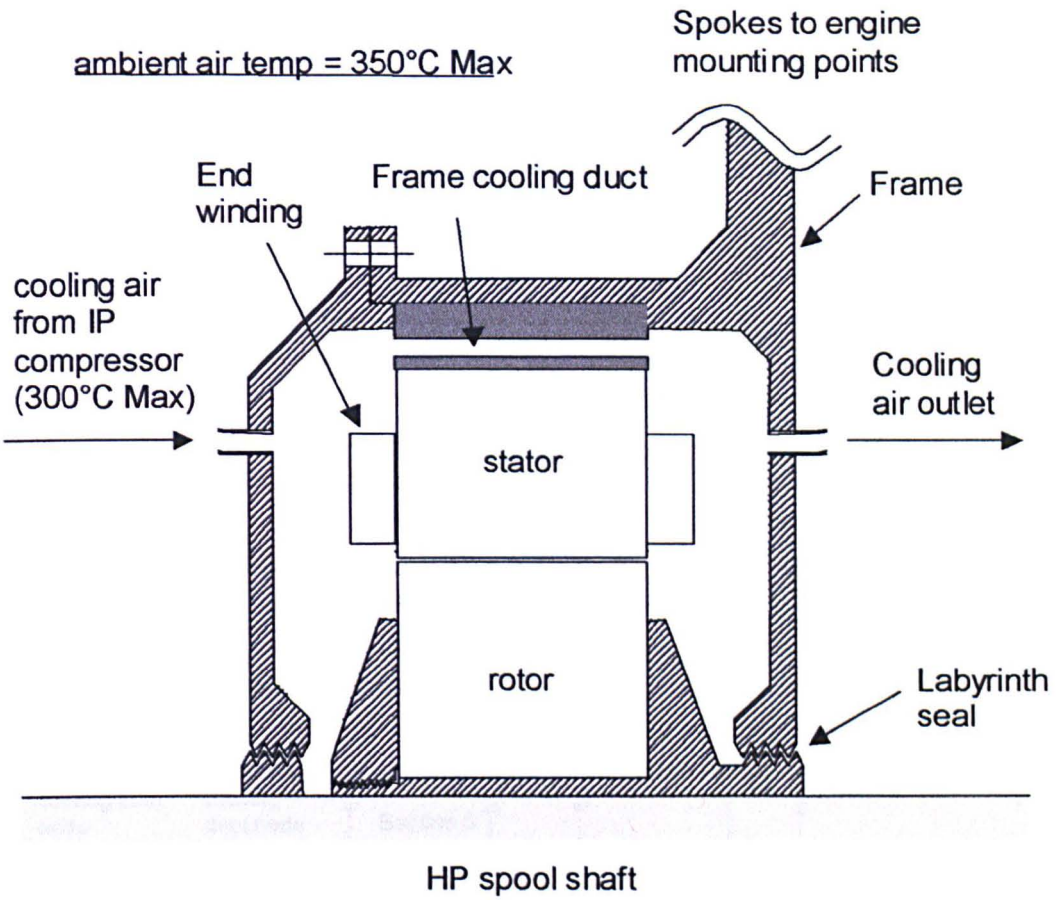

Fig 6.1a. Axial cross-sectional view of potential air-cooling for HP machine.

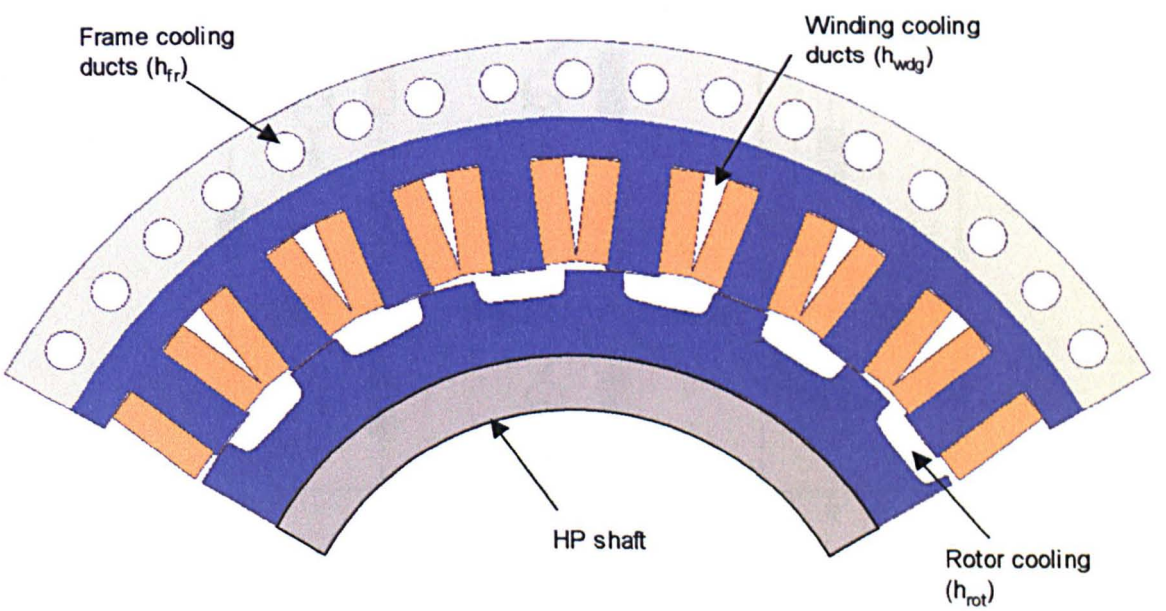

Fig 6.1b. Machine cross-section showing the location of axial cooling ducts through the stator windings and frame.

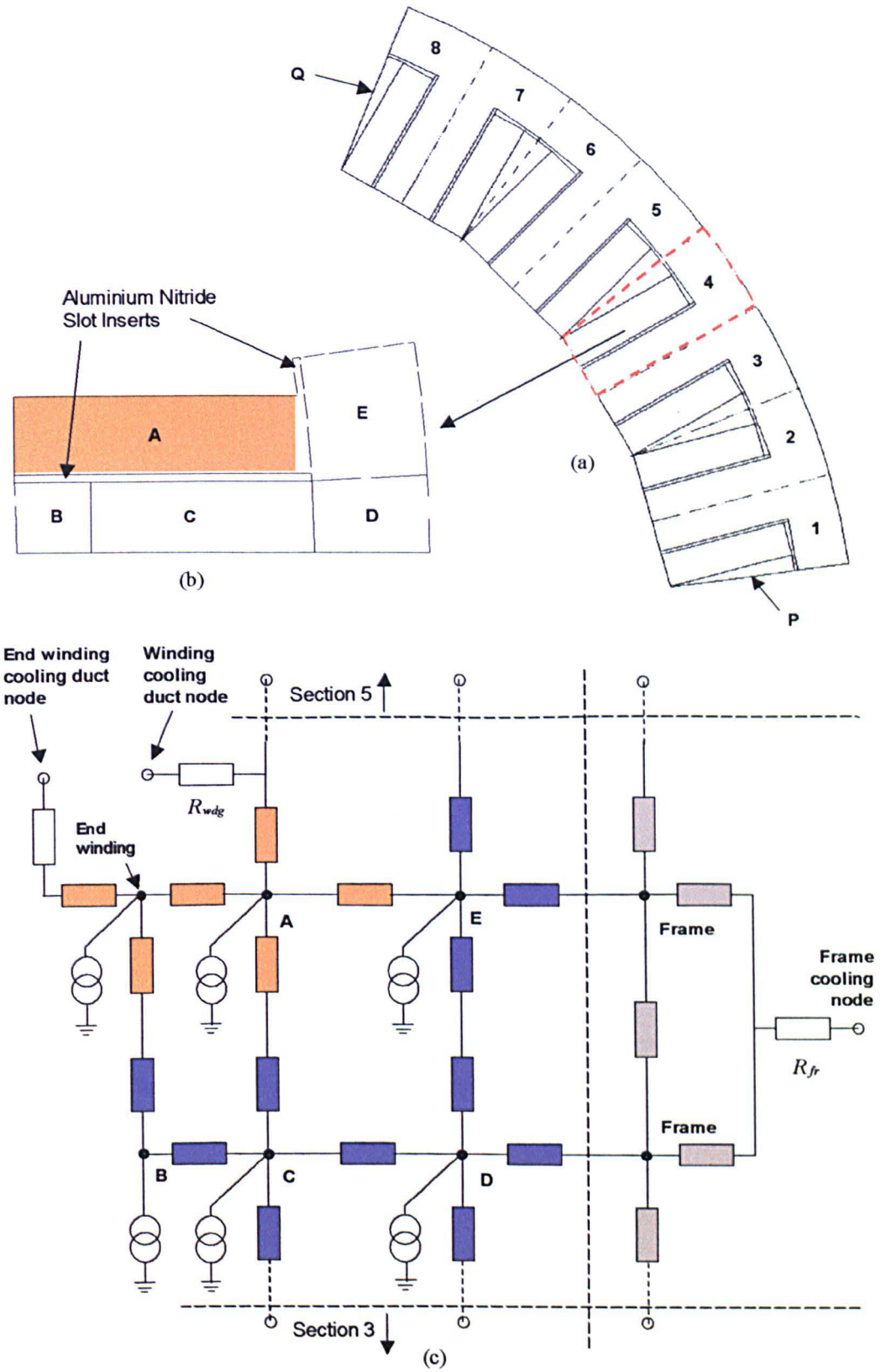

Fig. 6.2(a) SR machine stator sector considered in the thermal model comprising 8 sections. (b) Subdivision of the section into A: winding, B: tooth tip, C: tooth body, D and E: back iron. (c) Simplified circuit diagram of section 4, showing connection to the frame and interconnecting nodes between adjacent sections 3 and 5.

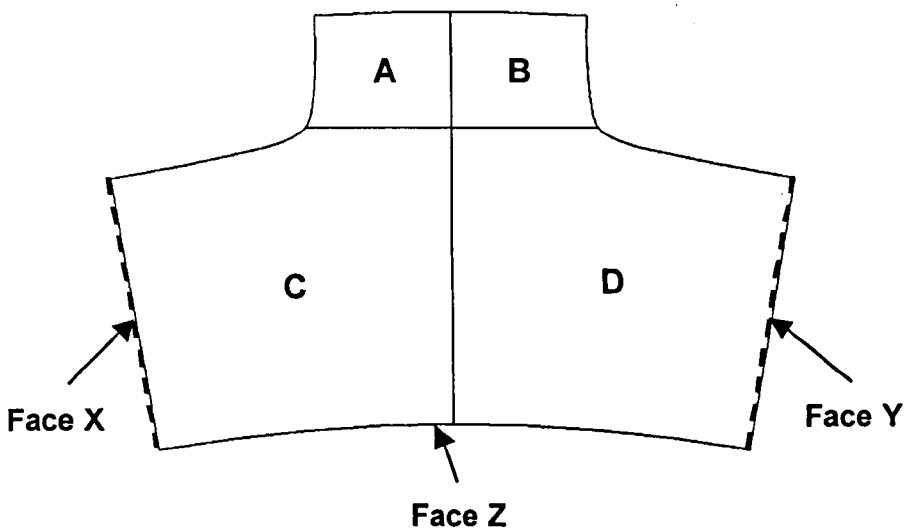

Figure 6.3(a). Rotor discretisation for the thermal model, considering regions A, B, C and D of 1 tooth pitch. Faces X and Y are cyclic boundary conditions (zero heat flux), whilst Face Z is maintained at a constant temperature of 350°C.

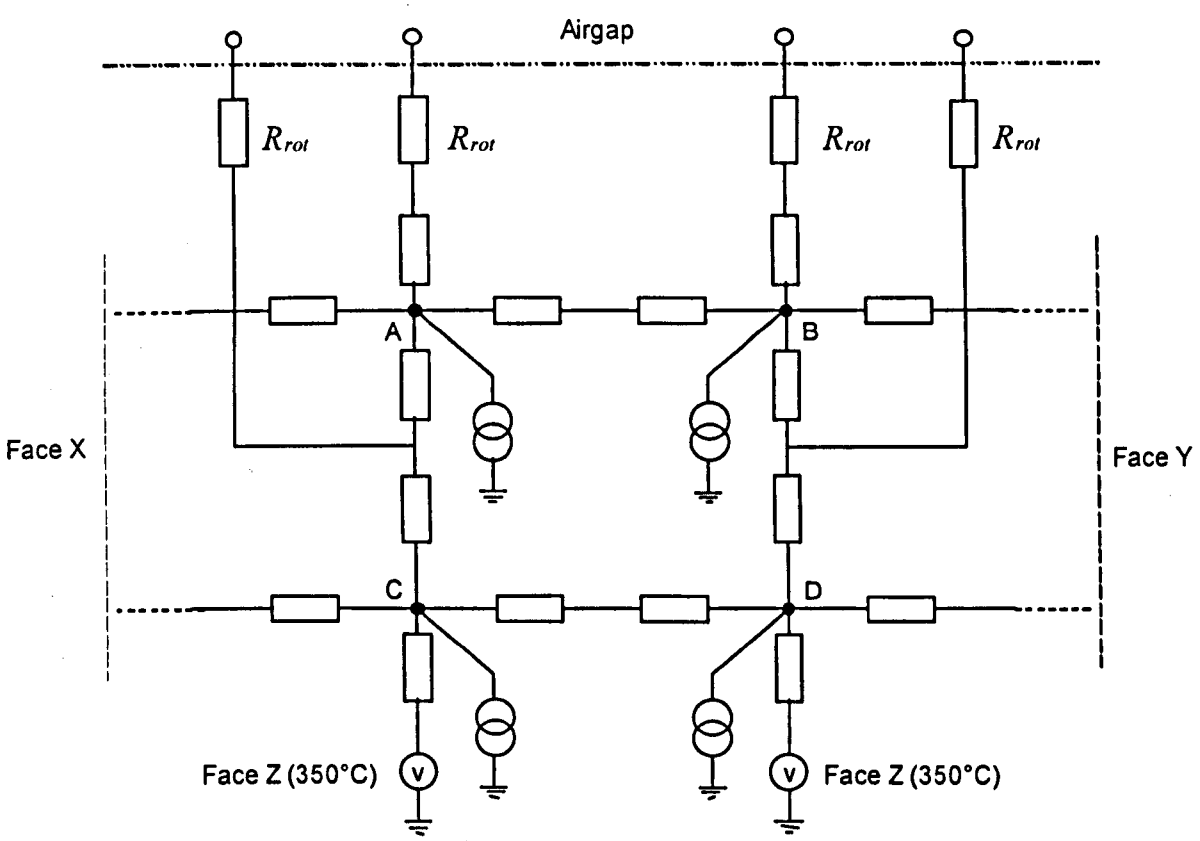

Figure 6.3(b). Thermal network of the rotor section considered in figure 6.3(a).

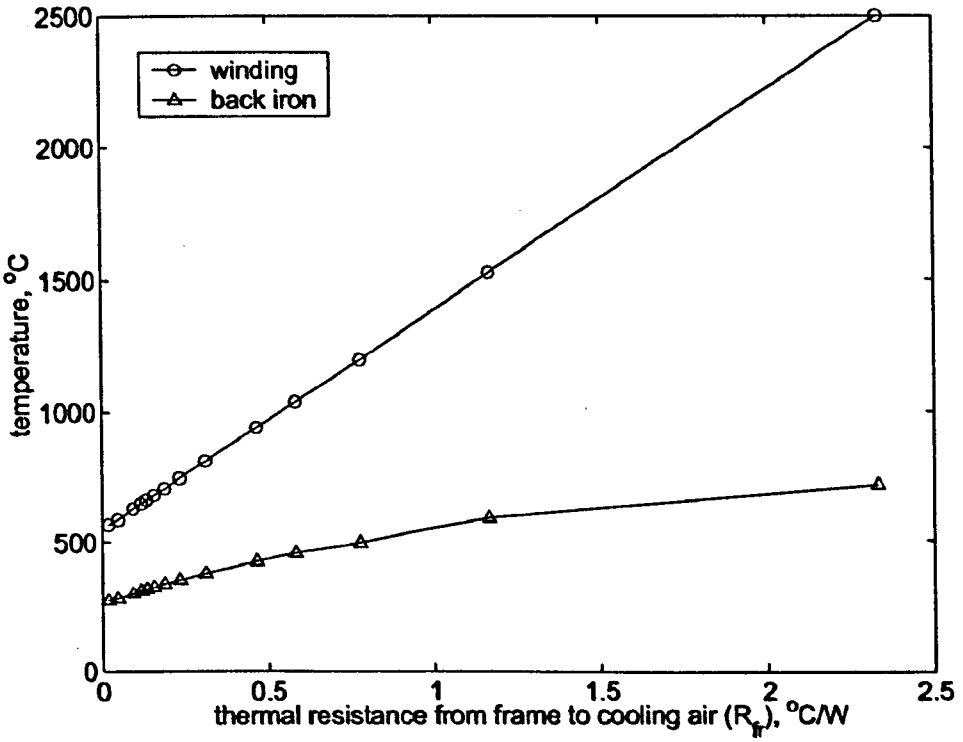

Figure 6.4. Winding and back iron temperatures in the SR machine at 13500rpm, 100kW, with conduction heat transfer in the slot region, for values of thermal resistance between 0.017 and 2.33 K/W.

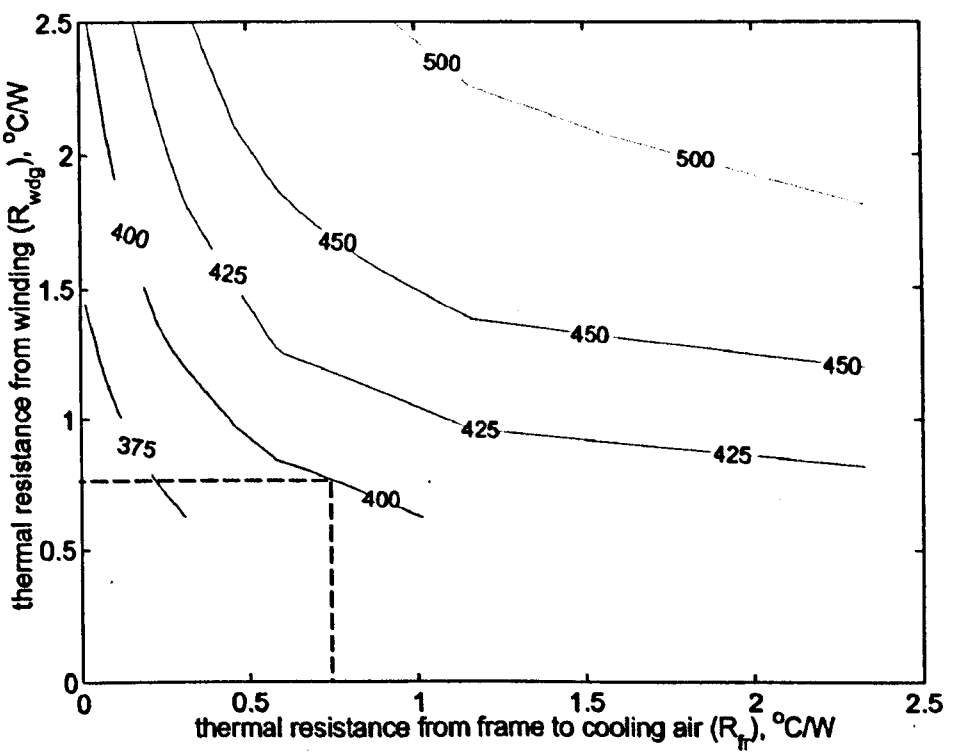

Fig 6.5. Contours of steady-state winding temperature (for a machine with a Hiperco 50HS rotor and Hiperco 50 stator) for various levels of cooling from the frame and winding, at 13500rpm, 100kW.

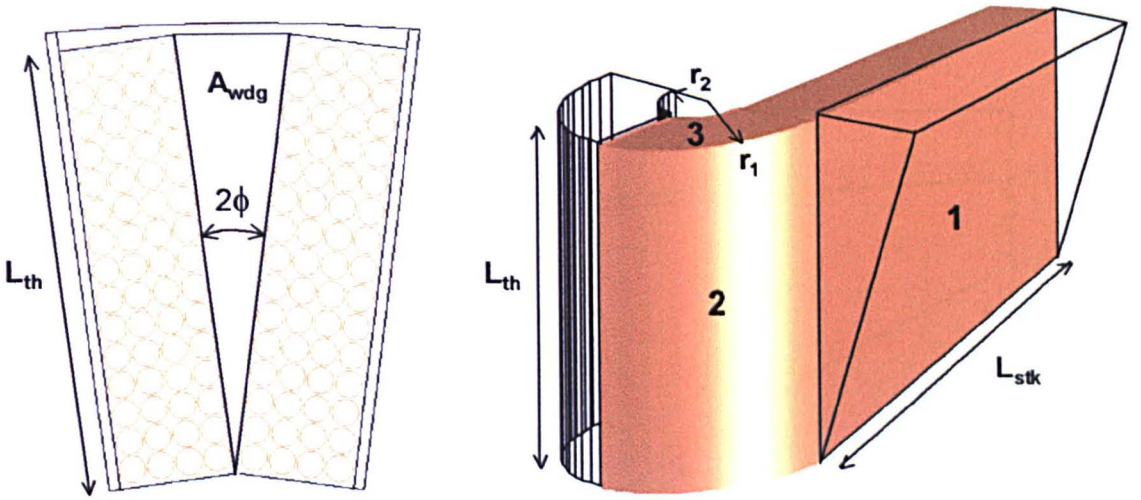

(a) (b)

Figure 6.6. (a) Duct area considered for forced air-cooling of the winding. (b) Winding surfaces considered in the evaluation of heat transfer from winding to the coolant,

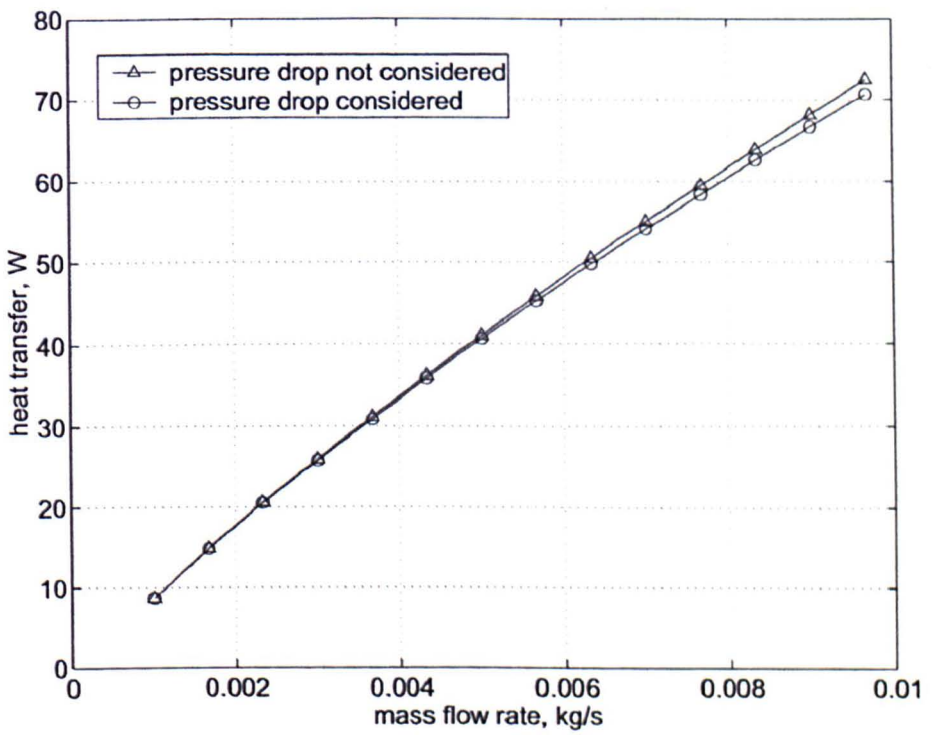

Figure 6.7. Rate of heat transfer from the winding duct as a function of mass flow rate, with and without the consideration of pressure drop through the duct.

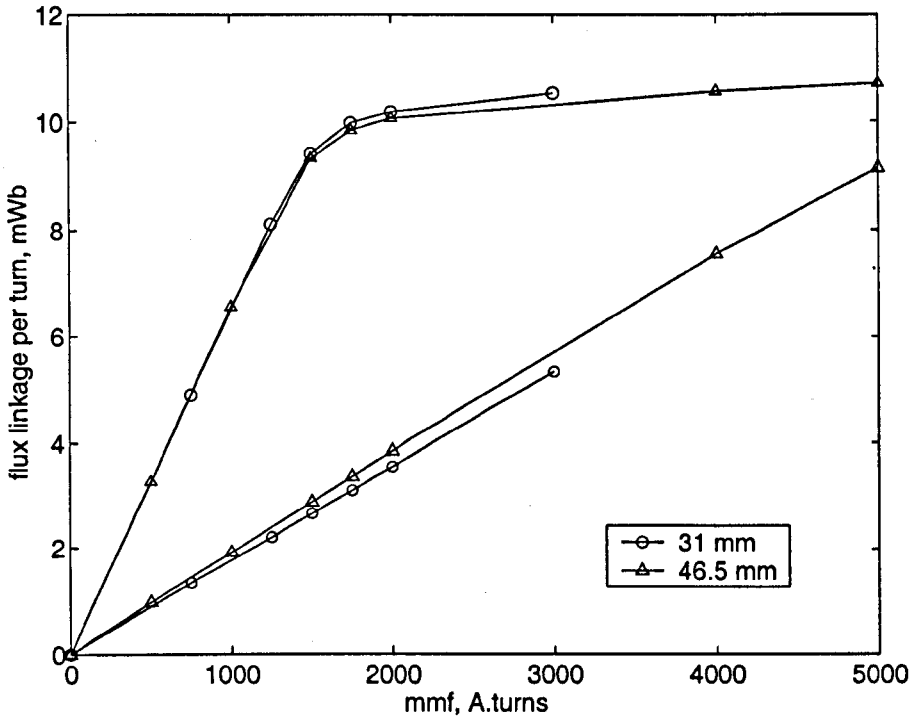

Figure 6.8. Flux linkage versus current for slot depths of 31mm and 46mm respectively (representing a 50% increase in slot depth).

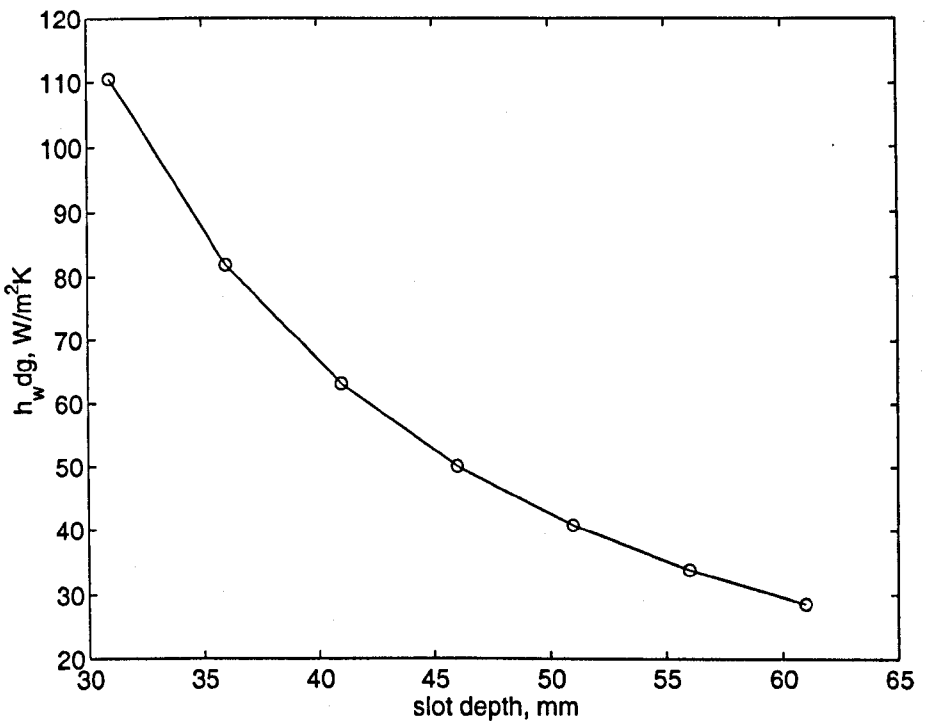

Figure 6.9. Variation in heat transfer coefficient from the winding to cooling air (h_{wdg}) necessary to maintain the winding temperature at 400°C, as a function of the slot depth.

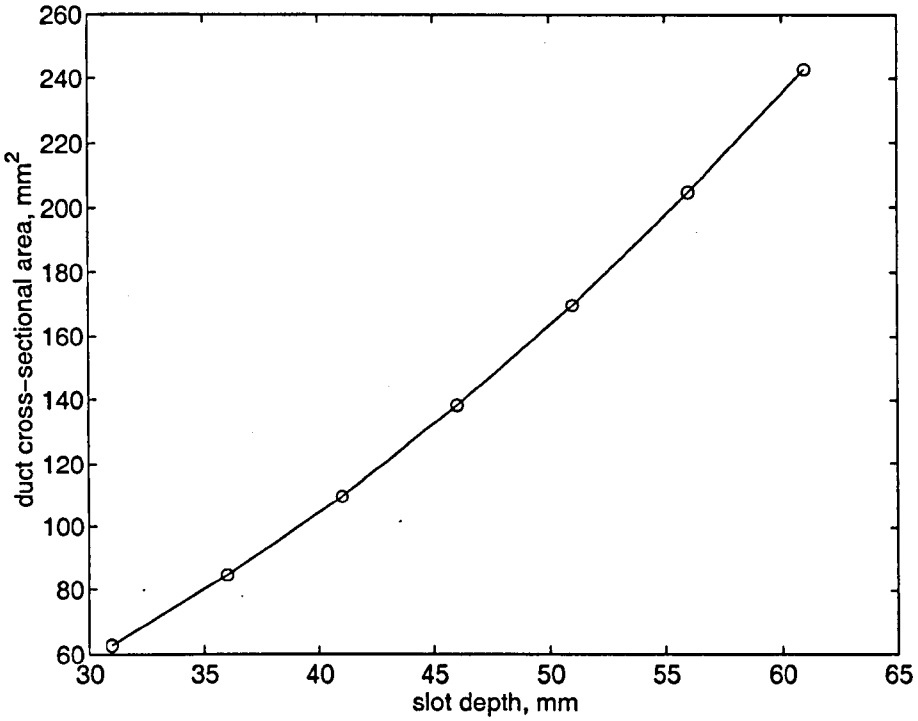

Figure 6.10. Increase in stator winding duct cross-sectional area with slot depth.

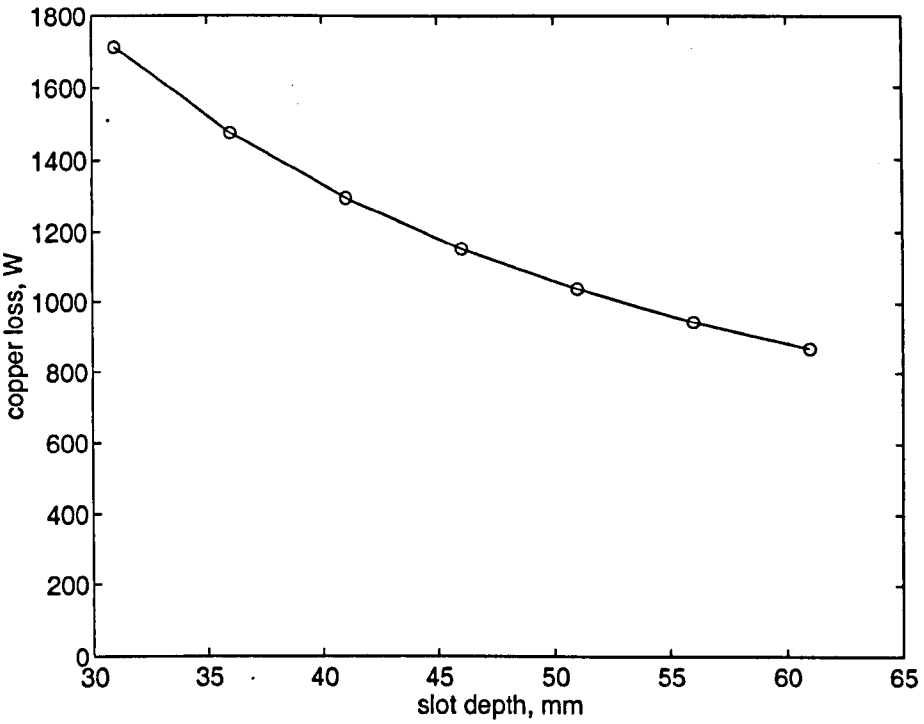

Figure 6.11. Variation in copper loss with slot depth.

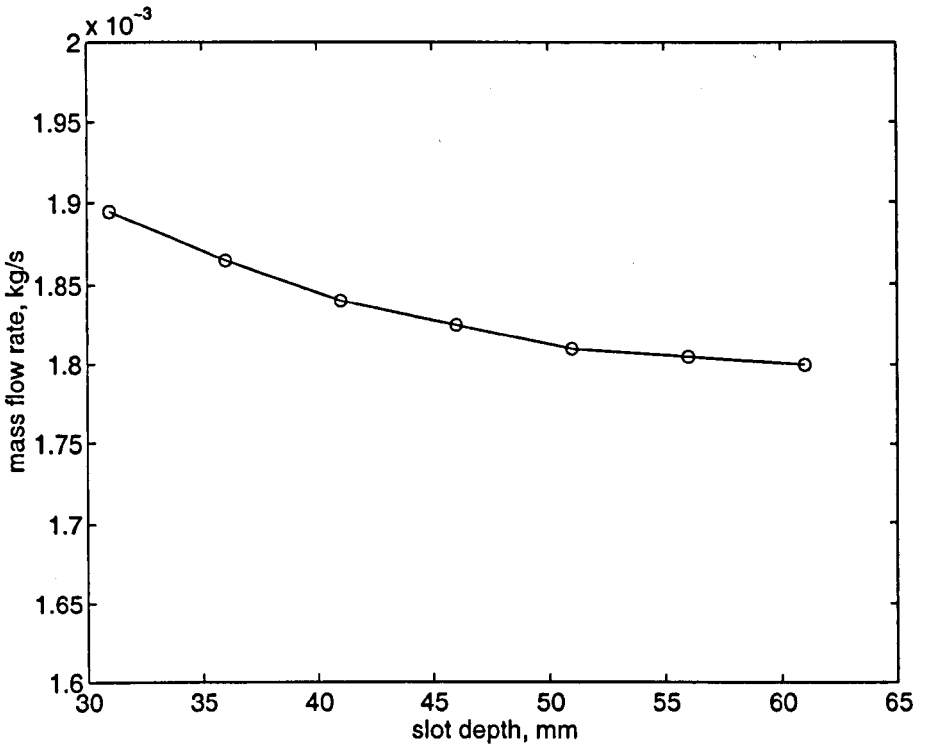

Figure 6.12. Variation in mass flow rate through the stator winding duct necessary to maintain the winding temperature at 400°C, as a function of the slot depth.

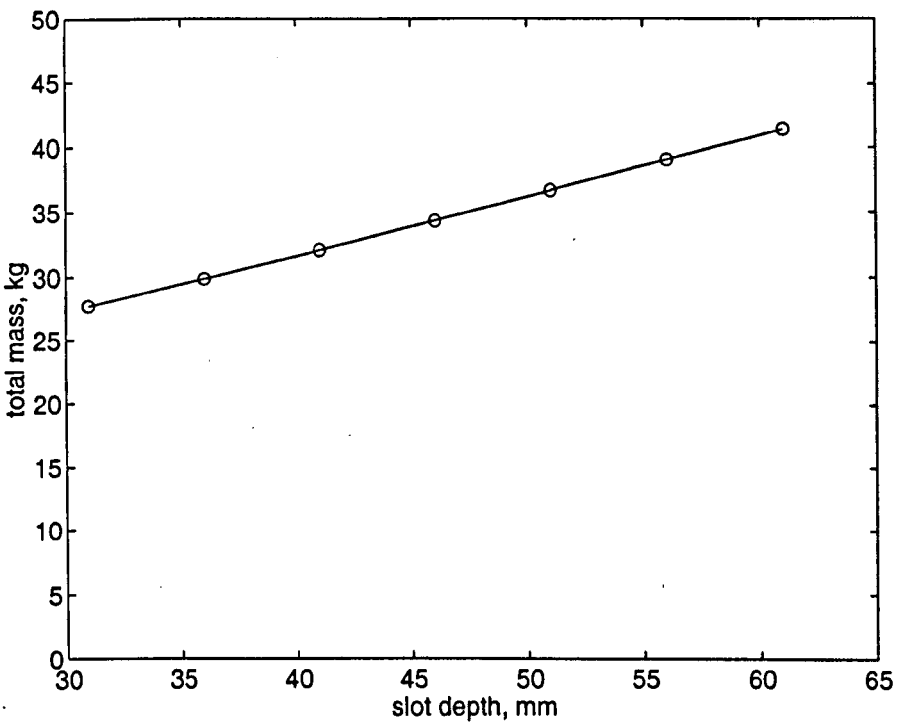

Figure 6.13. Increase in total machine mass with slot depth.

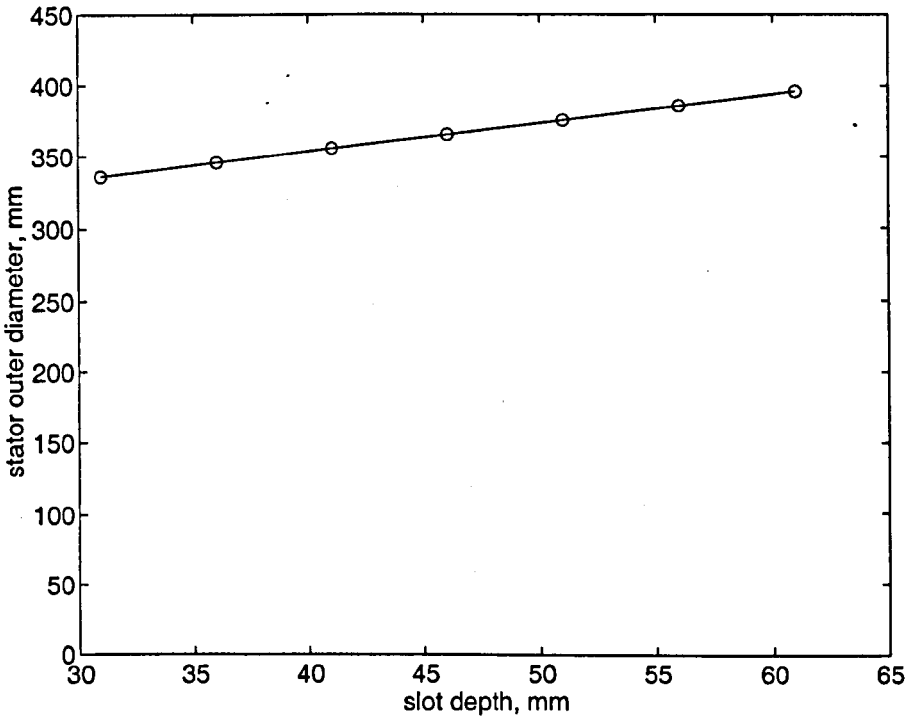

Figure 6.14. Variation in stator outer diameter with slot depth.

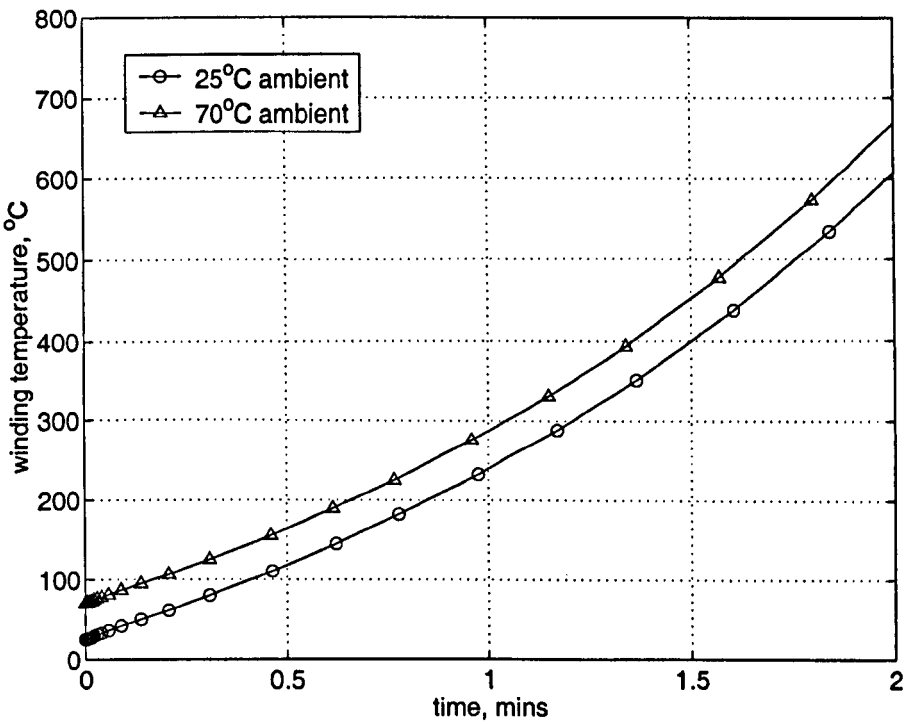

Figure 6.15. Winding temperature rise during starting for an ambient temperature of 25°C and 70°C respectively.

CHAPTER 7

CONCLUSIONS

This thesis has embraced the thermal, mechanical and electromagnetic design of high integrity electrical machines for aerospace, specifically a permanent magnet brushless DC (BLDC) machine for application in an electro-hydraulic actuator, and a switched reluctance (SR) starter/generator for application in the core of a large civil jet engine. It has shown the importance of considering each of these disciplines in the design of such high integrity machines. Table 7.1 summarises the main conclusions for both the BLDC machine and the SR machine in terms of these disciplines, while the following points are regarded as being particularly important in terms of novelty:

- Development of a modular rotor for a switched reluctance machine in order to overcome limitations imposed by the mechanical strength of the lamination material.
- A systematic finite element study on the influence of convective heat flow and conductor geometry/position on heat transfer within a stator slot.

7.1 Thermal modelling of high integrity electrical machines for aerospace

The combination of a high power density and harsh operating environment have made the development of detailed thermal models a necessity for both machines in order to attain a satisfactory level of reliability from the various components that constitute an electrical machine. A detailed lumped parameter model has been developed for temperature estimation in both machines (details in Appendices B and C) that has been validated under various encapsulation processes for the case of the BLDC machine. The accuracy of the thermal models has been shown to be highly dependant on the accuracy of the input data, such as the various heat transfer coefficients within the winding and frame, and the conductor bundle thermal conductivity, the latter of which has been measured in this thesis. A comprehensive study was carried out using finite element

analysis and computational fluid dynamic models to investigate heat transfer in the winding region with various packing factors, conductor geometries, numbers of conductors, conductor positions within the slot and encapsulation processes. It was found that in general, a fully encapsulated slot gives significant benefits in terms of reduced winding temperature and an increase in thermal capacity, thus reducing both the steady state temperature, and transient temperatures experienced over a duty cycle. FE analysis also showed that the random placement of individual conductors within a slot (as would be the case in a practical machine) could cause a large error in the estimation of winding temperature by as much as 20% for a low number of turns i.e. less than 6. It was also shown that a winding region can be successfully modelled with a solid finite element model for a naturally ventilated machine, without recourse to more elaborate methods such as computational fluid dynamics. Further development of the thermal model to include the effects of non-homogenous loss between adjacent stator teeth, and forced air cooling of the frame, winding and end windings, was employed for the switched reluctance machine in order to estimate cooling requirements. It has been shown that on full load and speed, with high specific levels of heat dissipation, and running in an ambient temperature of 350°C, the SR machine can be sufficiently forced cooled using the bleed air from the jet engine, albeit this requiring ~25% of the total bleed air from the engine. The transient thermal behaviour of the machine under starting conditions was also simulated, from which it was established that there is sufficient heat capacity (even with no additional encapsulation) to accommodate a representative starting cycle.

7.2 Mechanical considerations of the switched reluctance machine

The combination of a high rotor speed and severe constraints imposed upon the volume envelope of the switched reluctance machine resulted in a high level of mechanical stress in the rotor. These problems were further compounded by the reduced mechanical strength of the cobalt iron laminations at the elevated operating temperature of 400°C. Finite element analysis was employed to establish the maximum diameter for a conventional SR rotor operating at 13500rpm and 60% of the lamination material yield strength, whilst maintaining an acceptable level of magnetic saliency. This constraint

limited the rotor to a diameter of 248mm, which is considerably less than would be desirable electromagnetically. A novel modular rotor construction was proposed in which separate laminated pole modules are attached to a higher strength non-magnetic hub, thus permitting a machine with a larger rotor diameter to be operated at the same speed. It was also found that the laminated modules are subjected to significantly lower levels of stress than the single piece lamination, hence there is scope to change the heat treatment of the lamination material in order to trade mechanical strength for better magnetic properties in terms of higher saturation flux density, and lower hysteresis losses. The modules may be attached to the hub using friction welding or induction brazing techniques, although it is recognised that there are many manufacturing issues that must be overcome before this topology of machine can be considered for service in such a safety critical application.

7.3 Electromagnetic design of a novel modular rotor SR machine

Although the modular rotor machine design has the same number of stator and rotor poles as the conventional rotor SR machine, the nature of the short flux paths dictates that two phases are excited at any one time, and hence double the number of phases are required in order to start and commutate the machine correctly. Magnetostatic finite element analysis has been employed in comparing the design with two SR machines with conventional rotors, one with a reduced diameter due to mechanical constraints, and the other of similar diameter that would be operating beyond specified mechanical safety limits. It was found that, although the aligned to unaligned inductance ratio of the modular rotor machine was smaller than that of the similar sized conventional machine, the peak and average static torque capability were very similar. An interesting characteristic of the modular rotor machine was noted during the finite element study, whereby it exhibits a region of negative torque close to the unaligned position. Another feature of the modular rotor is that a significant degree of saliency is generated by the large gap between adjacent modules rather than between the module teeth, hence the height of the teeth can be reduced beyond the limits of well-established design guidelines for conventional SR rotors without incurring a large reduction in saliency. In summary, although these machines may be an attractive option for an embedded machine in a jet

engine, it is unlikely that these types of machines will be preferred to conventional SR machines in the vast majority of applications due to their high number of phases, and relatively complex rotor topology.

7.4 Fluid friction losses

The drive for higher reliability resulted in a BLDC machine directly coupled to a hydraulic pump with no dynamic seal, thus allowing hydraulic fluid to flow through the airgap annulus and out the non-drive end of the machine. The associated drag losses caused a large drop in efficiency, particularly at low loads. Well-established analytical methods were used to estimate the drag losses, and were further developed to include the effects of axial temperature rise in the airgap, with test results showing good agreement with predicted values. This approach was then employed in establishing an airgap height that gave the best compromise between the conflicting requirements of a large gap in order to reduce drag losses, and a smaller gap in order to reduce copper losses. A sub-optimal airgap length that generated minimum copper losses over a wide operating range in terms of speed, load and temperature was found to be between 1 and 2 mm. It was also demonstrated that for the most onerous operating condition of –55°C (at which the viscosity of the fluid is some two orders of magnitude higher than at room temperature) the resulting drag torque might pose problems in terms of starting, and hence necessitate an increase in the VA rating of the inverter.

Table 7.1. Main conclusions

	BLDC	SR
Thermal	• Full encapsulation reduces winding temperature considerably, and increases transient capability in terms of thermal capacity • Conductor placement can introduce a large error in temperature estimation • Lumped parameter model can be as accurate as FE model due to uncertainties in contact coefficients, and conductor placement	• 49% Cobalt Iron aging problems limit operating temp to 400°C • Jet engine bleed air can provide sufficient cooling for an HP starter/generator
Electromagnetic		• Modular rotor machine is competitive with a conventional machine of the same diameter • Negative torque region is observed close to the unaligned position • Modular SR machine retains a significant aligned to unaligned inductance ratio when the rotor tooth height is reduced to zero
Fluid friction	• Fluid must be pre-heated above 0°C to minimise inverter size • Drag loss has a strong influence at low loads • Flooded airgap should be between 1 and 2mm	
Mechanical		• A novel modular rotor design has been developed for SR machines operating at high levels of mechanical stress • Enables design of larger diameter and/or higher speed SR machines

7.5 Further work

- Further analysis of the modular rotor switched reluctance machine in terms of dynamic analysis and different commutation schemes in order to maximise the torque capabilities (and how to cope with the negative torque region).

- Investigation of iron losses in the modular rotor machine, as these are potentially lower given the significantly reduced volume of iron that carries flux per revolution, and the ability to employ a material with a lower specific loss density in the rotor.

- Research into the feasibility of joining rotor tooth modules to a non-magnetic, high strength hub material.

- Thermal aspects of machines operating at high temperature using novel cooling schemes such as employing the rotor to act as an impeller air pump to enable forced air cooling of the end windings.

APPENDIX A

T-NETWORK OF THERMAL RESISTANCES

The cylinder shown in figure A1 can be represented as an equivalent T-network of thermal resistances in the radial direction as illustrated in Figure A2. The stator back iron, for example, is modelled as a cylindrical region. θ_1 and θ_2 are the outer and inner surface temperatures of the cylinder, and θ_m is the mean temperature of the cylinder. r_1 and r_2 are the outer and inner radii of the cylinder respectively, and L is the axial length of the cylinder.

R1, R2 and Rm are thermal resistances that model heat flow in the cylinder. They arise from the solution of Fourier's equation of heat conduction through a cylindrical wall with internal heat generation in the radial direction. The central node in the network would give the mean temperature if there were no internal heat generation or thermal storage. However, the superposition of internal heat generation, for example: iron loss in the back iron region, gives rise to a temperature lower than the temperature at the central node. This results in a negative value for the resistance Rm in the T-network.

The heat conduction equation is solved independently for radial and axial directions, and if necessary, for the circumferential direction. Equations A1 to A3 present, for example, solutions for the radial case only.

$$R1 = \frac{1}{4\pi k_r L}\left[1 - \frac{2r_2^{\,2}\ln(r_1/r_2)}{\left(r_1^{\,2}-r_2^{\,2}\right)}\right] \tag{A1}$$

$$R2 = \frac{1}{4\pi k_r L}\left[\frac{2r_1^{\,2}\ln(r_1/r_2)}{\left(r_1^{\,2}-r_2^{\,2}\right)} - 1\right] \tag{A2}$$

$$Rm = \frac{-1}{8\pi\left(r_1^{\,2} - r_2^{\,2}\right)k_r L}\left[\left(r_1^{\,2} + r_2^{\,2}\right) - \frac{4 r_1^{\,2} r_2^{\,2} \ln\left(r_1 / r_2\right)}{\left(r_1^{\,2} - r_2^{\,2}\right)}\right] \qquad \text{(A3)}$$

where r_1 is the outer radius of the cylinder and r_2 the inner radius. k_r is the thermal conductivity of the cylinder in the radial direction. (Independent solution allows different values for k in each direction, enabling for instance, the effects of laminated steel and conductor bundles to be modelled).

Thermal capacity of a given lumped region is calculated using the mass and specific heat capacity, and is given by:

$$C = \rho c V \qquad \text{(A4)}$$

where C is the thermal capacitance (J/K), ρ is the density (kgm^{-3}), and c is the specific heat capacity of the material in the region ($Jkg^{-1}K^{-1}$). V is the volume of the region (m^3).

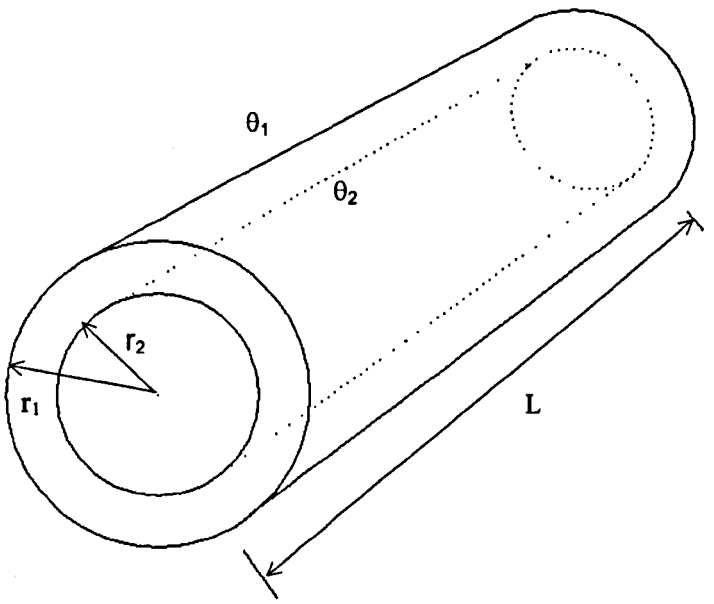

Figure A1. Cylindrical section considered in equations A1to A3.

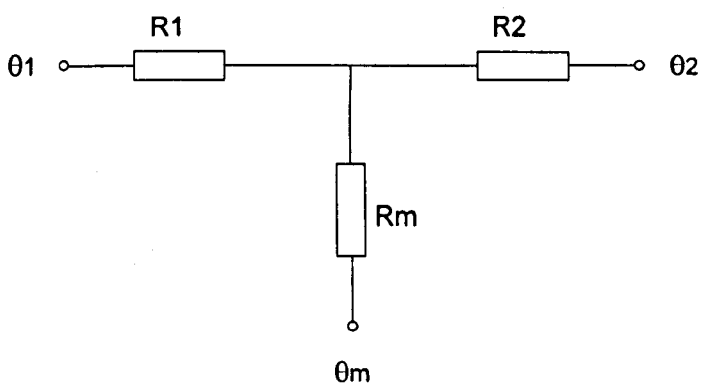

Figure A2. Equivalent T-network representing radial heat flow in a cylinder

APPENDIX B
BRUSHLESS DC PERMANENT MAGNET MACHINE THERMAL MODEL

The thermal network for the BLDC machine is shown in figures B1 to B8. The notation used in labelling the individual components of the network is described below.

Regions:

FR	Frame
BI	Back Iron
CB	Conductor Bundle
TB	Tooth body
TT	Tooth tip
EW	End winding

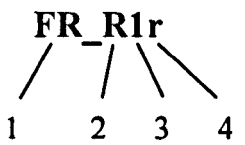

Position 1: **FR** refers to the Frame region, (and **BI** refers to the back iron and so forth).

Position 2: **R** refers to a thermal resistance. (**C** in this position denotes a thermal capacitance)

Position 3: The number **1** refers to the outer thermal resistance for the case of a cylinder and trapezoid. The number **2** in this position refers to the inner thermal resistance. The letter **m** in this position refers to the thermal resistance to the mean temperature point of the T-network as described in Appendix A.

Position 4: **r** denotes heat flow in the radial direction. **a** in this position denotes heat flow in the axial direction, and **c** in this position denotes heat flow in the circumferential direction. i.e. around the machine.

i.e. **TT_Rmr** is the thermal resistance to the mean temperature point in the tooth tip in the radial direction, and **TT_RC** is the thermal capacitance of the tooth tip region.

Description of the BLDC machine thermal network.

The lumped parameter thermal network has been developed using SABER® simulation software that allows models to be constructed over a number of hierarchical levels. The top level of the model is shown in figure B1 where it can be seen that the stator has been split into three axial sub-system blocks labelled 'Radial' and two blocks labelled 'Left End' and 'Right End'. The three central blocks describe radial, axial and circumferential heat flow in the stator iron and windings, while the blocks attached at each end of the stator describe heat flow in the end windings and end plates. These blocks are all connected together in the axial direction as would be expected, and also in the radial direction to the frame sub-system block. All sub-system blocks have a node labelled AMB. This is the ambient node that provides a ground reference point used to define the ambient temperature, and to set the initial level of thermal storage. The summation blocks at the bottom of figure B1 feed back the winding temperature to the copper loss model, where an average winding temperature is used to calculate the loss.

It is possible to trace sub-system block nodes down through each level of hierarchy, for instance, the node BI_1 appears on all the blocks labelled 'Radial'. This node is part of the back iron (BI) and can be found in the next level down in the hierarchy that is shown in figure B2. The node is situated at the top left in figure B2, and is connected to the back iron sub-system block by the node BI_A1. In turn, this node can be traced through to the back iron region thermal network shown in figure B3, this representing the final level in the model hierarchy. The node is again situated at the top left of figure B3 and is connected to the thermal resistance BI_R1a in the back iron axial heat flow T-network (lumped T-networks representing heat flow are described in Appendix A). Other sub-system block nodes can be traced back to the T-network level in a similar way. It is possible to see the various T-networks describing heat flow in three directions in figure B3, although the circumferential heat flow path is connected to an adjacent section of back iron within the block. Figure B5 shows the three separate T-networks more clearly in the tooth body region model, where it can be seen that all the T-networks are connected at the mean temperature

node at the centre of the figure. Heat generation is introduced at this node from a control signal input (TB_loss) that is generated in another block, and converted to an electrical current source using the SABER® block *var2i*. Thermal storage (TB_C) is also introduced at this node. An additional resistance of 1MΩ was connected across the current source to stabilise the simulation during start-up, and was shown to have a negligible effect on predicted temperatures.

The end winding and end plate sub-system block (labelled 'Right End' and 'Left End' in figure B1) are based on the same T-network models used in the stator, with additional thermal resistances to model heat flow between the end winding, end plate and frame as shown in figure B7. The end winding posed some problems in terms of the coordinate system used in representing heat flow in the respective directions. The coordinate system used to model the end winding was turned through 90° with respect to the stator axis so that the end winding could be described with a conventional cylindrical geometry as shown in figure B7a.

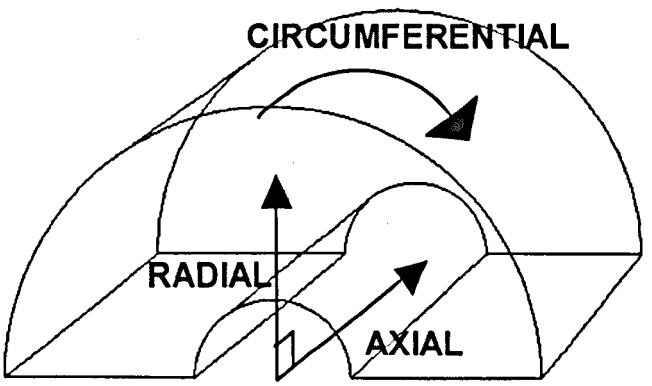

Fig. B7a. End winding and associated coordinate system.

Thermal network parameters

The following tables give predicted values of thermal network parameters for the various regions of the thermal model for a BLDC machine with process 1, 2 and 3 winding encapsulation. The value for BI_R1r can be found from the table by going to the column labelled 'Back Iron' and selecting the first value down in the row labelled 'R1' of the section labelled 'Radial' on the left hand side.

Additional thermal network parameters listed in the tables

Frame Contact	Thermal contact resistance between the stator stack and the frame
EP > Pump	End plate to pump thermal contact resistance
EP > amb	End plate to ambient thermal resistance

End space thermal parameters

EW > EP	End winding to end plate thermal resistance
EW > FR	End winding to frame thermal resistance
BI > EP	Back Iron to end plate thermal resistance
TB > EP	Tooth body to end plate thermal resistance
TT > EP	Tooth tip to end plate thermal resistance

For process 1 and 2 winding encapsulation, the thermal resistances in the end space are calculated by standard expressions for heat flow between flat plates [INC 90], whilst under process 3, these are calculated using standard expressions for conduction heat flow in a solid [INC 90].

References:

[INC 90] F.P. Incropera, D.P. Dewitt. 'Introduction to heat transfer.' 2nd Edition. John Wiley and sons Ltd, 1990.

Model nomenclature:

Figure B1:

BI, TB, TT, EW, WDG are losses introduced from a separate loss model in the back iron, tooth body, tooth tip, end winding, and conductor bundle region respectively.

AMB	Ambient temperature node
ambient	Ambient temperature node
EPL	Node connecting the frame to the left hand end plate
EPR	Node connecting the frame to the right hand end plate
FR_1 to FR_3	Radial heat flow nodes connecting the frame to the three stator sub-system blocks.
BI_loss	Iron loss in the back iron region
CU_loss	Copper loss in the conductor bundle region
EW_loss	Copper loss in the end winding region
TB_loss	Iron loss in the tooth body region
TT_loss	Iron loss in the tooth tip region
CB_temp	Conductor bundle temperature feedback node for calculation of copper losses
EP	End plate temperature node

Figure B4:

SLR	Slot liner radial thermal resistance
SL_PL	Slot liner inner thermal resistance (facing the tooth tips)
SLC	Slot liner circumferential thermal resistance
v2var	Voltage to Control interface. Measurement and feedback of winding temperature

BLDC Model - Thermal Parameters

Process 1: Bare Winding

		Back Iron	Conductor Bundle	Tooth Body	Tooth Tip	End Winding	End Plate
Radial	R1	0.0885	9.8309	0.4894	0.0922	10.5688	
	R2	0.0944	13.1555	0.4894	0.0922		
	Rm	-0.0304	-3.8311	-0.1631	-0.0307	-4.6928	
Axial	R1	34.1034	0.3759	54.3513	118.4877	54.5153	1.0479
	R2	34.1034	0.3759	54.3513	118.4877		
	Rm	-11.3678	-0.1253	-18.1171	-39.4959	-18.1718	-0.3493
Circ	R1	1.1761	14.5026	0.2195		0.7376	
	R2	1.1761	14.5026	0.2195			
	Rm	-0.3920	-4.8342	-0.0732		-0.2459	
Capacity		48.00	21.08	60.27	21.75	20.68	207.53

Total Mass (kg)	24.7	Frame Contact	0.041	TB->EP	2785.4
Slot liner (Radial)	6.4	EW->EP	1181.6	TT->EP	56787.3
Slot liner (Circ)	6.3	EW->FR	280.8	EP->Pump	0.009
Slot liner (inner)	9.9	BI->EP	6539.2	EP->amb	6.5

BLDC Model - Thermal Parameters

Process 2: Vacuum Pressure Impregnation

		Back Iron	Conductor Bundle	Tooth Body	Tooth Tip	End Winding	End Plate
Radial	R1	0.0885	5.1564	0.4894	0.0922	5.5434	
	R2	0.0944	6.9002	0.4894	0.0922		
	Rm	-0.0304	-2.0094	-0.1631	-0.0307	-2.4614	
Axial	R1	34.1034	0.3759	54.3513	118.4877	28.5938	1.0479
	R2	34.1034	0.3759	54.3513	118.4877		
	Rm	-11.3678	-0.1253	-18.1171	-39.4959	-9.5313	-0.3493
Circ	R1	1.1761	7.6068	0.2195		0.7376	
	R2	1.1761	7.6068	0.2195			
	Rm	-0.3920	-2.5356	-0.0732		-0.2459	
Capacity		48.00	22.70	60.27	21.75	22.27	207.53

Total Mass (kg)	24.8	Frame Contact	0.041	TB->EP	2785.4
Slot liner (Radial)	3.2	EW->EP	1181.6	TT->EP	56787.3
Slot liner (Circ)	3.1	EW->FR	280.8	EP->Pump	0.009
Slot liner (inner)	4.9	BI->EP	6539.2	EP->amb	6.5

BLDC Model - Thermal Parameters

Process 3: Fully Encapsulated

		Back Iron	Conductor Bundle	Tooth Body	Tooth Tip	End Winding	End Plate
Radial	R1	0.0885	2.5347	0.4894	0.0922	2.7250	
	R2	0.0944	3.3919	0.4894	0.0922		
	Rm	-0.0304	-0.9878	-0.1631	-0.0307	-1.2100	
Axial	R1	34.1034	0.3759	54.3513	118.4877	14.0557	1.0479
	R2	34.1034	0.3759	54.3513	118.4877		
	Rm	-11.3678	-0.1253	-18.1171	-39.4959	-4.6852	-0.3493
Circ	R1	1.1761	3.7392	0.2195		0.7376	
	R2	1.1761	3.7392	0.2195			
	Rm	-0.3920	-1.2464	-0.0732		-0.2459	
Capacity		48.00	50.97	60.27	21.75	69.73	207.53

Total Mass (kg)	27.2	Frame Contact	0.041	TB->EP	64.9
Slot liner (Radial)	1.6	EW->EP	9.0	TT->EP	179.8
Slot liner (Circ)	1.6	EW->FR	5.0	EP->Pump	0.009
Slot liner (inner)	2.5	BI->EP	81.5	EP->amb	6.5

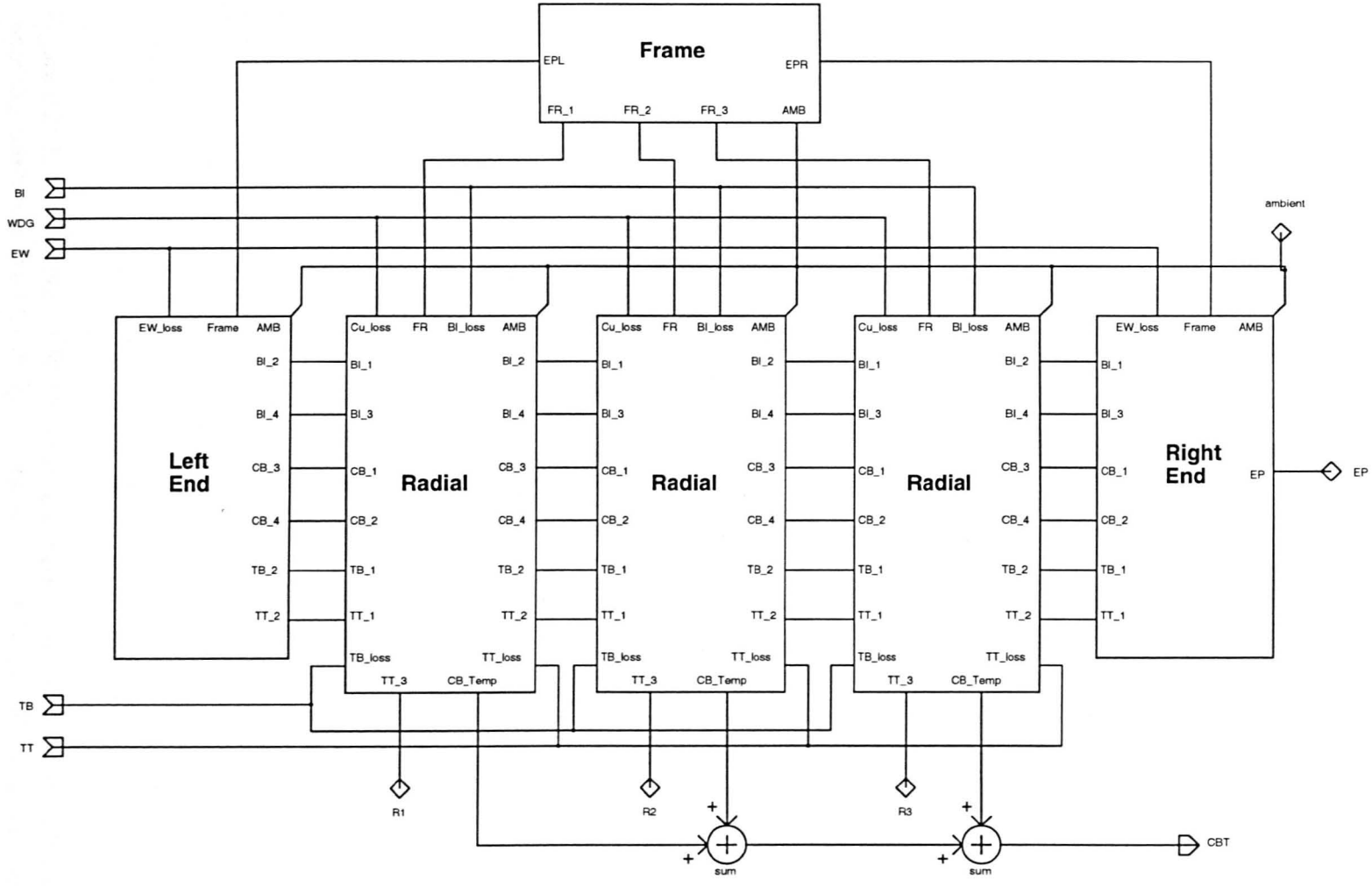

Figure B1. Top level of BLDC machine thermal model.

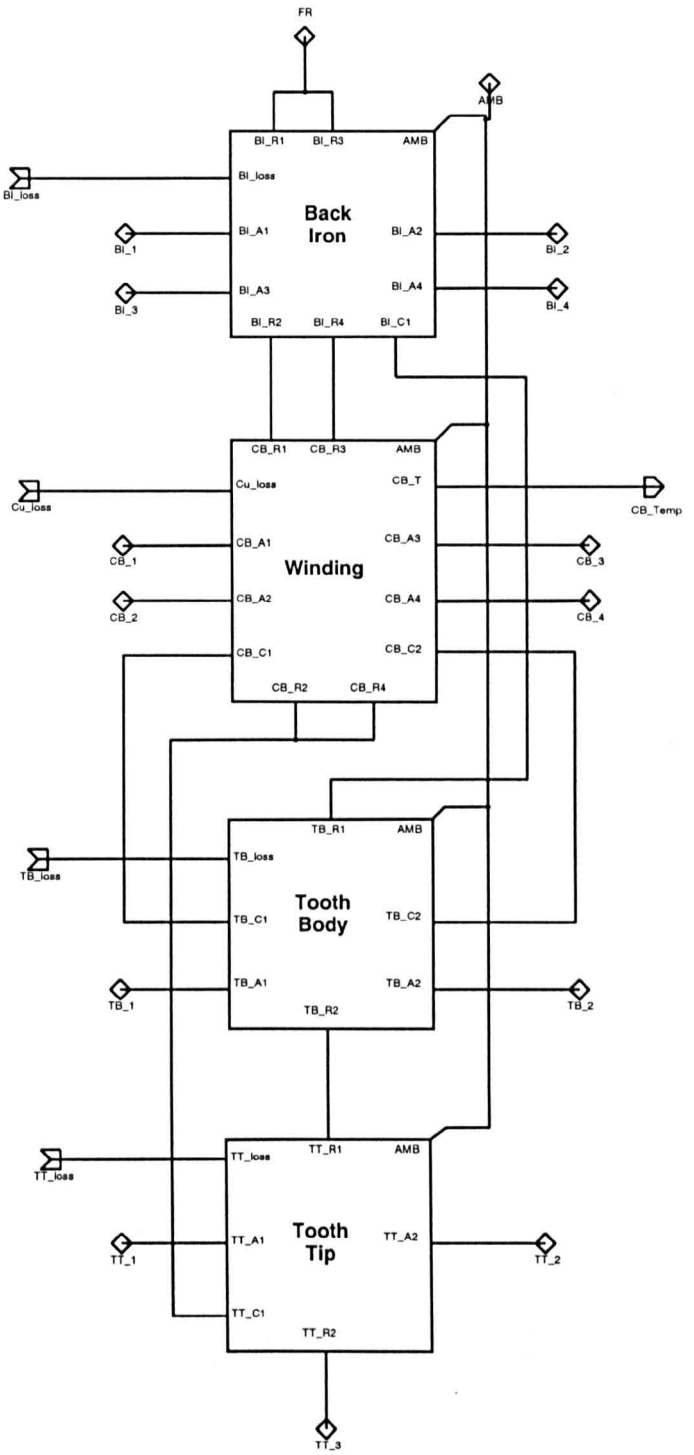

Figure B2. Radial section of BLDC machine thermal model showing the back iron, winding, tooth body and tooth tip with respective radial, axial and circumferential connections.

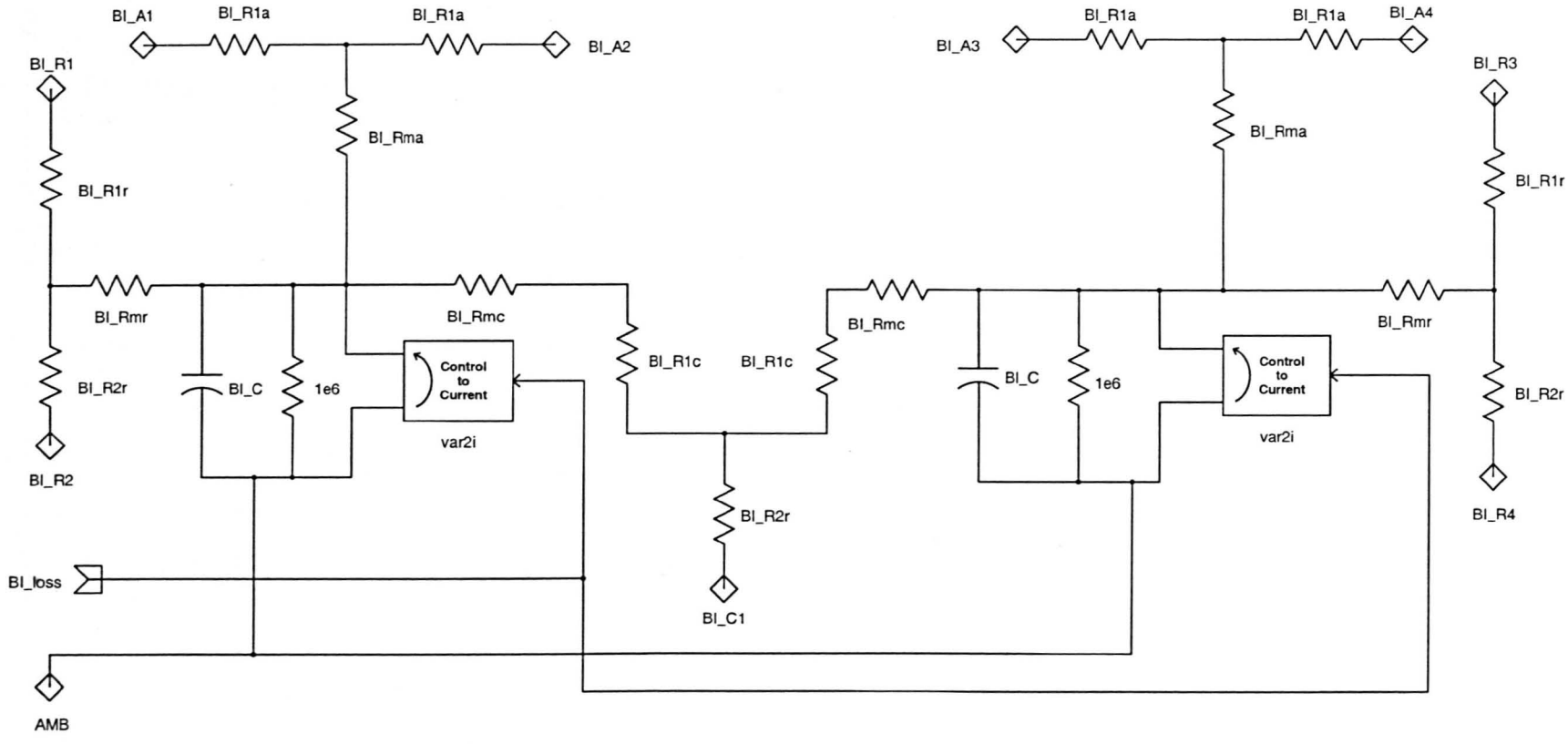

Figure B3. Back iron region model.

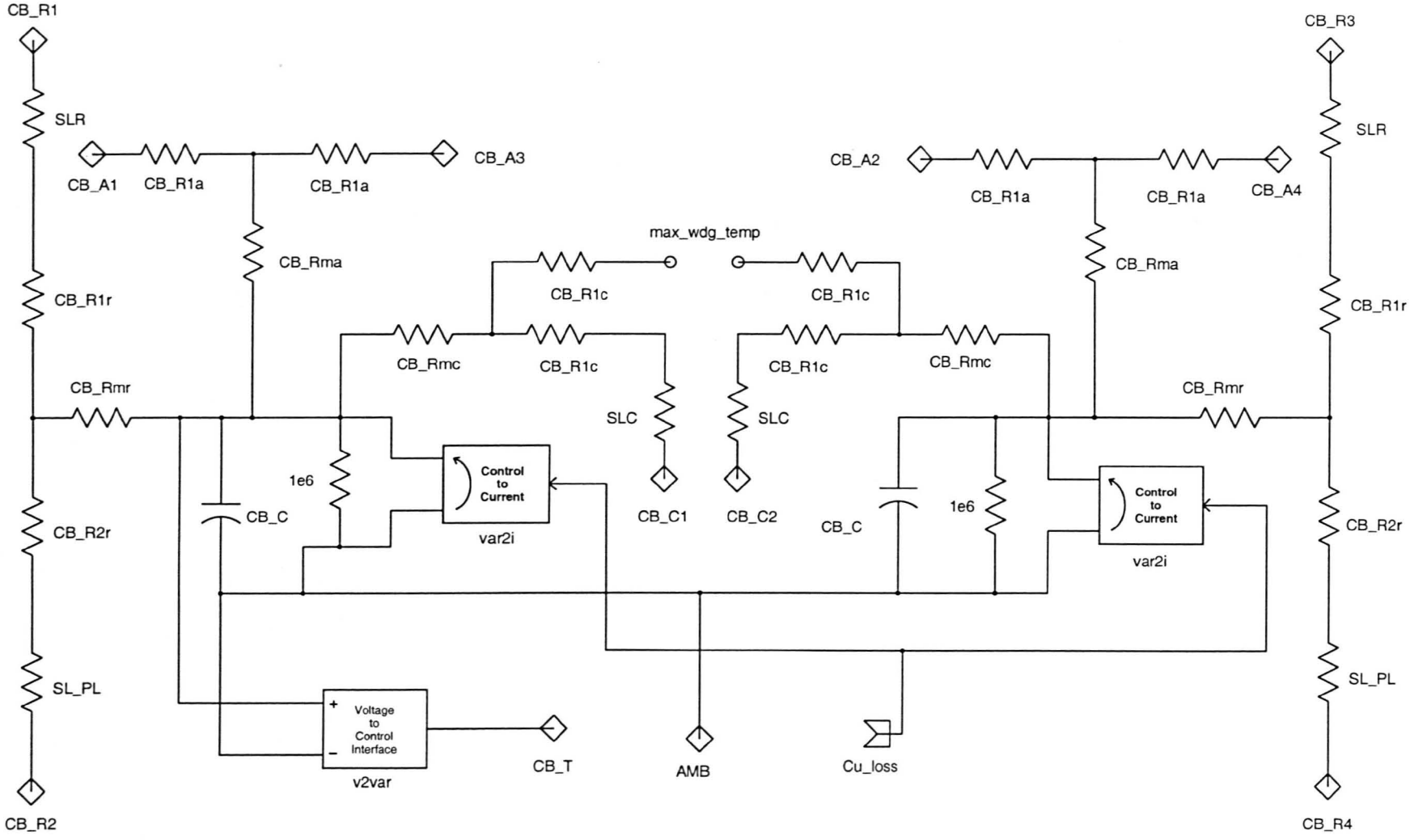

Figure B4. Conductor bundle region model.

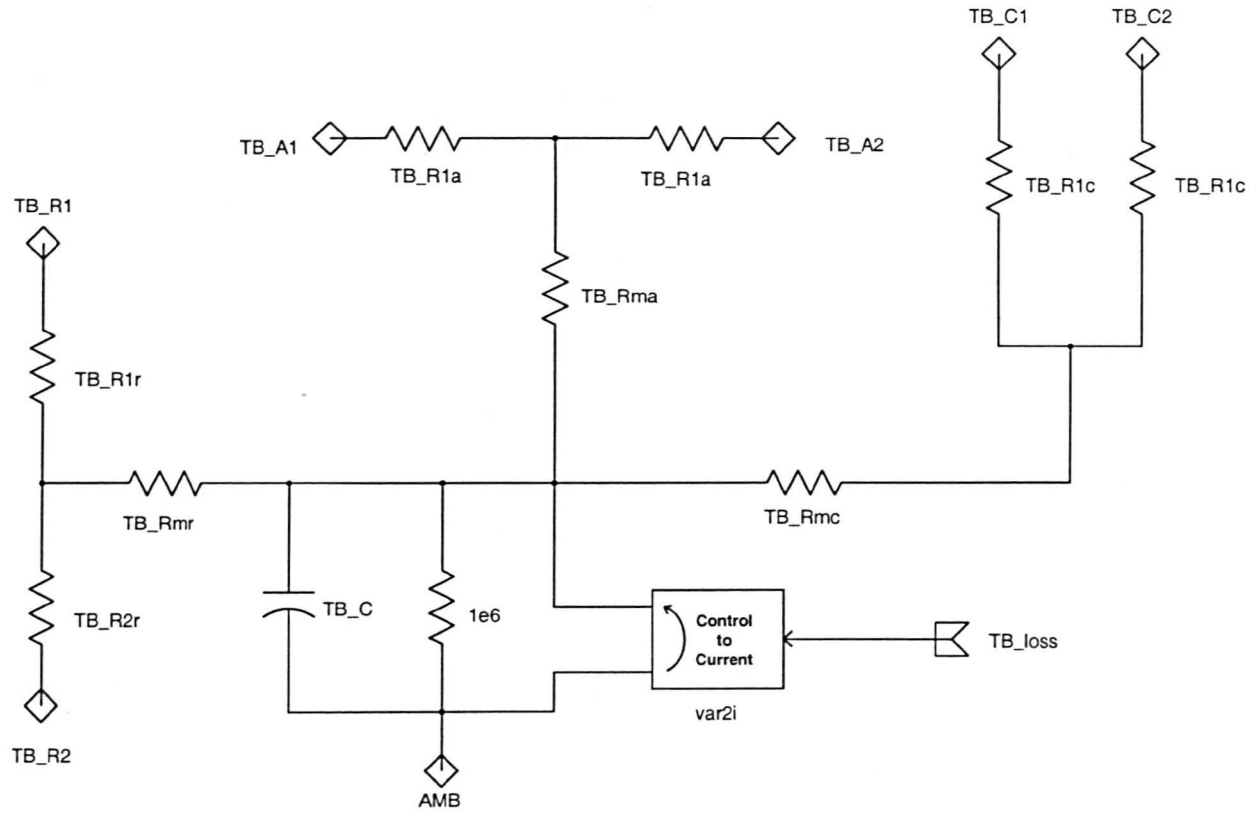

Figure B5. Tooth body region model.

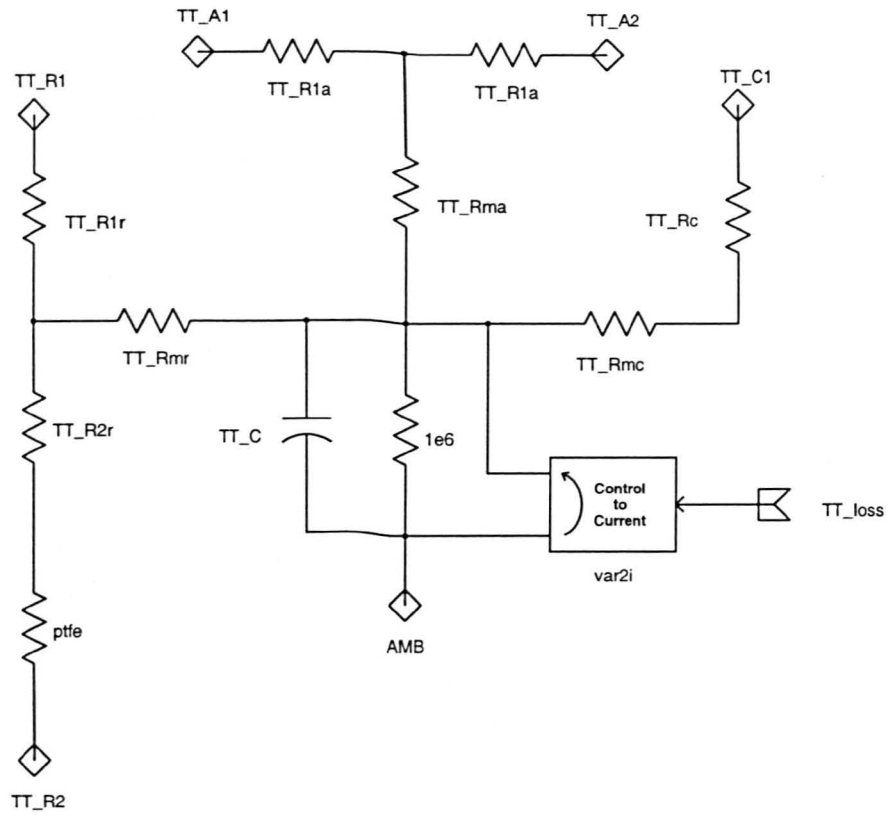

Figure B6. Tooth tip region model.

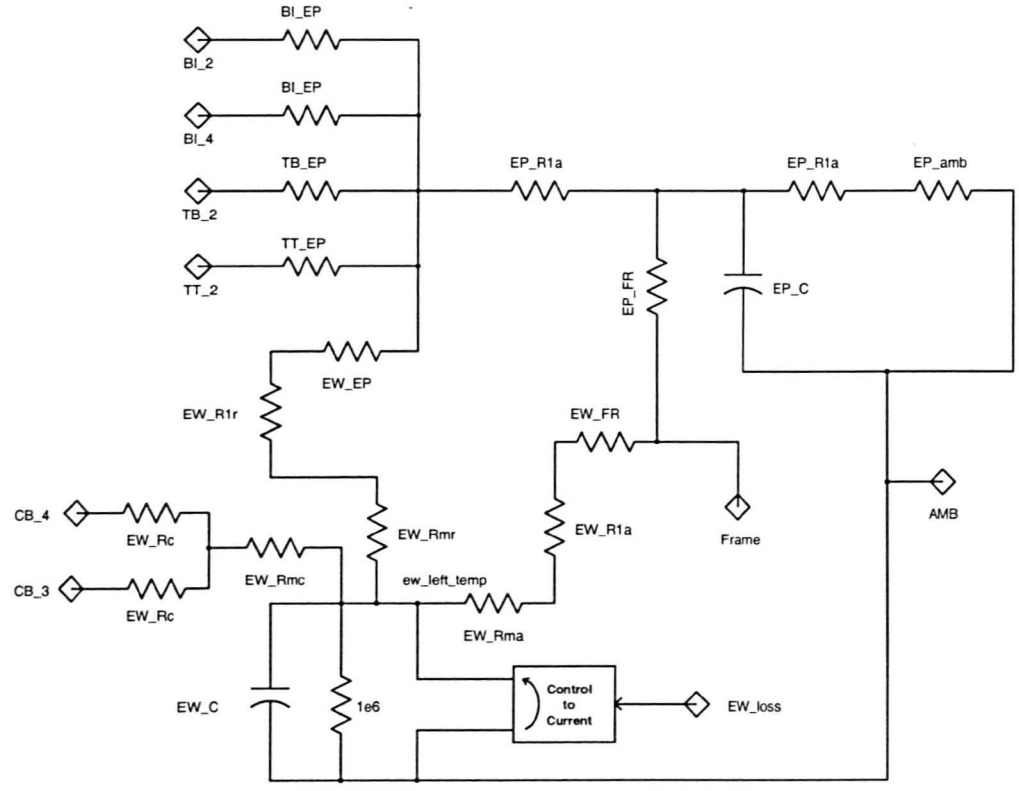

Figure B7. End winding and end plate model.

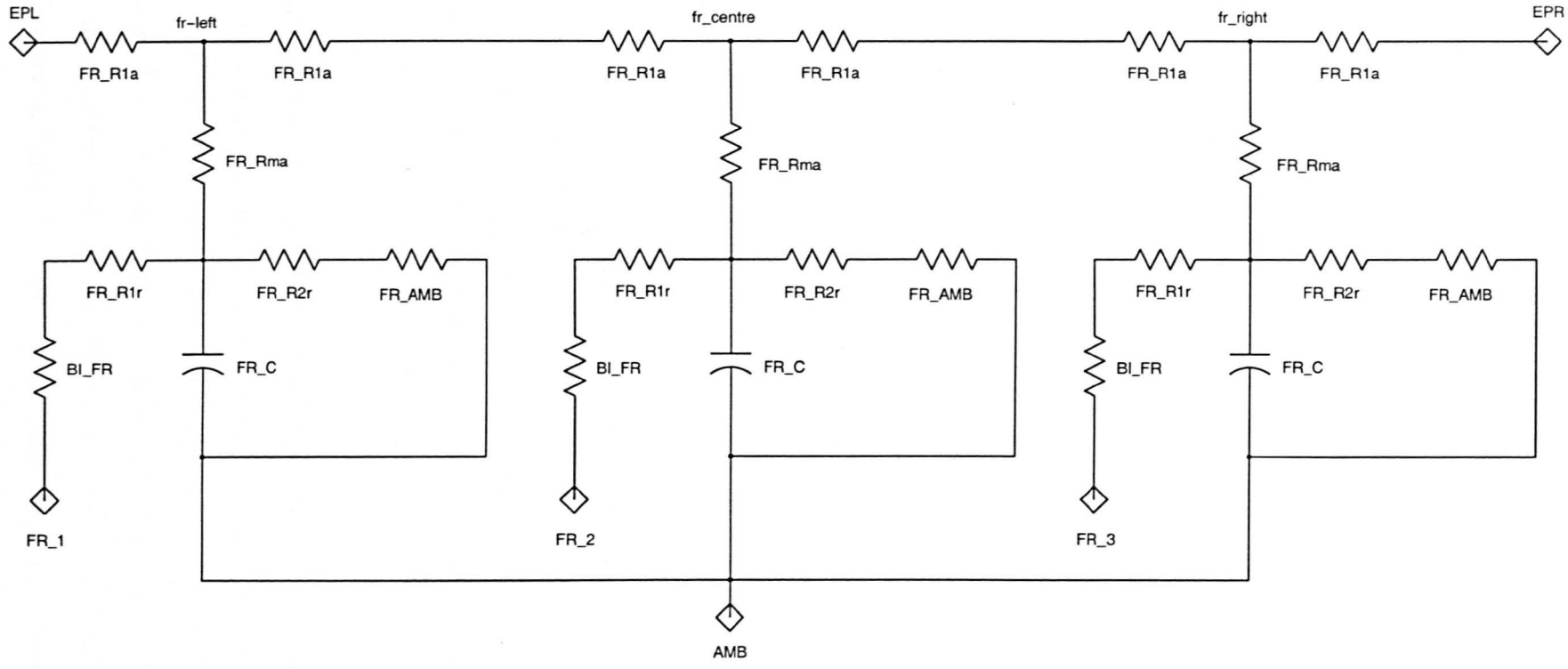

Figure B8. Frame model.

APPENDIX C

SWITCHED RELUCTANCE MACHINE THERMAL MODEL

Appendix B presents an explanation of the notation used in the SABER® hierarchical thermal networks developed for both the BLDC machine and the SR machine.

Although the SR machine thermal model was constructed using the same hierarchical principles as the BLDC machine thermal model, it has a larger number of nodes due to the multiple duplication of each section in order to include the effects of distributed loss in the stator iron. The axial sub-division has also been removed due to the short stack length of the SR machine, and the relatively low temperature variation expected across the machine. The second level in the hierarchy is also considerably different, as the back iron sub-system block of the BLDC model has been split into two discrete blocks, while the conductor bundle block now represents half a slot (as opposed to a full slot in the BLDC model).

The top level in the SR thermal model is shown in figure C1 showing the 8 separate sub-system blocks representing sections 1 to 8 in figure 6.2(a). These are connected together via circumferential heat flow nodes BI_1, BI_2, CB_1 and TB_2, representing the back iron, conductor bundle, and tooth body respectively. It can be seen from figure C1 that section 1 is also connected to section 8 to meet the boundary conditions specified in Chapter 6, section 3. The 8 sections are also all connected to nodes f1 to f16 on the frame sub-system block via nodes *top1* and *top2,* which can be traced through to the second level in the hierarchy (figure C2) where they connect to the radial heat flow path in the back iron sub-system block (the network schematic diagram for which is shown in figure C3).

Iron losses are considered temperature independent (they have already been calculated for 400°C operation) and are introduced as constant control signals in blocks labelled BI, TB, and TT at the top level of the hierarchy as shown in figure C1, representing iron losses in the back iron, tooth body and tooth tip respectively. The iron losses are 'injected' at their correct location in the model via a signal bus shown as a bold interconnecting line in figure C1. Temperature dependant copper losses are generated by feeding back the winding temperature from one of the 8 sections to the network of gains

and summations in the bottom left hand corner of figure C1, where it may be seen that copper losses and end winding losses are generated separately.

The voltage source at the top of figure C1 is connected between ground and the ambient temperature node and dictates the ambient temperature used in the thermal model.

The nomenclature used in the SR machine thermal model is given below with respect to the individual figures, although figures C3, C5 and C6 are not included as the parameters used within these regions are described in Appendix B.

Model nomenclature

Figure C1:

amb	Ambient temperature node
BI	Back iron loss sub-system block
BI_LOSS1	Iron loss in the back iron region
BI_1	Nodes connecting adjacent back iron sections (circumferential heat flow)
BI_2	Nodes connecting adjacent back iron sections (circumferential heat flow)
cbt	Feedback of conductor bundle temperature
CB_1	Nodes connecting adjacent conductor bundle sections (circumferential heat flow)
CB_LOSS	Copper loss in the conductor bundle region
EW_loss	Copper losses in the end winding region
f1 to f16	Radial heat flow path nodes at the frame inner surface
r1 to r8	identifies sections 1 to 8 in the iron loss sub-system blocks
TB	Tooth body iron loss sub-system block
TB_2	Nodes connecting adjacent tooth body sections (circumferential heat flow)
TB_LOSS	Iron losses in the tooth body region
top1	Node connecting outer surface of the back iron to the frame
top2	Node connecting outer surface of the back iron to the frame
TT	Tooth tip iron loss sub-system block
TT_LOSS	Iron losses in the tooth tip region

Figure C2:

BI_loss	Iron loss in the back iron
BI_A1/2	Axial heat flow node connection on the back iron sub-system block
BI_C1/2	Circumferential heat flow node connection on the back iron sub-system block

BI_R1	Outer radial heat flow node connection on the back iron sub-system block
BI_R2	Inner radial heat flow node connection on the back iron sub-system block
CB_A1/2	Axial heat flow node connection on the conductor bundle sub-system block
CB_C1/2	Circumferential heat flow node connection on the conductor bundle sub-system block
CB_R1	Outer radial heat flow node connection on the conductor bundle sub-system block
CB_R2	Inner radial heat flow node connection on the conductor bundle sub-system block
CB_loss	Copper loss in the conductor bundle region
t_out	winding temperature feedback node on conductor bundle sub-system block
EW_loss	Copper loss in the end winding region
EW_A1/2	Axial heat flow node connection on the end winding sub-system block
T_loss	Iron loss in the tooth body region
T_A1/2	Axial heat flow node connection on the tooth body sub-system block
T_C1/2	Circumferential heat flow node connection on the tooth body sub-system block
T_R1	Outer radial heat flow node connection on the tooth body sub-system block
T_R2	Inner radial heat flow node connection on the tooth body sub-system block
TT_loss	Iron loss in the tooth tip region
TT_A1/2	Axial heat flow node connection on the tooth tip sub-system block
TT_R1	Outer radial heat flow node connection on the tooth tip sub-system block
TT_R2	Inner radial heat flow node connection on the tooth tip sub-system block

Figure C4:

sl_circ	Slot liner resistance in the circumferential direction
sl_radial	Slot liner resistance in the radial direction

The numbered thermal resistance (66) represents the forced cooling by connecting the outer cooled surface of the conductor bundle (CB_C1) to ambient (see figure 6.6).

Figure C7:

The numbered thermal resistances represent the forced cooling on each surface as detailed in figure 6.6(b) by connecting the outer cooled surface of the end winding to ambient.

Figure C8: Frame model

R_amb This represents the thermal resistance R_{fr} as used in the analysis of Chapter 6.

Figure C9: Rotor model

All thermal parameters and iron losses have been directly input to the model thermal network. The four current sources represent iron losses in regions A to D of figure 6.3(a) and (b), whilst the four radial thermal resistances at the top of the figure (labelled 12.5 and 16), represent the resistances R_{rot} in figure 6.3(b).

Input Parameters:

The predicted thermal network parameters used in the switched reluctance machine thermal model are shown in the following set of tables for slot depths ranging from 31 mm to 61 mm. The overall mass of the machine is also shown.

SR machine thermal parameters

Slot depth = 31.0mm

		Back Iron	Conductor Bundle	Tooth Body	Tooth Tip	Rotor Tooth body	Rotor Back Iron	End Winding
Radial	R1	0.3706	12.2361	1.0375	0.3458	0.3188	0.5425	1.8637
	R2	0.3893	14.6347	1.0375	0.3458	0.3188	0.5989	
	Rm	-0.1266	-4.4785	-0.3458	-0.1153	-0.1063	-0.1897	-0.7577
Axial	R1	130.9917	0.3937	47.6626	142.9879	137.0614	110.5243	
	R2	130.9917	0.3937	47.6626	142.9879	137.0614	110.5243	
	Rm	-43.6639	-0.1312	-15.8875	-47.6626	-45.6871	-36.8414	
Circular	R1	0.2965	3.5770	0.1085				
	R2	0.2965	3.5770	0.1085				
	Rm	-0.0988	-1.1923	-0.0362				
Capacity		25.31	30.43	34.80	11.59	12.10	60.00	22.02

Total Mass (kg) 27.78

Slot liner (Radial) 1.03

Slot liner (Circ) 0.57

SR machine thermal parameters

Slot depth = 36.0mm

		Back Iron	Conductor Bundle	Tooth Body	Tooth Tip	Rotor Tooth body	Rotor Back Iron	End Winding
Radial	R1	0.3597	13.5746	1.2048	0.4016	0.3188	0.5425	1.6048
	R2	0.3774	16.5943	1.2048	0.4016	0.3188	0.5989	
	Rm	-0.1228	-5.0281	-0.4016	-0.1339	-0.1063	-0.1897	-0.6525
Axial	R1	127.0698	0.3273	41.0428	123.1284	137.0614	110.5243	
	R2	127.0698	0.3273	41.0428	123.1284	137.0614	110.5243	
	Rm	-42.3566	-0.1091	-13.6809	-41.0428	-45.6871	-36.8414	
Circular	R1	0.3057	3.1860	0.0935				
	R2	0.3057	3.1860	0.0935				
	Rm	-0.1019	-1.0620	-0.0312				
Capacity		26.09	36.24	40.41	13.46	12.10	60.00	26.23

Total Mass (kg) 29.90

Slot liner (Radial) 0.98

Slot liner (Circ) 0.49

SR machine thermal parameters

Slot depth = 41.0mm

		Back Iron	Conductor Bundle	Tooth Body	Tooth Tip	Rotor Tooth body	Rotor Back Iron	End Winding
Radial	R1	0.3495	14.7974	1.3722	0.4574	0.3188	0.5425	1.4091
	R2	0.3662	18.4630	1.3722	0.4574	0.3188	0.5989	
	Rm	-0.1192	-5.5434	-0.4574	-0.1525	-0.1063	-0.1897	-0.5729
Axial	R1	123.3759	0.2777	36.0376	108.1128	137.0614	110.5243	
	R2	123.3759	0.2777	36.0376	108.1128	137.0614	110.5243	
	Rm	-41.1253	-0.0926	-12.0125	-36.0376	-45.6871	-36.8414	
Circular	R1	0.3148	2.8898	0.0821				
	R2	0.3148	2.8898	0.0821				
	Rm	-0.1049	-0.9633	-0.0274				
Capacity		26.87	42.33	46.02	15.33	12.10	60.00	30.64

Total Mass (kg) 32.08

Slot liner (Radial) 0.94

Slot liner (Circ) 0.43

SR machine thermal parameters

Slot depth = 46.0mm

		Back Iron	Conductor Bundle	Tooth Body	Tooth Tip	Rotor Tooth body	Rotor Back Iron	End Winding
Radial	R1	0.3399	15.9188	1.5395	0.5132	0.3188	0.5425	1.2560
	R2	0.3556	20.2470	1.5395	0.5132	0.3188	0.5989	
	Rm	-0.1158	-6.0276	-0.5132	-0.1711	-0.1063	-0.1897	-0.5106
Axial	R1	119.8907	0.2395	32.1205	96.3614	137.0614	110.5243	
	R2	119.8907	0.2395	32.1205	96.3614	137.0614	110.5243	
	Rm	-39.9636	-0.0798	-10.7068	-32.1205	-45.6871	-36.8414	
Circular	R1	0.3240	2.6577	0.0731				
	R2	0.3240	2.6577	0.0731				
	Rm	-0.1080	-0.8859	-0.0244				
Capacity		27.66	48.69	51.63	17.20	12.10	60.00	35.24

Total Mass (kg) 34.33

Slot liner (Radial) 0.90

Slot liner (Circ) 0.39

SR machine thermal parameters

Slot depth = 51.0mm

		Back Iron	Conductor Bundle	Tooth Body	Tooth Tip	Rotor Tooth body	Rotor Back Iron	End Winding
Radial	R1	0.3307	16.9505	1.7069	0.5690	0.3188	0.5425	1.1328
	R2	0.3456	21.9517	1.7069	0.5690	0.3188	0.5989	
	Rm	-0.1127	-6.4837	-0.5690	-0.1897	-0.1063	-0.1897	-0.4606
Axial	R1	116.5970	0.2092	28.9714	86.9142	137.0614	110.5243	
	R2	116.5970	0.2092	28.9714	86.9142	137.0614	110.5243	
	Rm	-38.8657	-0.0697	-9.6571	-28.9714	-45.6871	-36.8414	
Circular	R1	0.3331	2.4707	0.0660				
	R2	0.3331	2.4707	0.0660				
	Rm	-0.1110	-0.8236	-0.0220				
Capacity		28.44	55.33	57.24	19.07	12.10	60.00	40.05

Total Mass (kg) 36.63

Slot liner (Radial) 0.86

Slot liner (Circ) 0.35

SR machine thermal parameters Slot depth = 56.0mm

		Back Iron	Conductor Bundle	Tooth Body	Tooth Tip	Rotor Tooth body	Rotor Back Iron	End Winding
Radial	R1	0.3221	17.9027	1.8742	0.6247	0.3188	0.5425	1.0317
	R2	0.3362	23.5823	1.8742	0.6247	0.3188	0.5989	
	Rm	-0.1096	-6.9142	-0.6247	-0.2082	-0.1063	-0.1897	-0.4194
Axial	R1	113.4795	0.1848	26.3847	79.1540	137.0614	110.5243	
	R2	113.4795	0.1848	26.3847	79.1540	137.0614	110.5243	
	Rm	-37.8265	-0.0616	-8.7949	-26.3847	-45.6871	-36.8414	
Circular	R1	0.3423	2.3169	0.0601				
	R2	0.3423	2.3169	0.0601				
	Rm	-0.1141	-0.7723	-0.0200				
Capacity		29.22	62.25	62.85	20.94	12.10	60.00	45.06

Total Mass (kg) 39.00

Slot liner (Radial) 0.82

Slot liner (Circ) 0.32

SR machine thermal parameters Slot depth = 61.0mm

		Back Iron	Conductor Bundle	Tooth Body	Tooth Tip	Rotor Tooth body	Rotor Back Iron	End Winding
Radial	R1	0.3139	18.7841	2.0415	0.6805	0.3188	0.5425	0.9471
	R2	0.3272	25.1435	2.0415	0.6805	0.3188	0.5989	
	Rm	-0.1068	-7.3213	-0.6805	-0.2268	-0.1063	-0.1897	-0.3851
Axial	R1	110.5243	0.1646	24.2220	72.6660	137.0614	110.5243	
	R2	110.5243	0.1646	24.2220	72.6660	137.0614	110.5243	
	Rm	-36.8414	-0.0549	-8.0740	-24.2220	-45.6871	-36.8414	
Circular	R1	0.3514	2.1881	0.0552				
	R2	0.3514	2.1881	0.0552				
	Rm	-0.1171	-0.7294	-0.0184				
Capacity		30.00	69.45	68.46	22.81	12.10	60.00	50.27

Total Mass (kg) 41.42

Slot liner (Radial) 0.79

Slot liner (Circ) 0.29

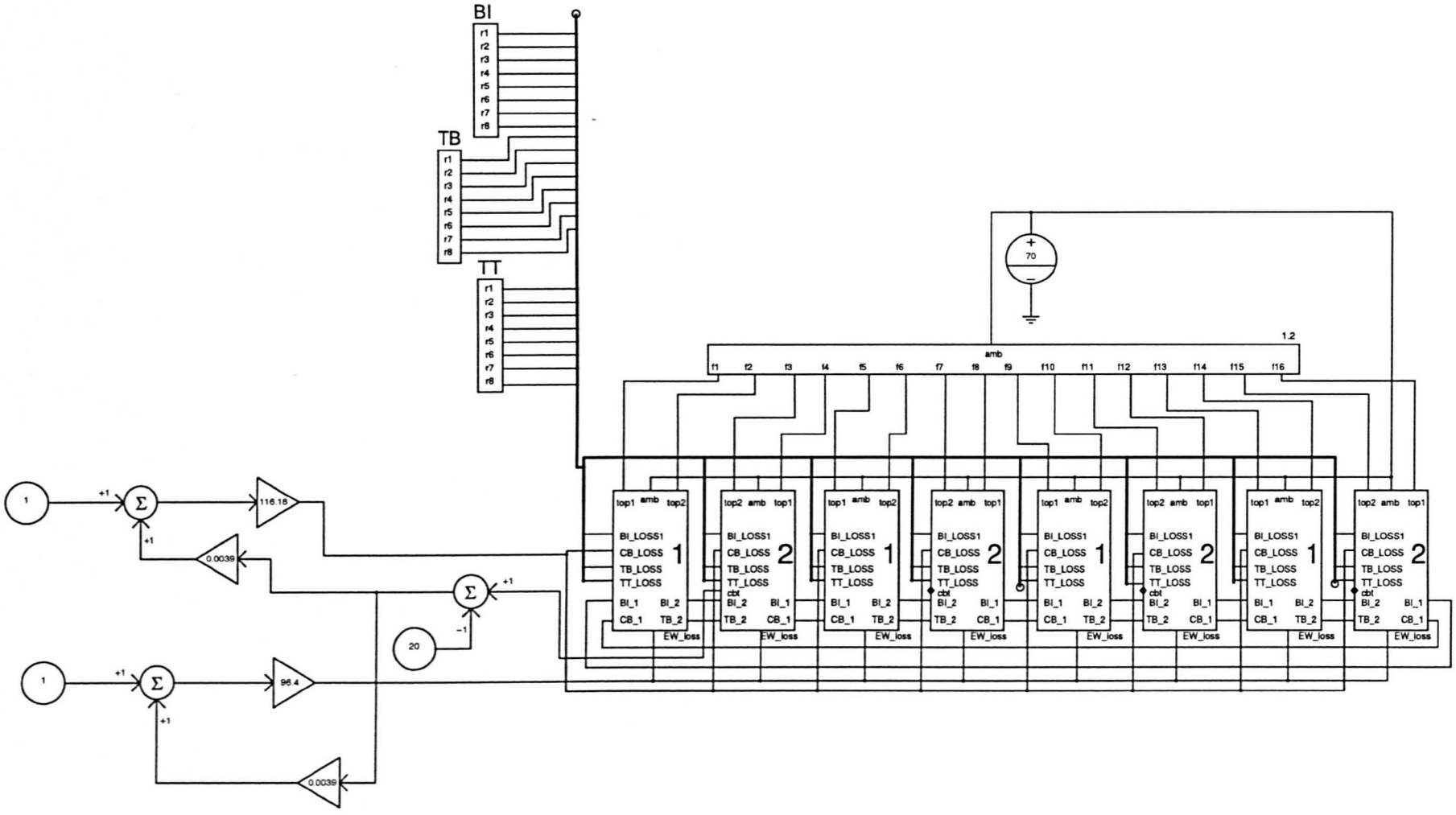

Figure C1. Top level of stator thermal model showing the 8 sections modelled.

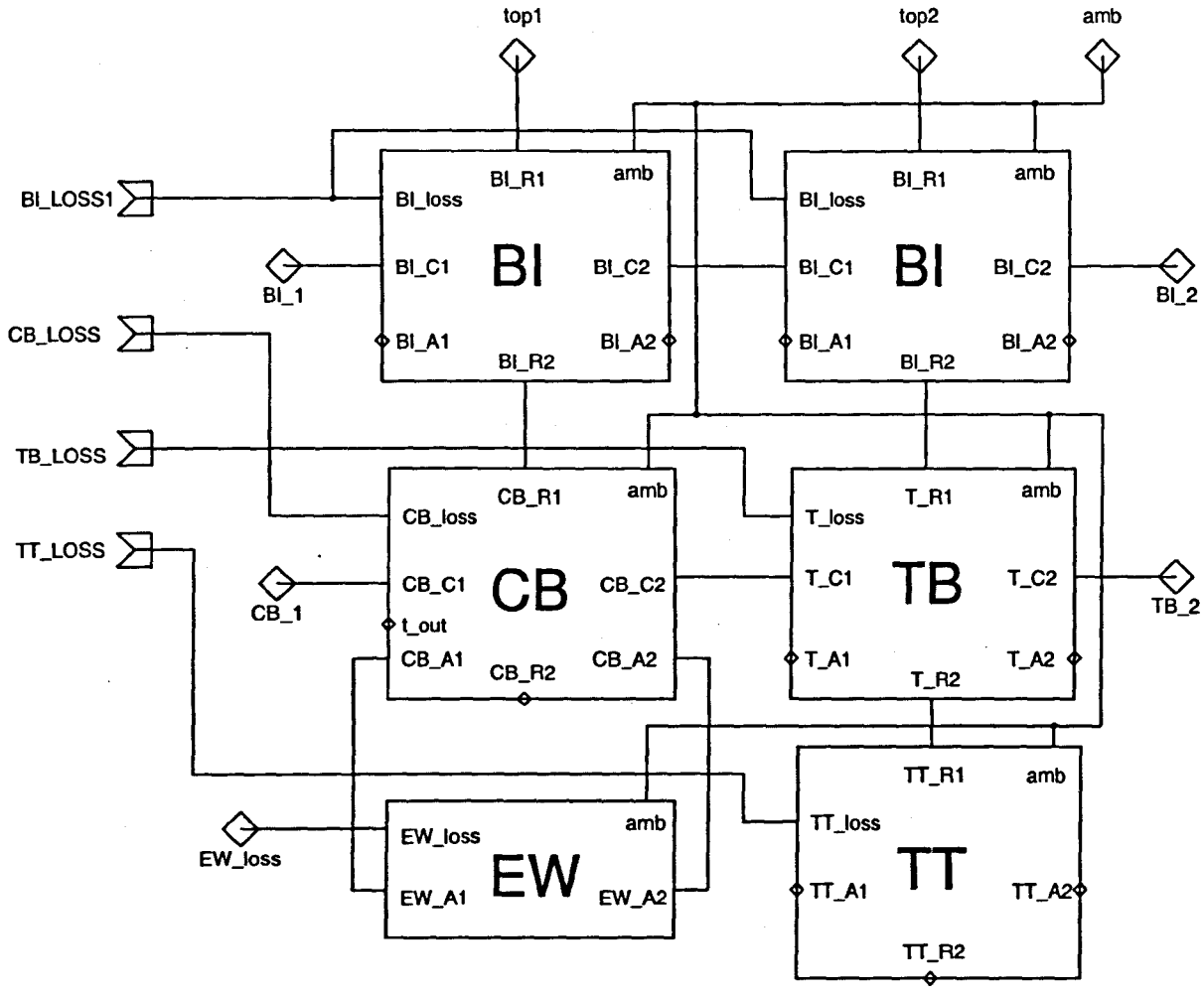

Figure C2. One half-slot section showing winding, back iron, tooth body, tooth tip, and end-winding

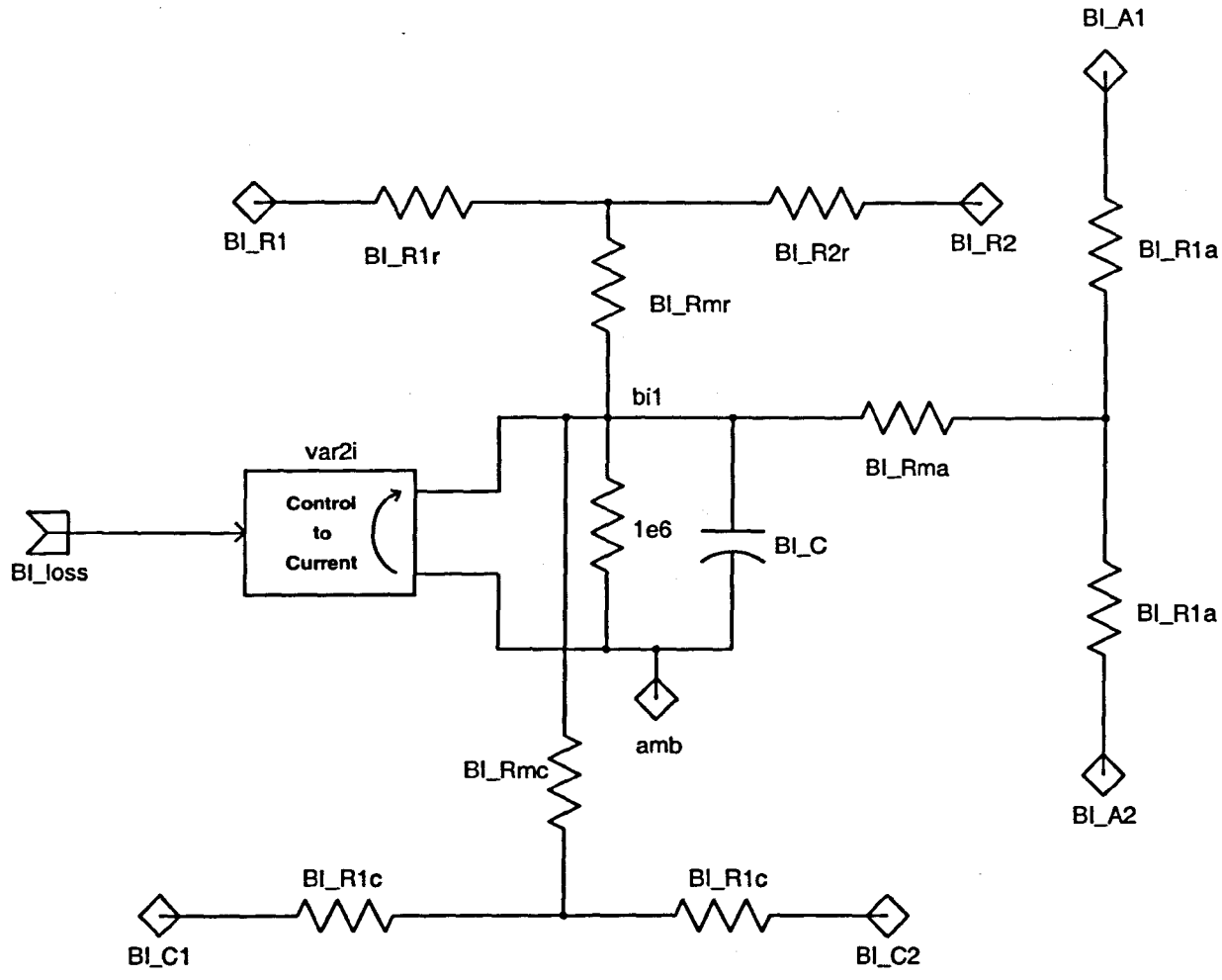

Figure C3. Back iron region

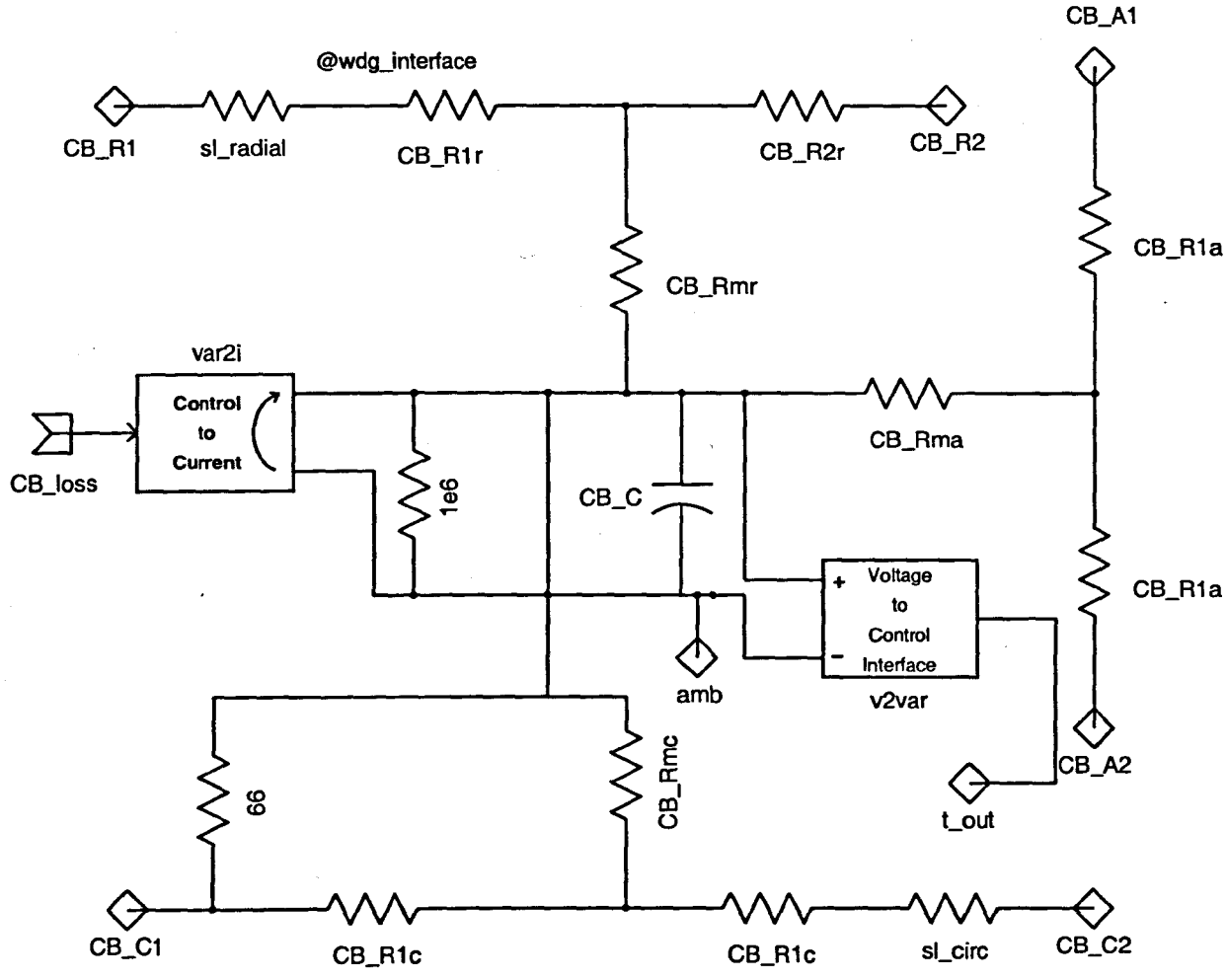

Figure C4. Conductor bundle region

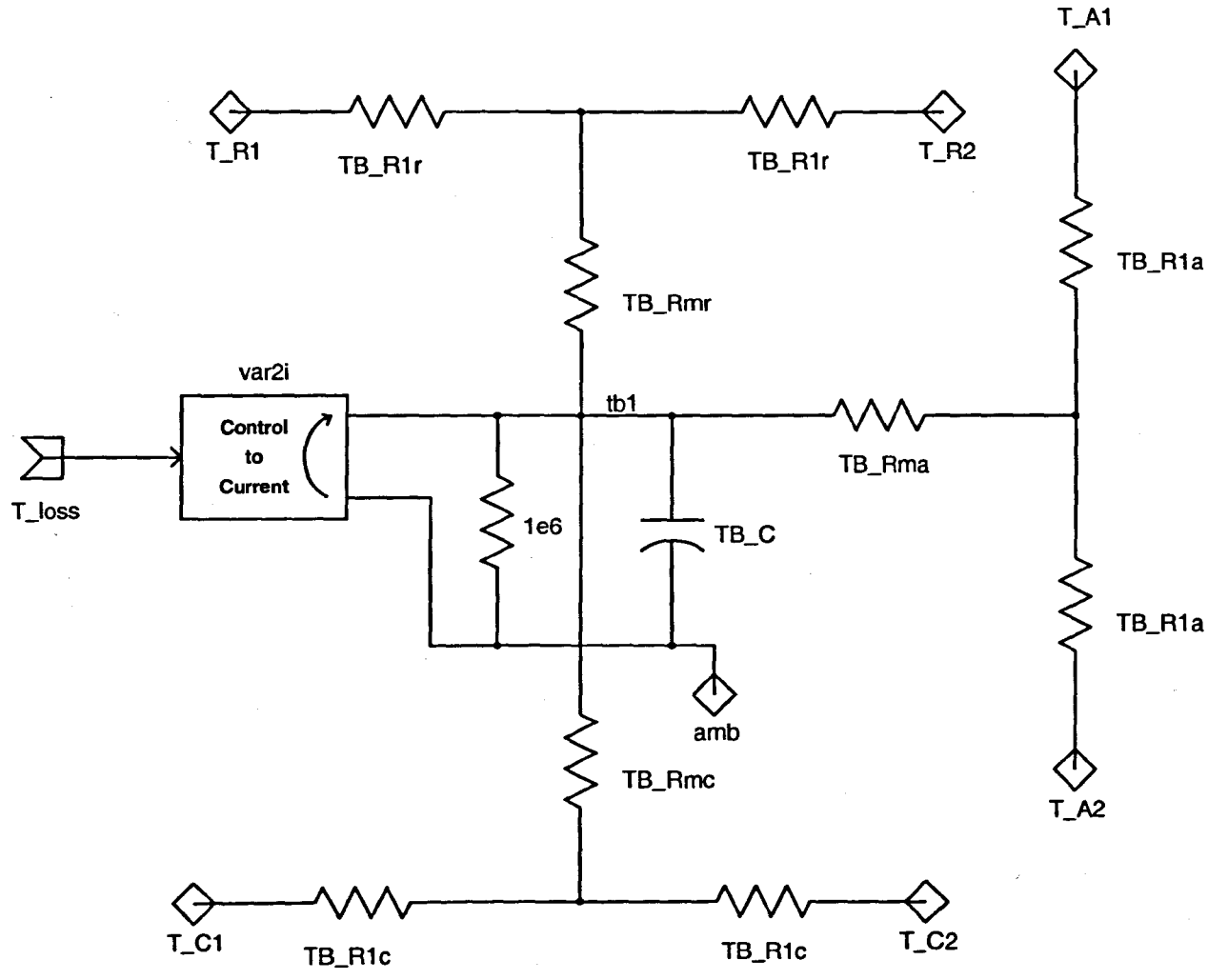

Figure C5. Tooth body region

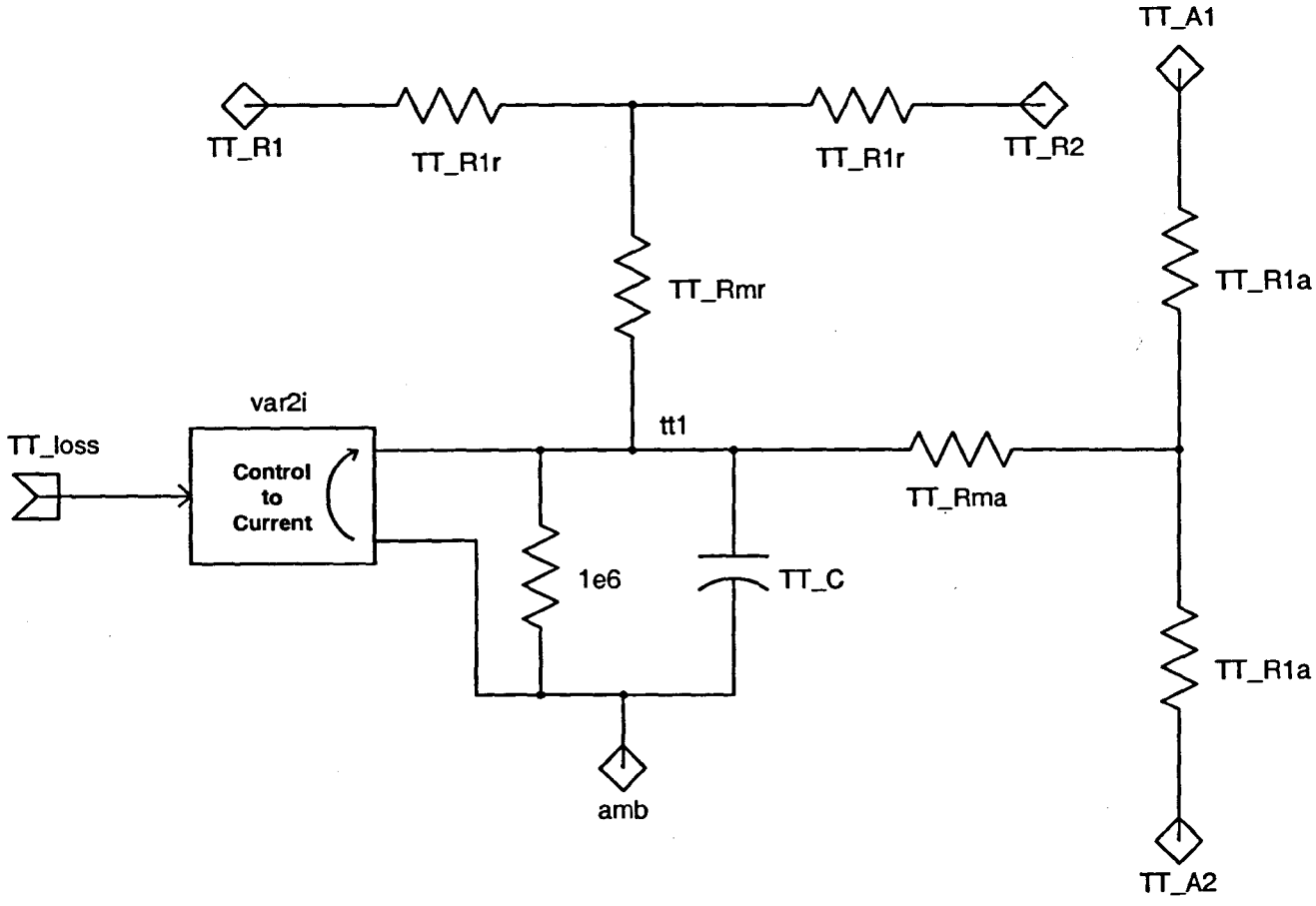

Figure C6. Tooth tip region

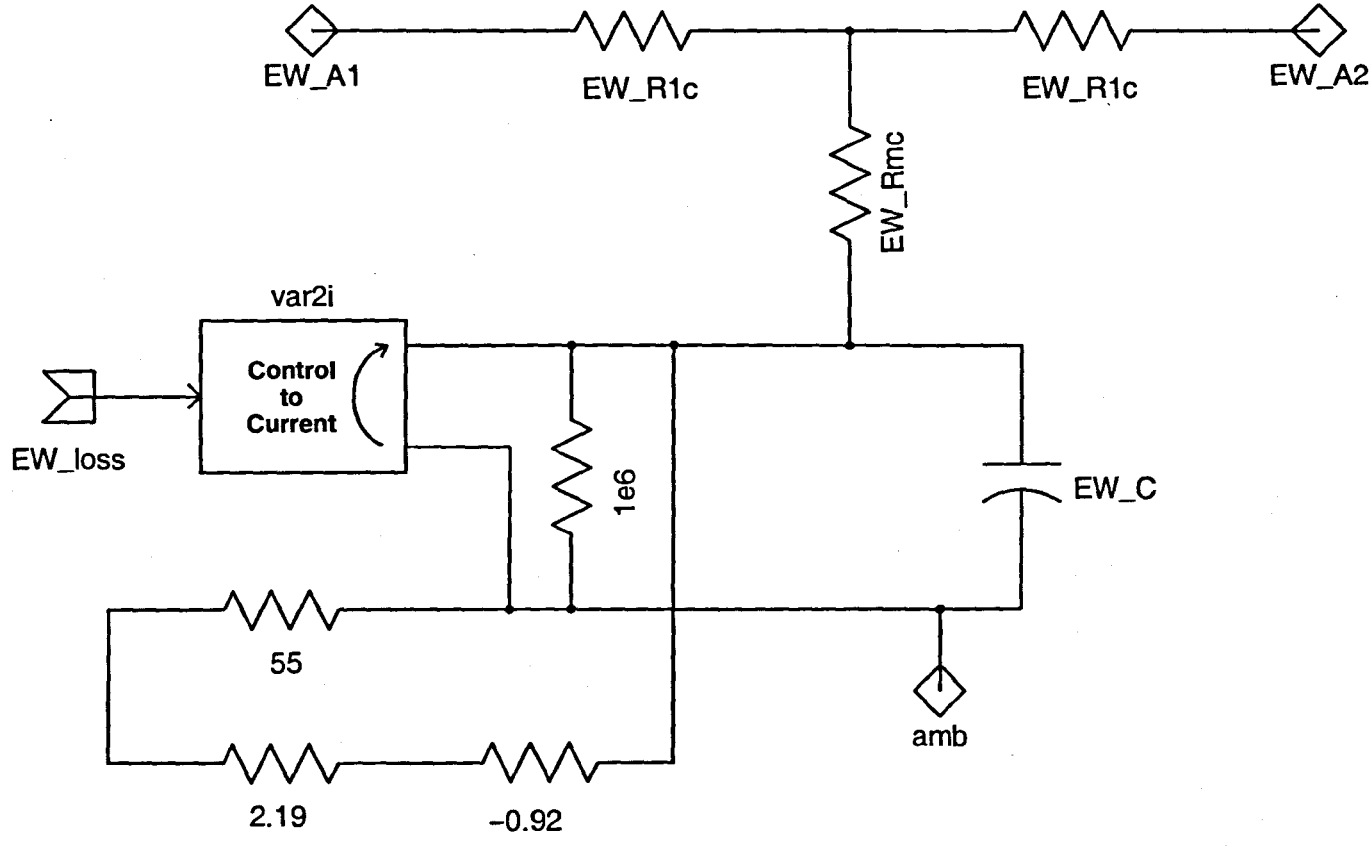

Figure C7. End winding region

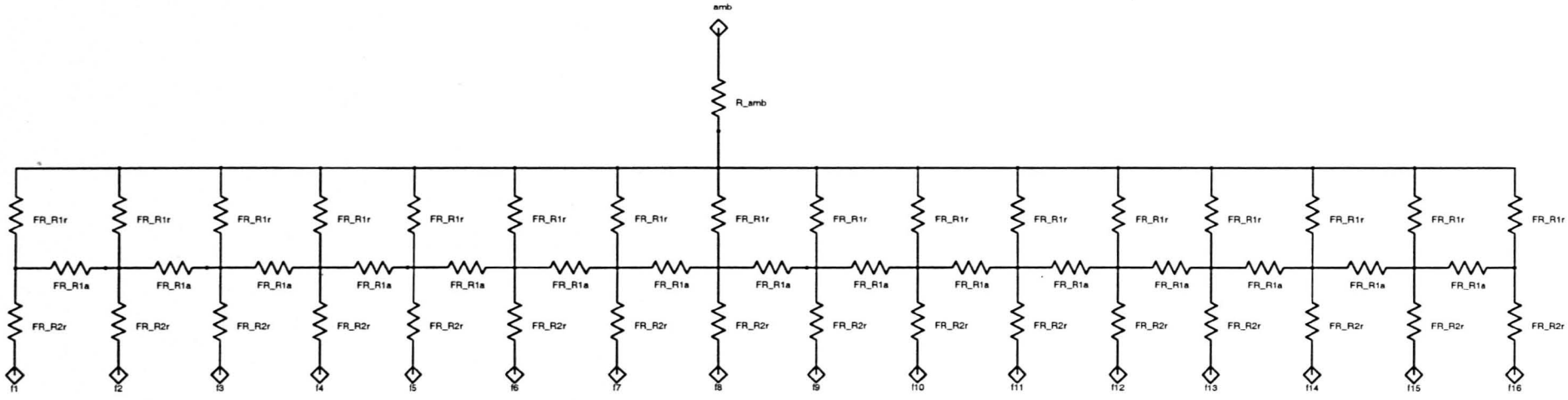

Figure C8. Frame region

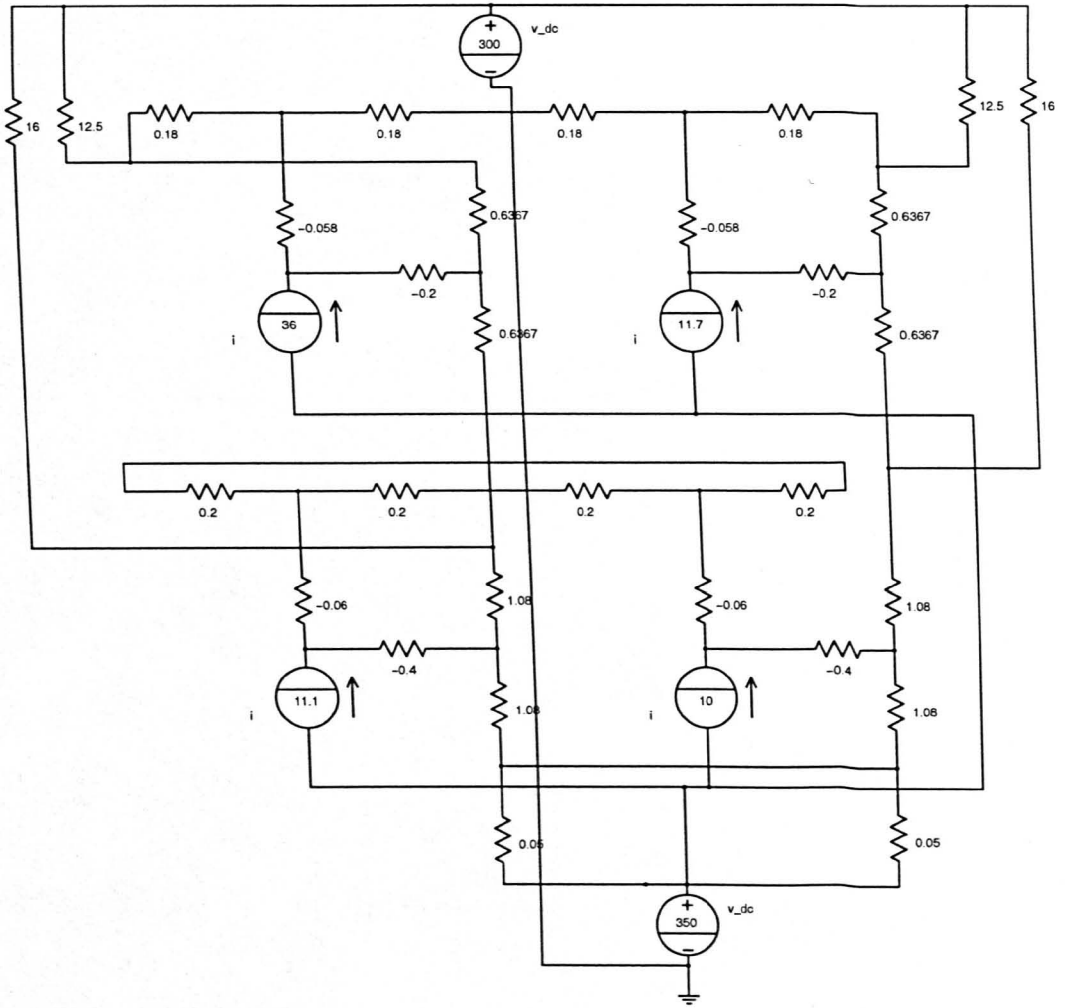

Figure C9. Switched reluctance rotor thermal model.